Crystallisation of Amorphous Fenofibrate and Potential of the Polymer Blend Electrospun Matrices to Stabilise in its Amorphous Form

Pratchaya Tipduangta, B.Pharm

Thesis submitted for the degree of Doctor of Philosopy

University of East Anglia

School of Pharmacy

November 2016

Abstract

Fenofibrate was chosen as the drug of interest in this study because of its poor water-solubility, highly unstable amorphous state and unpredictable crystallisation behaviour. The crystallisation behaviour of amorphous fenofibrate is essential information that primarily corresponds to the physical stability of solid dispersion formulations. This project aims to probe how to control the crystallisation of amorphous fenofibrate, enhance its aqueous solubility and improve its physical stability by using electrospun polymer blend matrices. A range of characterisation technologies including MTDSC, ATR-FTIR, PXRD, SCXRD, SEM, TEM, HS-PLM, nano-TA and ss-NMR were used to characterise the physicochemical properties of both the crystallisation process of fenofibrate, and fenofibrate solid dispersions. The amorphous fenofibrate was crystallised using heterogeneous nucleation techniques, including surface disruption and impurity addition (talc). The presence or absence of an open top surface (OTS) was found to be one of the key factors which dictated the crystallisation of the amorphous fenofibrate into specific polymorphs. The use of thermal treatment in addition to OTS was able to finely tune the selectivity of the crystallisation of fenofibrate to form I or/and form IIa. The use of a low percentage of talc as heterogeneous nuclei resulted in the crystallisation of the new fenofibrate polymorph III. The polymer blend fibres prepared by electrospinning were phase separated solid dispersions that improved the aqueous solubility of the fenofibrate in comparison to the fenofibrate crystals. The drug-polymer and polymer-polymer miscibility were found to be the key parameters that affected the physical stability of the incorporated amorphous drug and the phase separation in the formulations. Additionally, the *in situ* phase separation of the hydrophilic and hydrophobic polymers in the blends led to modified drug release. The drug release rate could be fine-tuned by altering the ratio of the polymers. The new knowledge generated by this work relates to the following areas: 1) an improved understanding of the crystallization process of fenofibrate and its polymorphic control; 2) the use of polymer blend matrices in electrospun fibres that leads to the stabilization of amorphous drugs when they are incorporated in those fibres; and 3) the modification of the drug release profiles via the use of hydrophilic and hydrophobic polymer blend matrices for electrospinning.

Acknowledgement

It has been a long journey through my PhD at the school of Pharmacy, University of East Anglia. I have made new friends, networks and developed my research skills. I would like to use this opportunity to show my appreciation to the people who have continuously supported me through this fantastic journey. First of all, I would like to express my gratitude to my supervisors, Dr. Sheng Qi and Dr. László Fábián, for their excellent supervision, numerous brilliant ideas, continuous encouragement, giving their precious time for discussions and patiently assisting me through my PhD. Besides, I am very grateful to have received the invaluable assistance of Prof. Peter Belton for devoting his time to numerous discussions and helping me with my solid state NMR and FTIR work. Many thanks to Dr. Li Ying Wang and Prof. Huiru Tang from the Wuhan Institute of Physics and Mathematics for helping with the solid state NMR experiments. Special thanks to Dr. Klaus Wellner from the Institute of Food Research, Norwich Research Park, for helping with the FTIR imaging and Mr. Khaled Takieddin for the single crystal data analysis. Furthermore, I would like to acknowledge financial support from the EU INTERREG IVA 2 Mers Seas Zeëen Cross-border Cooperation Programme. I would also like to express my gratitude to Associate Prof. Jakkapan Sirithunyalug, Faculty of Pharmacy, and Assistant Prof. Sukum Eitssayeamin, Department of Physics, Faculty of Science, Chiang Mai University, for their invaluable help on setting up the instruments and discussions on practical challenges. Besides, I am very grateful for the help of Dr. Siok Yee Chan, Dr. Maria De Fatima Gomes Pina, Dr. Kate Bowman, Dr Jonathan Moffat and Dr. Ziyi Yang who showed me a warm welcome to the UEA drug delivery group and gave assistance throughout the first year of my PhD.

I would like to extend my thanks to all my friends whom I met in the UK and who shared precious memories with me throughout my PhD at UEA: Ms Mariko Hori, Dr. Chan Yodle, Dr. Chatuphon Charoenkitpaiboon, Dr. Sasiri Chaichana, Mr. Kai Hui Leong, Dr. Choon Fu Goh, Dr. Varin, Mr. Chaya Vaddhanaphuti, Ms. Yang Xiao and Mr. Xin Liao. Regarding my thesis writing, I would like to thank Dr. Elise Wright, Dr. Gill Price and Dr. Jolyon Dodgson for helping me improve my writing. Thanks to all my colleagues in the School of Pharmacy and the Drug Delivery Group: Mr. Muqdad Alhijaj, Ms. Cholpon Rustem Kyzy, Ms. Valeria Gabrielli, Mr. Karol Nartowski and Ms. Susana Campos E Menezes Jorge Ramalhate.

Last but not least, I would not have been able to achieve this endeavour without the unconditional love, continuous support and encouragement from my beloved parents, Associate Prof. Pramote Tipduangta and Mrs. Wassana Tipduangta, and my grandparents, Mr. Marnit Bhurimratana and Mrs. Pimpa Bhurimratana. A special thanks to Ms. Kanokwan Heng-ia for her consistent encouragement.

Table of Contents

List of Figures

List of tables

Abbreviations

AFM Atomic force microscopy

API Active pharmaceutical ingredient

ATR-FTIR Attenuated Total reflectance fourier transform infrared

C_p Heat capacity

DE Double exponential

DSC Differential scanning calorimetry

DVS Dynamic vapour sorption

ES Electrospinning

FF Fenofibrate

FDM Fusion deposit model

GAB Guggenheim-Anderson-de Boer

GT Gordon-Taylor

HPMCAS Hymomellose acetate succinate

IM Injection moulding

OTS Open top surface

PCM Paracetamol

PVP Polyvinyl pyrrolidone

PXRD Powder X-ray diffraction

MTDSC Modulated temperature differential scanning calorimetry

Mw Molecular weight

SEM Scanning electron microscopy

ss-NMR Solid state nuclear magnetic resonance

TEM Transition electron microscopy

T_g Glass transition temperature

1. Chapter 1 Introduction

1.1 Background

Crystallisation is a transformation process from a liquid phase to an organised solid state structure (1). The liquid phase can be a supersaturated solution or supercooled liquid from melts which has high enthalpy and specific volume. Hence, it is thermodynamically favourable for a phase transition into a crystalline state when the temperature is lower than the melting point in supercooled liquid, and the concentration is greater than solubility in the supersaturated solution, which is more stable and has a lower energy state (1). Crystallisation begins with an aggregation of several molecules (nuclei) that act as seeds for the subsequent step of regular molecular assemble into crystalline structures. The supersaturated or supercooled liquid can crystallise into more than one possible crystalline structure (1-3), so called polymorphism. Therefore, controlling crystallisation into the desired polymorph is extremely important for the pharmaceutical industry. This can be used as a means to increase the aqueous solubility of poorly water-soluble compounds including active pharmaceutical ingredients (API) (3, 4). There are several factors that directly affect the resulting polymorphs of the crystallising substances. These include the interfaces of the crystallising substances, temperatures and foreign additives (5-8). However, up to now, the precise control of the crystallisation of certain polymorphs has remained a challenging task for the pharmaceutical industry, as there seems to be no universal rule that can be applied and each API needs to be investigated on a case by case basis.

Fenofibrate (FF) was chosen to be the main model drug in this project. Its amorphous form shows high driving forces to crystallise under the whole range of temperatures (9). However, amorphous FF is difficult to crystallise spontaneously because it has a high nucleation barrier (9, 10). Thus, it displays highly unstable and unpredictable crystallisation behaviour. Polymorphs of FF have been reported, but the knowledge of how to manipulate its crystallisation into a particular polymorph has not been fully established (11). In addition, FF is a biopharmaceutical classification system (BCS) class II drug that has high permeability and low solubility. The limited aqueous solubility of FF is another problem that needs to be addressed. This project probed both aspects of this API. The crystallisation control of amorphous FF was studied first.

Solid dispersion is one of the effective strategies that significantly improves the bioavailability of poorly water-soluble drugs. This concept was introduced more than half a century ago by Chiou and Riegelman (12). The APIs can exist in the solid dispersion matrices in crystalline form, amorphous suspension or molecular dispersions. The molecular dispersions have been reported to provide a better effectiveness for enhancing the aqueous solubility of the poorly water-soluble APIs in comparison to the crystalline

solid dispersion (13, 14). However, many of the commonly used molecular dispersion carriers are hygroscopic, which is favourable to uptake moisture. Thus, this potentially causes phase separation of the APIs during storage and eventually recrystallization. An attempt to use solid dispersion to increase the aqueous solubility issue of FF was then investigated in the second half of the project (15, 16).

Solid dispersions containing a polymer blend is a potential method that can efficiently increase the stability of amorphous drugs (17, 18). Blending hydrophilic and hydrophobic polymers can enhance the stability of the formulations by reducing the moisture uptake (18). Additionally, polymer blends have been used to formulate the modified release formulations used in drug delivery. The drug release rate from the solid dispersion matrices can be tailored by altering the proportion of water soluble and water insoluble polymers (19-21). These studies focused more on the applications of polymer blends, but a few had an emphasis on understanding the ternary blends of polymers and API because the ternary components of the polymer blends in the solid dispersion is a complex system. Hence, this project aims to gain a better understanding of polymer blended solid dispersions.

This project used electrospinning as the main stream preparation method for the solid dispersions. Electrospinning is a novel approach that renders polymer matrices into nano to micro sized fibrous structured (22-24). The small fibrous matrices of electrospun fibres offer benefits by increasing the surface area to volume ratio that results in enhancing the solubility of poorly water-soluble APIs with an ultrafast drug release (25-27). Therefore, electrospinning has the potential to be a platform for a solid dispersion containing polymer blended to stabilise the APIs in their amorphous state.

1.2 Amorphous materials

Amorphous is an isotropic non-crystalline solid state in which the structure has no order, including translational, orientational, conformational at any significant length scale (28, 29). However, amorphous APIs demonstrate complex structures caused by local anisotropy (28). This local anisotropy induces a short range order at the local scale. The distance of the short range order is within the nearest neighbour or the next nearest neighbour, which is usually less than 20-25 Å (28). The pairwise distribution function of amorphous piroxicam, which is obtained from the cryomilling of its crystalline form I, demonstrated its near neighbour interactions that correspond to the atom-atom distance of approximately 4.9-12.3 Å (30). Hence, the amorphous APIs show short-range order at the local scale because of the local anisotropic effect, but for the overall macroscopic picture, they are isotropic. The structure of amorphous materials is illustrated in **Figure 1.1a**.

A perfect crystal ideally represents a solid state that is organised and regular. The **Figure 1.1b** describe an appearance on the disorder in solid state due to the increase in

configuration entropy which refers to the thermodynamic disorder. An increase of the disorder in the solid state transform the crystal to meso-phase and eventually amorphous state which has no order its the structure. The degree of disorder increases (projected by a dashed arrow **Figure 1.1b**) as a result of losing the long-range order of the crystal. The kinetic disorder can be studied using powder X-ray diffraction. Crowley and Sheth demonstrated that grinding caused the crystal diffraction peaks of indomethacin and piroxicam to broaden (30, 31). Continual grinding leads to a broad baseline with no diffracted peak (halo pattern). The broadening of the diffracted peak reflects the increase of disorder in the solid state until it develops the highest disorder, which leads to an amorphous state. Additionally, thermal analysis can be used as a means to discriminate between crystalline and amorphous materials (28, 32). A solid state with a combination of order parameters (crystalline and meso-phase state) will exhibit a melting transition. An amorphous material will present a glass transition, which indicates no long-range order (**Figure 1.1b**).

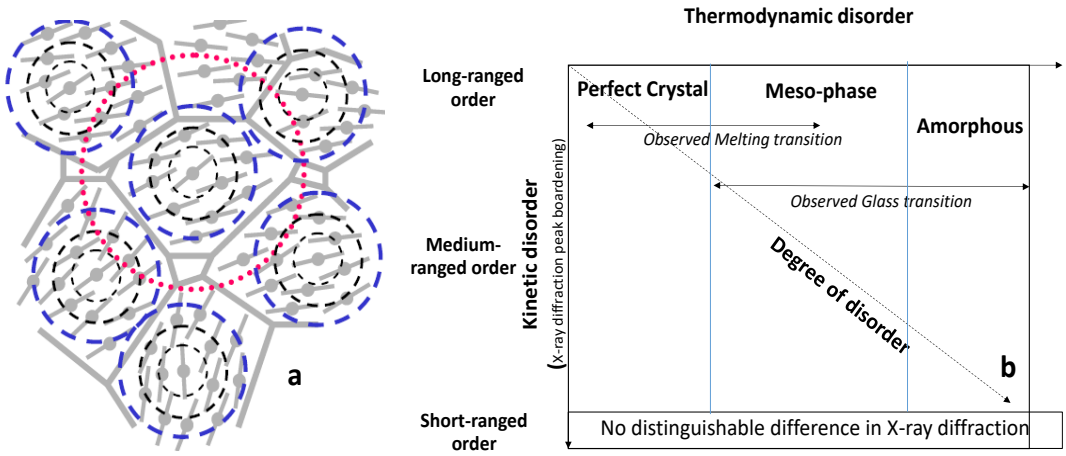

Figure 1.1 Structure of amorphous materials (a) and schematic diagram illustrating thermodynamic disorder and kinetic disorder of solid state (b). This figure is adapted from reference (28).

Figure 1.2 illustrates a schematic plot of the enthalpy or a specific volume of a solid compound as a function of temperature. The enthalpy or specific volume of a crystalline material demonstrate a small change upon heating because the molecules are packed in a lattice structure (32). After the temperature reaches its melting point, the molecules detach from the crystalline structure and transform into a liquid state that results in increased enthalpy and specific volume of the molecules. On cooling, the enthalpy and volume of the liquid follow the equilibrium of the supercooledliquid. However, a further cooling leads to the slope of the enthalpy and the specific volume deviating to the non-equilibrium state. The viscosity of the supercooled liquid significantly increases to 10^{12} from 10^{-3} Pa.s (32).

The temperature where the slope changes is defined as the glass transition temperature (T_g), which is a characteristic property of amorphous materials. The enthalpy and specific volume of the amorphous state are greater than a supercool liquid because it is in the non-equilibrium state. Therefore, the amorphous state inherents a high energy level and molecular motion (29, 32).

From the pharmaceutical perspective, the greater the enthalpy and specific volume of an amorphous state in comparison to the crystalline complement, demonstrates a potential benefit for enhancing the solubility and bioavailability of APIs (29, 32-34). Kim et al. reported that when amorphous atorvastatin was prepared from spray-drying and supercritical antisolvent there was a significant improvement in its aqueous solubility (34). The crystalline atorvastatin showed a saturated aqueous solubility at 140 $\mu g.ml^{-1}$, while the maximum saturated solubility of its amorphous form was approximatly 460 $\mu g.ml^{-1}$. Hancock and Parks reported an increase in the aqueous solubility of amorphous indomethacin over its crystalline α and γ polymorphs by approximately 2.8-4.5 fold (33). The short-range order in the amorphous structure, which require less energy to break down, and its high internal energy level are the factors that enhance the aqueous solubility of the amorphous materials (35).

However, the high internal energy can also lead to spontaneous conversion to the crystalline state. Wu et al. reported a crystallisation of amorphous indomethacin at a temperature below its T_g (36). Additionally, a similar observation for amorphous nifedipine showed that it was crystallised at its T_g, as reported by Zhu et al. (37). Moreover, a solvent-mediated conversion also occurs in amorphous atorvastatin and indomethacin during their dissolution (33, 34). Consequently, the drugs' aqueous solubility decreased. Hence, the amorphous state can potentially increase the aqueous solubility of APIs, but it also contains a risk of recrystallization to its thermodynamic stable crystalline state.

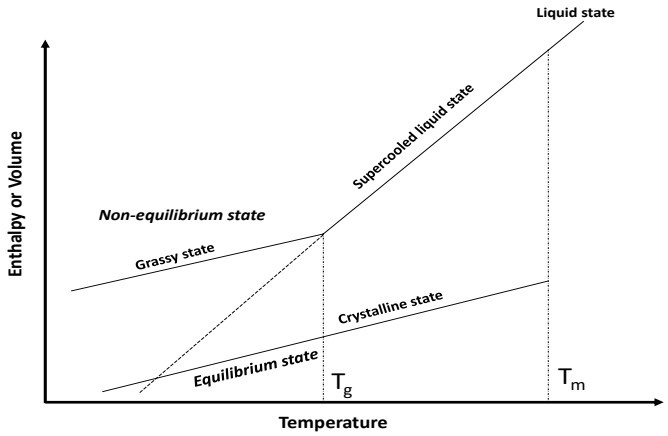

Figure 1.2 Diagram illustrating the changing enthalpy or volume according to temperature in different material states.This figure was adapted from reference (32).

The amorphous materials can be obtained various ways. Some materials naturally exist in an amorphous state, such as pharmaceutical polymers including PVP, hypromellose (HPMC) and ethyl cellulose. This is due to their long chain structure that is oriented randomly and entangled with each other (38). Moreover, crystalline materials can be transformed into an amorphous state after being processed by milling, rapid precipitation by anti-solvent addition, solvent evaporation and melt-cooling (5, 30, 31, 34, 36, 37, 39). Melt-cooling is the most well studied and effective approach to prepare an amorphous form from its crystal (36, 37, 40). However, it has not been applied to heat unstable compounds. Additionally, the multicomponent formulations of API and polymer can result in the amorphous state of the drug (12). This method is known as a solid dispersion, which will be discussed in detail in section 1.4.

1.3 Crystalline materials

Solid state materials that have a regular atomic/molecular arrangement with long range ordered are defined as crystals. Crystalline materials have a lower enthalpy and specific volume in comparison to the amorphous state, which implies that they are more thermodynamically stable (29, 32). Frequently, the same compound may exhibit more than one possible crystalline structure (2, 3). This phenomenon is called polymorphism, which will be discussed in detail in section 1.3.4. The differences in the structure arrangements usually affect the physicochemical properties of the materials, such as melting point, solubility, density, compressibility, bioavailability stability and reflective index (2, 3).

Figure 1.3 illustrates the molecular arrangements of crystals with polymorphs in comparison to the amorphous form.

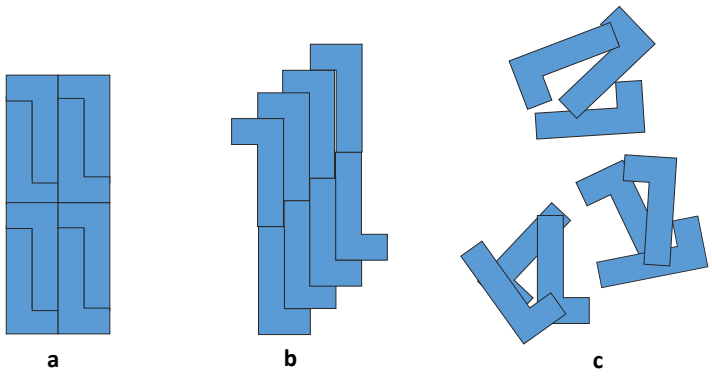

Figure 1.3 Molecular arrangement of materials with different solid states: the uniform molecular arrangement with long range order in crystalline materials (a) and (b), which are polymorph, and the irregular short range ordered of amorphous materials (c).

1.3.1 Crystallisation

Crystallisation is defined as a phase transformation from a non-crystal state, either liquid phase or amorphous state, to its corresponding crystalline solid phase (1, 2). This process involves both thermodynamics and kinetics. Crystallisation is composed of two essential steps, which are a nucleation step followed by crystal growth. The nucleation step is a thermodynamic process. Clusters or nuclei are formed as a result of changes in the Gibb's free energy at the molecular level (ΔG), which contributes to the sum of the surface free energy (ΔG_s) change and volume free energy change (ΔG_v), and the relationship is given in **equation 1.1** (41). Nucleation occurs when the size molecular aggregation surpasses the critical radius, which is known as the nucleation barrier (1).

$$\Delta G = \Delta G_v + \Delta G_s \quad \text{.....(1.1)}$$

Crystal growth is the subsequent step after nucleation. This step involves the kinetics of molecular diffusion to the site of nucleation, and the molecules integrate into uniform structures (1, 41).

1.3.2 Nucleation

Nucleation is a transition process in which the supersaturation liquid begins to form a new phase in the solid state. It can be categorised into primary nucleation and secondary nucleation (1). The nucleation that spontaneously occurs in the mother phase is defined as the primary nucleation, and this can be further sub-categoried into homogeneous and heterogeneous nucleation. In homogeneous nucleation, clusters appear randomly

throughout the whole sample, while heterogeneous nucleation occurs at preferential sites, for example, at the boundaries, surface, walls of containers, edges and impurities. Heterogeneous nucleation is more likely to occur than homogeneous nucleation because the surface energy at the preferential sites is low. Thus, this enhances the nucleation process. The secondary nucleation refers to a crystal of the solute that is used as a seed for the nucleation.

1.3.2.1 Primary nucleation

1.3.2.1.1 Homogeneous nucleation

The spontaneous appearance of a new phase in homogeneous matrices is referred to homogeneous nucleation. The homogeneous nucleation is a spontaneous molecular aggregation that involves the intermolecular bonding of the compound (1). Nucleation occurs when molecular aggregation surpasses the critical radius. After this point, the Gibb's free energy of the nucleation decreases with increase nucleus size until it reaches a negative value then nucleation proceeds. Consequently, the nucleation takes place as a new phase (solid phase) in the non-crystalline phase. The classical nucleation theory (CNT) is described using **equation 1.2** (41, 42).

$$\Delta G = -\frac{4}{3}\pi r^3 \Delta G_v + 4\pi r^2 \gamma^{SL} \quad \text{..... (1.2)}$$

where ΔG is the overall Gibb's free energy of the nucleation process and r is the radius of the nuclei. CNT assumes that the nuclei are in a spherical shape, which substitutes as the term $4/3\pi r^3$. ΔG_v is a change in the volume free energy. These are demonstrated in the first term on the right-hand side of **equation 1.2**. The second term on the right side presents the interfacial energy between the solid and liquid phases (ΔG_s) where γ^{SL} is the interfacial tension per unit area of the liquid phase. The Gibb's free energy reaches its maximum value (ΔG_{crit}) when r is equal to the critical radius (r_c). This is called the nucleation barrier. The ΔG_{crit} can be expressed in **equation 1.3**.

$$\Delta G_{\text{crit}} = \frac{16\pi\gamma^3 v^2}{3(kT ln S)^2} \quad \text{.....(1.3)}$$

In which v is the frequency of the molecular transportation at the solid-liquid interface, γ is the interfacial tension per unit area, k is the Boltzmann's constant ($J.K^{-1}$), T is the absolute temperature of nucleation and S represents the degree of supersaturation. Clusters that have a radius smaller than r_c dissolve rather than continue to grow as crystals because they minimise their free energy level (1). Therefore, the ΔG_{crit} is the minimum free energy level required for the nucleation step, which is given in **equation 1.3**. If the cluster radius exceeds the r_c, the Gibb's free energy continuously decreases until it goes below zero

(**Figure 1. 4**). After this point, nucleation occurs spontaneously since the Gibb's free energy of the system is negative.

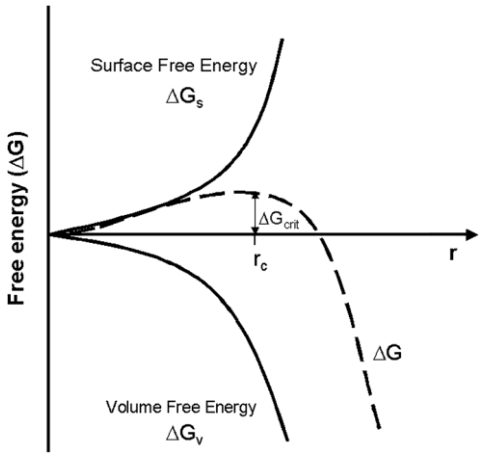

Figure 1. 4 Free energy diagram of homogeneous nucleation describing the existence of a critical nucleation barrier. Figure adapted from reference (43).

The nucleation rate (*J*) is the number of nuclei that form in the supersaturation phase per unit time in a specific volume. According to CNT theory, the factors, such as interfacial energy, mobility, thermodynamic driving force and molecular recognition, can influence *J* (1, 44). The rate of nucleation in the homogeneous nucleation can be described as:

$$J = A\ exp\left[\frac{16\pi\gamma^3 v^2}{3k^3T^3(\ln S)^2}\right] \quad \text{.....(1.4)}$$

where *A* is a frequency factor, γ is the interfacial tension, *v* is the frequency of molecular transportation at the solid-liquid interface, *k* is the Boltzmann constant, *T* is the absolute temperature of nucleation and S is the degree of supersaturation. In terms of the melt-supercooling, a similar expression of *J* in the homogeneous nucleation can be applied. However, the sharp increase in the viscosity upon the supercooling stage and nuclei not being a spherical shape leads to the unique characteristics of the nucleation of the melt (1, 45). A modified viscosity term is added to the equation by Turnbull and Fisher (45).

$$J = A\ exp\left[\frac{16\pi\gamma^3}{3kT_m\Delta H_f^2 T_r(\Delta T_r)^2} + \frac{\Delta G'}{KT}\right] \quad \text{.....(1.5)}$$

where *ΔG'* is the activation energy of the molecular motion required for nucleation, γ is the interfacial energy between the crystalline drug and the melt, ΔH_f is the heat of fusion, T is the absolute temperature of the nucleation process, T_m is the melting temperature of the drug in Kevin, T_r is the reduced temperature obtained from T/T_m and ΔT_r is $1\text{-}T_r$.

1.3.2.1.2 Heterogeneous nucleation

In fact, homogeneous nucleation is rarely happened. It only occurs in small volume containers that are less than 100 µL and under a carefully controlled environment (3, 46). A larger volume of a solution frequently contains foreign bodies, i.e., atmospheric dust, which can potentially act as active hetero-nuclei to induce the crystallisation process (1). Therefore, most nucleation occurs via heterogeneous nucleation. The Gibb's free energy of heterogeneous nucleation (ΔG_{hetero}) is a proportion of the Gibb's free energy of the homogeneous nucleation (ΔG_{homo}) to the factor $S(\theta)$, as described in **equation 1.6**.

$$\Delta G_{hetero} = \Delta G_{homo} . S(\theta) \quad \text{.....(1.6)}$$

Heterogeneous nucleation always occurs at preferential sites, such as the wall of a container, phase boundaries and impurity sites. The effect of the interfacial tension at these sites plays an important role in the nucleation process. The contact angle of the foreign phase and the solid surface is defined as θ, which corresponds to a wetting of the solid-liquid interface (1). The relationship of the contact angle (θ) to the interfacial tension is described in **equation 1.7**.

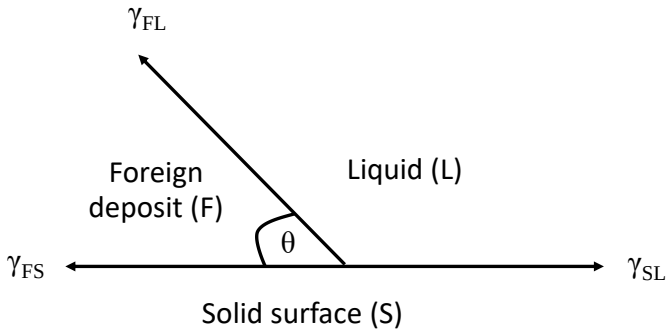

Figure 1.5 Interfacial tension at the boundary of the solid surface, foreign deposit and liquid phase. This figure is adapted from reference (1).

$$cos\theta = \frac{\gamma_{SL} - \gamma_{FS}}{\gamma_{FL}} \text{.....(1.7)}$$

where γ_{SL} is the interfacial tension of the solid-liquid phase, γ_{FL} is the interfacial tension of the foreign deposit-solid phase and γ_{FL} is the interfacial tension of the foreign deposit-liquid phase. The relationship between $cos\theta$ and $S(\theta)$ can be explained using **equation 1.8** (47).

$$S(\theta) = \frac{(2+\cos\theta).(1-\cos\theta)^2}{4} \text{.....(1.8)}$$

This equation suggests that if the contact angle (θ) is 180°, then $S(\theta)$ is equal to 1. When θ is less than 180°, the factor $S(\theta)$ will be between 0 and 1. This indicates that the nucleation process is favorable in a presence of a heterogeneous phase in the supercooled liquid because it requires less overall Gibb's free energy than the homogeneous nucleation process (1).

The heterogeneous nucleation demonstrates several advantages over the homogeneous nucleation. It is a standard approach to crystallising organic and inorganic compounds (7, 48-53), since the heterogeneous nucleation shows a better process control than the homogeneous nucleation. Particularly, heterogeneous nucleation using impurity additives is an efficient and controllable process. Consequently, it is one of the approaches that is used to crystallise materials at the industrial scale (2). In addition, another advantage of heterogeneous nucleation when using impurity additives is that it can control the crystallisation into a particular polymorphic form (7, 8, 50, 51). Chadwick et al. successfully used the heterogeneous approach via the addition of an impurity to induce a supersaturation solution of PCM to crystallise to a particular polymorph (7). They used 4-aminophenylacetic acid, which has a similar crystalline unit cell to the PCM form II, to induce the supersaturate solution of PCM to crystallise into its form II. The authors also showed that by using different impurities, such as L-histidine, graphite and D-mannitol, which had no structural relations, resulted in the stable paracetamol form I (7). Therefore, the structure of the additive strongly influences the polymorph it induces.

Lang et al. and Price et al. demonstrated the use of heterogeneous nucleation polymeric additives to control the crystallisations of APIs (8, 51). The supersaturated solutions of PCM, 5-methyl-2-[(2-nitrophenyl)amino]-3-thiophenecarbonitrile (ROY), carbamazepine and sulfamethoxazole crystallised into their specific polymorphs in the presence of particular polymers. For example, adding 2-ethoxyethyl methacrylate (EMMA) into a PCM supersaturated solution resulted in the PCM polymorph II crystallisation. While the use of methyl acrylic acid (MAA) and *N*-methacryloylmorpholine (MAM) showed high selectivity to the monoclinic form I of PCM (8). Price and colleagues suggested that the functional group of a monomer unit in the polymer chain is the primary driving force to stabilise a given crystal nucleus. Subsequently, it results in the controlled production of a particular polymorph (8).

However, there is no universal rule that can be applied to the impurity additives to control the crystallisation into a specific polymorph. The experiments in this area have been mostly based on trial and error (7, 51). One additive may show a polymorphic control effect in one substance, but applying the same additive to another compound may not result in the same effect. Therefore, the selective polymorph crystallisation phenomenon is explained by the interface interaction and intermolecular interaction between the impurity and compound

molecules that favour the crystallisation into a specific polymorph (7, 8). This effect needs to be considered case by case.

1.3.2.2 Secondary nucleation

The term "secondary nucleation" is defined as nucleation that occurs in the presence of a solute crystal (seed) in its supersaturation solution. The seeds serve as a trigger to form a new solid phase in the liquid phase (1). Secondary nucleation is broadly used in the industrial scale production of crystalline organic and inorganic materials, such as KCl, $MgSO_4$ and α-glucose (54-56). The seeding technique offers advantages of a narrow crystal size distribution when there is not much secondary nucleation and the easy initiation of difficult crystallisations (57). The seeds are deliberatly added into the supersaturation solution, which is continuously agitated. The seeds spread through the reactor and induce crystallisation from the supersaturated solution. The active seeds were reported to be between 200-500 µm. The seeds that were smaller than 100 µm did not produce secondary nucleation (1). Moreover, the seeds act as a template for the crystal to grow into the specific polymorph (57).

1.3.3 Crystal Growth

Crystal growth is the step after nucleation. The molecules regularly arrange themselves into a solid crystalline structure that has a lower free energy in comparison to a supersaturated liquid (1, 41). Crystal growth is composed of two main processes, which are a diffusion step and a surface crystal integration step. Theories of crystal growth and crystal growth kinetic will be discussed in this section.

1.3.3.1 Crystal growth theories

The concept of the solute molecules adsorbed on the crystal surface in a layer by layer manner was introduced by Volmer in 1939 (1, 47). Volmer's adsorption layer theory suggested that there is a mobile self-adsorbed layer on the crystal surface that has a thickness of approximately 1 nm but does not exceed 10 nm (1, 58). The crystallising substances arrive at the surface of the crystal and integrate to the kink of the crystalline surface. Once the whole surface is complete, the next layer of the crystal initiates from a monolayer island (two-dimensional nucleation). The two-dimensional nucleation occurs in a similar manner to the homogeneous nucleation, but it requires only half the energy to form in comparison to an ordinary homogeneous nucleation (1). Later, Kossel proposed another model of crystal growth by layers with regards to Volmer's theory. The flat crystal

surfaces consist of a moving step of monoatomic height (59), as illustrated in **Figure 1.6**. The crystalline surfaces contain more than one kink. The crystallising substances integrate to the kinks and move along the monolayer. The new layer occurs from the surface nucleation, which usually commences at the corners (1).

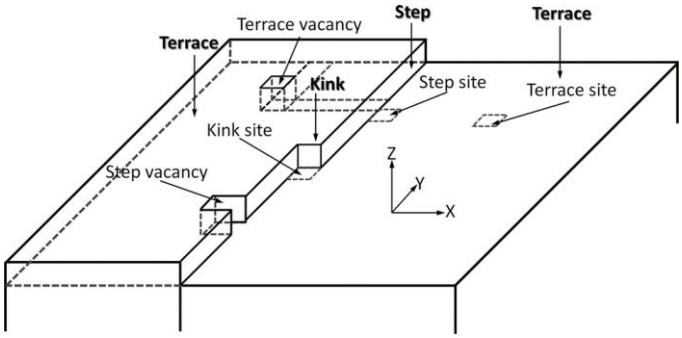

Figure 1.6 Kossel's model of monomatic height layer crystal growth at the surface of the crystal. This figure is reproduced from reference (60).

1.3.3.2 Kinetic of crystal growth in supersaturated solution

A rate limiting step in crystal growth can be either a diffusion step or an integration step. If the diffusion of the crystallising substance from the bulk is slow in comparison to the integration process, the crystal growth of that substance will be controlled by the diffusion step. Otherwise, if the concentrations of the crystallising unit at the crystalline surface and bulk are equal, the crystal growth is dominated by the integration process (61). These two steps occur under the influence of different concentration driving forces, which are represent in **equations 1.9** and **1.10**.

$$\frac{dm}{dt} = k_d A(c - c_i) \quad \text{.....(1.9)}$$

and

$$\frac{dm}{dt} = k_r A(c_i - c_e) \quad \text{.....(1.10)}$$

where m is the mass deposit in time *t*, *A* is the surface area of the crystal, k_d is the coefficient of mass transfer by diffusion, k_r is the rate constant of the surface integration process, *c* is the solute concentration in the bulk solution (supersaturation), c_i is the concentration at the liquid-solid interface and c_e is the equilibrium saturated concentration. In practice, c_i is difficult to measure, thus the overall concentration driving it is represented by c-c_e (1).

A general equation for the crystallisation process based on the overall concentration driving force can be described **equation 1.11**.

$$\frac{dm}{dt} = K_G A(c - c_e\ )^g \text{.....(1.11)}$$

$$K_G = \frac{k_d k_r}{k_d + k_r} \text{.....(1.12)}$$

where, K_G is the overall crystal coefficient, A is the surface area of the crystal and g is the order of the crystal growth process (54). K_G is obtained from the **equation 1.12**. The large k_r results in the rapid surface crystal integration. Thus, K_G is approximate to $k_{d,}$ when the crystallisation is controlled by the diffusion step. In contrast, a huge k_d implies low diffusion resistance ($K_G \approx k_r$), hence, the crystallisation is controlled by the surface integration (1).

1.3.3.3 Kinetics of crystal growth from melts

The previous crystal growth kinetic section applied to the crystal growth in a supersaturated solution. The crystal grow rate from melts is influenced by the heat flow from the crystal surface to the bulk liquid instead of the concentration gradient (1). The crystallisation process from melts always follows the liberation of the heat of crystallisation. Thus, the surface of the crystal has a slightly higher temperature than the bulk supercooled liquid (62). The heat flow in the melts can be described by **equation 1.13**.

$$\frac{dq}{dt} = hA(T_i - T) \text{.....(1.13)}$$

where dq/dt is the heat flow, h is the film coefficient of the heat transfer, which is the thermal conductivity of the substance as a function of film thickness, A is the area of the growing solid surface, T is the temperature of the supercooled liquid and T_i is the temperature at the liquid-solid interface. It is noted that T_i and T_m is a similar value. The driving force of the heat transfer across the stagnant film close to the crystal surface is T_i-T. As seen from **equation 1.13**. The heat flow equation is similar to the mass transfer by diffusion in **equation 1.11**. Therefore, the crystal growth rate of the melts can be explained by **equation 1.14**.

$$\frac{dm}{dt} = K'_G A(T_m - T)^{g'} \text{.....(1.14)}$$

where m is the mass deposit in time t, A is the surface area of the crystal, K'_G is the overall crystal coefficient of the melts, T_m is the melting temperature of the substance and g' is the exponent, which has a value in the range of 1.5 to 2.5 (1). The overall driving force of the crystal growth is the degree of the supercooling that is equal to T_m-T.

1.3.4 Polymorphism

Polymorphism in material sciences is defined as the ability of the same atoms or molecules to exist in more than one distinct crystalline structure. The differences in the crystalline structure arrangement affect their physical and chemical properties, i.e., melting point, compressibility and solubility (2-4). In the cases of solvates and hydrates, the organic solvent or water molecule alters the original crystalline structure of the organic compound. This is called a "pseudopolymorph" because it contains two types of molecules.

The polymorphisms are divided into two sub-types, which are conformational polymorph and packing polymorph. The conformation polymorph is the existence of the different conformers of the same molecule (2). The difference in molecular conformation leads to a new crystalline structure. Ritonavir is an example of a conformational polymorph. Two polymorphs of ritonavir exhibited "cis" and "trans" conformation around the carbamate linkage resulting in two different crystal structures. These two polymorphs demonstrate markedly different solubility properties (63). In the packing polymorph, the molecules illustrate an identical conformation, but they have a different molecular arrangement. This results in a different crystalline structure. The cause of the different crystalline structure is due to the way that the molecules interact with each other. PCM is an example of a packing polymorph (64, 65).

The polymorphism phenomenon is common and widely observed in APIs. Approximately 90% of commercial APIs exhibit polymorphism (3). Thus, careful attention is required to select the right polymorphic form for the formulation. Metastable polymorphs have higher free energy, which can be used to enhance the aqueous solubility of the lipophilic drug (35). For example, the metastable polymorphs of phenobarbital, spironolactone and carbamazepine demonstrate better aqueous solubility in comparison to their stable polymorph (66-68). However, using the metastable polymorph of APIs carries a risk of polymorphic transformation to their stable polymorphs upon storage or during dissolution (67, 69, 70). The metastable anhydrous carbamazepine showed *in situ* transformation by converting to dihydrate after being suspended in an aqueous medium for one hour. However, this transformation was inhibited by adding PEG or HPMC into the formulation (67). The *in situ* conversion is a potential problem that can impede the use of metastable polymorphs for pharmaceutical commercial products. Therefore, the thermodynamically stable polymorph is commonly used as an API in dosage forms.

1.3.4.1 Monotropism and enantropism

Polymorphic conversion of polymorphs is an important issue that needs to be fully understood. A new API polymorph that has a bioavailability remarkablly lower than that of the original form can have serious effects on the therapeutic levels of the dosage form (71). The polymorphic system can be categorised into two classes, which are monotropism and enantiotropism.

Monotropism is a system that presents only one stable polymorph at any temperature and pressure. A metastable polymorphic form will convert to the more stable form on ageing or at an elevated temperature (2, 3). **Figure 1.7a** shows an energy-temperature diagram of a monotropic polymorph of polymorph 1 and 2. The Gibb's free energy of polymorph 1 is lower than that of polymorph 2 in the whole range of the temperatures until the melting point of polymorph 1. This is an indication that polymorph 1 is the stable polymorph while polymorph 2 is the metastable polymorph. The intercept of the stable and metastable polymorphs can be obtained from an extrapolated value (virtual transition point) beyond the melting point of the stable polymorph. Examples of APIs that demonstrate a monotropic relationship among their polymorphs are ritonavir (63), PCM (72), itraconazole (73), FF and sulfanilamide (74).

On the other hand, enantiotropism is a system in which each polymorph shows its stable domain at a different range of temperatures at a given pressure. One polymorphic form interconverts to another polymorph when it passes a transition temperature (2, 3). As seen from the energy-temperature diagram in **Figure 1.7b**, before the transition temperature, polymorph 1 has a lower Gibb's free energy than polymorph 2. However, after the transition temperature, the Gibb's free energy of polymorph 2 becomes lower than polymorph 1. This reflects that polymorph 2 is the stable polymorph after the Gibb's free energy of polymorph 2 is lower than that of polymorph 1. There are some APIs that have enantiotropism, for instance, norfloxacin (75), sulfathiazole (76), cisplatin (77) and benfluorex hydrochloride (78).

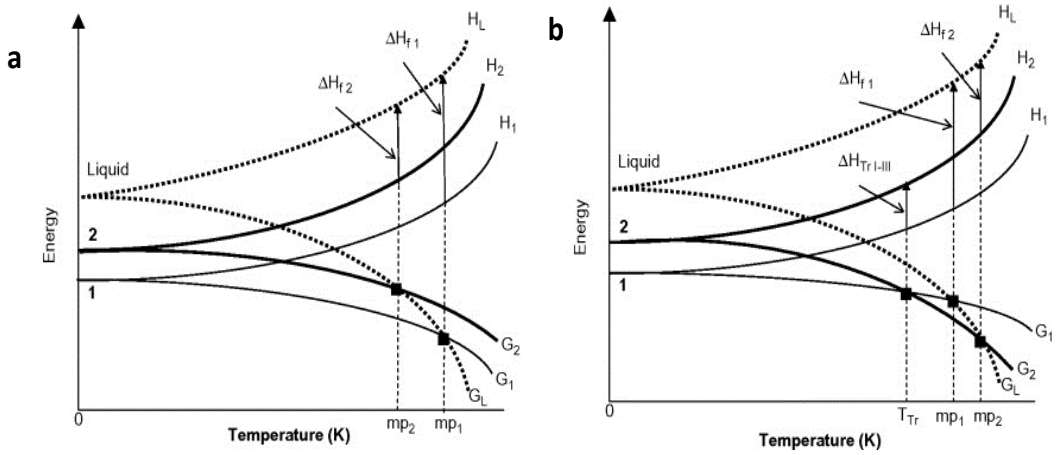

Figure 1.7 Diagram of energy vs. temperature of monotropic (a) and enantiotropic (b) polymorphs (79).

There are some rules that aid the understanding, characterisation and classification of a polymorphic system. This allows for a distinction between the monotropic and enantiotropic systems. The most frequently used prediction rules were proposed by Burger and Ramberger to classify the relationship between two polymorphs (80): they are the heat of transition rule, the heat of fusion rule, density rule and infrared rule (80).

- **The heat of transition rule** states that if an endothermal transition is observed at a temperature, it may be assumed that the transition temperature is below that point. Hence, the two polymorphs are enantiotropic (80). On the contrary, if an exothermal transition is observed at a temperature, it is assumed that there is no transition point below that point, or the transition temperature is higher than the exothermal event. Otherwise, the two polymorphs are monotropic (80). The heat of transition rule has been applied to a broad range of compounds and demonstrates an extremely precise prediction (99% accuracy). Barbas et al. showed evidence of a small endothermic event for a solid-solid transition that occurred at 196°C, which was before the melting enthalpies of norfloxacin at 211 and 220°C for the A and B forms, respectively (75). Therefore, this transition demonstrates an enantiotropic behaviour of norfloxacin.

- The heat of transition is often difficult to observe by DSC (80). Thus, the difference between the heat of fusion for the two polymorphs can be used to clarify the heat of transition rule. **The heat of fusion rule** states that "if the high melting point polymorph demonstrates the smaller heat of fusion. The two form are usually enantiotropic. Conversely, if the high melting point polymorph shows the higher heat of fusion. The two form are monotropic " (80). An exception applies to this rule when the melting point between the two polymorphs is greater than 30K or

the enthalpy of the two polymorphs is significantly diverse (2). This rule demonstrates essentially the highly accurate predictability (81). The enantiotropic behaviours of carbamazepine forms III (175°C) and I (189°C) were determined using the heat of fusion rule. Behme and Brooke reported the melting enthalpies of carbamazepine to be 29.3 and 26.4 J/mol for forms III and I, respectively (82). The authors concluded that forms III and I of carbamazepine were enantiotropic.

- **The density rule** is based on the packing principle of non-hydrogen bonding compounds. The most thermodynamically stable polymorph demonstrates a higher density than the less stable polymorph. This is due to a stronger van der Waals interaction in the stable polymorph. This rule shows high precision and accuracy in a polymorph pair that has a density difference greater than 2% (81). The substances that show polymorphic density differences less than 1% may due to experimental error or hydrogen bonds may be present in the structure (3, 81). An exception is noted when the hydrogen bond dominates the crystal packing. It results in large voids in the crystalline structure with a resulting low density (2). The metastable form II of PCM shows a higher density than the stable form I. Nelyubina et al. explained that the PCM form II demonstrates a greater number of weak non-specific interactions (C-H…O, C-H..π and H..H contact), which provides a high density to the polymorph II (83).

- **The infrared rule** can be applied to the polymorphs that involve hydrogen bonds in their crystalline structure. The rule states that if the first absorption band in the infrared spectrum of a hydrogen-bonded molecular crystal is higher for one modification than for the other, that form may be assumed to have a larger entropy. Therefore, the polymorph that absorbs infrared at a higher frequency is less stable at 0 K (80). This rule is based on the principle of a strong hydrogen bonding being associated with a decrease in the entropy and an increase in the frequencies mode. The strength of the hydrogen bond corresponds to the intramolecular OH and NH bonds. Thus, the infrared frequencies decrease in relation to the strength of the hydrogen bonds (2, 80). Burger and Ramberger noted that a compound that contains a CO-NH group, i.e., PCM, does not follow this rule. Moynihan and co-workers reported the N-H stretching of monoclinic (form I) and orthorhombic (form II) at 3326 and 3324 cm^{-1} (84). There were no significant differences between these polymorphs. Therefore, PCM is an exception to the infrared rule. Otherwise, it shows 90% accuracy for the polymorph type prediction (81), for example, sulfamoxole, sulfamethoxypyridine, theophylline and tolbutamide (81).

The monotropic system behaves in a similar way to the amorphous state as the metastable crystalline polymorphs eventually convert the stable polymorph over the whole range of the temperature. While for the enantiotropic system, each polymorph has its own stability temperature region. Thus, controlling the temperature may aid the stability of the desired polymorphic forms. In practice, monotropism and enantiotropism are intrinsic properties that can be anticipated but cannot be altered (3).

The metastable crystalline polymorphs and the amorphous state are both thermodynamic unstable and demonstrate different physical properties than the stable crystalline state. The conversion to the lower energy state for these substances is inevitable. To utilise the metastable crystalline polymorphs and amorphous state, the stabilization of these two metastable states is required (4, 67). The amorphous state intrinsically has higher free energies than the metastable crystalline polymorph (9, 29). Consequently, it has a better efficiency for improving the solubility than the metastable polymorphs. In addition, a vast body of literature has been devoted to understanding and establishing an approach to stabilise the amorphous state (29, 32). Thus, there is a better understanding of the stabilising methods in relation to the metastable crystalline polymorphs (4). Solid dispersion is one of the most popular approaches to stabilise drugs in their amorphous form (12, 13, 85). The details of solid dispersion will be discussed in detail the section 1.4.

1.3.5 Factors affecting crystallisation

There are several factors that influence the thermodynamic and kinetic aspects of crystallisation. These factors are the temperature, interface of supercooled liquid and impurity additives.

- **Temperature**

Temperature is an important factor that involves both thermodynamic and kinetic aspects of crystallisation. The thermodynamic aspects of nucleation are influenced by temperatures, as seen in the relationship in **equations 1.4** and **1.5**. A suitable temperature leads to the maximum nucleation rate, which is in between T_g and T_m (44). On the other hand, the temperature also affects the kinetic aspect of crystal growth (1). As seen in **equations 1.13** and **1.14**, it is a driving force for crystal growth from the melts. The high supercooling degree ($T-T_m$) leads to a fast crystallisation (10).

In addition, different polymorphs can be obtained from the supercooled liquid that crystallises at different temperature ranges. Gunn et al. reported that the nifedipine α form only crystallised above 120°C. It was noted that even the amorphous nifedipine, which contained crystals of the α form, was cooled to a temperature under 110°C. It crystallised

as a β form or X form (37). In another study, Tao and co-workers used different polymorphs of mannitol crystals, including α, β and δ, as seeds in the amorphous mannitol. The authors observed that the amorphous mannitol crystallised in the β form above 160°C. While only the α-form of mannitol was observed at crystallisation below 140°C. The polymorph that crystallised in the amorphous mannitol was irrespective of the initial seeds (5). Therefore, it is a temperature-dependent switching polymorph effect.

- **Interfaces of supercooled liquid**

The interface during the crystallisation of a supercooled liquid plays an important role for the crystal growth kinetics and polymorphs. The open top surface (OTS) is the interface of the supercooled liquid that is in contact with the air and humidity. The thin layer of molecules on the OTS demonstrates a faster mobility in comparison to the bulk (5, 36). As a consequence, the OTS enhances the crystal growth. Zhu et al. reported β nifedipine growth at the surface was an order of magnitude faster than in the bulk (between two coverslips) (37). In another study from the same group, Wu et al. observed that the amorphous indomethacin between coverslips had no crystallisation over six months. The partial crystallisation of indomethacin between sandwiched coverslips demonstrated a very slow crystal growth rate at 15μm per month. While the OTS indomethacin was covered with indomethacin crystals within 12 hours (36). It is noted that the stable indomethacin γ form was the only polymorph that grew on the surface of the amorphous indomethacin.

On the other hand, the other interface of the supercooled liquid, which is in contact with the substrate, can influence the polymorph of the sample. This phenomenon is call substrate-induced phase (86). It is caused where the surface of the substrate influences the molecular orientation of the supersaturated liquid. Silicon substrates have been reported for stabilising metastable polymorphs of PCM and phenytoin (6, 87, 88). Yeager et al. reported the dip coating of the silicon substrates in PCM yielded the PCM in form II on the substrate. The PCM form II was stable on the substrate for several months without a transformation to the stable form I (87). Ehmann et al. obtained the metastable PCM form III on a silicon wafer substrate that was prepared from a spin coating method followed by a rapid heat treatment after the sample preparation (88). Reischl et al. prepared a new polymorph of the anticonvulsant drug, phenytoin, by a drop casting on glass substrates. The new phenytoin polymorph showed a better solubility than the original crystalline powder (6).

- **Impurity additives**

Impurity additives demonstrate various effects on the crystallisation process. The effect of impurity induced heterogeneous nucleation and the control of the polymorph of the crystals were discussed earlier. Another aspect of impurity additives that contradicts the previous

application is an inhibition of the crystallisation. One to three percent of polymer additives in amorphous APIs can inhibit their crystallisation (44, 89-92). Trasi et al. studied the effect of different polymers, including polyvinyl pyrrolidone (PVP), hypromellose acetate succinate (HPMCAS), Eudragit E and polyacrylic acid (PAA), on the nucleation and crystal growth of amorphous PCM (44). The authors observed that PVP and PAA were effective PCM crystal growth inhibitors while HPMCAS and Eudragit E demonstrated poor crystal growth inhibition. PVP and PAA demonstrate hydrogen bonds with the PCM. Thus, the hydrogen bonding between the drug and polymer is a key factor that inhibited the PCM crystal growth (44, 90). HPMCAS was an excellent PCM nucleation inhibitor (44). The authors suggested that the largest monomer size of HPMCAS among those polymers used in their study resulted in the inhibition of the PCM nucleation. Additionally, Konno et al. used PVP and HPMCAS to inhibit the crystallisation of amorphous felodipine (89). These polymers equally decreased the nucleation rate of felodipine. The authors speculated that the polymer additive increases the kinetic of the nucleation barrier of felodipine (89). Therefore, the polymer additive demonstrated a strong crystalline inhibition in the amorphous APIs through impeding the nucleation and crystal growth. Adding one to three percent of polymer can be a potential way to stabilise the amorphous API without changing the thermodynamic driving force of the crystallisation process (40).

1.3.6 Crystallisation behaviour of organic compounds

Baird and co-workers performed a study on the crystallisation behaviour of 51 organic compounds (93). They categorised the compounds into three groups based on the absence or presence of crystallisation in the heat/cool/reheat cycle of DSC experiments. Class I compounds exhibited a partial or complete crystallisation in the cooling cycle. Examples of class I compounds are caffeine, carbamazepine, indoprofen and theophylline. The crystallisation class II molecules occurred upon the reheat cycle. PCM, celecoxib, droperidol and flurbiprofen demonstrated crystallisation during the reheat program. Thus, they were assigned to be the class II compounds. The class III compounds did not show any evidence of drug recrystallization during the cooling or reheating programs in the DSC experiments, even when using a slow heat-cooling rate ($1°C.min^{-1}$), such as ritonavir, itraconazole, ketoconazole, loratadine and FF.

The APIs are small organic molecules in which the crystallisation tendency is related to the intermolecular interaction that is potentially provided by their functional groups (29). If the molecules demonstrate hydrogen donors and acceptors in their molecular structure, they are capable of establishing an inter-molecular hydrogen bond. For example, the monoclinic and orthombic PCM crystal structures are formed through the intermolecular hydrogen

bonding between the drug molecules (64, 65). These bonds are NH..O and OH..O. This strong molecular interaction results in the amorphous PCM requiring a small amount of mobility to crystallise spontaneously (9). In contrast, some molecules have only hydrogen acceptors, i.e., a carbonyl group, in their structure. These molecules lack strong inter-molecular bonds. Consequently, they can at most form a dipole-dipole, van der Waals forces or weak hydrogen bond between the carbonyl group and the acidic C-H group (94).

FF, the model compound used in this project, is a good example of the molecules in this aspect because its structure contains only a carbonyl group. The crystalline packing of FF occurs through the intermolecular weak hydrogen bond of CH…O (95). The amorphous FF exhibits a high molecular mobility and high enthalpic driving force over the entire temperature range. However, Baird et al. and Amstad et al. observed that the supercooled FF did not spontaneously crystallise (10, 93). This is because it has high configurational entropy that implies a low probability of the molecules properly orienting for the initiation of nucleation (9). Therefore, nucleation was a rate limiting step of FF crystallisation that is the likely causes for the weak interactions of the drug molecules (10). In addition, Amstad et al. reported that the crystal growth of FF had a diffusion-limit that was influenced by the temperature (10). However, the controlled crystallisation of FF into its specific polymorphs is still poorly understand.

To fill this knowledge gap, the use of heterogeneous nucleation can be a potential way to control the crystallisation of amorphous FF. Controlling factors that affects crystallisation including the temperature, OTS of the sample and type of impurity, which may shed light on possible means to control amorphous FF crystallisation or even dictate it to crystallise into a specific polymorph.

1.4 Solid dispersions

Solid dispersions were first introduced by Sekiguchi and Obi in 1961 (12, 96). Solid dispersions refer to solid matrices that consist of at least two components: a drug and an inert carrier. The carriers of the solid dispersion can be either crystalline or amorphous materials where the drug can be molecular dispersion, amorphous clusters or micro drug crystals embedded in the matrices (12). The solid dispersions offer advantages related to particle size reduction, enhanced wettability and the drug in the amorphous state (35). Amorphous drugs have high internal energy and favour dissolution. As one of the many examples, Jung and co-workers prepared a solid dispersion of the poorly water soluble drug itraconazole with Eudragit E and AEA® (97). The authors observed a 141-146 fold aqueous solubility increase in comparison to the crystalline itraconazole. Another poorly water soluble drug, felodipine, was prepared as solid dispersions with PVP, HPMC and

poloxamer. The dissolution rates of the felodipine solid dispersions with these polymers were remarkable improved in a range between 60-80 fold in comparison to its crystals (98). Since, the solid dispersions demonstrate many promising results in enhancing the bioavailability of poorly water-soluble drugs (12-14, 99), the solid dispersion technology has been applied in the pharmaceutical industry and some solid dispersion products have been commercialised (99-101). **Table 1.1** summarises a list of the marketed solid dispersion products.

Table 1.1 Marketed solid dispersion products (99-101).

Trade name	**Carrier**	**Manufacturing method**	**Company**
Gris-PEG® (Griseofulvin)	PEG	Melt process	Novartis
Sporanox® (Itraconazole)	HPMC	Spray layering	Janseen
Cesamet® (Nabilone)	Povidone	Unknown	Meda pharm
Kaletra® (Lopinavir and Ritonavir)	PVP-VA	Melt-extrusion	Abbott
Isoptin® SRE-240 (Verapamil)	HPMC/HPC	Melt-extrusion	Soliqs
Nivadil®(Nivaldipine)	HPMC	Unknown	Astellas
LCP-Tacro® (Tracolimus)	HPMC	Melt-extrusion	Life-cycle Pharma
Intelence® (Etravirine)	HPMC	Spray drying	Tibotec
Certican® (Everolimus)	HPMC	Spray drying	Novartis
Afeditab® (Nifedipine	PEG and Poloxamer	Melt/absorb on carrier	Elan Corp.
Fenoglide® (Fenofibrate)	PEG and Poloxamer	Melt process	Santarus
Ozudurex® (Dexamethasone)	PLGA	Melt-extrusion	Allergan
Rezulin®(Troglitazone)	HPMC	Unknown	Pfizer
Zelboraf®(Vermurafenib)	HPMCAS	Unknown	Genentech
Incivek®(Telaprevir)	HPMCAS	Unknown	Vertex Pharmaceuticals
Crestor®(Rosuvastatin)	HPMC	Unknown	Astrazeneca
Prograf®(Tacrolimus)	HPMC	Unknown	Astellas

1.4.1 Classification of solid dispersions

Solid dispersions can be broadly classified into two classes according to the physical state of the APIs, which are non-molecular solid dispersion and molecular solid dispersion (solid solution) (13). The non-molecular solid dispersions demonstrate two separate phases of either amorphous or crystalline drugs and carriers, whereas the molecular solid dispersions show a single phase of drugs and carriers. The following section will discuss the structures and definitions of each solid dispersion class along with their advantages and disadvantages.

1.4.1.1 Non-molecular solid dispersion

1.4.1.1.1 Eutectic mixtures

A eutectic mixture is formed after two components are mixed in the proper ratio at a suitable temperature as illustrated in **Figure 1.8**. The compounds A and B are in a miscible liquid phase at the eutectic ratio while other ratios demonstrate phase separation of either solid A with liquid B or solid B with liquid A. The eutectic mixture is formed by the loose molecular interaction of the binary components, which do not include a chemical bond formation (12). As the temperature continuously decreases at the eutectic proportion, both the A and B components rapidly crystallise together.

An application of eutectic mixtures is to form solid dispersion matrices of crystalline drug and water-soluble crystalline polymer. The practically water-insoluble FF was reported to form a eutectic mixture PEG 8000 at a ratio of 25:75 (drug:polymer) (102). The authors estimated that a few micron-sized crystalline FF particles were entrapped in the PEG 8000 matrices, and this was a result of a significant increase in the dissolution of the drug. Additionally, FF also formed a eutectic mixture with acetylsalicylic acid at the ratio of 0.958:0.042 (drug: acetylsalicylic acid). FF solubility increased three-fold compared to the untreated FF (103). Yong and co-workers reported that a eutectic mixture of poorly aqueous ibuprofen and menthol was successfully formed at a ratio of 4:6 for the drug and menthol (104). Ibuprofen's aqueous solubility was significantly increased by 2.5 fold in the eutectic mixture proportion. These examples of eutectic mixtures show a promising means of improving the water solubility of poorly water-soluble APIs. The increase in the drug dissolution can be explained by the Noyes-Whitney equation (**equation 1.15**).

$$\frac{dm}{dt} = DA\left(\frac{C_s - C}{h}\right) \quad \text{……..……...(1.15)}$$

where *dm/dt* is a rate of drug dissolution in the medium per unit of time, *D* is the diffusion coefficient, *A* is the surface area, C_s is the saturated concentration in the medium, *C* is the

bulk concentration solution and h is the thickness of the diffusion layer. Thus, the reduction in the drug particle size from forming a eutectic mixture results in an increase in the surface area (*A*). As a consequence, the rate at which the drug dissolves in the media increases.

A eutectic mixture for a solid dispersion is more physically stable than an amorphous solid dispersion because both the drug and carrier are in the crystalline state (105). Moreover, the preparation of the eutectic mixture solid dispersions is simple by physically mixing the two components and heating them. The eutectic mixture solid dispersion increased the wettability and particle size reduction of the APIs (12). However, the eutectic mixture solid dispersions are inferior when improving the aqueous solubility of poorly water soluble drugs in comparison to the molecular dispersion. As the drugs are in crystalline states, which still requires energy to dissolve (13), the eutectic mixture is not a method of choice for preparing a solid dispersion.

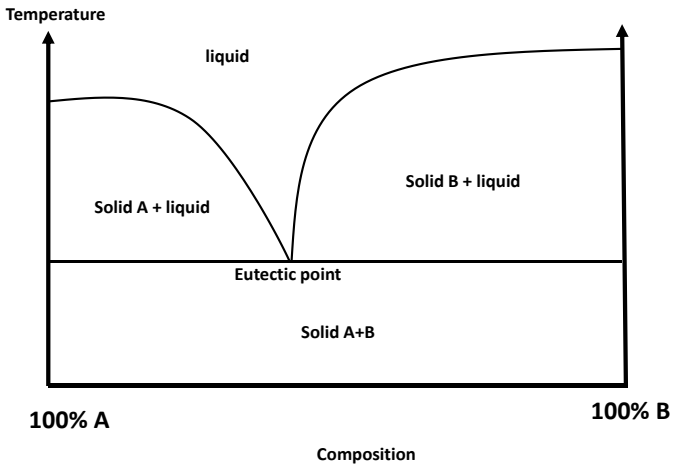

Figure 1.8 Phase diagram of a eutectic mixture of compounds A and B.

1.4.1.1.2 Solid dispersions containing crystalline drug

A solid dispersion containing a crystalline drug is a binary system in which the crystalline API is dispersed in an amorphous carrier. It shows the advantages of improving the wettability of the crystalline drug and minimising the aggregation of the drug crystals (12, 106). Brettmann et al. prepared a solid dispersion crystalline albendazole suspended in PVP matrices via free surface electrospinning (106). This formulation improved the wettability and reduced the crystalline albendazole aggregation resulting in the dissolution enhancement in comparison to the crystalline drug powder. Kawabata et al. demonstrated that the crystalline solid dispersions of tranilast in HPMC improved the physicochemical properties and solubility of the drug (107). The solid dispersion containing the crystalline tranilast formulation significantly improved the dissolution of the drug, in which the drug release reached 97% within 10 minutes. Whereas the crystalline drug dissolved only 10% over 60 minutes. Moreover, the solid dispersion containing crystalline tranilast

demonstrated a better photostability when expose to UV in comparison to its amorphous formulation. This is because the crystalline drug is more chemically stable than its amorphous state (107). However, the crystalline drugs still require some energy to break down their crystals before dissolving. There are solid dispersions containing crystalline drugs that are less efficient when improving the solubility in comparison to the system in which API exists at their molecular level or amorphous state.

1.4.1.2 Molecular dispersions (solid solutions)

Molecular dispersions refer to a one-phase system in which the API and carrier homogeneously mix at the molecular level or near molecular level as the amorphous state (108). It provides superior advantages in comparison to the non-molecular solid dispersion class. A molecular dispersion is more efficient when improving the solubility of the APIs because it maximises the surface area of the formulations, since the API molecules are reduced to the absolute size at the molecular level or in the amorphous state (13). Thus, no further energy is required to break down the API crystalline structure before it dissolves. The drug dissolution rate depends on the dissolution of the carriers (14). As soon as the carrier molecules dissolve, the drug molecules release to the media (13, 109). Therefore, the molecular dispersed solid dispersions provide a faster release than the non-molecular solid dispersions. The molecular dispersions can be further subcategorised according to the carrier types (crystalline and amorphous molecular dispersions).

1.4.1.2.1 Crystalline molecular dispersions

Crystalline molecular dispersion is a homogeneous single phase of API in the crystalline matrices. The solubility of API in the crystalline carrier is usually low. Goldberg et al. suggested that the molecular dispersions of sulfathiazole in urea were formed at the drug content of 5% w/w (110). The structures of crystalline molecular dispersions can be further classified according to how the solutes (drug molecules) are entraped in the solvent structure (crystalline matrices): these classes are substitutional and interstitial molecular dispersions. The solute molecules substitute in the lattice of the solvent molecules due to their sizes being similar (**Figure 1.9a**), and this refers to the substitutional molecular dispersion. Whereas in an interstitial molecular dispersion, the solute molecules are significantly smaller than the solvent molecules, approximately less than 20% of the solvent size (12). Hence, the solute is entrapped in the interstitial space between the solvent lattices (**Figure 1.9b**). For example, the molecular dispersion of API in PEG is classified as an interstitial molecular dispersion due to the difference in the size between the two components (111).

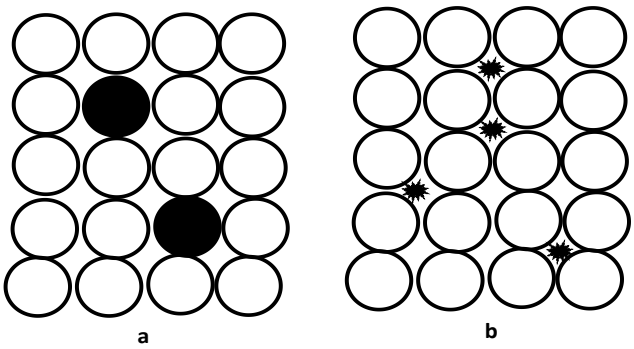

Figure 1.9 Diagram showing the formation of the crystalline molecular dispersions: substitutional molecular dispersion (a) and interstitial molecular dispersion (b). The solute molecules are highlighted in black. This figure is adapted from reference (12).

1.4.1.2.2 Amorphous molecular dispersions

Amorphous molecular dispersions use amorphous carriers as matrices. The APIs are molecularly dispersed in chains of the amorphous carriers (12). Naturally existing amorphous polymers are common matrices used in amorphous molecular dispersions, i.e., PVP, polyvinyl pyrrolidone co-vinyl acetate (PVP-VA), HPMC and poly(meth)acrylate have been intensively studied (97, 112, 113). The structure of the amorphous molecular dispersion has been proposed to be the APIs irregularly trapped in between polymer chains that impedes the drug mobility from the high energy barrier of the polymer chain network, and as a consequence, it minimizes the API mobility and enhances the stability (13) (**Figure 1.10a**). However, the recrystallization of the drugs in polymer matrices has been continuously reported. A new model for the molecular dispersion structure, which was obtained from a computer modeling approach, was purposed by Ouyang (114). The model suggests that drug molecules that are on the surface of the coiled polymer chain (as illustrated in **Figure 1.10b)** are easy to mobilise and aggregate, and this may result in the physical instability of the solid dispersion (114). The thermodynamic stability of the amorphous drug in a molecular dispersion has also been widely studied and identified as the cause of the physical instability of the molecular dispersions.

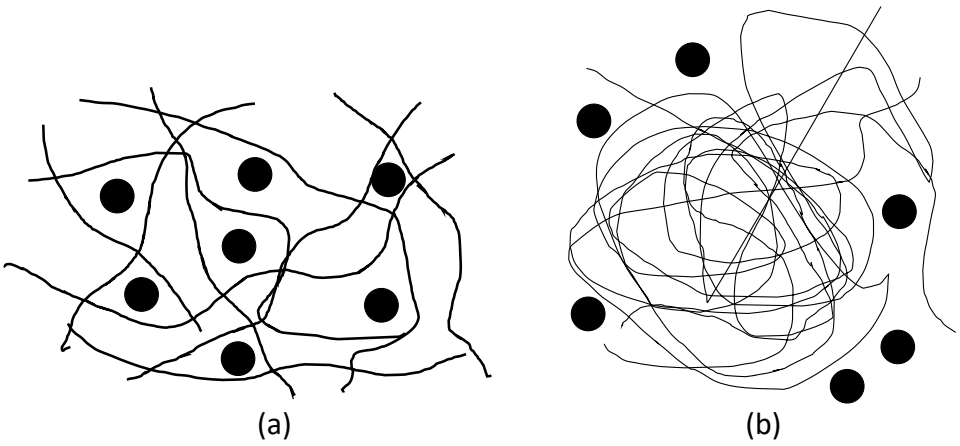

Figure 1.10 Schematic diagram illustrating the structures of an amorphous solid dispersion with polymer matrices: the conventional model (a) and the new model proposed by Ouyang (b). Adapted from reference (114).

1.4.2 Thermodynamic stability of molecular dispersions

The thermodynamics of the molecular dispersions offers a fundamental understanding, which is a prerequisite for developing the solid solution formulations because they inherit a physical insatiability (35, 115, 116). The amorphous drug has a high intrinsic energy level that thermodynamically favours crystallisation (29, 32). The amorphous drug recrystallization leads to a significant decrease in the dissolution of the solid dispersion formulations (35, 117). The crystallisation of the molecular dispersions starts from the drug molecules migrating to form an amorphous drug rich phase. The configuration entropy of the amorphous drug rich phase will eventually lead to the nucleation and crystal growth on ageing. The crystallisation process of the amorphous drug can be a slow process in the amorphous molecular dispersions. It may require weeks, months or years, due to the high viscosity of the amorphous polymer matrices that impede the mobility of the drug molecules (40). Furthermore, factors such as API concentration, temperature, humidity, miscibility and polymer-drug interactions can significantly influence the physical stability of the solid dispersion (115, 118-122). The physical instability of the molecular dispersions (including amorphous-amorphous phase separation and crystallisation of amorphous drug) can be traced and often predicted by the glass transition temperatures, relaxation time, interaction of drug-polymer and polymer-drug miscibility of the system.

1.4.2.1 Glass transition

Glass transition is a reversible kinetic transition that occurs when a brittle glass transforms to a rubbery state as the temperature increases (38). Below a glass transition temperature (T_g), the molecules of the glassy material are practically immobilized. However, beyond

this transition temperature, the molecules are liberated and increase their mobility (32). T_g is a step change in heat capacity that can be observed from a differential scanning calorimeter (DSC) and dynamic mechanical analysis (DMA) (32). It is a characteristic property of amorphous materials, and it is always lower than the melting point of the materials.

In a blend system, a T_g is an indication of the miscibility between the two components (or more). The immiscible the binary mixture demonstrates a double T_g of the individual materials. On the other hand, a single T_g indicates a homogeneous mix of binary components. The theoretical prediction of the T_g in the homogeneous system can be estimated using the Gordon-Taylor (GT) equation (123, 124). This equation assumes that the two components are miscible, and the free volume is additive (125). This equation was firstly developed for the polymer blends, but it has been proven to be capable of predicting the drug-polymer blends (123, 124). The GT is described as

$$T_{g_{12}} = \frac{W_1 T_{g_1} + K W_2 T_{g_2}}{W_1 + K W_2} \quad \text{……..……..(1.16)}$$

where W_1 and W_2 are fractions of the two components, T_{g1} and T_{g2} are glass transition temperatures in Kelvin of each material and K is a constant that can be obtain from the Simha-boyer rule (126).

$$K \approx \frac{T_{g_1} \rho_1}{T_{g_2} \rho_2} \quad \text{……...……..(1.17)}$$

where ρ is the true density of the component. Additionally, K can be calculated using the Couchman-Karasz model. K is defined as

$$K \approx \frac{\Delta C_{p_2}}{\Delta C_{p_1}} \quad \text{……...(1.18)}$$

where ΔCp_1 and ΔCp_2 are the different heat capacity changes at T_g for each component (127). Moreover, the GT model can be modified to calculate a T_g of the tertiary blends (123).

The discrepancy between the experimental values and the predicted values indicates an interaction of the two components. A positive deviation refers to a strong intermolecular interaction of the two components, such as hydrogen bonding. Whereas a negative deviation implies that the like-molecules have a greater interaction among themselves rather than forming an interaction between different molecules (119, 124). Additionally, moisture uptake in the solid dispersion can cause a decrease in the T_g due to water having a plasticising effect.

1.4.2.2 Molecular mobility and structural relaxation

The glassy state is a non-equilibrium state in which the enthalpy, entropy and the volume deviates from the supercooled liquid. Thus, the amorphous form embeds high enthalpy and configuration entropy in comparison to their crystalline counterpart (32). Upon storage, the glass relaxes by releasing its extra enthalpy and configurational entropy to reach a new equilibrium. The structural relaxation is a process in which the amorphous material releases its extra energy and the time duration for this process is called the relaxation time (128). The relaxation behaviour is important because it correlates to the molecular mobility of the system. Molecular mobility is an essential parameter to determine the stability in the molecular dispersion system. High molecular mobility leads to the phase separation and crystallisation of the amorphous drug. To determine the relaxation time, the Adam-Gibbs-Vogel model is used

$$\tau = \tau_0 exp\left[\frac{DT_0}{T\left(\frac{1-T_0}{T_f}\right)}\right] \quad \text{.....(1.19)}$$

where τ is the molecular relaxation time constant, τ_0 is the relaxation time at the high-temperature limit, D is the material parameter associated with the material fragility and T_0 is the zero temperature mobility. T_f is the fictive temperature, and when above T_g, the T_f is equal to the experimental temperature. While when below T_g, the T_f in most cases is similar to the T_g (129, 130).

There are two types of relaxation found in amorphous materials: alpha relaxation (global molecular mobility) and beta relaxation (local molecular mobility) (32, 128). The alpha relaxation refers to neighbouring molecules changing their relative position. The time in which the molecules diffuse through the inter-particulate distance is defined as the relaxation time, which increases when near T_g (128). Hence, the alpha relaxation involves the whole molecule via global molecular mobility and it is responsible for the glass transition. While, the beta relaxation links to a local mobility that is related to the molecular mobility below the T_g. The beta relaxation is faster than the alpha relaxation because it involves only intra-molecule movement, such as part of the side chain moving in an amorphous polymer or atoms spinning in small organic compounds (128).

The global and local mobility of amorphous polymers and small organic molecules, such as APIs, can be observed by using analytical techniques, including dielectric relaxation spectroscopy, thermal stimulated current, solid state nuclear magnetic resonance (ss-NMR), DMA and DSC (128). These methods based on different analytical principles provide information on both the alpha and beta relaxation of the molecules. The dielectric relaxation spectroscopy is based on a measurement of the reorientation of dipoles under the

electrical field and variable frequency. It is a direct determination of the relaxation times, including both alpha and beta relation. The NMR approach measures the emitted and the absorbed radio frequencies of the nuclei under a magnetic field, which is the origin of molecular motion. Its merit is that there is a correlation between the chemical stability and local mobility. DSC relies on the thermally induced transition, which involves both alpha and beta relaxation (128).

The molecular mobility of the APIs is linked to their crystallisation. Thus, it is an important factor that governs the stability of the amorphous phase. Typically, pharmaceutical molecular dispersions are composed of at least two components. The multicomponents demonstrate a more complex relaxation behaviour than a single component system. In molecular dispersions, a small reorientation motion, which shows the heterogeneity of the system, is observed as beta-relaxation below the T_g as well as alpha-relaxation (131). This molecular mobility leads to nucleation and crystal growth (132). Furthermore, the processing parameters also affect the mobility of the molecular dispersions (133, 134). Briefly, preferable molecular dispersions should demonstrate a high conformation entropy and low mobility because it is physically stable.

1.4.2.3 Theoretical miscibility estimation of drug and polymer

- **Solubility parameter approach**

The solubility parameter (δ) is based on the principle of cohesive energy. The cohesive energy is defined as the energy that binds the atoms and molecules together (135). The values of the cohesive energy are the energy that is required to separate an atom or molecule to an infinite distance. The cohesive energy reflects the overall intermolecular interaction, including hydrogen bonding, van der Waals interaction, covalent bonding, dipole moment interaction and ionic bonding (136).

There have been several methods developed to calculate the δ, such as Hoy, Fedor and Hoftyzer and Van Kevelen (135, 137-139). The errors in the estimation values between the different approaches are less than 10% (135). Fedor's method is a simple method to predict the δ with high accuracy. The δ estimation of Fedor's approach is based on the addition of the atoms and group contribution to the heat of vaporization and molar volume (137). The equation below expresses the δ as a square root of the cohesive energy density.

$$\delta = \left(\frac{\sum E_v}{\sum V_m}\right)^{1/2} \quad \text{.....(1.20)}$$

where E_v is the heat of vaporization and V_m is the molar volume. The values of E_v and V_m of the atoms or groups are reported in the literature (135, 137). The δ are reported with the unit of $MPa^{1/2}$.

The solubility parameter was initially developed for a simple liquid mixture. The application of the solubility parameter extends to different areas including foods, polymers and pharmaceutics (136, 138, 140, 141). The application of solubility parameters in the pharmaceutical area is used for predicting unknown properties of materials, evaluating processing effects on the material properties and predicting the incompatibility and interactions of the drug and the polymer (136). To predict the theoretical drug-polymer miscibility, the solubility parameters have been used and have shown a potential application to predicting accurately the miscibility of the drug-polymer (136, 142-144). The similar values of the solubility parameters imply a good miscibility of the two components. Foster et al. categorised the miscibility of the drug-polymer based on their $\Delta\delta$ into three groups, which are miscible ($\Delta\delta<2$), partial miscible ($\Delta\delta$ 2-10) and immiscible ($\Delta\delta>10$) (140). Therefore, the theoretical miscibility estimation, such as solubility parameter, can be an approximate guideline to predict the miscibility of the drug and polymer in a solid solution system (136, 144, 145).

- **Melting point depression approach**

The melting point depression approach has been used to study the polymer-polymer and API-polymer interactions (144, 146, 147). The principle behind this approach is that if the crystalline API and amorphous polymer are miscible, then interactions, such as hydrogen bonding, will occur between the components (144). The chemical potential of the mixture would be lower than the pure component (146). This results in melting point depression. Conversely, if drug and polymer are immiscible with no interaction occurring between the two compounds, then the melting point depression is not expected.

The melting point depression is a simple method that can estimate the interaction of the drug and polymer. The drug and polymer are physically mixed and are slowly heated by DSC with a slow underlying heating rate (1-2 $C°.min^{-1}$) to allow the interaction of the drug and polymer to occur. Marsac et al. demonstrated the application of the melting point depression to predict the miscibility of PVP-felodipine and PVP-nifedipine (144, 148). The melting points of these two drugs were depressed as the ratio of PVP increase. Additionally, the data from the melting point depression experiments can be used to estimate the Flory-Huggins interaction parameter of the drug and polymer (X), which is used to calculate the solid solubility of the drug in the polymer (144, 148).

1.4.2.4 Interaction of drug and polymer

In addition to immobilising drugs in polymers with a high T_g and storing them at least at 50K below the T_g of the system (29), another practical approach to preventing the amorphous drug recrystallization is to establish an interaction between the drug and the polymer, such as dipole-dipole, van de Waals and hydrogen bonding. The interaction between the drug and the polymer is a potential strategy to enhance the physical stability in a molecular dispersion (118).

Forming a hydrogen bond requires a hydrogen donor and a hydrogen acceptor group in the drug and the polymer structure. The polymers that contain a carbonyl group (hydrogen donor group) can establish a hydrogen bond with APIs that contains a hydroxyl or amide group (hydrogen donor group) (89, 112, 113, 121, 122, 142, 144). Taylor et al. and Matsumoto et al. observed the hydrogen bonding of indomethacin with both PVP and PVP-VA through the carbonyl group of the polymers and hydroxyl group of the drug (112, 113). PCM also demonstrated a hydrogen bond with PVP via the carbonyl-hydroxyl route (24). In addition, felodipine tolbutamide, lacidipine and nifedipine can establish hydrogen bonds with PVP through their amide group (89, 142). The hydrogen bonding between drug and polymer promotes a miscibility between the blend couple resulting in an increase in the T_g of the blend and restricting the mobility of the drug molecules (124).

The molecules often contain atoms that have different electronegativity. Consequently, the electrons in the molecules are pulled to the atom that has the highest electronegativity, i.e., fluorine, oxygen, chlorine and bromine. This leads to a non-uniform electron distribution in the molecules (molecular dipoles) (149, 150). Therefore, some regions of the molecule have positive electric charges while other regions have negative electric charges. APIs and polymers also contain highly electronegativity atoms in their molecules. Hence, the dipole-dipole interactions between the drug and polymer molecules are expected. On the other hand, the molecules that have no dipole moment, exhibit a van de Waals interaction. The van de Waals interaction is a universal force among organic molecules. However, it is a very weak interaction (148).

The interaction of ketoconazole with PVP is an example of a dipole-dipole interaction of the drug and polymer (148, 151). Both ketoconazole and PVP lack a hydrogen donor group. Thus, they cannot form a hydrogen bond with each other. This was confirmed by an absence of a PVP carbonyl peak shift to the lower wave number (148). Marsac speculated that the interaction of PVP and ketoconazole occurred via a dipole-dipole interaction because it has a large dipole moment (6.03 Debye), which is likely to be an interaction with the polar molecule of PVP (3.91 Debye). A van de Waals interaction is another possible

interaction between ketoconazole and PVP because the large molecular size of the drug may contribute to this interaction (148).

1.4.3 External factors affecting physical stability of molecular dispersions

Storage temperature and moisture are external factors that influence the physical stability of molecular dispersions. They accelerate the molecular mobility of APIs and carriers, which consequently links to the physical instability of the molecular dispersion including its phase separation and amorphous drug recrystallization (118, 121, 122).

1.4.3.1 Temperature

Temperature is a parameter that affects pharmaceutical products in many ways, including the degradation of APIs and excipients, storage conditions and manufacturing process. In the molecular dispersion, it directly links to the mobility of the molecules. A higher temperature implies, a higher molecular mobility (128). Storing solid dispersions at elevated temperatures increases the molecular mobility of the API in the formulation resulting in a phase separation and recrystallization of the drug in the molecular dispersions. In fragile glass materials, the temperature T_0 from **equation 1.19,** in which the molecules have zero mobility, is approximately 50 K below their T_g (29, 32). Therefore, it is recommended to store amorphous APIs at least at 50K below their T_g to enhance the stability of the molecular dispersion formulations (29).

1.4.3.2 Moisture uptake

Moisture uptake is one of the important factors influencing the stability of pharmaceutical products during the manufacturing process and storage (152). In the molecularly dispersed formulations, it is important to study the moisture sorption behaviour of drugs and carriers because moisture enhances the mobility of the amorphous drug and polymer resulting in a phase separation and API recrystallization (153, 154). Many commonly used matrices, such as PVP, PVP-VA and PEG, are hygroscopic.

As an example, moisture uptake by PVP has been widely studied (118, 121, 122, 154). Moisture absorption by PVP based molecular dispersions can lead to phase separation of the amorphous drug and its recrystallization (118, 121, 122). The hydrogen bonding between the drug-polymer can be degraded by moisture. Marsac et al. observed that the hydrogen bond between felodipine and PVP was degraded at a humidity >75% RH. The humidity induced the immiscibility of the drug and polymer resulting in the crystallisation of the amorphous felodipine (121). However, Vasanthavada et al. and Forster et al. observed a reduction in the moisture uptake in solid dispersion formulations, in which the hydrogen bonding was presented. The non-degraded hydrogen bond in an indomethacin-

PVP resulted in the solid dispersion absorbed 7.4% w/w moisture, which was lower than the degraded hydrogen bond in the solid dispersion of lacidipine-PVP, nifedipine-PVP and tolbutamide-PVP, as their moisture uptakes were 13, 11.6 and 11.7%, respectively (142). The authors explained that the moisture uptake by PVP was due to its free carbonyl group binding to water molecules. The formation of hydrogen bonds in the drug-polymer reduces the number of the free carbonyl groups in the polymer. Hence, there is a smaller number of hydrogen acceptor groups in the polymer that are available for water to interact with, which results in a decrease in the moisture uptake of the solid dispersion (142). Consequently, the non-degraded hydrogen bonding of the API and polymer enhanced the stability of the amorphous drug in the molecular dispersions.

The kinetics of the moisture absorption by the pharmaceutical system can be influenced by a number of factors, including the hygroscopicity of the material, the density of the matrices, the surface area and the geometry of the system (119). Moisture uptake normally includes two main steps that are at the adsorption and absorption stages. The adsorption stage is when moisture covers the surface of the material. The absorption stage is when the moisture penetrates into the material resulting in hydration and swelling. It is important to understand the kinetics of the moisture absorption. As the stability of the formulation directly relates to its rate and capacity for moisture uptake. The kinetic sorption models can be used to predict the moisture sorption and describe their moisture sorption behaviours. The Peleg, Guggenheim-Anderson-De-Bour and double exponential models have been wildly used to investigate the kinetics of moisture absorption processes of food and pharmaceutical materials (120).

1.4.4 Solid dispersions containing polymer blends

Polymer blends have been wildly applied to various industries, such as plastics, food packaging and biomedical, to alter the physicochemical properties of the materials (155-158). The use of synthetic and natural polymer blends in the biomedical area has increased over recent decades (159). In pharmaceutical research, polymer blends have been used in a range of formulations with different functionalities, including as emulsifying agents, flocculating agents, coatings and solid dispersion matrices for controlled release or specific site release (17, 19, 117, 160, 161). The polymer blended approach was selected in this study for the formulation of solid dispersions because it demonstrates many advantages, including improving the polymers properties (enhance spinnability of eletrospun fibres) (162), reducing moisture uptake of the formulations (18) and can be used for modified release formulations (21, 163). To formulate a polymer blended solid dispersion, an

understanding of the polymer-polymer miscibility and the effect of the API on the polymer blends are needed, which will be discussed in this section.

1.4.4.1 Polymer-polymer miscibility

The fundamental theory of polymer blending is based on the thermodynamics of the mixing of a binary system. This process can be described using **equation 1.21**.

$$\Delta G_m = \Delta H_m - T\Delta S_m \quad \ldots\ldots\ldots\ldots\ldots\ldots\ldots\ldots\ldots\ldots(1.21)$$

where, ΔG_m is the change in the Gibb's free energy of the mixing process, T is the absolute temperature of the mixing process, ΔH_m is the enthalpy of the mixing and ΔS_m is the entropy of the mixing. The negative value of ΔG_m refers to a spontaneous process in the mixing. The ΔS_m is determined from the possible arrangements of the molecules, and it is always a positive value. The heat of mixing is frequently positive for non-polar compounds. However, an exception applies when the compound is attracted to another, such as hydrogen bonding (38). Therefore, the sign of the ΔG_m relies on the heat of the mixing.

A similar thermodynamic theory for the mixing applies to the polymer blends. The polymer blends can be homogeneous or heterogeneous depending on their miscibility. Complete miscibility leads to homogeneous blends of the components. In contrast, partial miscible or immiscible of the blends results in a heterogeneous mixture. A positive value of ΔG_m indicates a phase separation of the two polymers. It is noted that the polymers are long chain structures with high molecular weights. This nature leads to a low entropy of mixing for the polymers in comparison to other low molecular weight compounds (38). Thus, this enhances the immiscibility in the polymer blends. The immiscible polymers demonstrate a clear boundary between the two phases that consequently increases the brittleness of the blend materials (164, 165).

Flory-Huggin theory is a hypothetical lattice in space theory that is used to explain the thermodynamics of the polymer-solvent interaction on the basis of the Gibb's free energy laws (166). It can be applied to estimate the miscibility of the solvent-solvent, solvent-polymer, polymer-polymer and drug-polymer mixes (144, 147, 148). The thermodynamic mixing of the polymer-polymer as based on the Flory-Huggins lattice theory can be described as

$$\Delta G_m = RT(n_1 ln\emptyset_1 + n_2 ln\emptyset_2 + n_1\emptyset_2\chi_{12}) \ldots\ldots\ldots\ldots\ldots\ldots\ldots(1.22)$$

where ΔG_m is the Gibb's free energy change in the polymer-polymer mixing, R is the gas constant, T is the temperature in Kevin, n_1 is the mole fraction of the polymer$_1$, n_2 is the number of the mole fraction of the polymer$_2$, ϕ_1 is the volume fraction of the polymer$_1$, ϕ_2

is the volume fraction of the polymer$_2$ and X_{12} is Flory-Huggin interaction of polymer$_1$ and polymer $_2$ (166). The Flory-Huggins parameter (X) can be determined from experiments, including the solubility parameter and melting point depression (144, 147, 148).

As an example of using Flory-Huggins to predict the miscibility of a polymer-polymer pair, Nishi et al. used Flory-Huggins theory to estimate the miscibility of poly(vinylidene fluoride) and poly(methyl methacylate) (147). The X values of these polymers were determine using the melting depression approach, which is -0.295 at 160°C. This value indicates that poly(vinylidene fluoride) and poly(methyl methacylate) are miscible at 160°C.

1.4.4.2 Effect of drug incorporation in polymer blended systems

The polymer blends are frequently immiscible or partially miscible because of their low entropy of mixing (38). Incorporating API into the polymer blends creates ternary blends in which it is possible that the drug may enhance the miscibility between the polymer blends. However, if the heterogeneous blend still exists. The drug miscibility of each polymer needs to be taken into account because it affects the distribution of the API in the case of a phase separation in the polymer matrices (18, 167). Six and co-workers prepared an immiscible polymer blend from Eudragit E and PVP-VA with itraconazole loading via a hot-melt extrusion (167). The authors observed that the double T_g of these two polymers decreased because the drug was inducted into each polymer phase. The PVP-VA phase demonstrated a lower degree of T_g depression. This contributes to an uneven API partition due to the polymer-drug miscibility. Yang et al. also observed similar results for the phase separation of PVP-VA/Eudragit E blends with felodipine loading, which showed as a double T_g (18). The authors performed the theoretical calculation for felodipine in each phase and discovered that the drug is likely distributed to the PVP-VA phase rather than the Eudragit E phase. This contributes to felodipine having a better miscibility to PVP-VA as it can form a hydrogen bond between the NH of the drug and the carbonyl group of the polymer (89).

Drug-polymer miscibility plays a key role in controlling the drug distribution between the two phase separated phases. The API is likely to partition into the phase that is more miscible, for example, the polymer phase that can form a hydrogen bond between the drug and polymer (18, 89). Based on this concept, the drug can be guided to one phase rather than the other phase. Therefore, controlling the drug distribution can be used to benefit the physical stability of the solid dispersion containing partially miscible or immiscible polymer blends. A lyophilic drug, which cannot form a hydrogen bond, is likely to be

miscible with the hydrophobic polymer. Consequently, incorporating this drug into the polymer blend matrices of the hydrophilic and phobic polymer results in an uneven drug distribution to the hydrophobic polymer phase. Hence, the drug in this phase can be protected from moisture that increases the physical stability of the amorphous drug.

1.4.4.3 Applications of polymer blends in drug delivery

Polymer blends demonstrate numerous applications in drug delivery, including film coating for modified release, increased mucoadhesion of the buccal tablets and solid dispersion matrices (19, 21, 161). In the particular area of solid dispersions containing polymer blends, they demonstrate equivalent or superior benefits in comparison to the ordinary binary solid dispersions, including improving the aqueous solubility of poorly water soluble drugs, increasing the physical stability of the amorphous drug in solid dispersions and alternating the drug release profiles (17). Bley et al. reported that there was no significant difference in the aqueous solubility enhancement of carbamazepine and nifedipine in PEG 1500 in comparison to carbamazepine and nifedipine in a polymer blended solid dispersion of PEG 1500 with PVP-VA or PVP (17). This is because a molecular dispersion can be achieved in both binary solid dispersions (drug-carrier) and ternary solid dispersions (drug-carriers). Thus, solid dispersions containing polymer blends show an equivalent potential to enhance the solubility of water insoluble APIs.

Another common application is blending hydrophilic and hydrophobic polymers to enhance the physical stability of the solid dispersion formulations by reducing their moisture uptake (18, 161). Alshahrani et al. demonstrated that the polymer blend solid dispersion of hypromellose acetate succinate (HPMCAS)/Soluplus with carbamazepine loading, which was prepared by hot-melt extrusion, reduced the moisture uptake of the formulation under an accelerated stress condition at 40°C/75%RH (161). Consequently, the polymer blend solid dispersion formulations showed a lower crystallinity in comparison to the binary carbamazepine-Soluplus formulation, which had a higher moisture uptake than the blends. Yang et al. used the immiscible blend pair of PVP-VA and Eudragit E to reduce the moisture uptake in their solid dispersion with felodipine (18). The moisture sorption of the PVP-VA/Eudragit E blend extrudate was decreased four times in comparison to the PVP-VA alone, which lead to the stability enhancement of the formulations.

Solid dispersions containing polymer blends have also been used to alter the release profile of the formulation, such as a biphasic drug release and sustained release. Yu et al. prepared a polymer blend of PVP and ethyl cellulose (EC) using coaxial electrospinning, which manipulated a core-shell structure phase separation in the electrospun fibre structures (21).

This resulted in biphasic drug loading, in which the outer layer of PVP released the API as a burst release and then there was a sustained release from the EC phase. Quinten et al. prepared polymer blended matrices tablets from HPMC and EC for the sustained released purpose. The matrix tablets of HPMCAS/EC at a 1:1 ratio showed metoprolol sustained released profiles over 24 hours (163).

1.4.5 Methods for preparing solid dispersions

There are various ways to prepare solid dispersions of APIs and carriers. These methods can be categorised into two primary methods, which are melting based and solvent evaporation based methods. The melting based method involves heating to melt an API and a carrier to obtain solid dispersions, whereas both the API and carrier are dissolved in a mutual solvent in the solvent evaporation based method, and subsequently the solvent is removed to obtain solid dispersions. This section will describe the general methods of solid dispersion preparations along with discussions of their advantages and disadvantages. It should be noted that the electrospinning method, which is the primary method used in this study will be introduced in detail in section 1.5.

1.4.5.1 Melting based methods

The melting based method was the original approach that Sekiguchi and Obi used to produce the fast release solid dispersions in 1961 (96). The principle of the melting based method is that the carrier and API are melted. The increased mobility of the molten liquid allows the two components to mix homogeneously. Afterwards, the molten matrices of the API and the carrier are cooled to solidify them. The solid dispersion prepared by the fusion method often requires pulverisation to break down the solid matrices. The conventional fusion method has several disadvantages, including thermal degradation of the API and a phase separation that causes insufficient mixing of the API and the carrier (35).

Hot-melt extrusion (HME) is a modern melting based method that combines mixing with the heating process to enhance the product homogeneity (168, 169). Hot-melt extruders are composed of four major compartments: a feeder hopper, a mixing screw, a heating barrel and a die, as seen in **Figure 1.11**. The API and carrier are frequently premixed before loading into the hopper. The screw is the most important part of the hot-melt extruder because it drives the API and carrier through a mixing process in the heating barrel where high temperatures and screw shearing enhance the homogeneity of the mixing (168, 169). As a result, HME is an efficient mixing process in comparison to the conventional melting based method due to the twin screws mixing. The homogeneously mixed matrices of the API and carrier are forced through the die, where the matrices' shapes are dictated. In

addition, HME does not require the use of organic solvents, which makes it more environmentally friendly than processes such as spray drying.

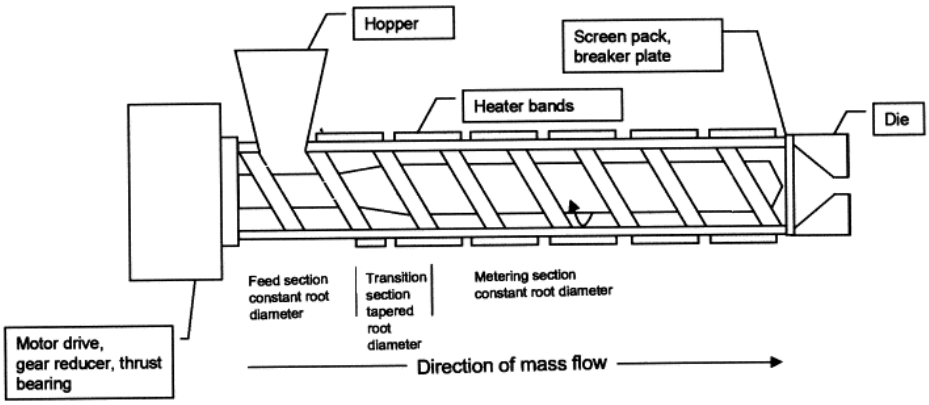

Figure 1.11 Schematic diagram of a hot-melt extruder, reproduced from reference (168).

HME is widely used in the pharmaceutical industrial as a technology to prepared solid dispersion formulations because it is robust and feasible to scale up to mass production. Thus, many commercial solid dispersion products are manufactured by HME, i.e., Kaletra® (Abbott), Isoptin SRE ® (Abbott) and Ozdurex® (Allergan) (99, 169, 170). The advantage of a fast residence time may allow HME to process thermal labile API. DiNuzio et al. prepared a solid dispersion of thermosensitive hydrocortisone with PVP-VA with a lab scale hot-melt extruder (171). The residence of mixing was 5 min, with which hydrocortisone did not show any degradation. However, the residence time may increase due to the screw length in industrial scale extruders. Thus, HME is not recommended as the first choice preparation for thermal labile APIs.

In addition, HME can be equipped with downstream processes, including pelletization, milling and injection moulding (168, 169). As an example, injection moulding (IM) is a downstream unit that is used to produce final dosage forms for pharmaceutical products. IM is a versatile and rapid manufacturing technology that has been used widely in the plastics industry to produce objects that have different geometries and sizes (172, 173). An IM machine consists of two major compartments, including an injection unit and a clamping unit, as seen in **Figure 1.12**. The HME can serve as an injection unit in which thermoplastic or thermoset materials are heated, mixed and injected into the clamping unit (168, 169). The clamping unit is the terminal stage of the IM process. It has a two half parts that combine into a three-dimensional shape of the desired object. The IM cycle begins with the heat soften materials being injected into the closed mould cavity with the high pressure generated from the screw of the injection unit. The clamp unit tightly shuts to

maintain pressure during the injection step. After the injection, the melts cool down and solidify in the mould cavity shape. Subsequently, the final product is ejected from the mould and a new cycle starts. Hence, IM is a continuous manufacturing process.

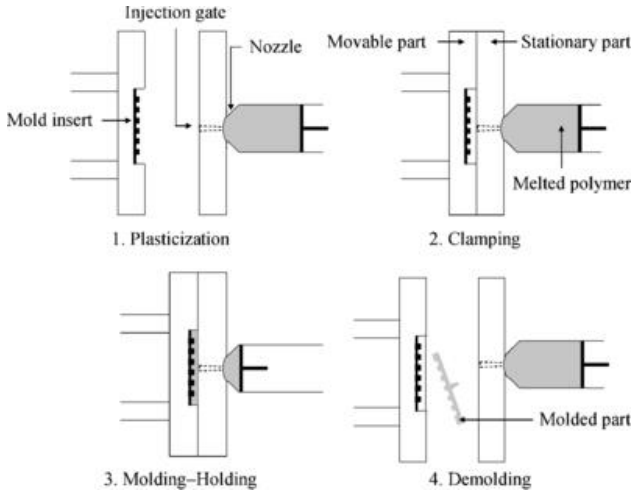

Figure 1.12 Schematic diagram of injection moulding process, reproduced from reference (172).

IM has been applied to the pharmaceutical industry as a down-stream process to produce final dosages from HME (168, 169). IM can produce various geometries of products, including films, tablets, rods and rings. Therefore, it can be applied to manufacture various types of dosage forms for different drug delivery systems, such as the oral route, implant device and intravaginal inserts (163, 174, 175). The tablets that are produced from IM can be instantly released or sustain-released depending on the polymers that are used as the tablet matrices. The instant release tablets used low viscosity HPMC, polyvinyl alcohol and sodium starch glycolate as the tablet matrices (176), while sustained-release tablets are produced from a blend between EC and HPMC (163). However, there are several drawbacks to IM that need to be considered, including the involvement of heat in the process. Hence, IM is not suitable for manufacturing thermal-labile APIs. Even though IM allows the production of a variety of shapes, changing the object shape requires a different mould, which is inconvenient and carving a mould is rather expensive. Therefore, IM is a technology that has potential to be used for industrial scale manufacturing process for thermal-insensitive pharmaceutical products because it is a continuous process with high product reproducibility.

Fused deposition modelling (FDM) is a heated base technology that has been applied to constructing a 3D object (177, 178). It produces a 3D object by depositing, layer-by-layer, semi-molten materials on the stage. A schematic graphic of an FDM apparatus is shown in **Figure 1.13**. The thermoplastic filaments, i.e., PVA or PCL, are used as materials for FDM

printing. The filaments are forced by the roll compactors through the heating zone where they enter a semi-molten state. The semi-molten thermoplastic is extruded to the nozzle tip and deposited at the desired area on the stage. Then, the stage lowers, and another layer of the semi-molten product is deposited on top of the previous layer. These processes are repeated to build the object in a layer-by-layer manner (177). However, the layer-by-layer deposition can cause a surface defect in the staircase and chordal effect.

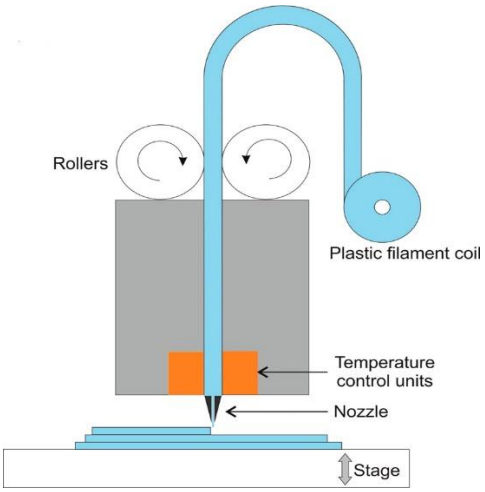

Figure 1.13 Schematic diagram of fused deposition modelling printer, reproduced from reference (177).

FDM technology can be applied to pharmaceutical applications, particularly, as a means to prepare tablets (179-181). The drug loaded filament of the FDM can be prepared by soaking commercial filaments in a drug solution (179, 180) or preparing by HME (181). Goyanes et al. prepared aminosalicylic acid PVA tablets using FDM. The drug content in the printed tablets was dependent on their infill (180). The authors soaked the commercial PVA filament in a concentrated API ethanol solution. The drug loading in the FDM filaments was achieved via passive diffusion. However, using this method it is difficult to control the drug content in the filaments. This results in a very low drug content (approximately 0.3%) (180). The HME process can be a better platform to produce drug loaded filaments. The drug and FDM polymer are homogeneously mixed and extruded at the desired filament diameter as needed for the FDM machine. Therefore, the difficulty of minimising API content variation in the FDM filament is overcome by HME (181). One example describes how Pietrzak and co-workers successfully prepared FDM filaments using HME (181). The authors produced FDM filaments from methacrylic polymers, including Eudragit E, RS and RL grades, and a cellulose based polymer (hydroxylproply cellulose) loaded with a model drug, theophylline. These filaments demonstrated an excellent printing property with 91-95% dose accuracy (181).

FDM is a potential platform to produce solid state formulations with precise API contents. Therefore, it is a suitable concept for producing personalised medicine, in which the drug content can be modified for the individual patient. Furthermore, FDM is a benchtop machine with a reasonable price. Thus, it is a promising technology for future medication. The FDM process is limited by the printing temperature for the materials, for example, PVA and PCL soften above 200°C (178, 179). The high temperature of the FDM process might not be suitable for printing low degradation temperature APIs.

1.4.5.2 Solvent evaporation based methods

An organic solvent is frequently used as a medium to dissolve the API and the carrier to enhance the mixing. Subsequently, a solvent removal process is conducted to obtain solid dispersions (13, 85). The solvent method is particularly suitable for producing solid dispersions of thermo-sensitive drugs. However, the significant disadvantage of this method is the environmental hazard caused by the toxicity of a large volume of organic solvents for disposal (168). In addition, the solvent residue in the solid dispersions is another concern due to its toxicity to humans. It can also plasticize the solid dispersions resulting in physical instability.

Spray dying is a processing method that transforms the solution or suspension into solid products. It is commonly used in various fields, such as food, ceramic, paint, fertiliser and pharmaceutical industries (182, 183). It is frequently employed as a solid dispersion preparation method for improving BCS class II and IV drugs (34, 97). For preparing solid dispersions, organic solvents are commonly used. The API and the carrier are dissolved in their mutual solvent. A schematic diagram for spray dried unit is depicted in **Figure 1.14**. In the first chamber, the solution for spray drying is fed to an atomiser at a pre-heated temperature by a peristatic pump. The solution is sprayed into microsized droplets by an atomiser and then these droplets are dispersed in the hot inert gas inlet (dry nitrogen). Consequently, the droplets rapidly solidify into micropaticles, usually within a milisecond (182-184). These microparticles are convected to the second chamber where they are collected into a particle vessel by a cyclone.

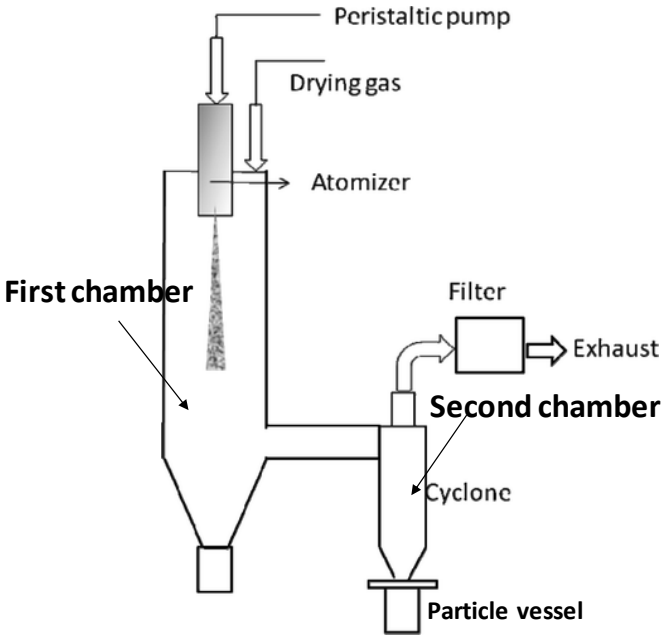

Figure 1.14 Schematic diagram of a spray dried unit, adapted from reference (185).

Spray drying has been successfully used to prepare amorphous particles of poorly water-soluble APIs, such as atorvastatin, albendazole, griseofulvin, hydrocortisone, indomethacin, testosterone and piroxicam (34, 186). The spray dried particle size is in the range of micrometres, which results in an increased surface area of the solid dispersion formulations. Spray drying demonstrates a continuous process that is cost-effective and easy to scale up (182, 183). Thus, it is commonly used for industrial scale manufacturing. Therefore, spray drying has been used to manufacture some of the marketed solid dispersion products, including Intelence® and Certican® (99).

In comparison to spray drying, spin coating has no heating element in the process. It has been widely used in many industrial areas, such as microelectronic applications, protective coating (against UV, starching, corrosion and humidity) and paint coating (187-189). A substrate is placed on the spinning chuck and then small droplets of drug and carrier solution are applied to the spinning substrate. The substrate attaches to the spinning chuck by vacuum force during the spinning process. The high-speed spinning creates centrifuge forces that cause a strong sheer to the solution. As a consequence, the droplets spread radially on the substrate. This process occurs with subsequent solvent evaporation, which results in a thin film of a few microns thickness after completing the solvent removal process (188). A schematic diagram of the spin coating is illustrated in **Figure 1.15**.

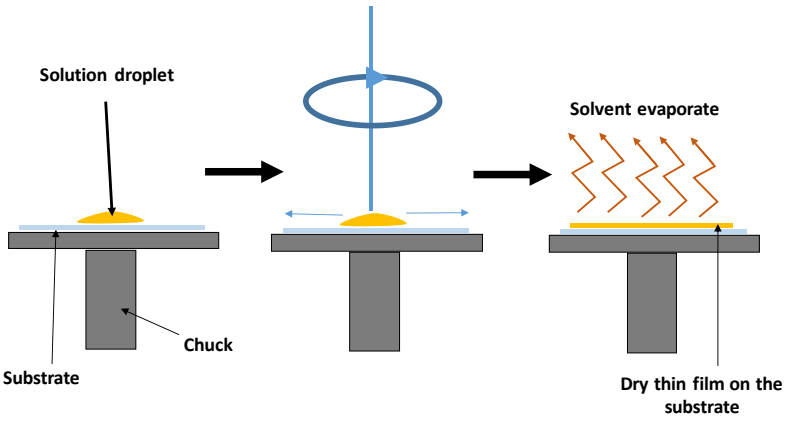

Figure 1.15 Schematic diagram of spin-coating procedure preparing a thin film on a substrate.

In pharmaceutical research, it has been used to study the crystallisation of an amorphous drug (190) and to prepare a drug eluting coating contact lens (191). Qi et al. prepared amorphous felodipine using a spin coating technique and investigated the crystallisation of the amorphous drug under a high humidity condition (190). Paudel et al. suggested that the data that was obtained from varying the time, rotation speed and processing temperature of the formulation prepared by spin coating can provide essential information about the phase structure during the spray drying process (182). In addition, spin coating has been used as a preparation method to understand the behaviour of solid dispersions. Konno et al. reported that a thin film solid dispersion of felodipine with a polymer, such as PVP, HPMC and HPMCAS, can inhibit the crystallisation of the amorphous drug (89). The application of spin coating in the pharmaceutical field is limited only to lab research, and the industrial application of spin coating in the pharmaceutical industries has not been established.

1.5 Electrospinning

Electrospinning is a processing technique using electrostatic forces to fabricated non-woven micro to nano sized fibres from either a molten or solution polymer. Electrospun polymeric fibres demonstrate a broad range of applications in filtration, nanosensors, protective clothes, tissue engineering and drug delivery (25, 27, 192-195). In general, an electrospinning apparatus consist of four main compartments that are a solution reservoir, solution flow regulator, high voltage supplier and collector, as illustrated in **Figure 1.16a.** A solution reservoir typically connects to a capillary where the polymeric solution is continuously forced through by a flow regulator to form a pendant drop. A positive electrode from the high voltage source attaches to a metal part of the capillary. The electrospinning process starts after mutual charges are applied to the polymeric solution. As a consequence, when increasing the electrical field, the pendant drop transforms into a

conical shape due to repulsive forces between the mutual charges, which is known as a Taylor cone **(Figure 1.16b)**. The solution jet emits from the apex of the Taylor cone where the polymeric solution accelerates toward to the collector. The solution jet undergoes a chaotic movement that causes the electrical field to oscillate. Therefore, it increases the path length to the collector resulting in enhanced solvent evaporation and a reduction in the diameter of the jet before solidifying as a nano to micro fibre at the collector (22).

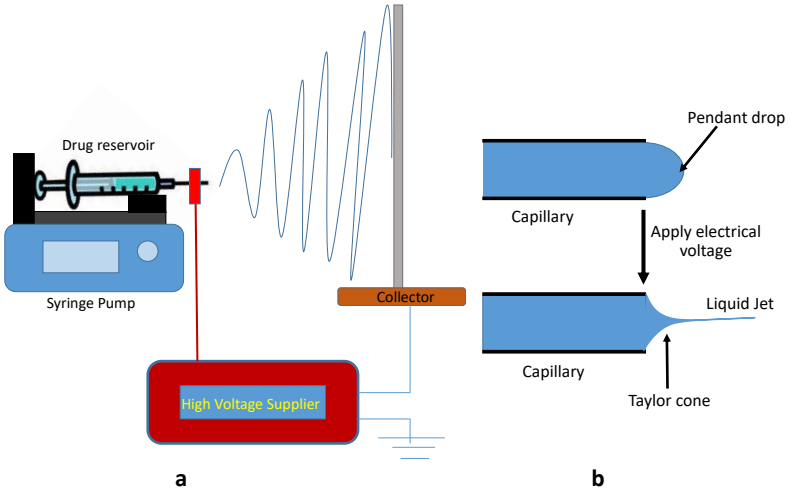

Figure 1.16 Diagram of electrospinning setup (a) and Taylor cone formation (b).

Electrospinning is a promising method to prepare solid dispersions. It demonstrates potential benefits over the other solid dispersion preparation methods (25-27, 133). In comparison to the melting based methods and spray drying, electrospinning has no heating element. Thus, it is suitable for preparing solid dispersions of thermosensitive APIs. The process of solvent evaporation for the electrospinning takes only a few microseconds (193, 196). As a consequence, the API is immediately entrapped in polymer matrices in a molecularly dispersion manner. Hence, electrospinning can be used to achieve molecular dispersions. The non-woven solid dispersion electrospun fibres are the final products that can be used directly after preparation and do not require any additional downstream processing, i.e., oral mats, transdermal patches and wound healing scaffolds (25-27, 197-199). However, the solid dispersions that are produced from HME require IM as a terminal process to shape the final products or pulverise the extrudates before compressing into tablets (168, 169, 176). Therefore, electrospinning is a single step process to achieve the final products.

In addition, electrospinning technology shows many benefits in pharmaceutical drug delivery research, which are evident from the large increase in the number of electrospinning research articles (27). The electrospinning setting is simple which can be a custom-made apparatus, in comparison to HME, IM and spray drying (193, 200). Therefore, it comes with accessible prices. Electrospinning requires a small amount of

material (milligrams to grams) for sample preparation for each batch. This shows advantages over HME and spray drying that require a greater quantity of the starting materials for sample preparation. Hence, electrospinning can be a reasonable choice for preparing expensive research specimens, for example, new drug candidate compounds, DNA, RNA and cells. In addition, using a special spinneret can modify the structure of the electrospun fibres at the nanoscale. This technique is called coaxial electrospinning and allows the rendering of a core-shell structure for the electrospun fibres in a nanometer range (21, 160, 201).

However, there are limitations associated with the electrospinning process. The optimisation process of electrospinning depends on many factors, i.e., type of polymer, solvent, molecular weight, concentration, feeding rate, applied voltage and distance from the spinneret to the collector (202). It requires an expertise and time to optimise these conditions. The conventional lab scale electrospinning has a significant drawback in terms of the low production rate, which impedes it from being scaled up into industrial scale production (203). Considering lab scale electrospinning, it can produce grams of electrospun fibres per hour. Free surface electrospinning is a solution to the low production rate of electrospinning. It could potentially increase the production to a kilogram per hour with a continuous electrospinning fabrication process (203), which will be discussed later in section 1.5.4.

1.5.1 Factors influencing electrospinning

There are three main categories of factors that can significantly affect the electrospinning process and the resulting fibre morphology. They are solution factors, apparatus parameters and environmental humidity. Therefore, attention must be carefully paid to the optimisation of these electrospinning parameters (22, 192, 204).

1.5.1.1 Solution factors

The electrospinning solution is defined as the solutions that contain a spinnable polymer in a spinnable solvent. To determine whether a solution is suitable for the electrospinning process, the physical properties, such as concentration, molecular weight, solvent volatility, conductivity and dielectric, need to be taken into account (193, 202). Most solvents can provide sufficient conductivity for electrospinning. However, if prioritising relative to spinnability and significant fibrous morphology change, the polymeric concentration, molecular weight and solvent volatility are the important factors that need to be considered (204-206).

- Polymer concentration and polymer molecular weight

At given apparatus parameters (voltage, flow rate and distance), the spinnability of the polymer solution is determined by the concentration. The polymer chains entanglement

needs to be sufficient to maintain the fibrous structure against the contraction force from the surface tension that try to minimise the surface area. Otherwise, the contraction forces from the surface tension will occur and leave beaded defects on the fibrous structure (202). In the case of a very dilute solution, insufficient chain entanglement leads to the liquid jet breaking down into small droplets; this process is identified as electrospray (207). Increasing the concentration of the polymeric solution results in fewer beaded defects, enlarges the fibrous diameter and overall the fibres become uniform in diameter (208). As the concentration is proportional to viscosity, the highly concentrated solution prevents fibre formation due to inefficient solution flow control through the capillary (22). **Figure 1.17** illustrates the effect of polymer concentration on fibrous architecture formation.

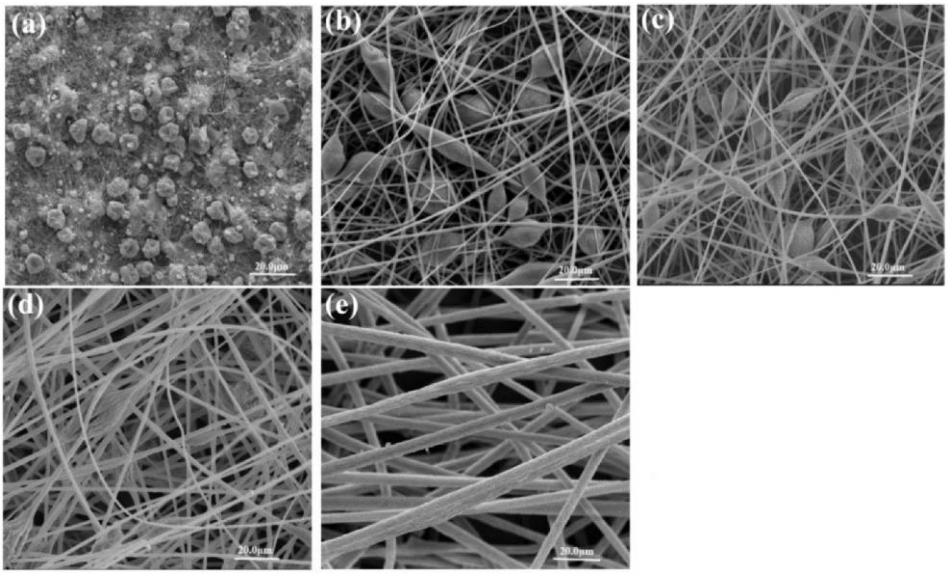

Figure 1.17 Scanning electron micrographs of electrospun polystyrene fibres on stationary Aluminium foil of 80 rpm and applied voltage of 15 kV with different concentrations of polystyrene /dimethylformamide solutions (**a**) 10%, (**b**) 23%, (**c**) 27%, (**d**) 32% and (**e**) 40% (w/v), reproduced from reference (209).

The molecular weight of the polymer chain is another factor that demonstrates an impact on the spinnability. The medium molecular weight PVP K-30 needs a concentration of at least 30% w/v in ethanol to form electrospun fibres, but the higher molecular weight grade PVP K-90 requires only 5% w/v in the same solvent to fabricate polymer fibres (23, 26, 210). The high molecular weight polymers enhance the polymer chain entanglement resulting in a reduction in the concentration that forms electrospun fibres.

- Solvent volatility

The choice of solvent is another important factor contributing to the spinnability of the polymer in the electrospinning process. To form solid fibres, volatile solvents are used as

the vehicle. The solvents used in electrospinning are expected to evaporate completely from the fibres before the fibres deposit on the collector (193, 211). Solvents with different volatilities influence the morphology and spinnability of the polymer at given concentrations. Wannatong and coworkers reported that polystyrene demonstrated different fibrous morphologies and percent yields among the six solvents used in their study (205). Tetrahydrofuran was the solvent of choice for polystyrene, which offered the highest percentage yield and uniform cylindrical fibrous structure. Moreover, the solvent volatility was reported to influence the formation of micro-nano pores on the electrospun fibres (212, 213). Megelski et al. and Luo et al. successfully prepared porous electrospun fibres from polystyrene and polymethyl silsesquioxane by using tetrahydrofuran for the polystyrene fibres and a mixture of propanol and methanol for the polymethyl silsesquioxane (212, 213). Organic solvents are often used as the vehicle for the preparation of solid dispersions from electrospinning because they are mutual solvents for drugs and polymers. In addition, organic solvents offer fast solvent evaporation that rapidly embeds the drug in the polymer matrices.

1.5.1.2 Apparatus parameters

In addition to the solution parameters, apparatus parameters are another set of factors that influence the spinnability. They can be classified as applied voltage, flow rate, capillary-collector distance and capillary modification. These parameters will be discussed in the following sections.

- Applied voltages

To transform a pendant drop to a Taylor cone, a sufficient applied voltage is a prerequisite. A Taylor cone is formed after the charges overcome the surface tension of the electrospinning solution (193, 200). Both positive and negative high voltage suppliers can be used. It is noted that the particular details of the electrospinning set up are different between a positive and negative high voltage supplier (202). An insufficient voltage leads to a surface tension rebound that causes beaded fibres. The required voltage needs to be maintained slightly above the point at which a stable Taylor cone is obtained to ensure the stability of the electrospinning process and to reduce the fibre diameter distribution. The increase in applied voltage results in an increase in the electrical field. Consequently, the fluid jet is accelerated and this increases the time of flight to the collector due to a higher degree of blending instability (200). This results in a decrease in the diameters of the electrospun fibres. However, the over executed high voltages decrease the Taylor volume until it moves to the side of the capillary (214). This phenomenon is caused by imbalances between the fluid fed through the capillary and the liquid jet that travels to the collector side. As a consequence, the side Taylor cone influences the solution flow that leads to increasing beading defects on the fibres (22, 214).

- Feeding rate

The amount of polymer solution in the electrospinning process is determined by the feeding rate. Gravity and pumps have been used to control the solution feeding from the reservoir (202). Pumps are frequently used because they offer a precise and adjustable feeding rate. The feeding rate influences the stability of the Taylor cone. At the given voltage, the fluid is drawn to a collector as it is influenced by an electrical field. To stabilise the Taylor cone, sufficient fluid needs to be fed through the capillary constantly. A high feed rate leads to an increased diameter of the electrospun fibres and bead defects because the amount of fluid has increased (215). An overly excuted feed rate causes a dripping of the solution because of the imbalance in the fluid feeding and fluid drawing to the collector. Therefore, a slow feed rate is preferable in electrospinning (22). Moreover, an electrospinning solution that prepares in organic solvents offers a quicker feed rate than a solution in an aqueous solvent because the volatility of the organic solvents is higher than that of the aqueous solvents.

- Spinneret to collector distance

The distance from the spinneret to the collector is another factor that affects the spinnability and morphology of the electrospun fibres (22). An appropriate distance is required to allow the liquid to completely dry before depositing on the collector. The distance in the electrospinning depends on the volatility of the solvent. A highly volatile solvent, such as dichloromethane, requires a short distance while water requires a longer distance to evaporate completely from the fibrous matrices (194, 216).

1.5.1.3 Environmental humidity during electrospinning process

Environmental humidity plays a significant role in the electrospinning process. It can reduce the solvent volatility and cause a clogging at the tip of the spinneret (210). Additionally, high humidity causes water condensation on the electrospun fibres, which affects the morphology of the fibres (210, 217). In the case of a hydrophilic polymer, such as PVP, the electrospun fibres fuse and form transparent films at a relative humidity greater than 60%RH (210).. On the contrary, hydrophobic polystyrenes in a THF solution were electrospun at different relative humidities. Circular pores with sizes between 60-190 nm were formed on the surface of the polystyrene at a relative humidity greater than 25%. The average pore size increased upon higher relative humidities. The authors explained that the moisture condenses into tiny droplets on the surface of the electrospun fibres during the flight of the liquid jets toward to the collector. After the small water droplets dry, they leave imprints as circular pores on the surface of the electrospun fibres (217).

1.5.2 Coaxial electrospinning

The modification of the spinnerets for the electrospinning can affect the physical properties and structure of the electrospun fibres. A phase-separated layer (known as the core-shell structure) can be created inside an electrospun fibre by using a modified capillary (coaxial needle) (20, 21, 160, 218). This needle is composed of at least two different diameters of needles overlaying each other. The apparatus set up is similar to the conventional electrospinning but requires another flow regulator unit as seen in **Figure 1.18**. One solution is fed through the core layer and the other one is fed at the shell layer. The outer layer solution is typically a spinnable polymer to form structural electrospun fibres while the core solution can be flexible and non-spinnable because it will be embedded in a core of electrospun fibres. The two solutions meet at the tip of the coaxial needle and are pulled by the electrostatic force toward the collector. The liquid jet solidifies, and the core-shell structure fibres are obtained (20, 160, 218). Additionally, the thickness of the outer and inner layers can be modified by adjusting the feeding rate of the external and the internal solutions (160).

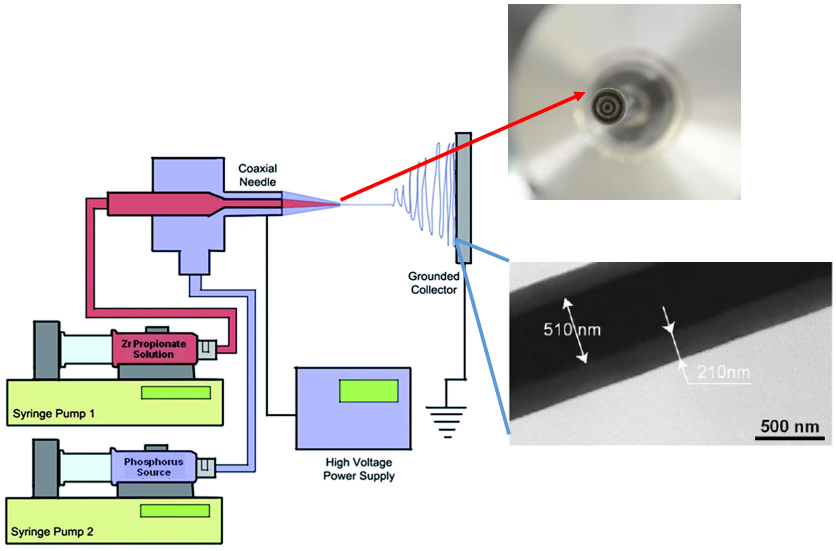

Figure 1.18 Coaxial electrospinning set up with modified capillary and structure of core-shell electrospun fibres under transition electron microscopy. This figure is adapted from reference (218).

The use of core-shell structured electrospun fibres expands many novel applications in tissue engineering and drug delivery (160, 201, 219). Chen et al. prepared coaxial electrospun fibres from collagen (shell) and polyurethane (PU) (core). The core-shell electrospun fibres of PU-collagen demonstrated a better cell viability than the pure collagen and PU electrospun fibres (219). The authors explained that the outer layer of the collagen mimicked the extracellular matrices, which enhanced cell viability, while the core PU

maintained the three-dimensional fibrous structure, which provides a good environment for the cell growth. In comparison with collagen fibres, it swollen into a hydrogel which is not a suitable condition for cell proliferation (219). In addition, core-shell electrospun fibres can be used as modified release devices for the oral drug delivery route (160, 201). The details of this application will be discussed in the next section.

However, there are several concerns about the coaxial electrospinning process. In comparison to the single spinneret electrospinning, it requires a much slower solution feeding rate of approximately less than 1 $ml.hr^{-1}$ (21, 160, 201), which is due to the core and shell solutions needing to slowly meet at the tip of the spinneret to form the core-shell structure before being accelerated toward to the collector. Consequently, the coaxial electrospinning has a very low production rate. Moreover, the core-shell structure is difficult to characterise. Transition electron microscopy is the only technique used to investigate the core-shell structure (20, 218, 219). This technique is based on the atomic density of the material. Particularly if the atomic densities of the core and shell are similar, it is very difficult to distinguish between the core and the shell structures.

1.5.3 Applications of electrospinning in drug delivery

Electrospinning has already demonstrated a wide range of applications in biomedical areas, such as tissue engineering, wound dressing and pharmaceutical drug delivery (25, 192, 196, 220). Electrospinning gained interest in pharmaceutics a decade ago. Many pharmaceutical researchers have been using the electrospinning technique to produce devices or solid dosage forms for various types of drug delivery system, such as transdermal patches, wound scaffolds and oral fibrous films (21, 23, 24, 26, 160, 198, 199, 221-228).

- Oral drug delivery

Electrospinning is a high potential technology that can produce molecular dispersions. This contributes to the ultrafast solvent evaporation that enhances the homogeneity of the drug and the carrier (26, 133, 229, 230). The advantages of molecular dispersion of APIs in electrospun fibrous matrices is improving the solubility of poorly water-soluble drugs and stabilising them. Yu et al. prepared electrospun fibres of ibuprofen, a poorly water-soluble drug, with a hydrophilic matrix PVP. The ibuprofen PVP electrospun fibres significantly improved the drug solubility in comparison to the physical mixture. In addition, ibuprofen completely dissolved within 30 minutes (26). Ignatious and co-workers showed that polyethylene oxide electrospun with nabumetone enhanced the aqueous solubility of the drug in comparison to its crystalline form. Furthermore, the electrospun fibrous formulation demonstrates a faster drug release rate than the nanocrystals formulation (25).

The molecular dispersion of API in electrospun matrices enhances the stability of the electrospun formulations. Brettmann et al. observed the different domain sizes of drug-polymer phase separation in the solid dispersion that was prepared by HME and electrospinning (133). The hot melt extrudate showed a domain size greater than 100 nm while the electrospun fibrous formulations exhibited domain sizes between 2 and 11 nm. In another study by the same group, the authors demonstrated that high drug loading electrospun fibres of indomethacin and aliskiren at 50% were stable under a storage condition of 40°C with a low humidity condition (231). Lopez et al. demonstrated that electrospining can stabilise indomethacin and griseofulvin in their amorphous form in PVP matrices for over eight months in a desiccator filled with silica gel (232).

Electrospining can be used to prepare various types drug delivery devices for the oral route, including immediate release, targeted release, sustained release and biphasic release, depending on the types of polymer matrices used. Hydrophilic polymers, including PVP, PEO and PVA, are used as matrices for immediate-release oral fibrous films for an oral route (21, 25, 26, 224, 233). These polymers quickly dissolve and release API when they are in contact with an aqueous media. The solid dispersion of PCM and PVP, which are prepared by electrospinning, demonstrated a faster drug release in comparison to the same formulation produced from freeze-drying, vacuum drying and heat drying methods (24). This follows from electrospun fibres having a high surface area to volume ratio.

The targeted release of electrospun fibres can be prepared using an enteric coated polymer or pH dependence dissolvable polymer, such as Eudragit L100 or Eudragit L100-55 (162, 201, 234). Yu's group prepared diclofenac sodium electrospun fibrous mats for colon targeted drug delivery using Eudragit L100-55 and Eugragit L100 as the fibre matrices. These polymers dissolve at a pH greater than 6.8. The authors observed that the diclofenac sodium loaded Eudragit L100-55 and Eugragit L100 electrospun fibres released the API at less than 5% in an acidic pH. While at the optimal pH, the diclofenac showed a complete release within 30 min (201, 234).

Therefore, electrospinning can be a potential way to produce molecular dispersions of FF, the main model drug in this study. This is due to the electrospinning stabilising FF molecules in the fibrous polymeric matrix as molecularly dispersed or in their amorphous state resulting in improvements in the physical stability of the molecular dispersion formulations. Moreover, the molecular dispersions of FF electrospun fibres may significantly improve its aqueous solubility and also provide a fast release because of its high surface area to volume ratio.

In addition, the modified release of electrospun formulations can be obtained by blending immediate release polymers and sustained release polymers in an appropriate ratio (21,

160). Yu et al. prepared electrospun fibres from coaxial electrospinning technology by varying the ratio of PVP and EC. The authors successfully achieved a biphasic release from PVP to EC in the proportion 1:1 (21). Jiang et al. reported a similar observation in which a biphasic drug release from electrospun fibres was obtained by blending PVP and Zein at the proportion 1:1 (160). These authors used the coaxial electrospinning to manipulate the core-sheath fibre structure. This technique has a very low production rate and requires special equipment for the double layer spinnerets. Therefore, the ideal system for the biphasic electrospun formulation would be a homogeneous phase of drug and polymer during storage that provides high stability. Upon dissolution, the *in situ* phase separation occurs between the hydrophilic and the hydrophobic polymers. The hydrophilic polymer provides immediate release while the API is slowly released from the hydrophobic polymer.

- Topical drug delivery applications

In topical drug delivery, electrospun fibres can be used as a potential means for transdermal and wound healing scaffold applications. Verreck et al. prepared electrospun matrices from non-biodegradable polyurethane (PU) for a transdermal patch application. The transdermal PU electrospun patch demonstrated the prolonged-release of the model drug itraconazole and ketanserin (197). Alhusein et al. prepared three-layered electrospun fibrous wound scaffolds from a sandwich of poly(ethylene-co-vinyl acetate) between PCL layers that contained an antibiotic, tetracycline (198). The scaffold could maintain the antibiotic release for 14 days.

Wound healing scaffolds demonstrate more complicated functions than the oral route dosage forms, including requiring different APIs to be released in various periods. Thakur et al. prepared electrospun scaffolds from poly-l-lactic acid that contained lidocaine (analgesic) and mupirocin (antibiotic). Lidocaine was instantly released at the early stage to subdue pain. Subsequently, mupirocin, an antiseptic, had sustained released from the scaffolds to minimise the risk of bacterial infection (227). In addition, the scaffolds from the electrospun fibres also offer advantages of absorbing wound secretions and providing air ventilation (235). These functions promote cell proliferation at the wounded area.

1.5.4 Future outlook for electrospinning in pharmaceutical industry

Electrospinning has recently attracted the attentions of pharmaceutics as a novel method for drug delivery, as shown by the numerous research studies and patent applications that rocketed in the past decade (25, 192, 220, 221, 236). It is a versatile technique that allows the production of various types of drug delivery devices, as aforementioned. Despite the fact that no commercial pharmaceutical product from electrospinning is available up to

now: conventional electrospinning has the disadvantage of a slow process. These problems impede the industrial production of electrospinning products.

The free surface electrospinning is a breakthrough for this problematic issue (203, 237). The schematic of the free surface electrospinning apparatus is illustrated in **Figure 1.19**. A wheel, which is wrapped in stainless wire rotates, generating approximatly 2.5-18 rpm during the operation (203). The wire is periodically dipped into a bath containing polymer solution. A thin layer of polymer solution is coated around the wire after it emerges from the bath. This layer rapidly forms multi-Taylor cones and initiates the electrospinning when the wire rotates parallel through a plate collector (203).

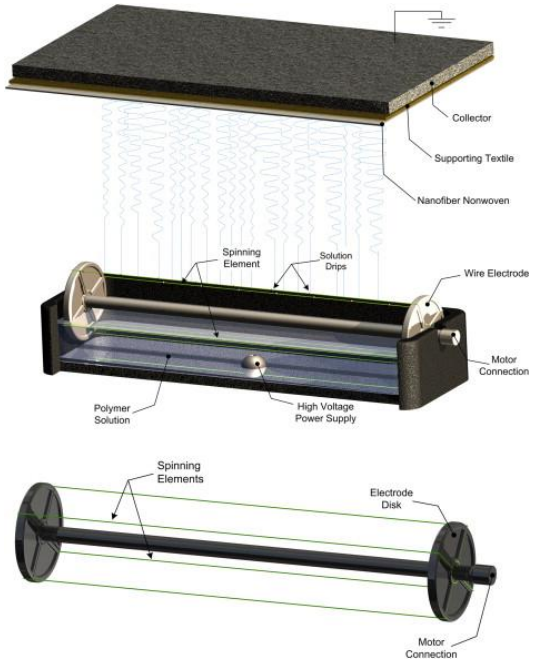

Figure 1.19 Schematic of wire electrode a free surface electrospinning apparatus. This figure is reproduced from reference (238).

Free surface electrospinning is a continuous production process. Hence, it is feasible to scale up electrospun fibre production to industrial scales. Recently, Forward and co-workers successfully prepared core-shell fibres of PEO and PS using free surface electrospinning (239). Thus, free surface electrospinning is a solution to solve the problem of low production amounts when using the coaxial electrospinning. Commercial free surface electrospinning machines are available from Inovenso Ltd. and Elmarco (237). Therefore, free surface electrospinning technology is a promising method that overcomes the limitations of conventional electrospinning. It can be a potential platform for manufacturing electrospun fibres for pharmaceutical applications at the industrial scale.

1.6 Aims of the project

FF is a poorly water-soluble drug. The factors controlling its crystallisation from the supercooled amorphous state have not been determined. The amorphous FF shows a high driving force for crystallisation over the entire range of temperatures. However, it has a high entropic barrier for crystallisation and high configuration entropy. This mean that the amorphous FF is difficult to crystallise spontaneously because it has a low probability to form an optimal orientation and conformation, which is favoured for the homogeneous nucleation (9, 10). Thus, nucleation is the rate-limiting step for FF crystallisation. Heterogeneous nucleation using impurity additives can be a potential means to control the crystallisation of the amorphous FF. In addition, the temperature and surface availability of the supercooled FF during the crystallisation are important factors that possibly affect the polymorphism of FF. Therefore, manipulating these factors may be a promising way to crystallise amorphous FF into particualar polymorphs.

To further improve the drug delivery of FF, solid dispersions can be an efficient approach.The solid dispersions containing polymer blends, which are produced from the electrospinning technique, could be a potential approach to address the problem of being poorly water soluble and the physical instability of amorphous FF. The electrospinning process is capable of preparing the molecular solid dispersions to enhance the aqueous solubilityof the poorly water-soluble drugs (25, 27). In addition, it provides a high surface area to volume ratio for the fibrous solid dispersion, which can offer a fast drug release (26, 27). Blending the hydrophobic polymer to the hydrophilic polymer can be a potential approach to reduce the moisture uptake of the solid dispersion formulations and to increase the physical stability of the amorphous FF. In this study, FF was formulated as electrospun fibres with the polymer blend matrices of PVP, a hydrophilic carrier, and more hydrophobic carriers, including HPMCAS, Soluplus or Eudragit E.

Another aspect of the control-release application, blending water soluble with water insoluble or pH dependent soluble polymers can be a potential way to formulate a tuneable release formualtion (21, 160, 162). Therefore the final stage of this project explored the potential of using polymer blended fibres for tuneable drug release. The water soluble polymer PVP and pH dependent soluble HPMCAS were used as the electrospun fibrous matrices for the biphasic drug release purpose. In addition, the *in situ* phase separation of the fibres during dissolution was studied in association with drug release.

The key objectives of this project are summarised below:

1. To fully understand the crystallisation behaviour of FF from its supercooled amorphous state. The heterogeneous nucleation approaches, included the surface disruption technique and impurity additives (talc), were used to crystallise amorphous FF. In chapter 3, the effect of external triggers, including crystal growth temperatures and open top surface of the amorphous FF during its crystallisation, were investigated. Chapter 4 explores the use of talc to crystallise amorphous FF, which results in the new polymorph of FF. Furthermore, the factors that influence a polymorphic transformation between the metastable form and the stable form were also studied.
2. To develop polymer blend based electrospun fibrous formulations to stabilise the amorphous FF, reduce moisture absorption, enhance physical stability and improve dissolution of the drug. Moreover, the influences of moisture uptake on the drug-polymer miscibility and structural deformation in the polymer blended electrospun fibres were also investigated (Chapter 5).
3. To provide detailed understandings of the phase separation in the electrospun polymer blend nanofibers. Using *in situ* phase separation of the polymer blend fibres to potentially manipulated the drug release rate was explored (Chapter 6).

1.7 References

1. Mullin JW. Crystallization: Butterworth-Heinemann; 2001.
2. Bernstein J. Polymorphism in molecular crystals: Oxford University Press; 2007.
3. Hilfiker R. Polymorphism: in the pharmaceutical industry: John Wiley & Sons; 2006.
4. Singhal D, Curatolo W. Drug polymorphism and dosage form design: a practical perspective. Advanced Drug Delivery Reviews. 2004;56(3):335-47.
5. Tao J, Jones KJ, Yu L. Cross-Nucleation between d-Mannitol Polymorphs in Seeded Crystallization. Crystal Growth & Design. 2007;7(12):2410-4.
6. Reischl D, Röthel C, Christian P, Roblegg E, Ehmann HMA, Salzmann I, et al. Surface-Induced Polymorphism as a Tool for Enhanced Dissolution: The Example of Phenytoin. Crystal Growth & Design. 2015;15(9):4687-93.
7. Chadwick K, Myerson A, Trout B. Polymorphic control by heterogeneous nucleation-A new method for selecting crystalline substrates. CrystEngComm. 2011;13(22):6625-7.
8. Price CP, Grzesiak AL, Matzger AJ. Crystalline Polymorph Selection and Discovery with Polymer Heteronuclei. Journal of the American Chemical Society. 2005;127(15):5512-7.
9. Zhou D, Zhang GGZ, Law D, Grant DJW, Schmitt EA. Physical stability of amorphous pharmaceuticals: Importance of configurational thermodynamic quantities and molecular mobility. Journal of Pharmaceutical sciences. 2002;91(8):1863-72.
10. Amstad E, Spaepen F, Weitz DA. Crystallization of undercooled liquid fenofibrate. Physical Chemistry Chemical Physics. 2015;17(44):30158-61.
11. Heinz A, Gordon KC, McGoverin CM, Rades T, Strachan CJ. Understanding the solid-state forms of fenofibrate–a spectroscopic and computational study. European Journal of Pharmaceutics and Biopharmaceutics. 2009;71(1):100-8.
12. Chiou WL, Riegelman S. Pharmaceutical Applications of Solid Dispersion Systems Journal of Pharmaceutical sciences. 1971; 60(9):1281-301.
13. Christian Leuner, Dressman J. Improving drug solubility for oral delivery using solid dispersions. European Journal of Pharmaceutics and Biopharmaceutics 2000;50: 47-60.
14. Serajuddin ATM. Solid dispersion of poorly water-soluble drugs: Early promises, subsequent problems, and recent breakthroughs. Journal of Pharmaceutical sciences. 1999;88(10):1058-66.
15. Urbanetz NA. Stabilization of solid dispersions of nimodipine and polyethylene glycol 2000. European Journal of Pharmaceutical Sciences. 2006;28(1–2):67-76.
16. Rumondor ACF, Stanford LA, Taylor LS. Effects of Polymer Type and Storage Relative Humidity on the Kinetics of Felodipine Crystallization from Amorphous Solid Dispersions. Pharmaceutical Research. 2009;26(12):2599-606.
17. Bley H, Fussnegger B, Bodmeier R. Characterization and stability of solid dispersions based on PEG/polymer blends. International Journal of Pharmaceutics. 2010;390(2):165-73.
18. Yang Z, Nollenberger K, Albers J, Craig D, Qi S. Microstructure of an Immiscible Polymer Blend and Its Stabilization Effect on Amorphous Solid Dispersions. Molecular Pharmaceutics. 2013;10(7):2767-80.
19. Karavas E, Georgarakis E, Bikiaris D. Felodipine nanodispersions as active core for predictable pulsatile chronotherapeutics using PVP/HPMC blends as coating layer. International Journal of Pharmaceutics. 2006;313(1–2):189-97.
20. Jiang H, Hu Y, Li Y, Zhao P, Zhu K, Chen W. A facile technique to prepare biodegradable coaxial electrospun nanofibers for controlled release of bioactive agents. Journal of Controlled Release. 2005;108(2–3):237-43.
21. Yu D-G, Wang X, Li X-Y, Chian W, Li Y, Liao Y-Z. Electrospun biphasic drug release polyvinylpyrrolidone/ethyl cellulose core/sheath nanofibers. Acta biomaterialia. 2012.
22. Sill TJ, von Recum HA. Electrospinning: Applications in drug delivery and tissue engineering. Biomaterials. 2008;29(13):1989-2006.
23. Yu D-G, Branford-White C, Shen X-X, Zhang X-F, Zhu L-M. Solid Dispersions of Ketoprofen in Drug-Loaded Electrospun Nanofibers. Journal of Dispersion Science and Technology. 2010;31(7):902-8.
24. Yu D-G, Branford-White C, White K, Li X-L, Zhu L-M. Dissolution improvement of electrospun nanofiber-based solid dispersions for acetaminophen. AAPS PharmSciTech. 2010;11(2):809-17.
25. Ignatious F, Sun L, Lee C-P, Baldoni J. Electrospun nanofibers in oral drug delivery. Pharmaceutical research. 2010;27(4):576-88.
26. Yu D-G, Shen X-X, Branford-White C, White K, Zhu L-M, Bligh SA. Oral fast-dissolving drug delivery membranes prepared from electrospun polyvinylpyrrolidone ultrafine fibers. Nanotechnology. 2009;20(5):055104.
27. Yu D-G, Zhu L-M, White K, Branford-White C. Electrospun nanofiber-based drug delivery systems. Health. 2009;Vol.01No.02:9.
28. Bates S, Zografi G, Engers D, Morris K, Crowley K, Newman A. Analysis of amorphous and nanocrystalline solids from their X-ray diffraction patterns. Pharmaceutical research. 2006;23(10):2333-49.
29. Yu L. Amorphous pharmaceutical solids: preparation, characterization and stabilization. Advanced Drug Delivery Reviews. 2001;48(1):27-42.
30. Sheth AR, Bates S, Muller FX, Grant DJW. Local Structure in Amorphous Phases of Piroxicam from Powder X-ray Diffractometry. Crystal Growth & Design. 2005;5(2):571-8.
31. Crowley KJ, Zografi G. Cryogenic grinding of indomethacin polymorphs and solvates: Assessment of amorphous phase formation and amorphous phase physical stability. Journal of Pharmaceutical sciences. 2002;91(2):492-507.

32. Hancock BC, Zografi G. Characteristics and significance of the amorphous state in pharmaceutical systems. Journal of Pharmaceutical sciences. 1997;86(1):1-12.
33. Hancock BC, Parks M. What is the True Solubility Advantage for Amorphous Pharmaceuticals? Pharmaceutical research. 2000;17(4):397-404.
34. Kim J-S, Kim M-S, Park HJ, Jin S-J, Lee S, Hwang S-J. Physicochemical properties and oral bioavailability of amorphous atorvastatin hemi-calcium using spray-drying and SAS process. International Journal of Pharmaceutics. 2008;359(1–2):211-9.
35. Vasconcelos T, Sarmento B, Costa P. Solid dispersions as strategy to improve oral bioavailability of poor water soluble drugs. Drug Discovery Today. 2007;12(23–24):1068-75.
36. Wu T, Yu L. Surface Crystallization of Indomethacin Below T g. Pharmaceutical Research. 2006;23(10):2350-5.
37. Zhu L, Wong L, Yu L. Surface-enhanced crystallization of amorphous nifedipine. Molecular Pharmaceutics. 2008;5(6):921-6.
38. Sperling LH. Introduction to physical polymer science: John Wiley & Sons; 2005.
39. Chen S, Xi H, Yu L. Cross-Nucleation between ROY Polymorphs. Journal of the American Chemical Society. 2005;127(49):17439-44.
40. Sun Y, Zhu L, Wu T, Cai T, Gunn EM, Yu L. Stability of Amorphous Pharmaceutical Solids: Crystal Growth Mechanisms and Effect of Polymer Additives. The AAPS Journal. 2012;14(3):380-8.
41. De Yoreo JJ, Vekilov PG. Principles of crystal nucleation and growth. Reviews in mineralogy and geochemistry. 2003;54(1):57-93.
42. Cubillas P, Anderson MW. Synthesis mechanism: crystal growth and nucleation. Zeolites and Catalysis: Synthesis, Reactions and Applications. 2010:1-55.
43. Myerson AS. Concluding remarks. Faraday Discussions. 2015;179(0):543-7.
44. Trasi NS, Taylor LS. Effect of polymers on nucleation and crystal growth of amorphous acetaminophen. CrystEngComm. 2012;14(16):5188-97.
45. Turnbull D, Fisher JC. Rate of Nucleation in Condensed Systems. The Journal of Chemical Physics. 1949;17(1):71-3.
46. Yamada M, Mossa S, Stanley HE, Sciortino F. Interplay between Time-Temperature Transformation and the Liquid-Liquid Phase Transition in Water. Physical Review Letters. 2002;88(19):195701.
47. Volmer M. Kinetik der phasenbildung. 1939.
48. Parambil JV, Poornachary SK, Tan RB, Heng JY. Template-induced polymorphic selectivity: the effects of surface chemistry and solute concentration on carbamazepine crystallisation. CrystEngComm. 2014;16(23):4927-30.
49. Caridi A, Kulkarni SA, Di Profio G, Curcio E, Ter Horst JH. Template-induced nucleation of isonicotinamide polymorphs. Crystal Growth & Design. 2014;14(3):1135-41.
50. Boukerche M, Mangin D, Klein J, Monnier O, Hoff C. Inducing the stable polymorph using heterogeneous primary nucleation. Chemical Engineering Research and Design. 2010;88(11):1474-8.
51. Lang M, Grzesiak AL, Matzger AJ. The Use of Polymer Heteronuclei for Crystalline Polymorph Selection. Journal of the American Chemical Society. 2002;124(50):14834-5.
52. Lu L, Dahle AK, StJohn DH. Heterogeneous nucleation of Mg–Al alloys. Scripta Materialia. 2006;54(12):2197-201.
53. Cantor B, Doherty RD. Heterogeneous nucleation in solidifying alloys. Acta Metallurgica. 1979;27(1):33-46.
54. Agrawal SG, Paterson AHJ. Secondary Nucleation: Mechanisms and Models. Chemical Engineering Communications. 2015;202(5):698-706.
55. Verdurand E, Bebon C, Colson D, Klein JP, Blandin AF, Bossoutrot JM. Secondary nucleation and growth of organic crystals in industrial crystallization. Journal of Crystal Growth. 2005;275(1–2):e1363-e7.
56. Kadam SS, Kramer HJM, ter Horst JH. Combination of a Single Primary Nucleation Event and Secondary Nucleation in Crystallization Processes. Crystal Growth & Design. 2011;11(4):1271-7.
57. Beckmann W. Seeding the Desired Polymorph: Background, Possibilities, Limitations, and Case Studies. Organic Process Research & Development. 2000;4(5):372-83.
58. Nancollas GH, Purdie N. The kinetics of crystal growth. Quarterly Reviews, Chemical Society. 1964;18(1):1-20.
59. Kossel W. Zur Energetik von Oberflächenvorgängen. Annalen der Physik. 1934;413(5):457-80.
60. Bahrig L, Hickey SG, Eychmuller A. Mesocrystalline materials and the involvement of oriented attachment - a review. CrystEngComm. 2014;16(40):9408-24.
61. Zipp GL, Rodríguez-Hornedo N. The mechanism of phenytoin crystal growth. International Journal of Pharmaceutics. 1993;98(1):189-201.
62. Kirkpatrick RJ. Crystal-growth from melt-review. American Mineralogist. 1975;60(9-10):798-814.
63. Bauer J, Spanton S, Henry R, Quick J, Dziki W, Porter W, et al. Ritonavir: an extraordinary example of conformational polymorphism. Pharmaceutical research. 2001;18(6):859-66.
64. Haisa M, Kashino S, Kawai R, Maeda H. The monoclinic form of p-hydroxyacetanilide. Acta Crystallographica Section B: Structural Crystallography and Crystal Chemistry. 1976;32(4):1283-5.
65. Haisa M, Kashino S, Maeda H. The orthorhombic form of p-hydroxyacetanilide. Acta Crystallographica Section B: Structural Crystallography and Crystal Chemistry. 1974;30(10):2510-2.
66. Kato Y, Okamoto Y, Nagasawa K, Ishihara I. New polymorphic forms of phenobarbital. Chemical & pharmaceutical bulletin. 1984;32(10):4170.
67. Kobayashi Y, Ito S, Itai S, Yamamoto K. Physicochemical properties and bioavailability of carbamazepine polymorphs and dihydrate. International Journal of Pharmaceutics. 2000;193(2):137-46.

68. Salole EG, Al-Sarraj FA. Spironolactone Crystal Forms. Drug Development and Industrial Pharmacy. 1985;11(4):855-64.
69. Phadnis NV, Suryanarayanan R. Polymorphism in anhydrous theophylline—implications on the dissolution rate of theophylline tablets. Journal of Pharmaceutical sciences. 1997;86(11):1256-63.
70. Zhang GGZ, Law D, Schmitt EA, Qiu Y. Phase transformation considerations during process development and manufacture of solid oral dosage forms. Advanced Drug Delivery Reviews. 2004;56(3):371-90.
71. Clas S-D. The importance of characterizing the crystal form of the drug substance during drug development. Curr Opin Drug Discov Devel. 2003;6(4):550-60.
72. Myrick ML, Baranowski M, Profeta LTM. An Experiment in Physical Chemistry: Polymorphism and Phase Stability in Acetaminophen (Paracetamol). Journal of Chemical Education. 2010;87(8):842-4.
73. Six K, Verreck G, Peeters J, Binnemans K, Berghmans H, Augustijns P, et al. Investigation of thermal properties of glassy itraconazole: identification of a monotropic mesophase. Thermochimica Acta. 2001;376(2):175-81.
74. Sekiguchi K, Tsuda Y, Kanke M. Dissolution Behavior of Solid Drugs. VI. Determination of Transition Temperatures of Various Physical Forms of Sulfanilamide by Initial Dissolution Rate Measurements. Chemical & pharmaceutical bulletin. 1975;23(6):1353-62.
75. Barbas R, Martí F, Prohens R, Puigjaner C. Polymorphism of Norfloxacin: Evidence of the Enantiotropic Relationship between Polymorphs A and B. Crystal Growth & Design. 2006;6(6):1463-7.
76. Kanke M, Sekiguchi K. Dissolution Behavior of Solid Drugs. II. Determination of the Transition Temperature of Sulfathiazole Polymorphs by Measuring the Initial Dissolution Rates. Chemical & pharmaceutical bulletin. 1973;21(4):878-84.
77. Ting VP, Schmidtmann M, Wilson CC, Weller MT. Cisplatin: Polymorphism and Structural Insights into an Important Chemotherapeutic Drug. Angewandte Chemie International Edition. 2010;49(49):9408-11.
78. Barrio M, Maccaroni E, Rietveld IB, Malpezzi L, Masciocchi N, Céolin R, et al. Pressure–temperature state diagram for the phase relationships between benfluorex hydrochloride forms I and II: A case of enantiotropic behavior. Journal of Pharmaceutical sciences. 2012;101(3):1073-8.
79. Newman AW, Childs SL, Cowans BA. Salt and Cocrystal Form Selection. Pharmaceutical Sciences Encyclopedia: John Wiley & Sons, Inc.; 2010.
80. Burger A, Ramberger R. On the polymorphism of pharmaceuticals and other molecular crystals. I. Microchimica Acta. 1979;72(3-4):259-71.
81. Burger A, Ramberger R. On the polymorphism of pharmaceuticals and other molecular crystals. II. Microchimica Acta. 1979;72(3-4):273-316.
82. Behme RJ, Brooke D. Heat of fusion measurement of a low melting polymorph of carbamazepine that undergoes multiple-phase changes during differential scanning calorimetry analysis. Journal of Pharmaceutical sciences. 1991;80(10):986-90.
83. Nelyubina YV, Glukhov IV, Antipin MY, Lyssenko KA. "Higher density does not mean higher stability" mystery of paracetamol finally unraveled. Chemical Communications. 2010;46(20):3469-71.
84. Moynihan HA, O'Hare IP. Spectroscopic characterisation of the monoclinic and orthorhombic forms of paracetamol. International Journal of Pharmaceutics. 2002;247(1–2):179-85.
85. Janssens S, Van den Mooter G. Review: physical chemistry of solid dispersions. Journal of Pharmacy and Pharmacology. 2009;61(12):1571-86.
86. Jones AOF, Chattopadhyay B, Geerts YH, Resel R. Substrate-Induced and Thin-Film Phases: Polymorphism of Organic Materials on Surfaces. Advanced Functional Materials. 2016;26(14):2233-55.
87. Yeager JD, Ramos KJ, Mack NH, Wang H-L, Hooks DE. Transformation and Growth of Polymorphic Nuclei through Evaporative Deposition of Thin Films. Crystal Growth & Design. 2012;12(11):5513-20.
88. Ehmann HMA, Werzer O. Surface Mediated Structures: Stabilization of Metastable Polymorphs on the Example of Paracetamol. Crystal Growth & Design. 2014;14(8):3680-4.
89. Konno H, Taylor LS. Influence of different polymers on the crystallization tendency of molecularly dispersed amorphous felodipine. Journal of Pharmaceutical sciences. 2006;95(12):2692-705.
90. Miyazaki T, Yoshioka S, Aso Y, Kojima S. Ability of polyvinylpyrrolidone and polyacrylic acid to inhibit the crystallization of amorphous acetaminophen. Journal of Pharmaceutical sciences. 2004;93(11):2710-7.
91. Cai T, Zhu L, Yu L. Crystallization of Organic Glasses: Effects of Polymer Additives on Bulk and Surface Crystal Growth in Amorphous Nifedipine. Pharmaceutical research. 2011;28(10):2458-66.
92. Ishida H, Wu T, Yu L. Sudden rise of crystal growth rate of nifedipine near Tg without and with polyvinylpyrrolidone. Journal of Pharmaceutical sciences. 2007;96(5):1131-8.
93. Baird JA, Van Eerdenbrugh B, Taylor LS. A classification system to assess the crystallization tendency of organic molecules from undercooled melts. Journal of Pharmaceutical sciences. 2010;99(9):3787-806.
94. Desiraju GR. The C−H···O Hydrogen Bond: Structural Implications and Supramolecular Design. Accounts of Chemical Research. 1996;29(9):441-9.
95. Tipduangta P, Takieddin K, Fábián L, Belton P, Qi S. A New Low Melting-Point Polymorph of Fenofibrate Prepared via Talc Induced Heterogeneous Nucleation. Crystal Growth & Design. 2015;15(10):5011-20.
96. Sekiguchi K, Obi N. Studies on Absorption of Eutectic Mixture. I. A Comparison of the Behavior of Eutectic Mixture of Sulfathiazole and that of Ordinary Sulfathiazole in Man. Chemical & pharmaceutical bulletin. 1961;9(11):866-72.

97. Jung J-Y, Yoo SD, Lee S-H, Kim K-H, Yoon D-S, Lee K-H. Enhanced solubility and dissolution rate of itraconazole by a solid dispersion technique. International Journal of Pharmaceutics. 1999;187(2):209-18.
98. Kim E-J, Chun M-K, Jang J-S, Lee I-H, Lee K-R, Choi H-K. Preparation of a solid dispersion of felodipine using a solvent wetting method. European Journal of Pharmaceutics and Biopharmaceutics. 2006;64(2):200-5.
99. Ali S, Kolter K. Challenges and opportunities in oral formulation development. Am Pharm Rev. 2012;15(7).
100. Vo CL-N, Park C, Lee B-J. Current trends and future perspectives of solid dispersions containing poorly water-soluble drugs. European Journal of Pharmaceutics and Biopharmaceutics. 2013;85(3, Part B):799-813.
101. Kawabata Y, Wada K, Nakatani M, Yamada S, Onoue S. Formulation design for poorly water-soluble drugs based on biopharmaceutics classification system: Basic approaches and practical applications. International Journal of Pharmaceutics. 2011;420(1):1-10.
102. Law D, Wang W, Schmitt EA, Qiu Y, Krill SL, Fort JJ. Properties of rapidly dissolving eutectic mixtures of poly(ethylene glycol) and fenofibrate: The eutectic microstructure. Journal of Pharmaceutical sciences. 2003;92(3):505-15.
103. Górniak A, Wojakowska A, Karolewicz B, Pluta J. Phase diagram and dissolution studies of the fenofibrate–acetylsalicylic acid system. Journal of thermal analysis and calorimetry. 2011;104(3):1195-200.
104. Yong CS, Oh Y-K, Jung SH, Rhee J-D, Kim H-D, Kim C-K, et al. Preparation of ibuprofen-loaded liquid suppository using eutectic mixture system with menthol. European Journal of Pharmaceutical Sciences. 2004;23(4–5):347-53.
105. Vippagunta SR, Wang Z, Hornung S, Krill SL. Factors affecting the formation of eutectic solid dispersions and their dissolution behavior. Journal of Pharmaceutical sciences. 2007;96(2):294-304.
106. Brettmann BK, Cheng K, Myerson AS, Trout BL. Electrospun Formulations Containing Crystalline Active Pharmaceutical Ingredients. Pharmaceutical research. 2013;30(1):238-46.
107. Kawabata Y, Yamamoto K, Debari K, Onoue S, Yamada S. Novel crystalline solid dispersion of tranilast with high photostability and improved oral bioavailability. European Journal of Pharmaceutical Sciences. 2010;39(4):256-62.
108. Rumondor ACF, Ivanisevic I, Bates S, Alonzo DE, Taylor LS. Evaluation of Drug-Polymer Miscibility in Amorphous Solid Dispersion Systems. Pharmaceutical research. 2009;26(11):2523-34.
109. Craig DQM. The mechanisms of drug release from solid dispersions in water-soluble polymers. International Journal of Pharmaceutics. 2002;231(2):131-44.
110. Goldberg AH, Gibaldi M, Kanig JL. Increasing dissolution rates and gastrointestinal absorption of drugs via solid solutions and eutectic mixtures I. Theoretical considerations and discussion of the literature. Journal of Pharmaceutical sciences. 1965;54(8):1145-8.
111. Craig DQM. Polyethyelene Glycols and Drug Release. Drug Development and Industrial Pharmacy. 1990;16(17):2501-26.
112. Matsumoto T, Zografi G. Physical Properties of Solid Molecular Dispersions of Indomethacin with Poly(vinylpyrrolidone) and Poly(vinylpyrrolidone-co-vinyl-acetate) in Relation to Indomethacin Crystallization. Pharmaceutical research. 1999;16(11):1722-8.
113. Taylor LS, Zografi G. Spectroscopic Characterization of Interactions Between PVP and Indomethacin in Amorphous Molecular Dispersions. Pharmaceutical research. 1997;14(12):1691-8.
114. Ouyang D. Investigating the molecular structures of solid dispersions by the simulated annealing method. Chemical Physics Letters. 2012;554:177-84.
115. Qian F, Huang J, Hussain MA. Drug–polymer solubility and miscibility: Stability consideration and practical challenges in amorphous solid dispersion development. Journal of Pharmaceutical sciences. 2010;99(7):2941-7.
116. Das SK, Roy S, Kalimuthu Y, Khanam J, Nanda A. Solid dispersions: an approach to enhance the bioavailability of poorly water-soluble drugs. International journal of pharmacology and pharmaceutical technology. 2012;1(1):37-46.
117. Wang X, Michoel A, Van den Mooter G. Solid state characteristics of ternary solid dispersions composed of PVP VA64, Myrj 52 and itraconazole. International Journal of Pharmaceutics. 2005;303(1–2):54-61.
118. Vasanthavada M, Tong W-QT, Joshi Y, Kislalioglu MS. Phase behavior of amorphous molecular dispersions II: Role of hydrogen bonding in solid solubility and phase separation kinetics. Pharmaceutical research. 2005;22(3):440-8.
119. Wegiel LA, Mauer LJ, Edgar KJ, Taylor LS. Crystallization of amorphous solid dispersions of resveratrol during preparation and storage—Impact of different polymers. Journal of Pharmaceutical sciences. 2013;102(1):171-84.
120. Qi S, Belton P, McAuley W, Codoni D, Darji N. Moisture uptake of polyoxyethylene glycol glycerides used as matrices for drug delivery: kinetic modelling and practical implications. Pharmaceutical research. 2013;30(4):1123-36.
121. Marsac PJ, Rumondor AC, Nivens DE, Kestur US, Stanciu L, Taylor LS. Effect of temperature and moisture on the miscibility of amorphous dispersions of felodipine and poly (vinyl pyrrolidone). Journal of Pharmaceutical Sciences. 2010;99(1):169-85.
122. Rumondor AC, Marsac PJ, Stanford LA, Taylor LS. Phase behavior of poly (vinylpyrrolidone) containing amorphous solid dispersions in the presence of moisture. Molecular Pharmaceutics. 2009;6(5):1492-505.

123. Lu Q, Zografi G. Phase behavior of binary and ternary amorphous mixtures containing indomethacin, citric acid, and PVP. Pharmaceutical research. 1998;15(8):1202-6.
124. Taylor LS, Zografi G. Sugar–polymer hydrogen bond interactions in lyophilized amorphous mixtures. Journal of Pharmaceutical sciences. 1998;87(12):1615-21.
125. Gordon M, Taylor JS. Ideal copolymers and the second-order transitions of synthetic rubbers. i. non-crystalline copolymers. Journal of Applied Chemistry. 1952;2(9):493-500.
126. Boyer RF, Simha R. Relation between expansion coefficients and glass temperature: A reply. Journal of Polymer Science: Polymer Letters Edition. 1973;11(1):33-44.
127. Couchman PR, Karasz FE. A Classical Thermodynamic Discussion of the Effect of Composition on Glass-Transition Temperatures. Macromolecules. 1978;11(1):117-9.
128. Bhattacharya S, Suryanarayanan R. Local mobility in amorphous pharmaceuticals—characterization and implications on stability. Journal of Pharmaceutical sciences. 2009;98(9):2935-53.
129. Andronis V, Zografi G. The Molecular Mobility of Supercooled Amorphous Indomethacin as a Function of Temperature and Relative Humidity. Pharmaceutical research. 1998;15(6):835-42.
130. Badrinarayanan P, Zheng W, Li Q, Simon SL. The glass transition temperature versus the fictive temperature. Journal of Non-Crystalline Solids. 2007;353(26):2603-12.
131. Shmeis RA, Wang Z, Krill SL. A Mechanistic Investigation of an Amorphous Pharmaceutical and Its Solid Dispersions, Part I: A Comparative Analysis by Thermally Stimulated Depolarization Current and Differential Scanning Calorimetry. Pharmaceutical research. 2004;21(11):2025-30.
132. Gunawan L, Johari GP, Shanker RM. Structural Relaxation of Acetaminophen Glass. Pharmaceutical research. 2006;23(5):967-79.
133. Brettmann B, Bell E, Myerson A, Trout B. Solid-state NMR characterization of high-loading solid solutions of API and excipients formed by electrospinning. Journal of Pharmaceutical Sciences. 2012;101(4):1538-45.
134. Bhugra C, Rambhatla S, Bakri A, Duddu SP, Miller DP, Pikal MJ, et al. Prediction of the onset of crystallization of amorphous sucrose below the calorimetric glass transition temperature from correlations with mobility. Journal of Pharmaceutical sciences. 2007;96(5):1258-69.
135. Van Krevelen DW, Te Nijenhuis K. Properties of polymers: their correlation with chemical structure; their numerical estimation and prediction from additive group contributions: Elsevier; 2009.
136. Hancock BC, York P, Rowe RC. The use of solubility parameters in pharmaceutical dosage form design. International Journal of Pharmaceutics. 1997;148(1):1-21.
137. Fedors RF. A method for estimating both the solubility parameters and molar volumes of liquids. Polymer Engineering & Science. 1974;14(2):147-54.
138. Hoftyzer P, Van Krevelen D. Properties of polymers. Elsevier, Amsterdam. 1976:152-5.
139. Hoy K. New values of the solubility parameters from vapor pressure data. Journal of Paint Technology. 1970;42(541):76-118.
140. Forster A, Hempenstall J, Tucker I, Rades T. Selection of excipients for melt extrusion with two poorly water-soluble drugs by solubility parameter calculation and thermal analysis. International Journal of Pharmaceutics. 2001;226(1–2):147-61.
141. Matsui T, Nagashima K, Fukamachi M, Shimoda M, Osajima Y. Application of the solubility parameter in estimating the sorption behavior of flavor into packaging film. Journal of Agricultural and Food Chemistry. 1992;40(10):1902-5.
142. Forster A, Hempenstall J, Rades T. Characterization of glass solutions of poorly water-soluble drugs produced by melt extrusion with hydrophilic amorphous polymers. Journal of Pharmacy and Pharmacology. 2001;53(3):303-15.
143. Djuris J, Nikolakakis I, Ibric S, Djuric Z, Kachrimanis K. Preparation of carbamazepine–Soluplus® solid dispersions by hot-melt extrusion, and prediction of drug–polymer miscibility by thermodynamic model fitting. European Journal of Pharmaceutics and Biopharmaceutics. 2013;84(1):228-37.
144. Marsac PJ, Shamblin SL, Taylor LS. Theoretical and Practical Approaches for Prediction of Drug–Polymer Miscibility and Solubility. Pharmaceutical research. 2006;23(10):2417-26.
145. Forster A, Hempenstall J, Tucker I, Rades T. The potential of small-scale fusion experiments and the Gordon-Taylor equation to predict the suitability of drug/polymer blends for melt extrusion. Drug Development and Industrial Pharmacy. 2001;27(6):549-60.
146. Zhao Y, Inbar P, Chokshi HP, Malick AW, Choi DS. Prediction of the thermal phase diagram of amorphous solid dispersions by flory–huggins theory. Journal of Pharmaceutical sciences. 2011;100(8):3196-207.
147. Nishi T, Wang TT. Melting Point Depression and Kinetic Effects of Cooling on Crystallization in Poly(vinylidene fluoride)-Poly(methyl methacrylate) Mixtures. Macromolecules. 1975;8(6):909-15.
148. Marsac PJ, Li T, Taylor LS. Estimation of Drug–Polymer Miscibility and Solubility in Amorphous Solid Dispersions Using Experimentally Determined Interaction Parameters. Pharmaceutical research. 2008;26(1):139-51.
149. Dewick PM. Essentials of organic chemistry. for students of pharmacy, medicinal chemistry and biological chemistry: Chichester, West Sussex, England ; Hoboken, N.J. : J. Wiley, c2006.; 2006.
150. McMurry J. Organic chemistry: Belmont, CA. : Thomson / Brooks/Cole, 2008.

7th ed. International student ed.; 2008.
151. Van den Mooter G, Wuyts M, Blaton N, Busson R, Grobet P, Augustijns P, et al. Physical stabilisation of amorphous ketoconazole in solid dispersions with polyvinylpyrrolidone K25. European Journal of Pharmaceutical Sciences. 2001;12(3):261-9.

152. Airaksinen S, Karjalainen M, Shevchenko A, Westermarck S, Leppänen E, Rantanen J, et al. Role of water in the physical stability of solid dosage formulations. Journal of Pharmaceutical sciences. 2005;94(10):2147-65.
153. Rumondor ACF, Marsac PJ, Stanford LA, Taylor LS. Phase Behavior of Poly(vinylpyrrolidone) Containing Amorphous Solid Dispersions in the Presence of Moisture. Molecular Pharmaceutics. 2009;6(5):1492-505.
154. Fitzpatrick S, McCabe JF, Petts CR, Booth SW. Effect of moisture on polyvinylpyrrolidone in accelerated stability testing. International Journal of Pharmaceutics. 2002;246(1–2):143-51.
155. Amass W, Amass A, Tighe B. A review of biodegradable polymers: uses, current developments in the synthesis and characterization of biodegradable polyesters, blends of biodegradable polymers and recent advances in biodegradation studies. Polymer International. 1998;47(2):89-144.
156. Marin E, Briceño MI, Caballero-George C. Critical evaluation of biodegradable polymers used in nanodrugs. International journal of nanomedicine. 2013;8:3071.
157. Siracusa V, Rocculi P, Romani S, Rosa MD. Biodegradable polymers for food packaging: a review. Trends in Food Science & Technology. 2008;19(12):634-43.
158. Yu L, Dean K, Li L. Polymer blends and composites from renewable resources. Progress in Polymer Science. 2006;31(6):576-602.
159. Cascone MG, Sim B, Sandra D. Blends of synthetic and natural polymers as drug delivery systems for growth hormone. Biomaterials. 1995;16(7):569-74.
160. Jiang Y-N, Mo H-Y, Yu D-G. Electrospun drug-loaded core–sheath PVP/zein nanofibers for biphasic drug release. International Journal of Pharmaceutics. 2012;438(1–2):232-9.
161. Alshahrani SM, Lu W, Park J-B, Morott JT, Alsulays BB, Majumdar S, et al. Stability-enhanced Hot-melt Extruded Amorphous Solid Dispersions via Combinations of Soluplus® and HPMCAS-HF. AAPS PharmSciTech. 2015;16(4):824-34.
162. Tipduangta P, Belton P, Fábián L, Wang LY, Tang H, Eddleston M, et al. Electrospun Polymer Blend Nanofibers for Tunable Drug Delivery: The Role of Transformative Phase Separation on Controlling the Release Rate. Molecular Pharmaceutics. 2016;13(1):25-39.
163. Quinten T, Beer TD, Vervaet C, Remon JP. Evaluation of injection moulding as a pharmaceutical technology to produce matrix tablets. European Journal of Pharmaceutics and Biopharmaceutics. 2009;71(1):145-54.
164. van de Witte P, Dijkstra PJ, van den Berg JWA, Feijen J. Phase separation processes in polymer solutions in relation to membrane formation. Journal of Membrane Science. 1996;117(1–2):1-31.
165. Lopez-Barron CR, Macosko CW. Characterizing Interface Shape Evolution in Immiscible Polymer Blends via 3D Image Analysis. Langmuir. 2009;25(16):9392-404.
166. Flory PJ. Principles of polymer chemistry: Cornell University Press; 1953.
167. Six K, Verreck G, Peeters J, Brewster M, Mooter GVd. Increased physical stability and improved dissolution properties of itraconazole, a class II drug, by solid dispersions that combine fast- and slow-dissolving polymers. Journal of Pharmaceutical sciences. 2004;93(1):124-31.
168. Breitenbach J. Melt extrusion: from process to drug delivery technology. European Journal of Pharmaceutics and Biopharmaceutics. 2002;54(2):107-17.
169. Crowley MM, Zhang F, Repka MA, Thumma S, Upadhye SB, Kumar Battu S, et al. Pharmaceutical Applications of Hot-Melt Extrusion: Part I. Drug Development and Industrial Pharmacy. 2007;33(9):909-26.
170. Ouyang D, Smith SC. Introduction to Computational Pharmaceutics. Computational Pharmaceutics. 2015:1-5.
171. DiNunzio JC, Brough C, Hughey JR, Miller DA, Williams Iii RO, McGinity JW. Fusion production of solid dispersions containing a heat-sensitive active ingredient by hot melt extrusion and Kinetisol® dispersing. European Journal of Pharmaceutics and Biopharmaceutics. 2010;74(2):340-51.
172. Julien G, Thierry C, Patrice M. Microinjection molding of thermoplastic polymers: a review. Journal of Micromechanics and Microengineering. 2007;17(6):R96.
173. Zema L, Loreti G, Melocchi A, Maroni A, Gazzaniga A. Injection Molding and its application to drug delivery. Journal of Controlled Release. 2012;159(3):324-31.
174. Rathbone MJ, Bunt CR, Ogle CR, Burggraaf S, Macmillan KL, Pickering K. Development of an injection molded poly(ϵ-caprolactone) intravaginal insert for the delivery of progesterone to cattle. Journal of Controlled Release. 2002;85(1–3):61-71.
175. Soriano I, Martín AY, Évora C, Sánchez E. Biodegradable implantable fluconazole delivery rods designed for the treatment of fungal osteomyelitis: Influence of gamma sterilization. Journal of Biomedical Materials Research Part A. 2006;77A(3):632-8.
176. Melocchi A, Loreti G, Del Curto MD, Maroni A, Gazzaniga A, Zema L. Evaluation of Hot-Melt Extrusion and Injection Molding for Continuous Manufacturing of Immediate-Release Tablets. Journal of Pharmaceutical sciences. 2015;104(6):1971-80.
177. Gross BC, Erkal JL, Lockwood SY, Chen C, Spence DM. Evaluation of 3D Printing and Its Potential Impact on Biotechnology and the Chemical Sciences. Analytical chemistry. 2014;86(7):3240-53.
178. Liu Tsang V, Bhatia SN. Three-dimensional tissue fabrication. Advanced Drug Delivery Reviews. 2004;56(11):1635-47.
179. Goyanes A, Buanz ABM, Basit AW, Gaisford S. Fused-filament 3D printing (3DP) for fabrication of tablets. International Journal of Pharmaceutics. 2014;476(1–2):88-92.
180. Goyanes A, Buanz ABM, Hatton GB, Gaisford S, Basit AW. 3D printing of modified-release aminosalicylate (4-ASA and 5-ASA) tablets. European Journal of Pharmaceutics and Biopharmaceutics. 2015;89:157-62.

181. Pietrzak K, Isreb A, Alhnan MA. A flexible-dose dispenser for immediate and extended release 3D printed tablets. European Journal of Pharmaceutics and Biopharmaceutics. 2015;96:380-7.
182. Paudel A, Worku ZA, Meeus J, Guns S, Van den Mooter G. Manufacturing of solid dispersions of poorly water soluble drugs by spray drying: Formulation and process considerations. International Journal of Pharmaceutics. 2013;453(1):253-84.
183. Broadhead J, Edmond Rouan S, Rhodes C. The spray drying of pharmaceuticals. Drug Development and Industrial Pharmacy. 1992;18(11-12):1169-206.
184. Cal K, Sollohub K. Spray drying technique. I: Hardware and process parameters. Journal of Pharmaceutical sciences. 2010;99(2):575-86.
185. Sen D, Mazumder S, Melo JS, Khan A, Bhattyacharya S, D'Souza SF. Evaporation Driven Self-Assembly of a Colloidal Dispersion during Spray Drying: Volume Fraction Dependent Morphological Transition. Langmuir. 2009;25(12):6690-5.
186. Mahlin D, Ponnambalam S, Heidarian Höckerfelt M, Bergström CAS. Toward In Silico Prediction of Glass-Forming Ability from Molecular Structure Alone: A Screening Tool in Early Drug Development. Molecular Pharmaceutics. 2011;8(2):498-506.
187. Mitzi DB, Kosbar LL, Murray CE, Copel M, Afzali A. High-mobility ultrathin semiconducting films prepared by spin coating. Nature. 2004;428(6980):299-303.
188. Norrman K, Ghanbari-Siahkali A, Larsen NB. 6 Studies of spin-coated polymer films. Annual Reports Section "C" (Physical Chemistry). 2005;101(0):174-201.
189. Parejo PG, Zayat M, Levy D. Highly efficient UV-absorbing thin-film coatings for protection of organic materials against photodegradation. Journal of Materials Chemistry. 2006;16(22):2165-9.
190. Qi S, Moffat JG, Yang Z. Early Stage Phase Separation in Pharmaceutical Solid Dispersion Thin Films under High Humidity: Improved Spatial Understanding Using Probe-Based Thermal and Spectroscopic Nanocharacterization Methods. Molecular Pharmaceutics. 2013;10(3):918-30.
191. Xie J, Tan JC, Wang C-H. Biodegradable films developed by electrospray deposition for sustained drug delivery. Journal of Pharmaceutical sciences. 2008;97(8):3109-22.
192. Huang Z-M, Zhang YZ, Kotaki M, Ramakrishna S. A review on polymer nanofibers by electrospinning and their applications in nanocomposites. Composites Science and Technology. 2003;63(15):2223-53.
193. Rutledge GC, Fridrikh SV. Formation of fibers by electrospinning. Advanced Drug Delivery Reviews. 2007;59(14):1384-91.
194. Li M, Mondrinos MJ, Chen X, Gandhi MR, Ko FK, Lelkes PI. Co-electrospun poly(lactide-co-glycolide), gelatin, and elastin blends for tissue engineering scaffolds. Journal of Biomedical Materials Research Part A. 2006;79A(4):963-73.
195. Sahoo S, Toh SL, Goh JCH. A bFGF-releasing silk/PLGA-based biohybrid scaffold for ligament/tendon tissue engineering using mesenchymal progenitor cells. Biomaterials. 2010;31(11):2990-8.
196. Richard-Lacroix M, Pellerin C. Molecular Orientation in Electrospun Fibers: From Mats to Single Fibers. Macromolecules. 2013;46(24):9473-93.
197. Verreck G, Chun I, Rosenblatt J, Peeters J, Dijck AV, Mensch J, et al. Incorporation of drugs in an amorphous state into electrospun nanofibers composed of a water-insoluble, nonbiodegradable polymer. Journal of Controlled Release. 2003;92(3):349-60.
198. Alhusein N, Blagbrough IS, De Bank PA. Electrospun matrices for localised controlled drug delivery: release of tetracycline hydrochloride from layers of polycaprolactone and poly(ethylene-co-vinyl acetate). Drug Delivery and Translational Research. 2012;2(6):477-88.
199. Chen J-P, Chang G-Y, Chen J-K. Electrospun collagen/chitosan nanofibrous membrane as wound dressing. Colloids and Surfaces A: Physicochemical and Engineering Aspects. 2008;313–314:183-8.
200. Subbiah T, Bhat GS, Tock RW, Parameswaran S, Ramkumar SS. Electrospinning of nanofibers. Journal of Applied Polymer Science. 2005;96(2):557-69.
201. Yu D-G, Xu Y, Li Z, Du L-P, Zhao B-G, Wang X. Coaxial Electrospinning with Mixed Solvents: From Flat to Round Eudragit L100 Nanofibers for Better Colon-Targeted Sustained Drug Release Profiles. Journal of Nanomaterials. 2014;2014:8.
202. Ramakrishna S, Fujihara K, Teo W-E, Lim T-C, Ma Z. An introduction to electrospinning and nanofibers: World Scientific; 2005.
203. Forward KM, Rutledge GC. Free surface electrospinning from a wire electrode. Chemical Engineering Journal. 2012;183:492-503.
204. Tan SH, Inai R, Kotaki M, Ramakrishna S. Systematic parameter study for ultra-fine fiber fabrication via electrospinning process. Polymer. 2005;46(16):6128-34.
205. Wannatong L, Sirivat A, Supaphol P. Effects of solvents on electrospun polymeric fibers: preliminary study on polystyrene. Polymer International. 2004;53(11):1851-9.
206. Deitzel J, Kleinmeyer J, Harris Dea, Beck Tan N. The effect of processing variables on the morphology of electrospun nanofibers and textiles. Polymer. 2001;42(1):261-72.
207. Yurteri CU, Hartman RPA, Marijnissen JCM. Producing Pharmaceutical Particles via Electrospraying with an Emphasis on Nano and Nano Structured Particles - A Review. KONA Powder and Particle Journal. 2010;28:91-115.
208. Fong H, Chun I, Reneker D. Beaded nanofibers formed during electrospinning. Polymer. 1999;40(16):4585-92.
209. Huan S, Liu G, Han G, Cheng W, Fu Z, Wu Q, et al. Effect of experimental parameters on morphological, mechanical and hydrophobic properties of electrospun polystyrene fibers. Materials. 2015;8(5):2718-34.

210. De Vrieze S, Van Camp T, Nelvig A, Hagström B, Westbroek P, De Clerck K. The effect of temperature and humidity on electrospinning. Journal of materials science. 2009;44(5):1357-62.
211. Reneker DH, Yarin AL. Electrospinning jets and polymer nanofibers. Polymer. 2008;49(10):2387-425.
212. Megelski S, Stephens JS, Chase DB, Rabolt JF. Micro- and Nanostructured Surface Morphology on Electrospun Polymer Fibers. Macromolecules. 2002;35(22):8456-66.
213. Luo CJ, Nangrejo M, Edirisinghe M. A novel method of selecting solvents for polymer electrospinning. Polymer. 2010;51(7):1654-62.
214. Deitzel JM, Kleinmeyer J, Harris D, Beck Tan NC. The effect of processing variables on the morphology of electrospun nanofibers and textiles. Polymer. 2001;42(1):261-72.
215. Zong X, Kim K, Fang D, Ran S, Hsiao BS, Chu B. Structure and process relationship of electrospun bioabsorbable nanofiber membranes. Polymer. 2002;43(16):4403-12.
216. Luu YK, Kim K, Hsiao BS, Chu B, Hadjiargyrou M. Development of a nanostructured DNA delivery scaffold via electrospinning of PLGA and PLA–PEG block copolymers. Journal of Controlled Release. 2003;89(2):341-53.
217. Casper CL, Stephens JS, Tassi NG, Chase DB, Rabolt JF. Controlling Surface Morphology of Electrospun Polystyrene Fibers: Effect of Humidity and Molecular Weight in the Electrospinning Process. Macromolecules. 2004;37(2):573-8.
218. Subianto S, Donnadio A, Cavaliere S, Pica M, Casciola M, Jones DJ, et al. Reactive coaxial electrospinning of ZrP/ZrO2 nanofibres. Journal of Materials Chemistry A. 2014;2(33):13359-65.
219. Chen R, Huang C, Ke Q, He C, Wang H, Mo X. Preparation and characterization of coaxial electrospun thermoplastic polyurethane/collagen compound nanofibers for tissue engineering applications. Colloids and Surfaces B: Biointerfaces. 2010;79(2):315-25.
220. Munj HR, Nelson MT, Karandikar PS, Lannutti JJ, Tomasko DL. Biocompatible electrospun polymer blends for biomedical applications. Journal of Biomedical Materials Research Part B: Applied Biomaterials. 2014;102(7):1517-27.
221. Shi Y, Wei Z, Zhao H, Liu T, Dong A, Zhang J. Electrospinning of Ibuprofen-Loaded Composite Nanofibers for Improving the Performances of Transdermal Patches. Journal of Nanoscience and Nanotechnology. 2013;13(6):3855-63.
222. Taepaiboon P, Rungsardthong U, Supaphol P. Vitamin-loaded electrospun cellulose acetate nanofiber mats as transdermal and dermal therapeutic agents of vitamin A acid and vitamin E. European Journal of Pharmaceutics and Biopharmaceutics. 2007;67(2):387-97.
223. Wu X-m, Branford-White CJ, Zhu L-m, Chatterton NP, Yu D-g. Ester prodrug-loaded electrospun cellulose acetate fiber mats as transdermal drug delivery systems. Journal of Materials Science: Materials in Medicine. 2010;21(8):2403-11.
224. Nagy ZK, Nyúl K, Wagner I, Molnár K, Marosi G. Electrospun water soluble polymer mat for ultrafast release of Donepezil HCl. Express Polym Lett. 2010;4(12):763-72.
225. Yu D-G, Yang J-M, Branford-White C, Lu P, Zhang L, Zhu L-M. Third generation solid dispersions of ferulic acid in electrospun composite nanofibers. International Journal of Pharmaceutics. 2010;400(1):158-64.
226. Khil M-S, Cha D-I, Kim H-Y, Kim I-S, Bhattarai N. Electrospun nanofibrous polyurethane membrane as wound dressing. Journal of Biomedical Materials Research Part B: Applied Biomaterials. 2003;67B(2):675-9.
227. Thakur RA, Florek CA, Kohn J, Michniak BB. Electrospun nanofibrous polymeric scaffold with targeted drug release profiles for potential application as wound dressing. International Journal of Pharmaceutics. 2008;364(1):87-93.
228. Zhou Y, Yang D, Chen X, Xu Q, Lu F, Nie J. Electrospun Water-Soluble Carboxyethyl Chitosan/Poly(vinyl alcohol) Nanofibrous Membrane as Potential Wound Dressing for Skin Regeneration. Biomacromolecules. 2008;9(1):349-54.
229. Verreck G, Chun I, Peeters J, Rosenblatt J, Brewster ME. Preparation and characterization of nanofibers containing amorphous drug dispersions generated by electrostatic spinning. Pharmaceutical research. 2003;20(5):810-7.
230. Nagy ZK, Balogh A, Vajna B, Farkas A, Patyi G, Kramarics Á, et al. Comparison of electrospun and extruded soluplus®-based solid dosage forms of improved dissolution. Journal of Pharmaceutical sciences. 2012;101(1):322-32.
231. Brettmann BK, Myerson AS, Trout BL. Solid-state nuclear magnetic resonance study of the physical stability of electrospun drug and polymer solid solutions. Journal of Pharmaceutical sciences. 2012;101(6):2185-93.
232. Lopez FL, Shearman GC, Gaisford S, Williams GR. Amorphous formulations of indomethacin and griseofulvin prepared by electrospinning. Molecular Pharmaceutics. 2014;11(12):4327-38.
233. Quan J, Yu Y, Branford-White C, Williams GR, Yu D-G, Nie W, et al. Preparation of ultrafine fast-dissolving feruloyl-oleyl-glycerol-loaded polyvinylpyrrolidone fiber mats via electrospinning. Colloids and Surfaces B: Biointerfaces. 2011;88(1):304-9.
234. Shen X, Yu D, Zhu L, Branford-White C, White K, Chatterton NP. Electrospun diclofenac sodium loaded Eudragit® L 100-55 nanofibers for colon-targeted drug delivery. International Journal of Pharmaceutics. 2011;408(1–2):200-7.
235. Yang Y, Xia T, Zhi W, Wei L, Weng J, Zhang C, et al. Promotion of skin regeneration in diabetic rats by electrospun core-sheath fibers loaded with basic fibroblast growth factor. Biomaterials. 2011;32(18):4243-54.

236. Huang C, Soenen SJ, van Gulck E, Vanham G, Rejman J, Van Calenbergh S, et al. Electrospun cellulose acetate phthalate fibers for semen induced anti-HIV vaginal drug delivery. Biomaterials. 2012;33(3):962-9.
237. Persano L, Camposeo A, Tekmen C, Pisignano D. Industrial Upscaling of Electrospinning and Applications of Polymer Nanofibers: A Review. Macromolecular Materials and Engineering. 2013;298(5):504-20.
238. Sambaer W, Zatloukal M, Kimmer D. 3D modeling of filtration process via polyurethane nanofiber based nonwoven filters prepared by electrospinning process. Chemical Engineering Science. 2011;66(4):613-23.
239. Forward KM, Flores A, Rutledge GC. Production of core/shell fibers by electrospinning from a free surface. Chemical Engineering Science. 2013;104:250-9.

2.Chapter 2 Materials and methods

2.1 Introduction

This chapter discusses the basic information regarding the materials used in this study including APIs and polymers. Characterisation techniques used in this study are described, along with details of their experimental conditions.

2.2 Materials

2.2.1 Fenofibrate (FF)

FF (propan-2-yl 2-(4-[(4-chlorophenyl)carbonyl]phenoxy)-2-methylpropanoate) has been prescribed to treat hypercholesterolemia since 1970 (1). It is a prodrug in which fenofibric acid is its active form. The pharmacological effect of FF is to reduce low-density lipoprotein (LDL) and increase high-density lipoprotein (HDL) by binding to peroxisome proliferator-activated receptor alpha (PPARα) (1, 2). FF is categorised as a BCS class II drug because it is poorly aqueous soluble (0.8 µg/ml) but has a high permeability (>90%) through a lipid membrane (3, 4). Therefore, administrating FF with foods can increase the drug absorption (1). The nano crystallised (Tricor®) formulation and the solid dispersion with PEG (Fenoglide®) have been used to increase the bioavailability of FF (5, 6). Consequently, the FF content per the tablets can be reduced from 100 mg of the conventional FF tablets to 67 mg or less in FF nano crystallised and solid dispersion formulations (7, 8).

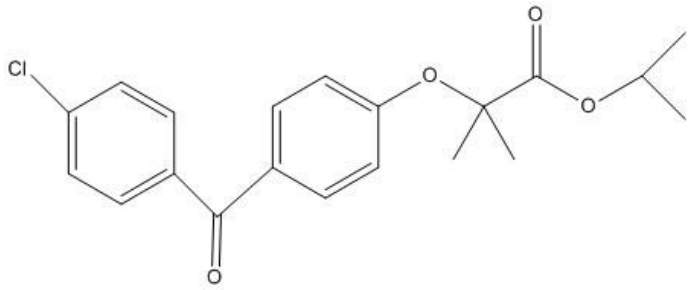

Figure 2.1 Molecular structure of FF

The amorphous fenofibrate does not spontaneously crystallise because it has high configuration entropy and high molecular mobility is required for crystallisation (9). Consequently, it has a low probability of molecular insertion to form nuclei for the nucleation. However, the amorphous FF crystallises immediately after being triggered by scratching its surface or seeding by using its crystal (10, 11).

Three FF polymorphs have been documented in Cambridge Structure Database (CSD). The stable form I (with a melting point at 80°C) is the standard polymorph used as API in commercial tablets and capsule formulation. Form I can be obtained by a slow solvent evaporation method (12). The metastable form II, initially reported by Di Martino and co-workers in 2001 (13), is produced by the recrystallization of amorphous FF from the melt. This metastable polymorph has a melting point at 74°C. It immediately converts to the stable form I via melt recrystallization during heating and melting again at 80°C (13-15) **(Figure 2.2)**. The melting point and PXRD data were reported by Di Martino and co-workers (13). Later, Heinz et al. reported the Raman spectrum of FF polymorph II (15). However, the literature of FF form II is rather confusing, as there is inconsistency in its characteristic data among different sources. Barlendiran and colleagues revealed the single crystal structure of FF form II as monoclinic crystal with no supporting information of its melting point and spectroscopic data (16). It is unclear whether the FF form IIs reported by the literature groups are the same polymorphs. To avoid the confusion that arises from these findings, the FF form II from Di Martino et al. and Heinz et al. will be addressed as FF form IIa in this study and the one from Barlendiran will be addressed as form IIb. The summary of physical properties of FF are reported in **Table 2.1**. The crystalline FF polymorph I used in this study was kindly donated by Merck Serono (Darmstadt, Germany).

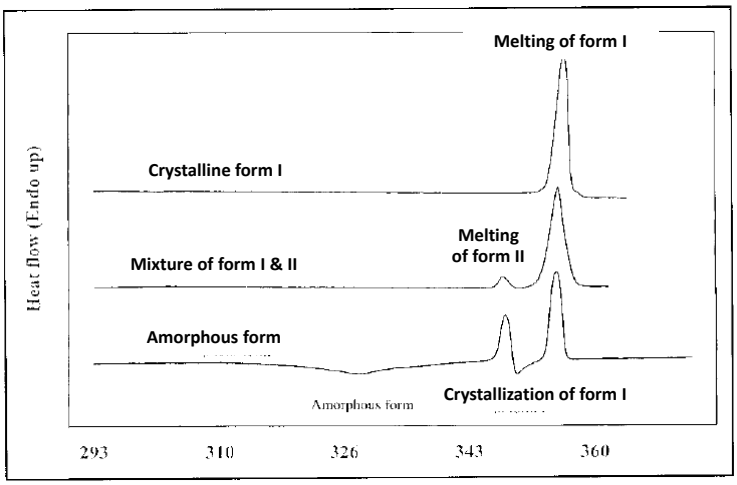

Figure 2.2 DSC thermogram of crystalline FF, a mixture of form I and II and amorphous FF. This figure is reproduced from reference (13).

2.2.2 Paracetamol (PCM)

PCM is an analgesic and antipyretic drug which has been used globally as an over-the-counter drug and was used as the model drug in this study. The IUPAC name of PCM is *N*-(4-hydroxyphenyl) ethanamide. An overdose of PCM leads to acute liver failure (17).

PCM is classified as a BSC class III according to the current guidelines, as highly water solubility and low permeability (18). The permeability of PCM is 80%, which slightly below the cut-off point between BCS class I and III, at 90% permeability. PCM has three reported polymorphic forms which include monoclinic form I, orthorhombic form II and the highly unstable form III (18-20). The PCM form II is prepared by melt recrystallization of amorphous PCM. The orthorhombic polymorph exhibits a sliding plane resulting in a good compressibility (19). However, the only monoclinic form I is used in commercial products due to it being the most thermodynamic stable form. PCM has a low T_g at 25°C (21). The amorphous of PCM is unstable at room temperature and immediately crystallises to its form I (22). This is because PCM can form intermolecular hydrogen bonds resulting in it having low configuration entropy and a low mobility required for crystallisation (9). The physical properties of PCM are summarised in **Table 2.1**. The PCM (purity >99%) used in this study was purchased from Sigma-Aldrich (Dorset, UK).

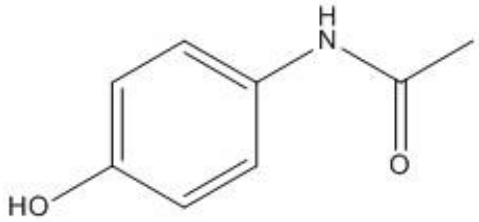

Figure 2.3 Molecular structure of PCM

Table 2.1 FF and PCM physical properties

Properties	**Fenofibrate**	**Paracetamol**
Molecular weight	360.83 g/mol	151.16 g/mol
Formula	$C_8H_9NO_2$	$C_8H_9NO_2$
pKa	-4.9 (3, 23)	9.5 (23)
Solubility	0.8 µg/ml (3)	14.3 mg/ml at 20°C 23.7 mg/ml at 37°C (18)
Log P	4.75 (3, 21)	0.28 (18)
Permeability	>90%	80% (18)
Density	1.29 g/cm^3 (24)	1.38 g/cm^3 (21)
Glass Transition	-20 °C (21)	25 °C (21)
Configuration entropy (ΔS)	76.6 J/mol.K (9)	43.0 J/mol.K (9)
Mobility required for crystallization (1/τ)	72.3 s^{-1} (9)	1.0 s^{-1} (9)

2.2.3 Talc

Talc or hydrous magnesium silicate ($H_2Mg_3(SiO_3)_4$) is a soft mineral according to the Moh's scale of hardness (25). The crystalline structure of talc is identified as triclinic (26), as illustrated in **Figure 2.4**. It exhibits a basal cleavage on the basal plane (001)(27). Talc has been used in various industrial products such as cosmetic, plastic, foods, ceramic, paper and pharmaceutical (28). It is chemically inert, hydrophobic, organophilic, with high thermal and low electrical conductivity. The Food and Drug Administration (FDA) have approved it as generally recognised as a safe (GRAS) excipient for the use as a glidant and anti-tablet adherent in oral pharmaceutical products (28). In this study, talc was used as an impurity additive to induce crystallisation of the amorphous FF in chapter 4. Talc used in this study has an average particle size of below 70 μm (labelled on the package). It was purchased from Sigma-Aldrich (Dorset, UK).

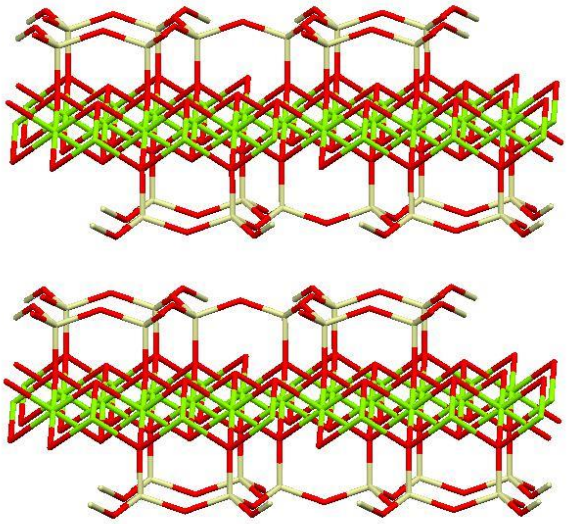

Figure 2.4 Packing arrangement of talc crystalline structure**.** The crystal parameters are obtained from the reference (26).

2.2.4 Polyvinyl pyrrolidone (PVP)

PVP is white free-flowing powder. The molecular structure of PVP monomer is illustrated in **Figure 2.5**. One mono unit of PVP, composed of a pyrrolidone ring connects with a polyvinyl backbone. PVP is an amorphous polymer. There are four grades of PVP which are commercially available, including PVP K12, PVP K17, PVP K30 and PVP K90, which have a molecular weight 2500, 9000, 50000 and 1250000 $g.mol^{-1}$, respectively. The high number of K reflects the high molecular weight, high viscosity and T_g (29). It is soluble in many solvents such as dichloromethane, ethanol, methanol, acetonitrile and water. It is an

official excipient in pharmacopoeia in which it has a range of applications including that of a binder in granulation, solubilizer, and carrier of solid dispersion formulations (28, 29).

A vast body of literature uses PVP as hydrophilic solid dispersion matrices. PVP enhances the aqueous solubility of poor water soluble APIs such as ibuprofen, griseofulvin and felodipine (31-33). PVP can form a hydrogen bond via its carbonyl group with a hydrogen donor of the drugs, i.e. hydroxyl and amide group resulting in an increase in the physical stability of the solid dispersion (31, 33). PVP solid dispersion can be produced by both melting based methods and solvent evaporation based methods including hot-melt extrusion, spray drying, co-evaporation, spin-coating, and electrospinning (29, 32, 34, 35). It is noted that the high molecular weight PVP-K 90 is not suitable for HME because the high T_g of the PVP (180°C) requires high processing temperatures which lead to drug and polymer degradation (36). In electrospinning, only PVP K30 and K90 are spinnable grades. The concentration of PVP K30 and K90 required for electrospinning are 30-40 and 5-15 %w/v, respectively in ethanol (34, 37).

However, the drawback of PVP is its high hygroscopic nature. The moisture absorbed by PVP plasticizes the solid dispersion matrices and increases mobility in which a reduction in the T_g of the solid dispersion matrices has been observed (33, 38). Consequently, it leads to phase separation and recrystallization of the amorphous drug in the solid dispersion matrices. It is believed that the hydrogen bonding between drug and PVP was disturbed by the moisture absorbed (38).

PVP-K90 was selected as a key polymer in this study to prepare solid dispersion formulations for electrospinning technique because it is spinnable even at low concentrations (5%w/v) and possibly enhances spinnability of another low molecular polymer that blends with it. Polymer blended electrospinning was used as the primary approach to developing electrospun formulations in this project. PVP was coupled with hydrophobic polymers including Eudragit E, Soluplus and HPMCAS in order to minimise the moisture uptake and increase the physical stability of the formulations. Another aspect of using a PVP polymer blended electrospun fibrous formulation is to prepare biphasic release formulations and PVP acts as the initial release phase. The PVP-K90 is the only grade used in this study. It was kindly donated by BASF (Ludwigshafen, Germany).

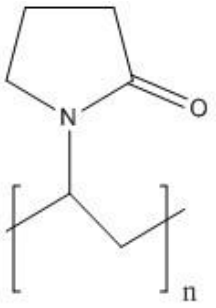

Figure 2.5 Molecular structure of the PVP monomer unit

2.2.5 Eudragit E

Eudragit E is the trade name of a cationic copolymer based on dimethylamino ethyl methacrylate, butyl methacrylate, and methyl methacrylate, as illustrated in **Figure 2.6**. It has an average molecular weight of approximately 47,000 $g.mol^{-1}$. Eudragit E has a characteristic amine-like odour and pH dependent dissolution which dissolves at pH lower than 5 but swells at pH greater than 5. It is non-hygroscopic, which absorbs less than 3% moisture w/w at 75% RH 22°C (39). Eudragit E naturally exists as amorphous and demonstrates a T_g at approximately 50°C (40). It has been used as stomach targeted delivery, a coating material for moisture protection, odour and taste masking and solid dispersion carriers for stabilising the amorphous APIs and enhancing physical stability (41, 42).

The solid dispersion of Eudragit E can be prepared with both melting based and solvent evaporation based methods. The low T_g of Eudragit E allows it to process easily by HME. The Eudragit E solid dispersion prepared by HME is well-documented for enhancing the aqueous solubility of poorly water-soluble APIs and increasing their physical stability (40, 43-45). Liu et al. prepared solid dispersions of indomethacin and Eudragit E by HME. The solid dispersion of Eudragit E significantly improved the solubility of indomethacin (45). Jung and co-workers prepared a solid dispersion of Eudragit E and itraconazole by spray drying. The solid dispersion spray drying particles were spherical and showed a diameter of approximately 1-10 µm. This formulation demonstrated a faster drug release than the marketed product (44). In electrospinning, few studies have reported the use of Eudragit E as electrospun matrices. Nagy et al. and Soti et al. reported that the spinnable concentration of Eudragit E is higher than 30% w/v in ethanol (46, 47). The carvedilol Eudragit E electrospun fibres demonstrated a ten fold increase in aqueous solubility in comparison to the crystalline drug and complete drug release within 3 minutes (46).

In this study, Eudragit E was blended with PVP in order to minimise moisture uptakes of the solid dispersion formulations in which physical stability was expected to increase. The

Eudragit E used in this study was kindly donated by Evonik Industries (Darmstadt, Germany).

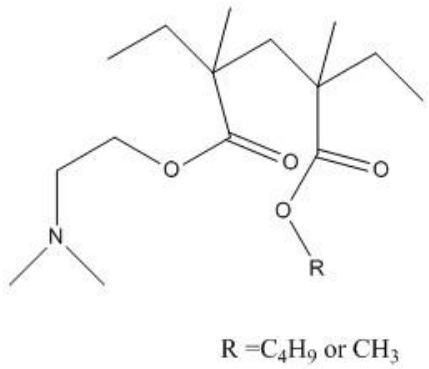

Figure 2.6 Molecular structure of mono unit of Eudragit E

2.2.6 Soluplus

Soluplus is an amphiphilic polymer whose structure is composed of polyvinyl caprolactam –polyvinyl acetate-polyethylene glycol graft copolymer, as illustrated in **Figure 2.7**. It has a molecular weight of approximately 118,000 $g.mol^{-1}$. Soluplusis considering as a new generation solid dispersion carrier which demonstrates dual properties of solid dispersion matrices and polymeric solubilizer (48). It forms micelles at a concentration of 7.6 $mg.ml^{-1}$and has a low T_g approximately 70°C. Soluplus was initially designed to be solid dispersion matrices for HME for enhancing the aqueous solubility of poorly water soluble drugs and maintaining supersaturated concentration during dissolution. Another advantage of SP is low hygroscopic material (49, 50). In addition, Soluplus is soluble in various kinds of organic solvents including, dichloromethane, ethanol, acetone, toluene and ethyl acetate (29). This allows Soluplus to be prepared with both melting based and solvent evaporation based solid dispersion preparation methods.

Nagy et al. successfully prepared Soluplus as electrospun fibres. At least 30% w/v of Soluplus in acetone was required to form electrospun fibres (51). In this study, Soluplus was coupled with PVP K-90. The blend fibrous matrices of PVP K90 and Soluplus were expected to minimise the hygroscopic nature of PVP resulting in the increased physical stability of the formulation and enhanced solubility of FF. Soluplus used in this study was kindly donated by BASF (Ludwigshafen, Germany).

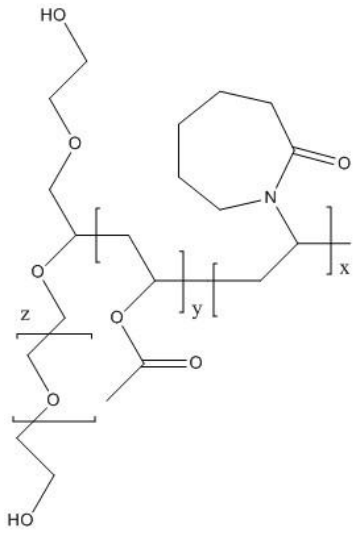

Figure 2.7 Molecular structure of Soluplus

2.2.7 Hypromellose acetate succinate (HPMCAS)

HPMCAS is a semi-synthesis polymer. The acetyl and succinoyl groups are added to the hypromellose backbone. It has an average molecular weight of around 17,000-20,000 $g.mol^{-1}$ (52). In comparison to the ordinary hypromellose (without succinoyl and acetyl substitution), HPMCAS demonstrates significantly less hygroscopicity (53). There are three grades of HPMCAS commercially available, L, M and H grade. Each grade has a different ratio of succinoyl and acetyl substitution. The different percentages of succinoyl and acetyl group substitutions lead to different solubility of the polymer at different pH (54). The relationship of percent succinoyl and acetyl substitution and the pH they dissolve is shown in **Table 2.2**. HPMCAS demonstrates T_g of approximately 120°C (55). HPMCAS is an approved excipient in the United States, British and Japanese Pharmacopoeia (56, 57). It is typically used as enteric coating materials. Moreover, HPMCAS has been used as solid dispersion carriers to improve the aqueous solubility of poorly water-soluble APIs. It can processed by both melt and solvent evaporation based methods including spray drying, co-evaporation and hot melt extrusion (53-55, 58, 59).

Up to now, to the best of our knowledge, there is no reported use of HPMCAS alone in electrospinning, but different grades of hypromellose have been reported as spinnable polymers (60). Therefore, in this study, HPMCAS was blended with PVP to reduce the hygroscopicity of the blend system. This was expected to improve the physical stability against humidity in the environment. In addition, HPMCAS is insoluble in acidic pH. Thus, this blends couple is expected to show a modified drug release in the acidic media in which burst drug release is from PVP and sustained drug release is from HPMCAS. The

HPMCAS L grade was used in this study. It was kindly donated by Shin-Etsu Chemical Co Ltd. (Niigata, Japan).

Table 2.2 The succinoyl and acetyl group substitution in HPMCAS grades and pH (54).

HPMCAS grade	Succinoyl (%)	Acetyl (%)	Dissolved pH
L-grade	15	8	>5.0
M-grade	11	9	>5.5
H-grade	7	12	>6.0

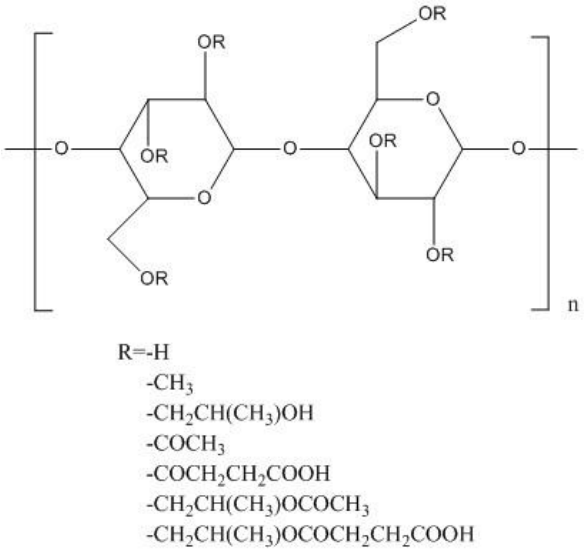

Figure 2.8 Structural formula of HPMCAS

Table 2.3 Summarised properties used in this study including T_g, water uptake and soluble pH

Polymers	T_g (°C)[a]	Water uptake at 75% RH 25°C (%w/w)[b]	Soluble pH[c]
PVP K-90	176±2.0	30.0±0.4	Any
Eudragit E	56±0.5	1.8±0.1	< 5
Soluplus	77±0.8	10.7±0.05	Any
HPMCAS-L	122±2.2	6.4±0.07	>5.0

[a] measured by MTDSC from raw materials in this study

[b] measured DVS from raw materials in this study

[c] reference (41, 50, 54)

2.3 Electrospinning general set up

A custom-made single spinneret electrospinning device (SS-ES) was used to prepare the electrospun fibrous formulations in this study. The electrospinning solution which contained API and polymer was poured into a 5 ml plastic syringe which was equipped with a syringe pump (Cole-Parmer, UK). The solution was fed through an 18 gauge blunt metal spinneret (Terumo, Tokyo, Japan) with a rate of 1.5 $ml.hr^{-1}$ and applying a voltage of 15 kV from an ES40P-20W high voltage power supply (Gamma high voltage research Inc, Ormond Beach, FL, USA). The custom- made drum collector was used to collect electrospun fibres with 500 RPM. The distance between the spinneret to the collector was fixed at 15 cm. For coaxial electrospinning (CS-ES), the solutions of the core and sheath layers were fed from separated syringe pumps at a rate of 0.5 mL/h to the coaxial needle (Linari engineering S.r.l., Pisa, Italy). The rest of the parameters, including distance from the spinneret to the collector and collector type, were similar to the SS-ES. All electrospinning experiments were performed under ambient conditions of 20 ± 2 °C/40 ± 5% relative humidity (RH). After the electrospinning process, the fibrous mats were peeled off from the collector stored in a 0% RH desiccator filled with phosphorus pentaoxide before analysis.

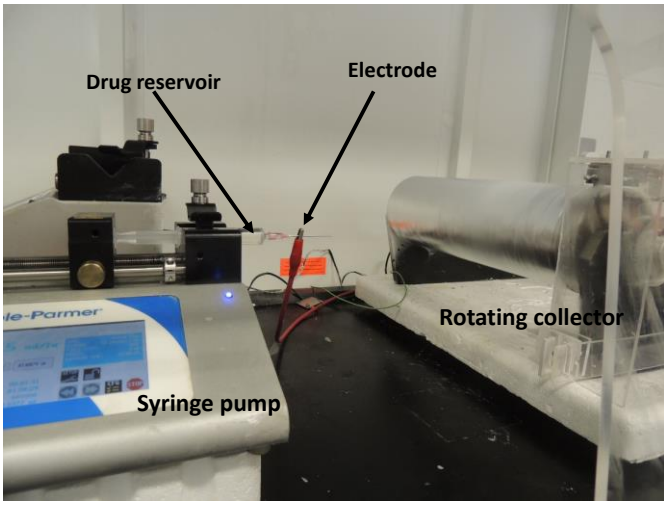

Figure 2.9 A custom-made single spinneret electrospinning with a rotating collector

2.4 General introduction to physicochemical characteristic techniques

The methods for characterisation of materials and formulations can be broadly divided into two groups, which are bulk characterisation techniques and imaging characterisation techniques. The bulk characterisation methods provide the average response of sample in both qualitative and quantitative measurements, such as DSC, PXRD, and ss-NMR. As the name implies, the imaging characterisation techniques emphasise on visualising a

particular region of the sample, for instance, SEM, TEM, FTIR microscopy, optical microscopy and atomic force microscopy (AFM). The combination of these two kinds of characterisation approaches provides essential information on understanding the physical state of the raw materials and formulations.

2.4.1 Differential scanning calorimetry (DSC)

2.4.1.1 Basic principle

DSC is a thermal base analytical technique which offers information on physical and energetic properties of materials. It is a frequently used method to analyse pharmaceutical materials. DSC provides both qualitative and quantitative data from endothermic, exothermic events (melting and recrystallization and a glass transition temperature) and heat capacity changes by measuring the energy differences between sample and reference (61, 62). Therefore, it is a benefit to characterise the polymorphic form of APIs, detecting the instability of API recrystallization in solid dispersions and investigating the miscibility of the drug and polymer (61, 63). DSC demonstrates numerous benefits such as the tiny amount required for a measurement, coverage of a broad range of temperatures (-120 to 600°C), fast analysis and simple sample preparation (62).

There are two instrument types of DSC which are power-compensated and heat flux DSC as shown in **Figure 2.10**. The power compensation DSC has two individual furnaces for sample and reference, which has the advantage of achieving higher heating and cooling rates because of its small furnace, while the heat flux DSC possesses a single furnace which contains both sample and reference pans. The single surface of heat flux DSC has the benefit of robust temperature control in comparison to the two separate furnaces of the power compensation DSC design. As a consequence, it demonstrates a better baseline than the power compensation DSC. Both power compensation and heat flux DSC have their benefits and drawbacks but are similar in terms of sensitivity and accuracy. Therefore, both DSC designs can be used to analyse the specimens with no supremacy (61, 62).

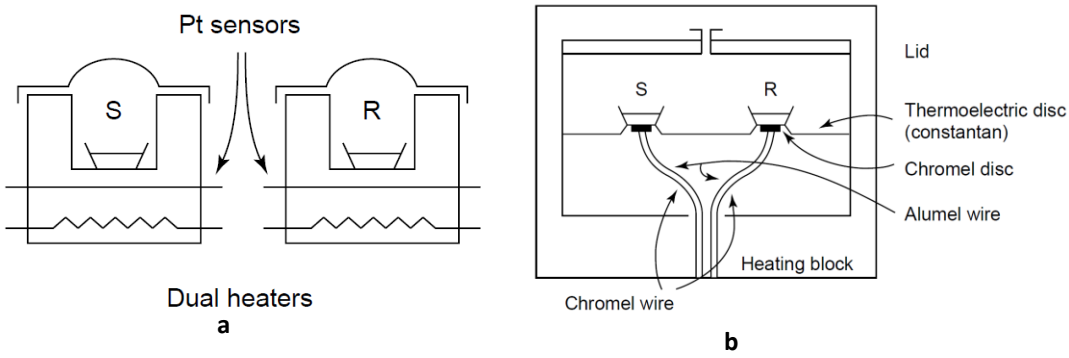

Figure 2.10 Schematic diagram of power-compensated DSC (a) and heat flux DSC (b). This figure is reproduced from reference (61).

The DSC measurement is based on the heat flow measurement. The DSC monitors the heat flow from the difference in temperature between the sample and reference (empty pan) by a thermocouple as a function of thermal resistance (61, 62). The **equation 2.1** shows how DSC acquires the heat flow signal.

$$\frac{\partial Q}{\partial t} = \frac{(T_R - T_S)}{R} \quad \text{.....(2.1)}$$

where *dQ/dt* is the heat flow, T_R is the temperature of reference; T_S is the temperature of the sample and *R* is thermal resistance of the sample. The data obtained from DSC is a plot of heat flow as a function of temperature. In another words, the heat flow term is an expression of heat capacity combined with the kinetics of the sample. **Equation 2.2** demonstrates the relationship of heat flow.

$$\frac{\partial Q}{\partial t} = C_p \cdot \frac{\partial T}{\partial t} + f(T,t) \quad \text{.....(2.2)}$$

where C_p is heat capacity, *dT/dt* is heating rate, and *f(T,t)* is the kinetic event. The kinetic event represents the temperature corresponding thermal event such as polymer relaxation, crystallisation, and melting. **Figure 2.11** illustrates thermal events observed by DSC, including glass transition, crystallisation exothermic and melting endothermic of PCM.

In the absence of the kinetic event, the heat flow corresponds to the baseline, and the C_p can be obtained from the difference of baseline value as a function of heating rate. The traditional C_p measurement from a standard DSC is described as

$$C_p = \frac{K\Delta Y}{b} \quad \text{.....(2.3)}$$

where *K* is calorimetric sensitivity obtained from a calibration, *ΔY* is the baseline difference in presence and absence of the sample and b is the heating rate. From this relationship, therefore, C_p is defined as energy in a specific unit which rises temperature 1K of the

substance. It also reflects the molecular motion available in the sample, including vibration, translation, rotation. It needs to be borne in mind that the standard DSC reports the total heat flow, which is the sum of the two terms in **equation 2.2** (62).

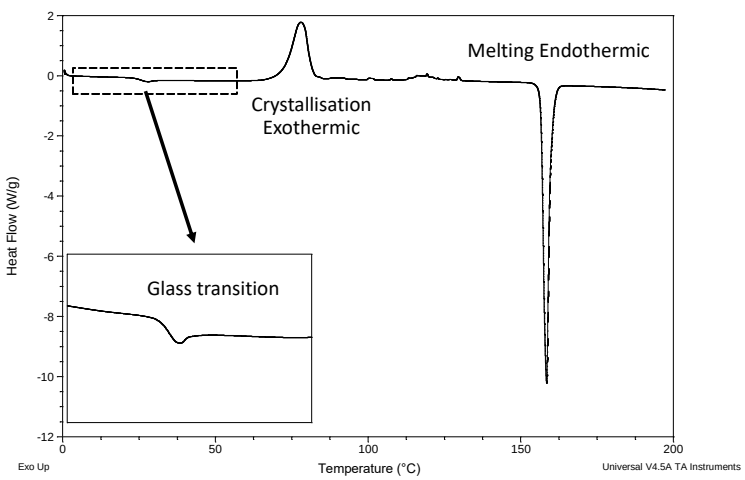

Figure 2.11 Example of standard DSC thermogram of PCM

2.4.1.2 DSC experimental conditions

A Q-2000 (TA Instruments, Newcastle, DE, USA), was used to perform the DSC experiments in this study. The Tzero calibration was used to calibrate the baseline. N-Octadecane, indium, and tin were used for temperature calibration. The DSC experiments were performed at heating rates of 2, 5, 10, and 20 °C.min^{-1} in the range between -40 to 120 °C. A constant nitrogen purge was applied at the 50 mL.min^{-1} rate. The standard DSC was used to examine the polymorphic form of crystalline FF samples in chapters 3 and 4. All of the FF crystalline samples were precisely weighed (1−3 mg), and TA standard aluminium crimped pans were used. Each sample was tested in triplicate.

2.4.2 Modulated temperature differential scanning calorimetry (MTDSC)

2.4.2.1 Basic principle

MTDSC is an extension to the standard DSC. It was developed by Gill et al. (64). It applies a perturbative heating or cooling program (mostly sine wave), unlike the standard DSC, which has a linear heating. The MTDSC heating program consists of three parameters, including underlying heating rate, modulated amplitude and modulated period. **Figure 2.12** illustrates the sinewave heating (solid line) in comparison to the linear heating (broken line). The combination of oscillating temperature program and fourier transform mathematical process allows the separation of different types of sample behaviour signal (62, 65). In comparison to the standard DSC, the whole term of heat flow is measured, which is a combination of heating rate dependent and absolute temperature dependent

responses, as stated in **equation 2.2**. The MTDSC offers the advantage of separating these two terms. The heating rate dependent term which is the first term on the right-hand side in **equation 2.2**. is a function of heat capacity to the proportion of heating rate. Therefore, the heating rate dependent transition effects by the heating program in which the fast heating rate results in a larger value in this term, and the event shows in this term is reversing. The T_g is an example of a thermal event that shows the reversing signal. On the other hand, the absolute temperature dependent transition is the second term on the right-hand side in **equation 2.2**. It is an irreversible response which, after the proceeding, cannot be reversed by cyclic heating or cooling, i.e. enthalpies relaxation before the T_g, cold crystallisation, curing, solvent evaporation and decomposition. Thus, this is known as a non-reversing signal (62, 64, 65). The flow chart in **Figure 2.13** describes the origin of signal deconvolution. The advantage of separating the reversing and non-reversing responses is to distinguish the overlapping thermal event, such as the relaxation enthalpy coinciding with the T_g and separating the broad peak of water loss that interferes with the glass transition in the hygroscopic materials (66).

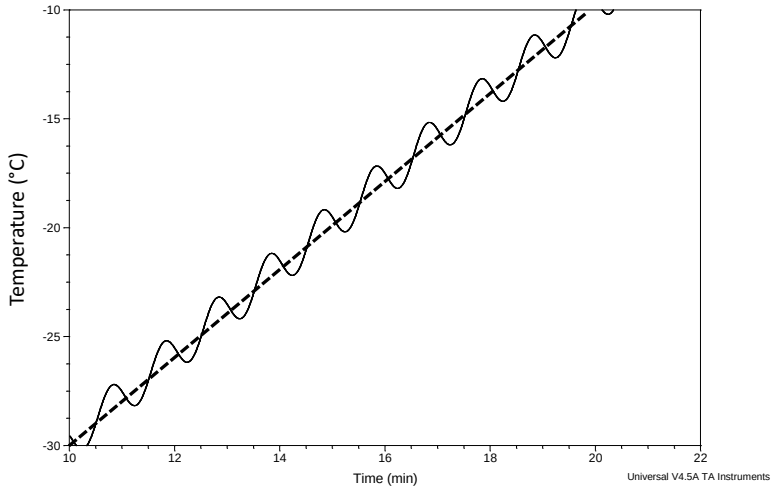

Figure 2.12 Sine wave heating in MTDSC (solid line) and linear heating in conventional DSC (broken line)

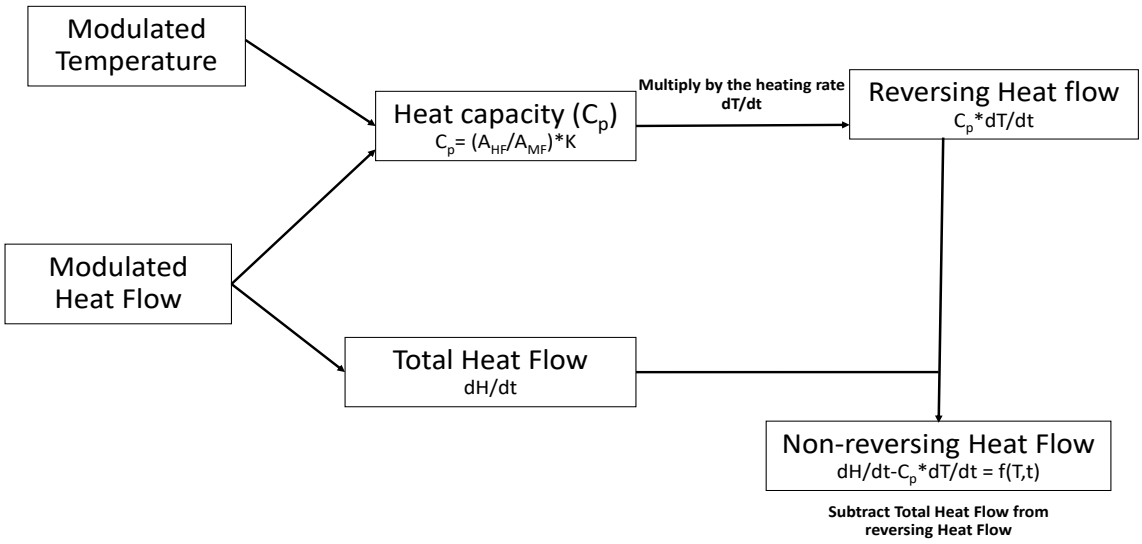

Figure 2.13 A flow chart illustrating an MTDSC signal deconvolution (adapted from reference (62))

C_p acquired from MTDSC is twice as accurate and precise as the standard DSC because MTDSC is less noisy and more precise (64, 65). In MTDSC, C_p is obtained by calculating the proportion of modulated heat flow amplitude (A_{HF}) to modulated heating rate amplitude (A_{HR}). Then, it is multiplied to the heat capacity calibration constant K, because of the non-ideal behaviour in the real heating cell, as seen in equation 2**.**4**.**

$$C_p = K \cdot \left(\frac{A_{HF}}{A_{HR}}\right) \text{.....(2.4)}$$

In the MTDSC experimental conditions, the longer period improves accuracy while the larger amplitude improves the signal-to-noise ratio (65). In order to satisfy these prerequisites, slow underlying heating is required (less than 5°C.min^{-1}) and at least six modulations on the thermal event are recommended to be applied during MTDSC experiments to accurately deconvolute the MTDSC signal.

2.4.2.2 MTDSC experimental conditions

A Q-2000 (TA Instruments, Newcastle, DE, USA), was used to perform MTDSC experiments in this study. The Tzero calibration was used to calibrate the baseline. N-Octadecane, indium, and tin were used for temperature calibration. The heat capacity calibration for the MTDSC experiment was calibrated in a temperature range of -60 to 200°C. A constant nitrogen purge was applied at the 50 mL.min^{-1} during the experiments. For the MTDSC study, a heating rate of 2 °C/min with a modulated amplitude of ±1 °C every 60 s was used for film casting and electrospun samples (Chapter 5 and Chapter 6). The solid dispersion formulation specimens, which were prepared from both film casting

and electrospinning, were cut and precisely weighed (1−3 mg). The isothermal MTDSC experiments were performed with modulated amplitude ±1 °C every 60 s for 2 hours. The reversing heat capacity of the isothermal MTDSC experiments was calibrated at 35, 40, 45, 60 and 70 °C. The FF crystalline samples were precisely weighted at 3-5 mg in each pan. TA standard aluminium crimped pans were used. Each sample was tested in triplicate.

2.4.3 Thermogravimetric analysis (TGA)

2.4.3.1 Basic principle

Thermogravimetric analysis (TGA) is a technique which monitors the weight of the sample as a function of temperature or time at a constant temperature in a controlled atmosphere (purging with nitrogen or dry air). The changes in mass are due to chemical or physical reaction, for example, solid-solid reaction, liquid-solid reaction and gas-liquid reaction, sublimation, and degradation. In pharmaceutics, TGA has been used for estimating the water content from the weight loss, desolvation of solvated APIs and decomposition of the APIs (62). For advanced application, it can be used to study the kinetics of the dehydration process, determining the drug content in mesoporous materials from the drug degradation (67, 68).

2.4.3.2 Thermogravimetric analysis operating conditions

In this study, a TGA Q5000 SA (TA Instrument, New castle, DE, USA) was used to examine the chemical stability of the different polymer of FF and to determine the water content in the formulation. The heating rate of 10°C.min^{-1} from room temperature to 400°C was used to investigate the degradation of FF and the isothermal at 120 °C for 60 min was used for determining the water content in the formulations.

2.4.4 Dynamic vapour sorption (DVS)

2.4.4.1 Basic principle

DVS is another gravimetric technique that is applied to analyse the solvent absorption behaviour (69-71) (most cases are water and in this study). DVS controls the vapour of water surrounding the sample and monitoring mass change at a controlled temperature. **Figure 2.14** illustrate the internal instrument structure of DVS. The desired humidity is obtained by passing a specific flow rate of dried nitrogen through a water reservoir. Then, the humidified nitrogen air enters a sealed chamber, which contains two identical quart pans hanging in the balance; one is an empty reference pan, and another loads the sample. The sample absorbs moisture from the environment and causes a mass change which is recorded against the time (72).

DVS demonstrates advantages for the study moisture sorption behaviour of foods and pharmaceutical materials (69-71, 73). There are two common modes that are widely used for DVS study which is isohume and sorption isotherm. The isohume experiments are conducted at fixed relative humidity and a certain temperature. The mass change is recorded as a function of time. The data from an isohume mode benefits the investigation of moisture sorption mechanisms such as peleg model, double exponential, and Fick's diffusion (69). The sorption isotherm is another DVS mode that monitors the mass change as ramping a water vapour concentration. The data obtained from this mode reflect an effect on relative humidity to the moisture sorption of the sample. Further information in depth from the sorption isotherm data can be obtained from fitting the data to Guggenheim-Anderson-de Boer and Peleg model in order to explain the kinetic moisture sorption of the sample (74, 75). The details of the mathematic model used in this study will be discussed in section 2.7.

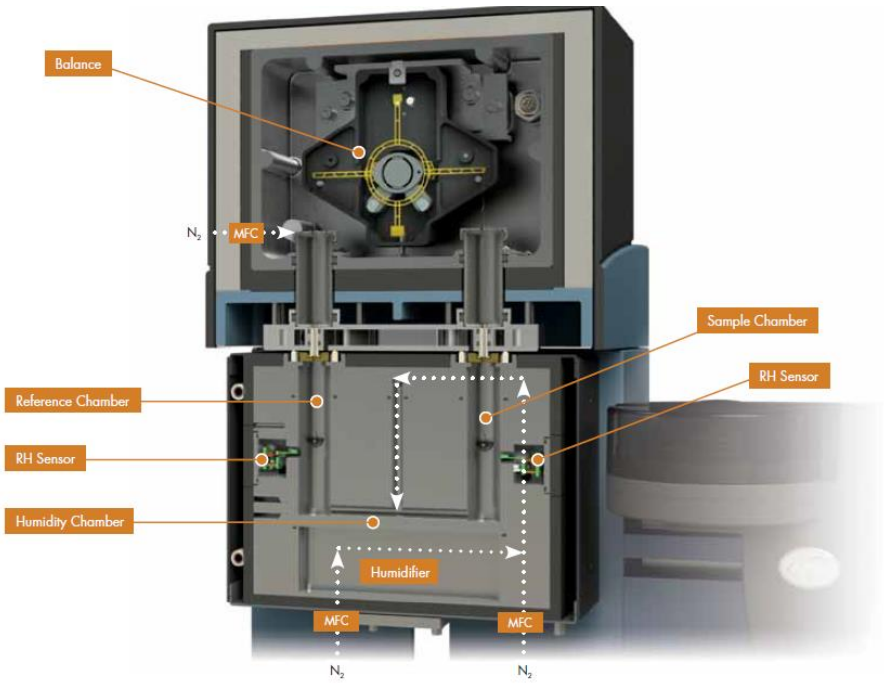

Figure 2.14 Diagram illustrating inner structure of Q5000 SA DVS. This diagram reproduces from TA Instrument brochure.

2.4.4.2 DVS operating conditions

A Q5000SA DVS (TA Instruments, Newcastle, DE, USA) was used to perform dynamic vapour sorption experiments in Chapter 5. The samples of cast films and fibrous formulations were freshly prepared and were cut into small pieces. Approximately 8-10 mg of the samples was placed into a quartz pan. During the experiment, the sample chamber was sealed shut, and the dry nitrogen purge through a water reservoir was used to control

humidity during the DVS experiments. All of the samples were dried under 0% RH for 100 min before starting the sorption experiments. In this study, sorption isotherm and isohumic experiments were performed. In the sorption isotherm, the samples were held at specific relative humidity from 10% to 90% for 300 min each humidity step. In the isohumic experiments, the samples were incubated at 75% RH for 400 min to study the kinetics moisture absorption of the samples.

2.4.5 Attenuated total reflectance Fourier transforms infrared spectroscopy (ATR-FTIR)

2.4.5.1 Basic principle

IR is an electromagnetic radiation that has a longer wavelength and lower frequency than the visible light. The IR can be divided into three types, according to their frequency as near, mid and far-infrared. The highest energy is near-infrared 14000 to 4000 cm^{-1}, then mid-infrared 4000 to 400 cm^{-1} and finally far-infrared 400 to 10 cm^{-1} (76). The IR spectroscopy principle is based on absorption spectroscopy. As the IR beam radiates the sample, the molecule absorbs the energy and creates a rotational-vibrational motion in its structure such as stretching, bending, wagging and rocking. These vibrational motions cause the alternation in dipole moment of the molecule, which can be measured by IR spectroscopy. In particular, the asymmetric motions result in a great dipole moment change which can be observed as a high-intensity peak in infrared spectroscopic results (77). The infrared spectra typically are shown in the plot of % transmittance or absorbance against wavenumber (cm^{-1}), which is the inversion of the wavelength. The absorbance in the IR spectrum depends on the properties of the individual functional group, i.e. –OH stretching at 3500 cm^{-1}, -CH_3 stretching at 3000 cm^{-1}, C=O stretching at 1800 cm^{-1} (78). The IR is a benefit in characterising the functional group in the interested structure or combining these absorbance peaks to allow the construction of a unique fingerprint for each chemical entity. The application of Fourier transforms the modern IR spectroscopy, shortens the time it takes to acquire the spectrum and improves the signal-to-noise ratio (79). The Fourier transform is a data-processing technique which turns raw data, which is recorded as the position of the mirror and the amount of light detected, known as an interferogram, to the designed spectrum.

Conventional IR spectroscopy suffers from a complicated sample preparation, for example, in which a few milligrammes of the solid sample need to be mixed with nujol and dispersed in KBr matrices, then compressed; the compressed KBr disc then provides a transparent window for the infrared measurement. This sample preparation process is rather complicated, time-consuming and may result in changes of the sample during the

preparation steps. Attenuated total reflectance (ATR) sampling is a solution to this problem. The ATR accessory employs the principle of internal reflection (80). The infrared beam passes through the ATR crystal, which has a high refractive index (mostly diamond). The beam reflects from the internal surface and creates an evanescent wave which penetrates into the sample approximately 0.5-5 µm. The sample absorbs the evanescent wave and returns the rest of the beam to the detector. Therefore, the sample must be in contact with the ATR crystal. A diagram of ATR reflection is illustrated in **Figure 2.15**. Furthermore, it is a non-invasive approach which minimises the damage to the sample during the experiment.

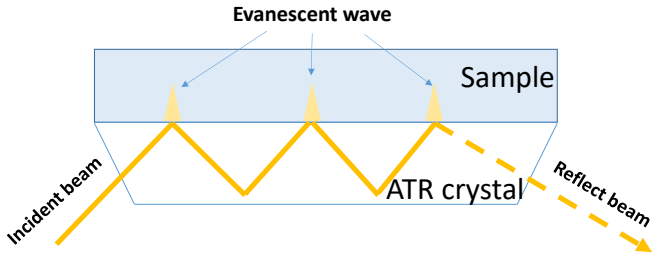

Figure 2.15 A schematic diagram demonstrating the principle of attenuated total reflectance

ATR-FTIR is a frequently used technique for the characterisation of pharmaceuticals (81, 82). It has many applications, including constructing a chemical fingerprint of each material. The commonly used APIs IR fingerprints are available in British Pharmacopeia. ATR-FTIR is sensitive to inter and intramolecular arrangement. Thus, it is a potential tool to distinguish the state of materials, including amorphous, crystalline and even polymorphs. ATR-FTIR has been used to detect the interaction of drug and excipients in solid dispersions including a hydrogen bonding which promotes miscibility in solid dispersion (33).

2.4.5.2 ATR-FTIR experimental conditions

In this study, ATR-FTIR was used to distinguish the polymorphic form of FF (Chapter 3and 4) and to study the interactions between drug and polymers in the formulations (Chapter 5 and 6). An IFS 66/S spectrometer (Bruker Optics Ltd., Coventry, U.K.) equipped with a Golden Gate heated top plate attenuated total reflectance accessory (Specac Ltd., Orpington, U.K) was used to perform the IR spectroscopic studies. A few milligrammes of raw materials, crystalline FF samples, film casting formulations and electrospun fibrous formulations were placed on the diamond crystal of the ATR accessory. Each spectrum was taken between 4000 and 550 cm^{-1} with 2.0 cm^{-1} resolution and 32 scans. All samples were examined in triplicate. OPUS software version 6.5 (Specac Ltd., Orpington, U.K) was used to analyse ATR-FTIR spectra.

2.4.6 FTIR microscopy

2.4.6.1 Basic principle

FTIR microscopy is an imaging technique that couples optical microscopy with the FTIR spectrometer. It has various types of applications in biology, biomedical, pharmaceutical and polymers science as a potential mapping tool to distinguish material components (83-85). Vogel and colleagues successfully acquired phase separation images with FTIR microscopy of the blends of poly(3- hydroxybutyrate) (PHB) with poly(L-lactic acid) (PLA) and poly(ε-caprolactone) (PCL), respectively (85). Moreover, the infrared spectrum can differentiate between the amorphous and crystalline state of APIs. Therefore, it can be potentially used for imaging the phase separation of an amorphous drug and polymer.

The operational modes of FTIR microscopy can be divided into two major modes, which are transmission mode and reflection mode. The transition mode is suitable for thin specimens which a laser can transmit through such as microparticles, thin films and a cross-sectional film prepared from microtoming, while the reflection mode requires a thicker (at least 15 μm) that can reflect a laser beam. This technique is particularly suitable for studying the surface of the sample. Unlike an ordinary FTIR spectrometer, the instrument of FTIR microscopy is equipped with a multi-channel focal plane array detector which consists of a small pixel plate. Consequently, it enables fast data collection and can collect the optical signal from the entire field (86). Currently, the available resolution of the plane array detector is between 64x64 to 256x256 pixels in which the spatial resolution of this technique is approximately 20 μm^2 per pixel (87).

2.4.6.2 FTIR microscopy experimental conditions

FTIR mapping was investigated by using a Nicolet iN10 MX Infrared Imaging Microscope (Thermo Fisher Scientific – Thermo Scientific Inc., Vienna, Austria). The small piece (1x1 cm) polymer cast films are placed on the stage, which is supported by a BaF_2 window and measured in the transmission mode. Each pixel size in the mapping was 25x25 μm^2 and was acquired from 16 scans with resolution 8 cm^{-1}in which a 16 element MCT was an imaging detector. The spectra were automatically corrected for atmospheric water vapour. The data were processed with Omnic Spectra software (Thermo Scientific Inc., Vienna, Austria). Different IR maps were generated for areas of selected peaks. The homogeneity of areas was tested by plotting correlation maps related to known spectra, or by performing PCA analysis in the region of 1800-800 cm^{-1}.

2.4.7 Single crystal and powder X-ray diffraction

2.4.7.1 Basic principle

X-ray diffraction is an important technique to characterise crystalline materials. X-ray is electromagnetic radiation with a small wavelength (approximately between 0.1 to 100Å), which is similar to the interatomic distance. When the X-ray beam passes through the crystalline matters, it is scattered by the electrons that surrounds an atom. The position of the diffracted peak can be explained by using Bragg's law, as seen in **equation 2.5.**

$$n\lambda = 2d\ sin\theta \quad \text{.....(2.5)}$$

where *n* in an integer of diffracted beam that reflects from the different layer and perfectly in phase with each other, λ is the wavelength of the X-ray beam, *d* is the spacing between atom layer; θ is the incident angle of the beam and the crystal plane. The Bragg's rule applies to both single crystal and powder X-ray diffraction.

Single crystal X-ray diffraction (SCXD) and powder X-ray diffraction (PXRD) are complementary techniques that have been used to study the crystalline structure of solid substances. The single crystal X-ray diffraction provides an internal crystalline structure such as bond length, atom position, cell dimensional and bond angle (77, 88). Thus, it is an absolute method to determine the structure of crystalline matters. A single piece of crystal is mounted to the needle shape sample holder and radiated by the X-ray beam at different angles. The beam scatters are recorded and used as the primary data to solve the crystalline structure. SCXD suffers from several disadvantages, for example, the time required for analysis, difficulty in obtaining an individual piece of single crystal (50-250 μm). SCXD is mainly used for identifying new crystalline structures including polymorph, solvate, and co-crystals (77, 82). The Cambridge Structural Database (CSD) is the largest crystallographic electronic database for crystalline materials; they have collected numerous crystallographic data from X-ray single crystals for the purpose of pharmaceutical drug discovery, materials development, research and education.

On the other hand, X-ray powder diffraction (PXRD) is a non-destructive method used to characterise crystalline materials and is accepted as a gold-standard approach (77, 82). In comparison to PXRD, SCXD has a single crystal orientation while powder in PXRD contains numerous crystals. Thus, it demonstrates all possible orientations of the crystalline materials. The sample was placed in a fixed position sample holder while the X-ray source and the detector were raised upwards in θ°. The diffraction peaks with intensity recorded at 2θ°.The PXRD is particularly sensitive to those long range orders of crystalline materials, in which individual crystalline matter demonstrates its patterns. Therefore, PXRD patterns can be used for identifying crystalline materials including their polymorphs

and solvates (82, 88). On the other hand, amorphous materials show a halo pattern (broad peak). PXRD can characterise the mixture of amorphous materials and crystallines, and the intensity of the PXRD peak reflects the degree of crystallisation of crystalline material. Therefore, PXRD is an effective technique to study solid dispersion formulations and evaluate their physical state (29).

The preferred orientation is a dramatic issue that influences the intensity of the PXRD pattern. It is caused by the non-spherical crystallite, which has a tendency to orient at a minimum volume (77). This phenomenon results in non-randomness, which leads to intensity decrease of Bragg's reflection for peaks that are not in reflecting position; increase for peaks in reflecting position (such as face of a platelet). The example of this effect was reported by the experimental sulfathiazole form III PXRD pattern, demonstrating the preferred orientation in comparison to the simulated pattern obtained from its single crystal data (89), illustrated in **Figure 2.16**.The preferred orientation can be eliminated by sufficient grinding prior to loading to the sample holder, the customary load sample on the side of the holder and by using spray drying as the preparation method (90). However, these methods have to be applied with caution because they are considerably effected to polymorphic transformations of the sample (77).

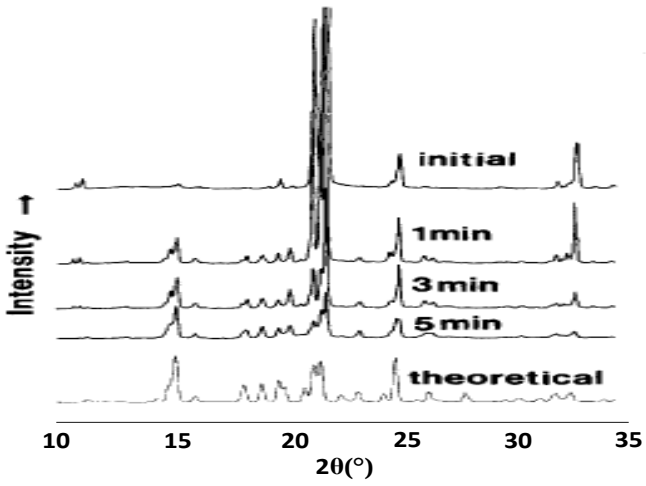

Figure 2.16 Preferred orientation of PXRD sulfathiazole form III is reduced by grinding. This figure was reproduced from reference (89).

2.4.7.2 Single crystal X-ray diffraction experimental operating conditions

The diffraction experiments were performed using an Oxford Diffraction Xcalibur-3/Sapphire3- CCD diffractometer (Oxford Diffraction Ltd., Oxford, UK) using graphite monochromated Mo−Kα radiation (λ = 0.71073 Å). Crystals of FF from II and III were colourless prisms. A single crystal was chiselled out from a solid array of crystals from a

melt, mounted on a glass fibre and fixed in the cold nitrogen stream on the diffractometer. Intensity data were measured using thin-slice ω and φ-scans at 140 K. The diffraction data were processed using the CrysAlisPro-CCD and-RED programs (91).

2.4.7.3 Single crystal structure solving

The structure was solved in SHELXT using the dual-space approach and refined with SHELXL, as implemented in the ShelXle GUI (92, 93). All non-hydrogen atoms were located from electron density maps and were refined with anisotropic thermal parameters. Hydrogen atoms were included in idealised positions and were refined with independent isotropic displacement parameters. The coordinates of hydrogen atoms were refined in riding mode while allowing rigid rotations of the methyl groups. The geometric measurements in this article were obtained using the programs PLATON and OLEX2 (94, 95). The graphic illustrations were created using Mercury (96). The single crystal data were analysed by Mr. Khaled Tekieddin.

2.4.7.4 Powder X-ray diffraction experimental operating conditions

A Thermo-ARL X'tra diffractometer (Ecublens, Switzerland) was used to perform PXRD experiments at ambient temperature and humidity. The crystalline samples were gently crushed with a mortar and a pestle to avoid the preferred orientation effect. The crushed powders were transferred to a sample holder. The physical mixture of drug and polymer were homogeneously blended in a mortar before transfer to the sample holders. The electrospun fibres samples were cut into small pieces and then packed onto the sample holders. A Cu Kα1 radiation source was used with 45 kV voltage and a current of 40 mA. The angular range was from 5° to 50° (2°θ) with a step size 0.01° and one second per step.

2.4.8 Scanning electron microscopy (SEM)

2.4.8.1 Basic principles

SEM is one of the electron microscopic classes in which the surface topology of an object is mapped with a focus electron beam. Typically, it has a high resolution and magnification (down to nanometer) in comparison with traditional optical microscopic techniques. The electron beam in generated from tungsten filament with 10-20 kV accelerating voltage is radiated to the surface of the sample. The SEM images are constructed from the secondary electron that is emitted from the excited atom from the electron beam. The specimens are examined in a high vacuum chamber in which temperature can be cryogenic, room temperature and elevated temperature (97).

The SEM demonstrates various applications in pharmaceutical formulation design and development. It has been used to investigate the morphology of crystalline material at high magnification, to examine the surface topography and to trace suspected APIs recrystallization in solid dispersion formulations. Additionally, it is a powerful tool to study the morphology of electrospun fibres including fibrous diameter, fibre orientation and defects on the fibres (34, 35).

2.4.8.2 SEM experimental operating conditions

A JEOL 5900 LV (Tokyo, Japan) scanning electron microscopy scanning electron microscope was used to examine the morphology of talcum, FF polymorphs I, III, spin-coated film, cast films and electrospun fibres. A small piece of film, fibrous mat or some drug crystals were attached to a sample stub and sputter coated with Au/Pd before imaging. The accelerated voltage was fixed at 20 kV.

2.4.9 Transmission electron microscopy (TEM)

2.4.9.1 Basic principles

Transmission electron microscopy is another type of electron microscopy class. It employs a similar principle to a light microscope, but TEM uses an electron beam instead of visible light. Therefore, it offers extremely high magnification, which can explore down to the nanoscale. A very thin specimen is mounted on a copper grid, which is later placed in a vacuum chamber. The electron beam is generated by a tungsten filament electron gun. The electron beam is finely focused on the specimen site by using an electromagnetic lens and transmitted through a thin layer of a sample. Consequently, some electron scatter depends on the density of the material. The transmitted electrons hit the fluorescent screen at the bottom of the TEM and create shadow images, in which the intensity of the darkness in the image relate to the density of the sample. Thus, this allows the internal structure of an interested specimen to be examined. TEM is a frequently used approach to study the core-shell structure of electrospun fibres (98, 99).

2.4.9.2 Transmission electron microscope operating conditions

Transmission electron microscopy characterization was performed at room temperature using a Philips CM30 instrument operating at 300 kV. The very thin layer of electrospun fibres including coaxial PVP-HPMCAS fibres and PCM PVP-HPMCAS fibres were supported on holey-carbon films on 300 mesh copper grids held within a double tilt sample holder. Images were collected on photographic films, which were scanned in order to generate digital images.

2.4.10 Hot stage polarised light microscopy (HS-PLM)

2.4.10.1 Basic principle

Hot stage polarised microscopy is coupled between a controlled temperature chamber and a polarised light microscopy. Polarised light is light with restricted oscillation frequency, obtained from passing unpolarized light through a polarizer. The polarised light can be used to determine the optical crystallographic properties of the crystalline APIs (62, 88). The heating chamber controls the temperature of the sample and allows the thermal behaviour of APIs to be studied at an elevated temperature such as melting, desolvation, crystallisation, and their crystal growth. A colour camera records the images as a function of temperature or against the time in case of the isothermal experiment. HS-PLM is an observation technique that is typically applied for investigating the crystal growth kinetics and also identifies the API crystals (62, 100).

2.4.10.2 HS-PLM operating conditions

A PLM model Leica DM LS2 (Wetzlar GmbH, Germany) equipped with a JVC camera with 5, 10 and 20x magnification was used to study the morphology of the crystalline FF and crystal growth of amorphous FF from the melts. The microscope coupled with a hot-stage Mettler Toledo FP82HT in which regulated by an FP90 central processor (Greifensee, Switzerland) was controlled from Software Studio Capture 1.6 from Mettler Toledo Ltd (Greifensee, Switzerland). The growth rate of FF was analysed by using ImageJ software. The average values of three measurements from different images were used.

2.4.11 Atomic force microscopy (AFM)

2.4.11.1 Basic principle

Atomic force microscopy is a surface probing technique, which has proven to have tremendous advantages in surface science, medicinal and biological research (101, 102). The AFM probe is composed of a sharp tip, facing the sample surface that is allocated at the end of a cantilever. The back of the cantilever is coated with reflective material. A laser beam is projected onto the back of a cantilever. The deflected laser beam is detected by a photodetector, which is used to monitor the probe position. In the operation, the tip is maintained close to the sample surface. Several forces such as van der Waals force or ionic force interact between the apex of the tip and the surface of the specimen during sample scanning. These forces contribute to a dislocation of the probe, which is monitored by the photodetector and feedback signal is sent back to maintain the probe position. The feedback

data is then used to create a topography image of the sample surface. The diagram in **Figure 2.17** illustrates the fundamental set up of an AFM system (103).

There are three common modes of AFM used for studying the topology of samples: contact mode, non-contact mode, and tapping mode. This study emphasises the contact mode because it was mainly used in this project and local thermal analysis, which is an extension of this mode. The AFM tip is in contact with the sample and dragged along the surface during an image scanning in contact mode. A probe is kept in a constant position using a feedback loop, and a surface topography is generated from the feedback signal (102). This mode is ideal for hard surface samples and force microscopy. It may cause damage to soft samples such as cell and tissue (101, 103). Thus, the contact mode AFM is commonly used for characterisation of the surface in materials science.

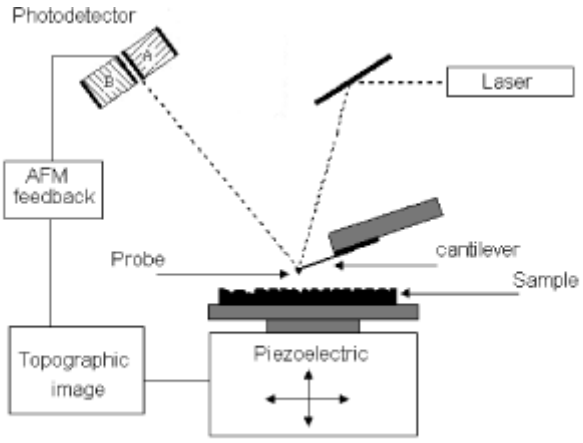

Figure 2.17 Schematic diagram of atomic force microscopic setup. This figure is reproduced from reference (103)

2.4.11.2 Local thermal analysis (LTA)

Frequently used thermal analysis techniques such as DSC, MTDSC and TGA test show a sample-average response, which is not site/local specific. In order to address this problem, Hammiche and co-workers developed a thermal probe approach which allows heating to occur locally at a particular site. This technique, namely local thermal analysis (LTA) (104), is an extension of conventional AFM contact mode. The AFM is equipped with a thermal probe that has the ability to heat up when electrical voltages are applied. There are two types of thermal probe available: micro and nanoprobe, according to the resolution site of each probe (105, 106). The thermal probe is landed on the interested location as in contact with the surface of the sample. Electrical voltages are applied to the probe resulting in its tip being heated. Then, the temperatures at the site reach a transition event such as melting or glass transition of the material, leading to the site softening and the probe sinking

into the surface of the sample. This causes the probe to dislocate, which is detected from a suddenly reducing of a laser deflection from the cantilever (106-108). The principle of LTA is illustrated in **Figure 2.18**.

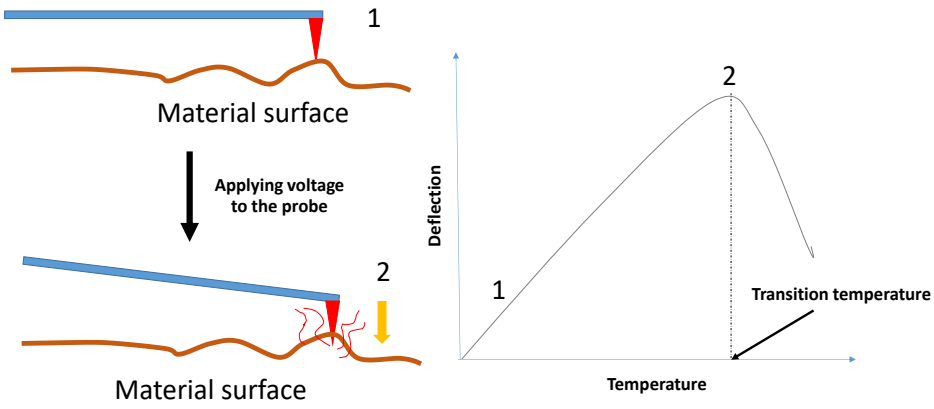

Figure 2.18 Schematic diagram of the principle of local thermal analysis, adapted from reference (105).

There are two types of LTA probes, which are micro and nano thermal probe (105). The microprobe is an AFM probe made from a Wollaston wire adapted cantilever probe, also known as Wollaston probe (109). The wires consist of a silver shell (75 µm diameter) and platinum core (5 µm diameter). The silver sheath is removed to expose the core platinum wire. The wire is bent to form a V-shape, which is a suitable probe shape. The mirror is attached to the top of the cantilever arms, which reflect a laser beam to the photodetector. The images of the micro thermal probe are demonstrated in **Figure 2.19a.** This probe provides spatial resolution of approximately 1 µm (109, 110). On the other hand, the nano thermal probe is produced from a micromachine. The image of the nano thermal probe is illustrated in **Figure 2.19b**. It consists of a silicon nitrile pyramidal tip, palladium resistor and cantilever (105). The height of the apex is approximately 5 µm with the narrowest point of 35 nm (105, 107). Thus, it can provide spatial resolution down to 50 nm (107). This is a significant improvement of the spatial resolution in comparison to the Wollaston probe. In this study, a nano thermal probe was used to examine the phase separation of the polymer blended formulations.

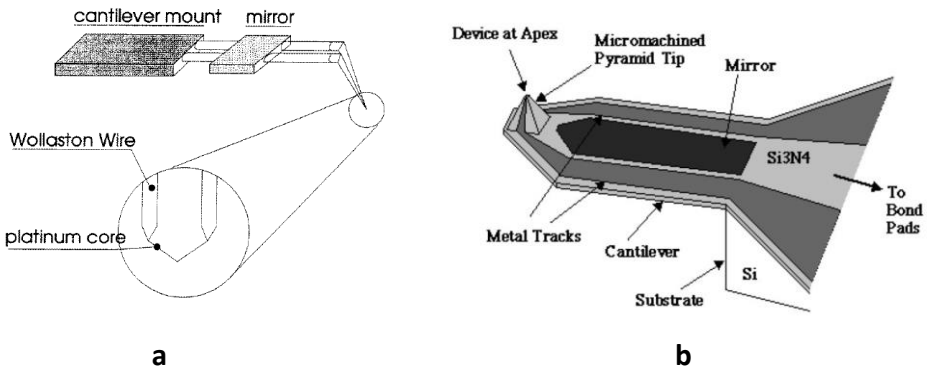

Figure 2.19 Schematic images of microprobe (a) and a nano thermal probe (b), reproduced from reference (105,109)

2.4.11.3 AFM contact mode and LTA operating conditions

A Caliber AFM (Veeco Instruments, Santa Barbara, CA, USA) equipped with a nano thermal analysis probe (Anasys Instruments, Santa Ba, CA, USA) with a spring constant of 0.5−3 $N \cdot m^{-1}$ was used to study the submicron morphological details of the cast and spin-coated blend films. The temperature calibration of LTA was performed using polycaprolactone (T_m 60 °C), polyethylene (T_m 130 °C), and polyethylene terephthalate (T_m 238 °C) prior to any sample analysis. Contact mode was used for acquiring the topographical images of the PVP-HPMCAS films, which were prepared by film casting and spin coating. The nano-TA probe was then moved to the point of interest for local thermal analysis. LTA was performed at 5 points for each acquired topographic image. All experiments were carried out at a heating rate of 10 $°C \cdot s^{-1}$.

2.4.12 Solid state nuclear magnetic resonance spectroscopy (ss-NMR)

2.4.12.1 Basic principle

Nuclear magnetic resonance (NMR) spectroscopy is a globally used and powerful technique that can determine both physical and chemical properties of material. The NMR principle is based on the resonance of nuclei under the influence of an external magnetic field (111, 112). Nuclei that have a sum of proton and neutron as an odd number are NMR active nuclei, including ^{1}H, ^{13}C, ^{15}N and ^{19}F (113). These isotopes demonstrate a half-integer spin (1/2, 3/2 and 5/2). They are on an equal energy level in the absence of the magnetic field. Under an external magnetic field, the spin splits into two different energy levels, whether the spin is aligned with or against the magnetic field; each level is given a magnetic quantum number (m), as shown in **Figure 2.20**. The low energy state always

contains a higher number of nuclei than the high energy state. Thus, it is possible to excite the lower energy nuclei to the higher energy level by applying radiofrequency pulses. After these nuclei are excited to the high energy level, they undergo relaxation processes by releasing energy and returning to the low energy level (112, 114). The time that it takes to return to equilibrium is called relaxation time.

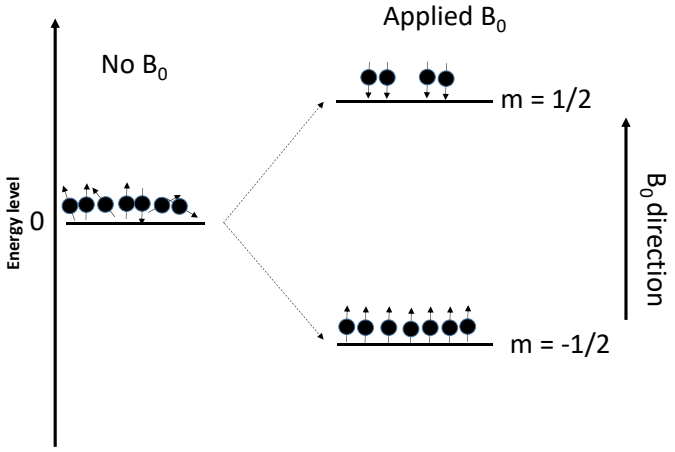

Figure 2.20 Energy levels of nuclei split into two different states after applying an external magnetic field.

In real atoms, the proton is surrounded by an electron cloud. The external magnetic field (B_0) influences the circulation of electrons, which causes the production of local magnetic fields (B_i) that oppose the external one. The proton with high electron density (electron donating group) has the shielding effect, while the proton locates near electron withdrawing group are less shielded (112, 114). The environment of atoms in the molecules plays an important role, and it affects the resonant frequency. Consequently, atoms in molecules demonstrate a different resonance frequency associated with their neighbour atoms. The NMR spectrum is reported in a chemical shift scale obtained from comparing the sample frequency to the standard frequency. Tetramethylsilane is commonly used as a standard in NMR experiments.

In the solution state, molecules move freely in various directions, resulting in the anisotropy being averaged to zero by the tumbling motions of the molecules. In contrast, solid materials contain molecules which are tightly packed. Consequently, they have limited mobility. Thus, the anisotropic effect in the solid sample is inevitable, resulting in peak broadening and decreased resolution (88, 115). The development of magic spin angle (MAS) results in an averaging out of the anisotropic effect by fast spinning the specimen at 54.74° with respect to the applied magnetic field. Spectral resolution can also be enhanced with cross polarisation (CP) experiments by improving the signal-to-noise ratio.

The combination of MAS and CP allows ss-NMR to be a robust approach to characterise solid state samples (88, 115-117).

Solid-state NMR spectroscopy is a powerful tool to characterise APIs and solid dispersions. The CP-MAS spectrum can be used to identify polymorphism and to investigate the interactions between drugs and polymers (82, 116, 118). Furthermore, solid-state NMR relaxometry is frequently applied to the study of small-scale phase separation in polymer blends (119). It is a high-resolution method in which its detection limit is beyond microscopic and thermal techniques (MTDSC). The heterogeneity of the blends is determined by measuring proton relaxation times, often referred to as longitudinal relaxation time in the laboratory frame (T_1) and longitudinal relaxation in the rotating time frame ($T_{1\rho}$). T_1 processes occur via dipole-dipole interactions and are influenced by molecular mobility, while $T_{1\rho}$ is sensitive to slower motions of the polymer chain such as polymer backbone mobility (117, 120). By combining these two relaxation times, one can estimate the upper and lower limit of phase separation down to the Å range (119, 121).

2.4.12.2 ss-NMR operating conditions

The proton spin−lattice relaxation time in the laboratory frame, T_1, and in the rotating frame, $T_{1\rho}$ were measured on a Bruker Mq- 20 spectrometer (Bruker BioSpin, Rheinstetten, Germany) (19.95 MHz) with a proton 90° pulse-length of 2.85 μs. T_1 was measured using the saturation-recovery pulse sequence (recycle delay-90°-τ-90°-acquisition) for the slowly relaxing pure drug and an inversion recovery sequence for the faster relaxing samples. The relaxation $T_{1\rho}$ was measured using the standard sequence (recycle delay-90°-spin lock-acquisition) with a spin-lock field of about 45 kHz. The ss-NMR experiments were conducted by Dr. Li Ying Wang and Prof. Huiru Tang from the Wuhan Institute of Physics and Mathematics, China.

2.6 *In vitro* dissolution study

Dissolution is a drug released test from solid or semisolid formulations to the medium which performs according to the official pharmacopoeia (56). The dissolution data is a very important piece of information for pharmaceutical products in term of both quality control (QC) and research and development (R&D). In the QC, the dissolution tests are performed to ensure batch consistency and that the products are manufactured according to their specifications. The deviations of the dissolutions test may reflect problems in the manufacturing process (122). This alerts the pharmaceutical industries to deal with the issue before products are released to the markets. From an R&D perspective, the dissolution

test provides the estimation of the drug release behavior, which potentially correlate to the *in vivo* drug release (122).

2.6.1 Preparation of dissolution media

In this study, the British Pharmacopoeia dissolution media pH 1.2 was used. To prepare this media, 250 ml of 0.2 M NaCl solution was added to 425 ml of 0.2 M hydrochloric acid and diluted to 1000 ml with distilled water. These acidic dissolution media were prepared according to the official procedure stated in the British Pharmacopoeia (56).

2.6.2 *In vitro* dissolution operating conditions

Drug release experiments were performed using the British Pharmacopeia paddle method by an apparatus II (Copley CIS 8000, Copley Scientific Ltd., Nottingham, U.K.). The experiments were performed at 37°C±0.5°C with a paddle speed rotation of 50 rpm. The pH 1.2 British Pharmacopoeia dissolution media were used. In the FF dissolution tests, 0.5% sodium lauryl sulphate reagent grade (purity >97%) (Fisher Scientific, Loughborough, UK) was added to the dissolution media as a surfactant. The media was sampled at times of 1, 3, 5, 7, 10, 20, 30, 60 and 120 mins and filtered through an 0.45 µm membrane (Minisart Sartorius, Goettingen, Germany). As all dissolution testing was performed under sink conditions, no recrystallization of the model drug as nanocrystals was expected to be formed after release from the formulation; therefore, the filtration method for treating the dissolution samples was appropriate. The drug concentration was measured by ultraviolet-visible spectroscopy at different time intervals.

2.6.3 Ultraviolet-visible spectroscopy (UV-VIS) for measurement of drug release.

2.6.3.1 Basic principle

Molecules absorb electromagnetic energy from ultraviolet or visible light, resulting in the electrons transitioning from a ground state to an excited state. The UV-VIS can be used to analyse organic compounds that contain conjugated bonds in their molecular structure. It is feasible for both qualitative and quantitative measurements (123). The UV-VIS quantitative measure obeys the Beer-Lambert law which states that the concentration and path length is proportion to the absorbance (56). The Beer-Lambert equation can be described as;

$$A = \varepsilon lc \qquad \text{.....(2.6)}$$

where *A* is the absorbance, $\mathcal{E}$ is the absorptivity coefficient; *l* is the path length of the cuvette and *c* is the concentration of drug in the media. This rule is only valid in the dilute medium where drug concentrations have a linear relation with UV absorbance (56).

APIs are organic compounds that contain conjugated bonds in their structure. Hence, UV-VIS can be used to quantify the concentration. FF and PCM demonstrate their maximum UV absorption wavelength at 298 nm and 245 nm, respectively. The calibration curves in this study were constructed by plotting different drug concentration against the UV absorbance at the λ_{max} of the model drugs, to obtain the absorptivity coefficient. The linearity of the plots with R^2 values greater than 0.999 has been achieved for both FF and PCM calibration curves.

2.7 Kinetic models

2.7.1 Kinetics models of drug release

2.7.1.1 Power law

Korsmeyer-Peppas model, also known as power law model, is a semi-empirical model (124). It offers the advantage of discriminating between the two general mechanisms of drug release, which are Fick's diffusion and case II transport (125). The equation is expressed as

$$\frac{M_t}{M_\infty} = kt^n \quad \text{.....(2.7)}$$

where M_t/M_∞ is the fraction of drug released at time *t* in relation to complete drug release at time infinity; *k* is a constant that reflects the geometric and structural characteristics of the device, and *n* is the diffusion exponential that provides indications of the mechanism of drug release. The electrospun fibres used in this study are cylindrical in shape. The exponential value, n, which is obtained from fitting release data to **equation 2.7**, can identify the mechanism of drug release as Fickian diffusion, anomalous transport, or Case-II transport (zero order diffusion). In the case where the dominating mechanism of release is Fickian diffusion for a cylindrical geometry, the *n* value is equal to 0.45; whereas for zero order diffusion, the *n* value is equal to 0.89 (126). Any value between 0.45 and 0.89 is regarded as anomalous transport in which the mechanism of drug release is a combination of both Fickian diffusion and Case-II transport. In the literature, it has been recognised that the most valid prediction using power law should be performed only on the first 60% drug release data due to the assumption of single dimensional release in cylinders (126).

The power law model has been used to fit with various kinds of formulations, including electrospun fibres (98, 99, 127, 128). A mechanism of drug release from both conventional

and core-shell structure electrospun fibres has been successfully elucidated. Shen et. al fitted the diclofenac release from Eudragit L 100-55 fibres in pH 6.8 media with the power law equation. The authors found that their electrospun fibres with low drug content 10-20% exhibited an anomalous transport while with high drug loading >30%, the release behaviour was dominated by Fickian diffusion (128). Yu et al. and Jiang et al. prepared core-shell electrospun fibres to form EC/PVP and zein/PVP respectively. The drug released profiles of these formulations were fitted to the power law model. Both studies showed that Fickian diffusion dominated the drug release in the core-shell fibrous formulations because the n values of each formulation were less than 0.45 (98, 99). In this study, the PCM released profiles from the PVP/HPMCAS blended electrospun formulations were fitted to the power law model in order to investigate the mechanism of drug release (chapter 6).

2.7.1.2 Biphasic released model

The biphasic released model developed in this study was based on the assumption that the polymer blend fibre mats contain two populations of immiscible polymer domains, which have independent drug release rates. For each population, the fraction of drug release at time t can be described by first-order mass transfer and expressed by **equation 2.9** in which M_t is the mass remaining at time *t*, *k* is the constant, and M_∞ is the total drug release at infinity.

$$M_t = M_\infty e^{-tk} \quad \text{..... (2.8)}$$

For the polymer blend electrospun fibres, two populations of domains, PVP-rich and HPMCAS-rich, were assumed to independently release the drug at different rates. The mass transfer, in this case, can be expressed using **equation 2.8**, in which k_a and k_b are exponents of the PVP-rich and HPMCAS-rich phases, respectively. This model was used to investigate the PCM released profiles in which the PVP-HPMCAS blended electrospun formulations were fitted to the biphasic released model in order to investigate the mechanism of drug release (Chapter 6). Note that this model assumes equal distribution of the drug in the two phases.

$$\frac{M_t}{M_\infty} = \left(e^{-tk_a} + e^{-tk_b}\right) \text{.....(2.9)}$$

2.7.1.3 Statistical analysis for models selection

Akaike statistical analysis (AIC) is a statistical method for the model selecting approach. It offers an estimation of model relative quality in comparison to other models (129). Particularly, AIC was used to compare the effectiveness of the mathematical models. This

method combines goodness-of-fit with a penalty score for extra variables. Adding more terms to model equations usually provides a better fit (lower R^2), but not necessarily a better description of the underlying processes. In this study, the power law (**equation 2.7**) and the biphasic released model (**equation 2.9**) were used to investigate the mechanism of PCM released from PVP/HPMCAS fibre mats by fitting to the drug released data. These models have different numbers of variables and their ability to describe the dissolution process cannot be judged objectively on the basis of R^2 values alone. Therefore, AIC with corrected finite sample size (AICc) was used to assess the quality of the power law and biphasic released model. The lower AICc values indicate more accurate models. The AIC and AICc can be expressed as;

$$AIC = u.\ln(SSE/2)+(2L+1) \quad \text{(2.10)}$$

$$AICc = AIC + (2(L+2)(L+3)/u-L-3) \quad \text{(2.11)}$$

where SSE is the sum of error residual from data fitting which is the difference between experimental data and predictive values, u is the number of the data point, and L is the number of the variables in the model.

2.7.2 Mathematic models for study kinetics of moisture sorption

In this study, three mathematical models, Guggenheim-Anderson-de Boer (GAB) model, Peleg model, and double exponential (DE) model, were used to fit with moisture sorption data obtained from DVS of electrospun fibres and cast films formulations. The purpose of the mathematical models fitting is to investigate the moisture sorption mechanism of the formulations.

The semi-empirical GAB model is a versatile model for fitting sorption isotherm data. It is a developed version of Brunauer-Emmett-Teller's equation respect to physical adsorption background theory (74, 75). The GAB model can explain sorption behaviour in a wide range of water activity from 0-0.9 and it is also recommended by the European Cooperation in Science and Technology (COST) as an equation for describing sorption behaviour in foods (75). The GAB model is expressed as

$$M = \frac{M_0 C_G K a_w}{(1-Ka_w)(1-Ka_w+CKa_w)} \quad \text{(2.12)}$$

where M is the moisture content, a_w is the water activity which is equal to the relative humidity at the equilibrium state, M_0 is the monolayer moisture content, C_G is Guggenheim

constant and *K* is the compensating constant for multilayer moisture adsorption. The M_0, C_G, and *K* were obtained from the data fitting. In this study, the equilibrium moisture contents from 10% RH to 90 RH% of the electrospun fibres were fitted with the GAB model.

The moisture uptake of amorphous materials in foods and pharmaceutics can be described by using Peleg and DE model (69) at a fixed relative humidity. The Peleg model is an empirical model purely derived from/based on mathematics without the support of physics theory. It is developed to fit with moisture sorption and frequently used to describe sorption behaviour in agriculture and foods (130). The Peleg model has been used to explain the hydration process of different materials, following the case II diffusion in which the waters rapidly accumulate at the surface of the materials in the adsorption stage **(**40, 131**)**. Then, the boundary of the water outer layer is gradually absorbed into the interior of the materials. The Peleg model can be expressed as

$$M_t = M_0 + \frac{t}{A_1 + A_2.t} \quad \text{.....(2.13)}$$

where M_t is the moisture content at time *t*, M_0 is the initial moisture content, A_1 is the Peleg rate constant, and A_2 is the Peleg capacity constant.

The moisture uptake behaviour of porous materials such as porous silica and activated carbons is complex. It combines adsorption and absorption in which the adsorption is the dominant process in the porous materials (40). The dynamic of this process can be described by using DE model.

$$\frac{M_t}{M_e} = A_1\left(1 - e^{-(k_1 t)}\right) + (1 - A_1)\left(1 - e^{-(k_2 t)}\right) \quad \text{.....(2.14)}$$

where M_t is the accumulated moisture uptake at time *t*, M_e is the equilibrium moisture content, k_1 and k_2 are adsorption rate constants, and A_1 and (A_1-*1*) are fractional contributions to the difference in adsorption of rate constant k_1 and k_2.

The moisture sorption data of the film casting and electrospun fibrous formulations obtained from DVS including sorption isotherm and isohume mode were averaged (n=3) and fitted to the GAB, Peleg and DE models to describe their moisture uptake behaviour. The data fitting experiments were performed using TableCurve 2D version 5.01 (systat software Inc, San Jose, California, USA).

2.8 References

1. Ling H, Luoma JT, Hilleman D. A review of currently available fenofibrate and fenofibric acid formulations. Cardiology Research. 2013;4(2):47-55.
2. Tziomalos K, Athyros VG. Fenofibrate: a novel formulation (Triglide™) in the treatment of lipid disorders: a review. International Journal of Nanomedicine. 2006;1(2):129-47.
3. Jamzad S, Fassihi R. Role of surfactant and pH on dissolution properties of fenofibrate and glipizide—a technical note. Aaps Pharmscitech. 2006;7(2):E17-E22.
4. Buch P, Holm P, Thomassen JQ, Scherer D, Branscheid R, Kolb U, et al. IVIVC for Fenofibrate Immediate Release Tablets Using Solubility and Permeability as In Vitro Predictors for Pharmacokinetics. Journal of Pharmaceutical sciences. 2010;99(10):4427-36.
5. Law D, Wang W, Schmitt EA, Qiu Y, Krill SL, Fort JJ. Properties of rapidly dissolving eutectic mixtures of poly(ethylene glycol) and fenofibrate: The eutectic microstructure. Journal of Pharmaceutical sciences. 2003;92(3):505-15.
6. Shegokar R, Müller RH. Nanocrystals: Industrially feasible multifunctional formulation technology for poorly soluble actives. International Journal of Pharmaceutics. 2010;399(1–2):129-39.
7. Guichard JP, Levy-Prades Sauron R. A comparison of the bioavailability of standard or micronized formulations of fenofibrate. Current Therapeutic Research. 1993;54(5):610-4.
8. Vogt M, Kunath K, Dressman JB. Dissolution enhancement of fenofibrate by micronization, cogrinding and spray-drying: Comparison with commercial preparations. European Journal of Pharmaceutics and Biopharmaceutics. 2008;68(2):283-8.
9. Zhou D, Zhang GGZ, Law D, Grant DJW, Schmitt EA. Physical stability of amorphous pharmaceuticals: Importance of configurational thermodynamic quantities and molecular mobility. Journal of Pharmaceutical sciences. 2002;91(8):1863-72.
10. Amstad E, Spaepen F, Weitz DA. Crystallization of undercooled liquid fenofibrate. Physical Chemistry Chemical Physics. 2015;17(44):30158-61.
11. Yang Z. Development of methods to predict and enhance the physical stability of hot melt extruded solid dispersion: University of East Anglia; 2013.
12. Watterson S, Hudson S, Svärd M, Rasmuson ÅC. Thermodynamics of fenofibrate and solubility in pure organic solvents. Fluid Phase Equilibria. 2014;367(0):143-50.
13. Di Martino P, Palmieri G, Martelli S. Evidence of a metastable form of fenofibrate. Die Pharmazie. 2000;55(8):625-6.
14. Górniak A, Wojakowska A, Karolewicz B, Pluta J. Phase diagram and dissolution studies of the fenofibrate–acetylsalicylic acid system. Journal of thermal analysis and calorimetry. 2011;104(3):1195-200.
15. Heinz A, Gordon KC, McGoverin CM, Rades T, Strachan CJ. Understanding the solid-state forms of fenofibrate–a spectroscopic and computational study. European Journal of Pharmaceutics and Biopharmaceutics. 2009;71(1):100-8.
16. Balendiran GK, Rath N, Kotheimer A, Miller C, Zeller M, Rath NP. Biomolecular Chemistry of Isopropyl Fibrates. Journal of pharmaceutical sciences. 2012;101(4):1555-69.
17. Larson AM, Polson J, Fontana RJ, Davern TJ, Lalani E, Hynan LS, et al. Acetaminophen-induced acute liver failure: Results of a United States multicenter, prospective study. Hepatology. 2005;42(6):1364-72.
18. Kalantzi L, Reppas C, Dressman JB, Amidon GL, Junginger HE, Midha KK, et al. Biowaiver monographs for immediate release solid oral dosage forms: Acetaminophen (paracetamol). Journal of Pharmaceutical sciences. 2006;95(1):4-14.
19. Joiris E, Martino PD, Berneron C, Guyot-Hermann A-M, Guyot J-C. Compression Behavior of Orthorhombic Paracetamol. Pharmaceutical Research. 1998;15(7):1122-30.
20. Di Martino P, Conflant P, Drache M, Huvenne J-P, Guyot-Hermann A-M. Preparation and physical characterization of forms II and III of paracetamol. Journal of thermal analysis. 1997;48(3):447-58.
21. Baird JA, Van Eerdenbrugh B, Taylor LS. A classification system to assess the crystallization tendency of organic molecules from undercooled melts. Journal of Pharmaceutical sciences. 2010;99(9):3787-806.
22. Martino PD, Palmieri GF, Martelli S. Molecular Mobility of the Paracetamol Amorphous Form. CHEMICAL & PHARMACEUTICAL BULLETIN. 2000;48(8):1105-8.
23. JEF R. Martindale: the extra pharmacopoeia. Pharmaceutical Press, London; 1993.
24. Henry R, Zhang G, Gao Y, Buckner I. Fenofibrate. Acta Crystallographica Section E: Structure Reports Online. 2003;59(5):o699-o700.
25. Yekeler M, Ulusoy U, Hiçyılmaz C. Effect of particle shape and roughness of talc mineral ground by different mills on the wettability and floatability. Powder Technology. 2004;140(1–2):68-78.
26. Rayner J. The crystal structure of talc. Clays and Clay Minerals. 1973;21:103-14.
27. Haubruge HG, Daussin R, Jonas AM, Legras R, Wittmann JC, Lotz B. Epitaxial Nucleation of Poly(ethylene terephthalate) by Talc: Structure at the Lattice and Lamellar Scales. Macromolecules. 2003;36(12):4452-6.
28. Rowe RC, Sheskey PJ, Quinn ME. Handbook of pharmaceutical excipients: Pharmaceutical press; 2009.
29. Kolter K, Karl M, Gryczke A, Ludwigshafen am Rhein B. Hot-melt extrusion with BASF pharma polymers: extrusion compendium: BASF; 2012.
30. PVP and more ... LUVITEC®, LUVICROSS® and COLLACRAL® VAL Versatile specialty polymers for technical applications.

31. Karavas E, Ktistis G, Xenakis A, Georgarakis E. Effect of hydrogen bonding interactions on the release mechanism of felodipine from nanodispersions with polyvinylpyrrolidone. European Journal of Pharmaceutics and Biopharmaceutics. 2006;63(2):103-14.
32. Shi Y, Wei Z, Zhao H, Liu T, Dong A, Zhang J. Electrospinning of Ibuprofen-Loaded Composite Nanofibers for Improving the Performances of Transdermal Patches. Journal of Nanoscience and Nanotechnology. 2013;13(6):3855-63.
33. Vasanthavada M, Tong W-QT, Joshi Y, Kislalioglu MS. Phase behavior of amorphous molecular dispersions II: Role of hydrogen bonding in solid solubility and phase separation kinetics. Pharmaceutical research. 2005;22(3):440-8.
34. Yu D-G, Branford-White C, Shen X-X, Zhang X-F, Zhu L-M. Solid Dispersions of Ketoprofen in Drug-Loaded Electrospun Nanofibers. Journal of Dispersion Science and Technology. 2010;31(7):902-8.
35. Yu D-G, Shen X-X, Branford-White C, White K, Zhu L-M, Bligh SA. Oral fast-dissolving drug delivery membranes prepared from electrospun polyvinylpyrrolidone ultrafine fibers. Nanotechnology. 2009;20(5):055104.
36. Chan SY. The Development of PVP-based Solid Dispersions using Hot Melt Extrusion for the Preparation of Immediate Release Formulations. Norwich: University of East Anglia; 2013.
37. De Vrieze S, Van Camp T, Nelvig A, Hagström B, Westbroek P, De Clerck K. The effect of temperature and humidity on electrospinning. Journal of materials science. 2009;44(5):1357-62.
38. Marsac PJ, Rumondor ACF, Nivens DE, Kestur US, Stanciu L, Taylor LS. Effect of temperature and moisture on the miscibility of amorphous dispersions of felodipine and poly(vinyl pyrrolidone). Journal of Pharmaceutical sciences. 2010;99(1):169-85.
39. Bley O, Siepmann J, Bodmeier R. Characterization of moisture-protective polymer coatings using differential scanning calorimetry and dynamic vapor sorption. Journal of Pharmaceutical sciences. 2009;98(2):651-64.
40. Qi S, Gryczke A, Belton P, Craig DQM. Characterisation of solid dispersions of paracetamol and EUDRAGIT® E prepared by hot-melt extrusion using thermal, microthermal and spectroscopic analysis. International Journal of Pharmaceutics. 2008;354(1–2):158-67.
41. Joshi M. Role of Eudragit in targeted drug delivery. Int J Curr Pharm Res. 2013;5(2):58-62.
42. Nikam VK, Kotade KB, Gaware VM, Dhamak R, Somwanshi SB, Khadse AN. Eudragit a versatile polymer: a review. Pharmacol online. 2011;1(1):152-64.
43. Verreck G, Decorte A, Li H, Tomasko D, Arien A, Peeters J, et al. The effect of pressurized carbon dioxide as a plasticizer and foaming agent on the hot melt extrusion process and extrudate properties of pharmaceutical polymers. The Journal of Supercritical Fluids. 2006;38(3):383-91.
44. Jung J-Y, Yoo SD, Lee S-H, Kim K-H, Yoon D-S, Lee K-H. Enhanced solubility and dissolution rate of itraconazole by a solid dispersion technique. International Journal of Pharmaceutics. 1999;187(2):209-18.
45. Liu H, Wang P, Zhang X, Shen F, Gogos CG. Effects of extrusion process parameters on the dissolution behavior of indomethacin in Eudragit® E PO solid dispersions. International Journal of Pharmaceutics. 2010;383(1–2):161-9.
46. Nagy ZK, Balogh A, Drávavölgyi G, Ferguson J, Pataki H, Vajna B, et al. Solvent-free melt electrospinning for preparation of fast dissolving drug delivery system and comparison with solvent-based electrospun and melt extruded systems. Journal of Pharmaceutical sciences. 2013;102(2):508-17.
47. Sóti PL, Bocz K, Pataki H, Eke Z, Farkas A, Verreck G, et al. Comparison of spray drying, electroblowing and electrospinning for preparation of Eudragit E and itraconazole solid dispersions. International Journal of Pharmaceutics. 2015;494(1):23-30.
48. Shamma RN, Basha M. Soluplus®: A novel polymeric solubilizer for optimization of Carvedilol solid dispersions: Formulation design and effect of method of preparation. Powder Technology. 2013;237:406-14.
49. Alshahrani SM, Lu W, Park J-B, Morott JT, Alsulays BB, Majumdar S, et al. Stability-enhanced Hot-melt Extruded Amorphous Solid Dispersions via Combinations of Soluplus® and HPMCAS-HF. AAPS PharmSciTech. 2015;16(4):824-34.
50. Hardung H, Djuric D, Ali S. Combining HME & solubilization: Soluplus®—the solid solution. Drug Deliv Technol. 2010;10(3):20-7.
51. Nagy ZK, Balogh A, Vajna B, Farkas A, Patyi G, Kramarics Á, et al. Comparison of electrospun and extruded soluplus®-based solid dosage forms of improved dissolution. Journal of Pharmaceutical sciences. 2012;101(1):322-32.
52. Fukasawa M, Obara S, eacute. Molecular Weight Determination of Hypromellose Acetate Succinate (HPMCAS) Using Size Exclusion Chromatography with a Multi-Angle Laser Light Scattering Detector. Chemical and Pharmaceutical Bulletin. 2004;52(11):1391-3.
53. Rumondor ACF, Stanford LA, Taylor LS. Effects of Polymer Type and Storage Relative Humidity on the Kinetics of Felodipine Crystallization from Amorphous Solid Dispersions. Pharmaceutical Research. 2009;26(12):2599-606.
54. Tanno F, Nishiyama Y, Kokubo H, Obara S. Evaluation of Hypromellose Acetate Succinate (HPMCAS) as a Carrier in Solid Dispersions. Drug Development and Industrial Pharmacy. 2004;30(1):9-17.
55. Al-Obaidi H, Buckton G. Evaluation of Griseofulvin Binary and Ternary Solid Dispersions with HPMCAS. AAPS PharmSciTech. 2009;10(4):1172-7.
56. COMMISSION. BP. *British Pharmacopoeia* London: TSO; 2016.
57. The Japanese pharmacopoeia: Thirteenth edition. Tokyo : Society of Japanese Pharmacopoeia : Distributed by Yakuji Nippo, 1996.; 1996.

58. Ghosh I, Snyder J, Vippagunta R, Alvine M, Vakil R, Tong W-Q, et al. Comparison of HPMC based polymers performance as carriers for manufacture of solid dispersions using the melt extruder. International Journal of Pharmaceutics. 2011;419(1–2):12-9.
59. Konno H, Handa T, Alonzo DE, Taylor LS. Effect of polymer type on the dissolution profile of amorphous solid dispersions containing felodipine. European Journal of Pharmaceutics and Biopharmaceutics. 2008;70(2):493-9.
60. Brewster ME, Verreck G, Chun I, Rosenblatt J, Mensch J, Van Dijck A, et al. The use of polymer-based electrospun nanofibers containing amorphous drug dispersions for the delivery of poorly water-soluble pharmaceuticals. Die Pharmazie - An International Journal of Pharmaceutical Sciences. 2004;59(5):387-91.
61. Clas S-D, Dalton CR, Hancock BC. Differential scanning calorimetry: applications in drug development. Pharmaceutical Science & Technology Today. 1999;2(8):311-20.
62. Craig DQ, Reading M. Thermal analysis of pharmaceuticals: CRC press; 2006.
63. Taylor LS, Zografi G. Sugar–polymer hydrogen bond interactions in lyophilized amorphous mixtures. Journal of Pharmaceutical sciences. 1998;87(12):1615-21.
64. Gill PS, Sauerbrunn SR, Reading M. Modulated differential scanning calorimetry. Journal of Thermal Analysis. 1993;40(3):931-9.
65. Coleman NJ, Craig DQM. Modulated temperature differential scanning calorimetry: A novel approach to pharmaceutical thermal analysis. International Journal of Pharmaceutics. 1996;135(1–2):13-29.
66. Royall PG, Craig DQM, Doherty C. Characterisation of moisture uptake effects on the glass transitional behaviour of an amorphous drug using modulated temperature DSC. International Journal of Pharmaceutics. 1999;192(1):39-46.
67. Salonen J, Laitinen L, Kaukonen AM, Tuura J, Björkqvist M, Heikkilä T, et al. Mesoporous silicon microparticles for oral drug delivery: Loading and release of five model drugs. Journal of Controlled Release. 2005;108(2–3):362-74.
68. Sheth AR, Zhou D, Muller FX, Grant DJW. Dehydration kinetics of piroxicam monohydrate and relationship to lattice energy and structure. Journal of Pharmaceutical sciences. 2004;93(12):3013-26.
69. Qi S, Belton P, McAuley W, Codoni D, Darji N. Moisture uptake of polyoxyethylene glycol glycerides used as matrices for drug delivery: kinetic modelling and practical implications. Pharmaceutical research. 2013;30(4):1123-36.
70. Roca E, Guillard V, Guilbert S, Gontard N. Moisture migration in a cereal composite food at high water activity: Effects of initial porosity and fat content. Journal of Cereal Science. 2006;43(2):144-51.
71. Rumondor AC, Marsac PJ, Stanford LA, Taylor LS. Phase behavior of poly (vinylpyrrolidone) containing amorphous solid dispersions in the presence of moisture. Molecular Pharmaceutics. 2009;6(5):1492-505.
72. Hunter NE. A spectroscopic and kinetic investigation into sugar glass. Norwich: University of East Anglia; 2009.
73. Carter BP, Schmidt SJ. Developments in glass transition determination in foods using moisture sorption isotherms. Food Chemistry. 2012;132(4):1693-8.
74. Al-Muhtaseb AH, McMinn WAM, Magee TRA. Moisture Sorption Isotherm Characteristics of Food Products: A Review. Food and Bioproducts Processing. 2002;80(2):118-28.
75. ANDRADE P RD, LEMUS M R, PÉREZ C CE. MODELS OF SORPTION ISOTHERMS FOR FOOD: USES AND LIMITATIONS. Vitae. 2011;18:325-34.
76. Stuart B. Infrared spectroscopy: Wiley Online Library; 2005.
77. Bernstein J. Polymorphism in molecular crystals: Oxford University Press; 2007.
78. Socrates G. Infrared and Raman characteristic group frequencies: tables and charts: John Wiley & Sons; 2004.
79. Griffiths PR, De Haseth JA. Fourier transform infrared spectrometry: John Wiley & Sons; 2007.
80. FT-IR Spectroscopy—Attenuated Total Reflectance (ATR)

2005:[1-4 pp.].
81. Salari A, Young RE. Application of attenuated total reflectance FTIR spectroscopy to the analysis of mixtures of pharmaceutical polymorphs. International Journal of Pharmaceutics. 1998;163(1–2):157-66.
82. Hilfiker R. Polymorphism: in the pharmaceutical industry: John Wiley & Sons; 2006.
83. Chan KLA, Kazarian SG. Fourier Transform Infrared Imaging for High-Throughput Analysis of Pharmaceutical Formulations. Journal of Combinatorial Chemistry. 2005;7(2):185-9.
84. Erukhimovitch V, Pavlov V, Talyshinsky M, Souprun Y, Huleihel M. FTIR microscopy as a method for identification of bacterial and fungal infections. Journal of Pharmaceutical and Biomedical Analysis. 2005;37(5):1105-8.
85. Vogel C, Wessel E, Siesler HW. FT-IR Imaging Spectroscopy of Phase Separation in Blends of Poly(3-hydroxybutyrate) with Poly(l-lactic acid) and Poly(ϵ-caprolactone). Biomacromolecules. 2008;9(2):523-7.
86. Prati S, Joseph E, Sciutto G, Mazzeo R. New Advances in the Application of FTIR Microscopy and Spectroscopy for the Characterization of Artistic Materials. Accounts of Chemical Research. 2010;43(6):792-801.
87. Bhargava R, Levin IW. Fourier transform mid-infrared spectroscopic imaging. Spectrochemical Analysis Using Infrared Multichannel Detectors. 2005:1-24.
88. Byrn SR, Pfeiffer RR, Stowell JG. Solid-state chemistry of drugs: Ssci Inc; 1999.
89. Anwar J, Tarling SE, Barnes P. Polymorphism of sulfathiazole. Journal of Pharmaceutical sciences. 1989;78(4):337-42.
90. Langford JI, Daniel L. Powder diffraction. Reports on Progress in Physics. 1996;59(2):131.

91. Programs CrysAlisPro. Abingdon, UK: Oxford Diffraction Ltd; 2010.
92. Hübschle CB, Sheldrick GM, Dittrich B. ShelXle: a Qt graphical user interface for SHELXL. Journal of applied crystallography. 2011;44(6):1281-4.
93. Sheldrick GM. SHELXT– Integrated space-group and crystal-structure determination. Acta Crystallographica Section A. 2015;71(1):3-8.
94. Dolomanov OV, Bourhis LJ, Gildea RJ, Howard JA, Puschmann H. OLEX2: a complete structure solution, refinement and analysis program. Journal of applied crystallography. 2009;42(2):339-41.
95. Spek AL. Structure validation in chemical crystallography. Acta Crystallographica Section D: Biological Crystallography. 2009;65(2):148-55.
96. Macrae CF, Bruno IJ, Chisholm JA, Edgington PR, McCabe P, Pidcock E, et al. Mercury CSD 2.0– new features for the visualization and investigation of crystal structures. Journal of applied crystallography. 2008;41(2):466-70.
97. Oatley CW, Nixon WC, Pease RFW. Scanning Electron Microscopy. In: Marton L, editor. Advances in Electronics and Electron Physics: Academic Press; 1966. p. 181-247.
98. Jiang Y-N, Mo H-Y, Yu D-G. Electrospun drug-loaded core–sheath PVP/zein nanofibers for biphasic drug release. International Journal of Pharmaceutics. 2012;438(1–2):232-9.
99. Yu D-G, Wang X, Li X-Y, Chian W, Li Y, Liao Y-Z. Electrospun biphasic drug release polyvinylpyrrolidone/ethyl cellulose core/sheath nanofibers. Acta biomaterialia. 2012.
100. Trasi NS, Taylor LS. Effect of polymers on nucleation and crystal growth of amorphous acetaminophen. CrystEngComm. 2012;14(16):5188-97.
101. Fotiadis D, Scheuring S, Müller SA, Engel A, Müller DJ. Imaging and manipulation of biological structures with the AFM. Micron. 2002;33(4):385-97.
102. Jalili N, Laxminarayana K. A review of atomic force microscopy imaging systems: application to molecular metrology and biological sciences. Mechatronics. 2004;14(8):907-45.
103. Bernardes-Filho R, Assis OBGd. Development of an algorithm for tip-related artifacts identification in AFM biological film imaging. Brazilian Archives of Biology and Technology. 2005;48:667-74.
104. Hammiche A, Reading M, Pollock HM, Song M, Hourston DJ. Localized thermal analysis using a miniaturized resistive probe. Review of Scientific Instruments. 1996;67(12):4268-74.
105. Pollock HM, Hammiche A. Micro-thermal analysis: techniques and applications. Journal of Physics D: Applied Physics. 2001;34(9):R23.
106. Reading M, Price DM, Grandy DB, Smith RM, Bozec L, Conroy M, et al., editors. Micro-thermal analysis of polymers: current capabilities and future prospects. Macromolecular Symposia; 2001: Wiley-Blackwell, 111 River Street Hoboken NJ 07030-5774 USA.
107. Harding L, King WP, Dai X, Craig DQM, Reading M. Nanoscale Characterisation and Imaging of Partially Amorphous Materials using Local Thermomechanical Analysis and Heated Tip AFM. Pharmaceutical Research. 2007;24(11):2048-54.
108. Reading M, Price D, Pollock H, Hammiche A, Craig D, Royal P. Thermal analysis for the 21st century. American laboratory. 1998;30:13-7.
109. Zhou L, Xu GQ, Ng HT, Li SFY. Scanning thermal microscope tip-induced chemical reaction on solid organometallic compound thin films. Journal of Vacuum Science & Technology B. 1997;15(6):1871-5.
110. Séverine G, Nathalie T, Philippe G. DC thermal microscopy: study of the thermal exchange between a probe and a sample. Measurement Science and Technology. 1999;10(9):805.
111. Duer MJ. Solid-state NMR spectroscopy : principles and applications: Oxford : Blackwell Science, 2002.; 2002.
112. Lambert JB, Mazzola EP. Nuclear magnetic resonance spectroscopy : an introduction to principles, applications, and experimental methods: Upper Saddle River, N.J. ; London : Prentice Hall, 2004; 2004.
113. Koutcher JA, Burt CT. Principles of nuclear magnetic resonance. Journal of nuclear medicine. 1984;25(1):101-11.
114. Ernst RR, Bodenhausen G, Wokaun A. Principles of nuclear magnetic resonance in one and two dimensions: Clarendon Press Oxford; 1987.
115. Brown SP, Spiess HW. Advanced Solid-State NMR Methods for the Elucidation of Structure and Dynamics of Molecular, Macromolecular, and Supramolecular Systems. Chemical Reviews. 2001;101(12):4125-56.
116. Harris RK. Applications of solid-state NMR to pharmaceutical polymorphism and related matters*. Journal of Pharmacy and Pharmacology. 2007;59(2):225-39.
117. Hawarden LE. Polymer drug dispersions: understanding structure and dynamics. Norwich: university of East Anglia; 2015.
118. Rezende CA, San Gil RAS, Borré LB, Pires JR, Vaiss VS, Resende JALC, et al. Combining Nuclear Magnetic Resonance Spectroscopy and Density Functional Theory Calculations to Characterize Carvedilol Polymorphs. Journal of Pharmaceutical sciences. 2016.
119. Wu R-R, Kao H-M, Chiang JC, Woo EM. Solid-state NMR studies on phase behavior and motional mobility in binary blends of polystyrene and poly(cyclohexyl methacrylate). Polymer. 2002;43(1):171-6.
120. Apperley DC, Forster AH, Fournier R, Harris RK, Hodgkinson P, Lancaster RW, et al. Characterisation of indomethacin and nifedipine using variable-temperature solid-state NMR. Magnetic Resonance in Chemistry. 2005;43(11):881-92.
121. Brettmann B, Bell E, Myerson A, Trout B. Solid-state NMR characterization of high-loading solid solutions of API and excipients formed by electrospinning. Journal of Pharmaceutical Sciences. 2012;101(4):1538-45.
122. Azarmi S, Roa W, Löbenberg R. Current perspectives in dissolution testing of conventional and novel dosage forms. International Journal of Pharmaceutics. 2007;328(1):12-21.

123. Banwell CN, McCash EM, McCash EM. Fundamentals of molecular spectroscopy: London ; New York : McGraw-Hill Book, 1994

4th ed.; 1994.
124. Gao Z. Mathematical modeling of variables involved in dissolution testing. Journal of Pharmaceutical sciences. 2011;100(11):4934-42.
125. Korsmeyer RW, Gurny R, Doelker E, Buri P, Peppas NA. Mechanisms of solute release from porous hydrophilic polymers. International Journal of Pharmaceutics. 1983;15(1):25-35.
126. Ritger PL, Peppas NA. A simple equation for description of solute release I. Fickian and non-Fickian release from non-swellable devices in the form of slabs, spheres, cylinders or discs. Journal of controlled release. 1987;5(1):23-36.
127. Li X, Kanjwal MA, Lin L, Chronakis IS. Electrospun polyvinyl-alcohol nanofibers as oral fast-dissolving delivery system of caffeine and riboflavin. Colloids and Surfaces B: Biointerfaces. 2013;103:182-8.
128. Shen X, Yu D, Zhu L, Branford-White C, White K, Chatterton NP. Electrospun diclofenac sodium loaded Eudragit® L 100-55 nanofibers for colon-targeted drug delivery. International Journal of Pharmaceutics. 2011;408(1–2):200-7.
129. Akaike H. A new look at the statistical model identification. Automatic Control, IEEE Transactions on. 1974;19(6):716-23.
130. Peleg M. An Empirical Model for the Description of Moisture Sorption Curves. Journal of Food Science. 1988;53(4):1216-7.
131. Pinto G, Esin A. Kinetics of the Osmotic Hydration of Chickpeas. Journal of Chemical Education. 2004;81(4):532.

3. Chapter 3 Crystallisation behaviour of amorphous FF: Triggers of crystallisation and polymorphic transformation

3.1 Introduction

Knowledge of the crystallisation behaviour of an amorphous drug is essential for formulating a solid dispersion formulation. FF is in the BCS class II, which requires a formulation approach to overcome its low aqueous solubility. Particle size reduction, including micro and nanocrystals, in lipid dispersion has been used in commercial products to solve this problem (1). Moreover, polymeric based amorphous solid dispersion formulations that improve the oral bioavailability of FF have been reported (2-5). In this study, FF was chosen as the primary model drug to develop the electrospun fibrous solid dispersions (Chapter 5). Therefore, it is essential to understand the crystallisation behaviour of amorphous FF, which will facilitate the investigation of the physical stability of the solid dispersions.

The systematic analysis of the relationship between the physical stability and a range of thermodynamic properties, including molecular mobility, configurational free energy and the entropic barrier to crystallisation of FF, PCM, ritonavir, ABT-229 and sucrose, have been reported by Zhou et. al (6). The study revealed that the molecules that have lower configurational entropies required less molecular mobility to spontaneously crystallise (6). The molecular mobility required for crystallisation is the inverse of the molecular relaxation constant (τ) that calculated at the crystallisation temperature. As an example, amorphous PCM has a low configurational entropy of 43.0 $J.mol^{-1}.K^{-1}$ and a molecular mobility requirement for crystallisation of $1.0x10^{-5}sec^{-1}$. While, amorphous FF has a higher configurational entropy (76.6 $J.mol^{-1}.K^{-1}$) than PCM, which leads to a higher molecular mobility requirement for crystallisation of $72.3x10^{-5}sec^{-1}$ (6). Therefore, amorphous FF demonstrates a lower tendency to crystallise spontaneously than amorphous PCM. Amorphous FF has a higher entropic barrier and high mobility that is required for crystallisation in comparison to PCM. This can possibly be attributed to weak intermolecular bonding (7, 8), which results in the low probability of FF molecules forming stable nuclei (9). However, the presence of external triggers, including scratching the surface or placing an FF seed on the surface of amorphous FF, resulted in an immediate crystallisation (9). In addition, FF has a fragility index (m) equal to 83.4 (6), which is classified as a fragile glass material (m >75) (10, 11). Fragile glass materials tend to exhibit greater changes in molecular mobility with temperature in comparison to strong glass materials (12). The combination of these properties of amorphous FF may lead to a high risk of physical instability in amorphous FF during storage.

This chapter aims to investigate the effect of the availability of an open top surface (OTS) and variations in incubation temperature on the crystallisation behaviour of amorphous FF prepared from the melt cooled method. The homogeneous nucleation of amorphous FF is a slow process (9, 13). This chapter used heterogeneous nucleation by surface disruption to initiate crystallisation of amorphous FF. The mechanism of scratching at the surface of the melt induce nucleation occurs via the heterogeneous nucleation. The stainless spatula that was used to scratch on the melt surface is considered as the impurity which was introduced into the supercooled liquid phase. The nucleation occurs at the site where the spatula was in contact with the supercooled liquid due to the contact angle of the spatula and the supercooled liquid phase aid to reduce Gibb's free energy of the nucleation process as describe in **equation 1.6**. Consequently, the nucleation took place after the spatula scratched the melt. The freshly prepared melt-cooled amorphous FF was scratched by a stainless-steel spatula to initiate the crystallisation. After the crystallisation initiation, the presence of an OTS and incubation temperatures during crystallisation and polymorphic transformation of the material were investigated. The rationale behind selecting these two variables as the primary factors in this chapter was because they can significantly impact the molecular mobility and crystallisation behaviour of amorphous materials (14, 15). This can be used to produce a desirable polymorph by intentionally manipulating the crystallisation conditions during large scale crystallisation of the APIs.

The existence of FF form II was verified in the sample crystallised with OTS and bulk crystallisation using a range of charaterisation techniques. In addition, the single crystal structure of FF form IIa was studied in detail to clarify the confusion related to the FF form IIs in the literature (as discussed in chapter 2). The physical stability of form IIa and the factors that influence the polymorphic conversion to the most stable form I were studied. The characteristic data of metastable FF form II available from the literature are shown in **Table 3.1**.

Table 3.1 Summary of the available data related to FF form II that is reported in the literature.

Available characteristic data of FF form II	**Assignment**	**References**
DSC (T_m at 74°C)	IIa	Di Martino et al. and Heinz et al.(16, 17)
PXRD pattern	IIa	Di Martino et al.(16)
Raman spectrum (ester carbonyl stretching at 1718 cm^{-1})	IIa	Heinz et al.(17)
Single crystal	IIb	Balendiran et al.(18)

3.2 Methodology

3.2.1 Materials

The details of the FF form I powder that was used in this chapter can be found in chapter 2 section 2.2.1.

3.2.2 Preparation of FF crystallisation samples

Approximately 3-5 mg of crystalline FF form I powder were placed on a glass slide and heated on a hot plate at 100 °C until they were completely molten. The glass slide was immediately removed from the hot plate to allow the sample to cool to room temperature. The surface disruption technique, involving the use of a stainless steel spatula to scratch the surface of the amorphous FF, was used to induce crystallisation. After surface scratching, a cover slip was immediately placed on top of the FF to sandwich the drug between the glass slide and the cover slip. These samples are referred to as "bulk crystalline FF samples" or B-FF in this study. The scratched samples that were left to crystallise with an OTS are referred to as "open top surface crystalline FF samples" or OTS-FF in the study. Immediately after the initiation of crystallisation by surface scratching, both sets of the sample were stored at ambient temperature or incubated in an oven at 40, 50, 60 or 70°C for 30 mins, after which the crystallisation was complete. This allowed the investigation of the effect of temperature on the crystallisation process. For B-FF samples, all characterisations were performed after the top cover slip was carefully removed. The stability of the OTS-FF and the B-FF was determined at room temperature by storing the samples for six months in glass vials that were sealed with a plastic cap and examined at one, three and six month intervals.

3.2.3 Characterisation methods

In this chapter, the OTS-FF and the B-FF were characterised by a range of characterisation techniques. OTS-FF was characterized by DSC, MTDSC, ATR-FTIR, PXRD and SCXRD, while B-FF was characterized by ATR-FTIR, PXRD and HS-PLM. The experimental methods for DSC, MTDSC, TGA, ATR-FTIR, SCXRD, PXRD, SEM and HS-PLM are presented in Chapter 2 in sections 2.4.1.2, 2.4.2.2, 2.4.3.2, 2.4.5.2, 2.4.7.2, 2.4.7.4, 2.4.8.2 and 2.4.10.2, respectively. The crystal structure of the FF form IIa was determined according to the procedure stated in section 2.4.7.3.

3.3 Results

3.3.1 Verification of existence of FF IIa

In this chapter, we determined that the availability of an OTS and crystal growth temperatures could influence the formation of FF IIa. The growth temperature of 40°C was observed to be the optimal growth temperature for FF IIa crystals. This was confirmed by the DSC and IR results. The DSC thermogram in **Figure 3.1a** shows that the amorphous FF, which crystallised at 40°C with an OTS (OTS-FF 40°C), had two endothermic melting peaks for FF at 74°C and 80°C. This DSC result indicates that the OTS-FF 40°C contained the FF forms IIa and I, in which the melting point of the metastable form IIa (at 74°C) matched with that in the literature (16, 17). The literature does not report the melting enthalpy of the pure FF form IIa. However, the single crystal structures of forms I and IIa are similar (as will be discussed in the next section). It was expected that FF forms I and IIa would demonstrate similar melting enthalpies. This allows the quantification of the amount of each form from the melting enthalpy values. FF IIa was the majority polymorph in this sample, as seen in the melting enthalpy of 57.9±1.8 J/g in comparison to form I that had a melting enthalpy of 27.9±5.6 J/g. Further evidence of FF IIa is the Raman spectrum that was reported by Heinz et al. (17). The authors showed that FF IIa has a Raman characteristic peak at 1718 cm^{-1}, which was assigned to ester carbonyl stretching (O_3-C_{17}). This functional group is both Raman and IR active (19); thus, it is expected to be observable at similar wavenumbers in the IR spectrum. **Figure 3.1b** shows the IR spectrum of the OTS-FF growth at 40°C. It demonstrates two peaks at 1727 and 1714 cm^{-1} that are the ester carbonyl stretching peaks from the FF forms I and IIa, respectively. It can be noted that the peak at 1714 cm^{-1} has a greater intensity than the other peak. This suggests that the OTS-FF 40°C was a mixture of forms I and IIa, which was dominated by form IIa. This result agrees with the DSC findings (**Figure 3.1a)**.

It is possible to obtain the pure IR spectrum of FF form IIa by subtracting the OTS-FF 40°C from the reference spectrum of the crystalline form I. The FF form I ATR-FTIR spectrum intensity used in this calcualtion was only 40% of the maximum, as the OTS-FF 40°C contained the equvalent of 40% FF form I. This assumption was made from the ratio of forms I and IIa from the DSC melting enthalpy values. The subtracted spectrum is shown in **Figure 3.1b**. There are a few regions in the subtracted spectrum that can be used to distinguish the differences between forms I and IIa, which include the =CH-H stretching of the benzene ring, methyl group stretching, ester carbonyl stretching, aryl ketone stretching and benzene ring stretching. Details of the peak assignment are reported in **Table 3.2**. The methyl stretching region and ester carbonyl stretching (O_3-C_{17}) can be used as indicator regions to distinguish the FF polymorphs in this chapter. It should be noted that

the small peak at 1727 cm^{-1} of the subtracted spectrum can be ignored due to the high molar absorptivity of the form I ester carbonyl at this wavenumber.

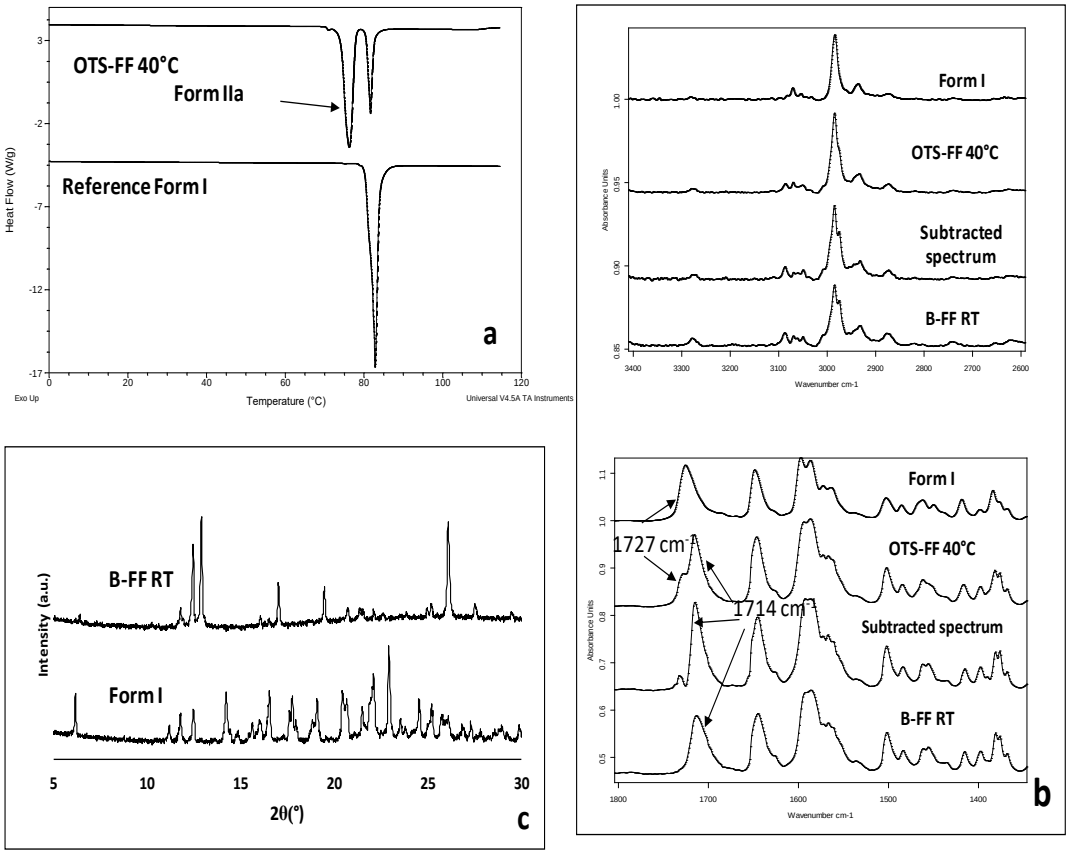

Figure 3.1 Characteristic data of FF IIa including DSC, ATR-FTIR and PXRD. (a) Melting points of OTS-FF 40°C in comparison to the reference form I. (b) ATR-FTIR spectra of reference form I, OTS-FF 40°C, the subtracted spectrum of OTS-FF 40°C and 40% intensity of the reference form I and B-FF RT in different regions, including 3400-1600 and 1800-1300 cm^{-1}. (c) PXRD pattern of B-FF RT in comparison to form I.

The ATR-FTIR spectrum of the B-FF, which crystallised between coverslips at room temperature (B-FF RT), resembles the subtracted spectrum in **Figure 3.1b**, which was expected to be the pure form IIa spectrum. Therefore, we can conclude that the B-FF RT crystallisation leads to a pure form of the FF IIa crystal. This sample was further examined by DSC; however, the DSC preparation for the sample, which has to scratch the crystal from the coverslip, can possibly cause a conversion of the IIa form to the I form (**Figure 3.2**). This demonstrated that mechanical triggers, such as scratching, have significant impacts on the FF polymorphic conversion from polymorph IIa to I. The PXRD pattern of the B-FF RT was different from the reference FF I PXRD (**Figure 3.1c)**. Therefore, the absence of an OTS during amorphous FF crystallisation at room temperature led to the

formation of pure FF IIa. The clarification of the IIa form and II form, which was reported by Balendiran et al. (assigned as form IIb), will be discussed in the next part.

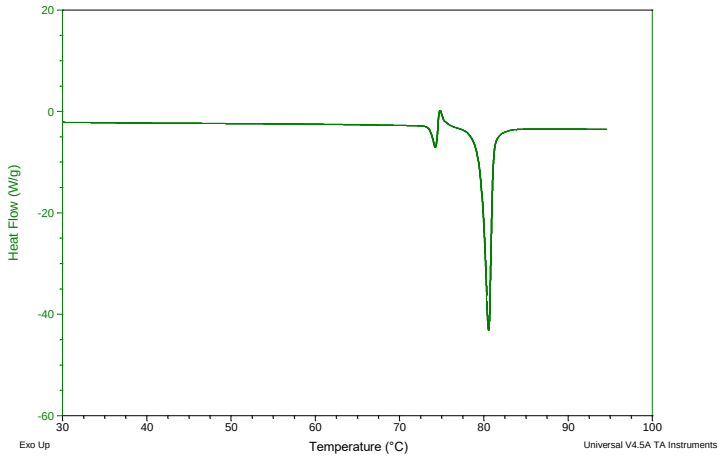

Figure 3.2 DSC of B-FF that was scratched from the coverslip. The form IIa in the B-FF immediately converted to the stable form I after the mechanical trigger of scratching.

ATR-FTIR was used to examine the upper open top surface and lower surface (in contact with the glass substrate) of the OTS-FF RT and OTS-FF 40°C samples. As illustrated in **Figure 3.3a**, the OTS-FF 40°C upper surface shows two ester carbonyl stretching peaks at 1727 and 1714 cm^{-1}, for which the 1714 cm^{-1} peak has a greater intensity than the other peak. This represents the co-existence of forms I and IIa at the OTS site, which was dominated by form IIa. While the lower surface of the crystal shows a single ester carbonyl stretching peak at 1714 cm^{-1}, which is characteristic of the form IIa. This result implies that the form IIa crystals were the only polymorph observed at the interface of the glass substrate site.

On the other hand, the OTS-FF RT showed two ester carbonyl stretching peaks (1727 and 1714 cm^{-1}) at both the upper and lower surface sites (**Figure 3.3b**). At the upper surface site, the intensity of the peak at 1727 cm^{-1} was higher than the other peak at 1714 cm^{-1}. This is an indication that the amount of the crystalline FF form I is greater than the form IIa. However, at the lower surface, it shows that the intensity of the ester carbonyl stretching was inverse to the upper surface. The intensity of the ester carbonyl stretching of form IIa (peak at 1714 cm^{-1}) was much greater than the other carbonyl stretching peaks of form I (at 1727 cm^{-1}). This result indicates that at the interface of the glass substrate site there is a greater amount of form IIa in comparison to that at the OTS site. The presence of an OTS during the crystallisation of amorphous FF can impact the polymorphic form of the drug. FF form I preferably grows at an OTS site while the preferable site for form IIa is in the bulk.

Table 3.2 Assignments of ATR-FTIR peaks of amorphous FF, FF form I and FF form IIa.

Band assignment	**Peak position (cm^{-1})**		
	Amorphous fenofibrate	**FF polymorph I**	**FF polymorph IIa**
=CH-H of benzene ring	3070	3071,3055,3034	3087,3069,3050
Methyl group stretching	2982,2938	2985,2937	2984,2975,2931
O_3-C_{17} ester carbonyl stretching	1728	1727	1714
O_1-C_7 Aryl ketone carbonyl stretching	1654	1650	1645
-CH=CH- benzene stretching	1505,1466	1520,1463	1518,1483
C-O-C of ester	1143	1143	1144
Aryl ether	1284	1285	1286
Benzene ring in plane deformation vibration	1248,1172,1116, 1014,972	1247,1173,1117, 1014,975	1241,1177,1117, 1013,968
Benzene ring out of plane deformation vibration	852,838,679	860,844,680	858,844,683
Cl_1-C_3 bending	762	765	763

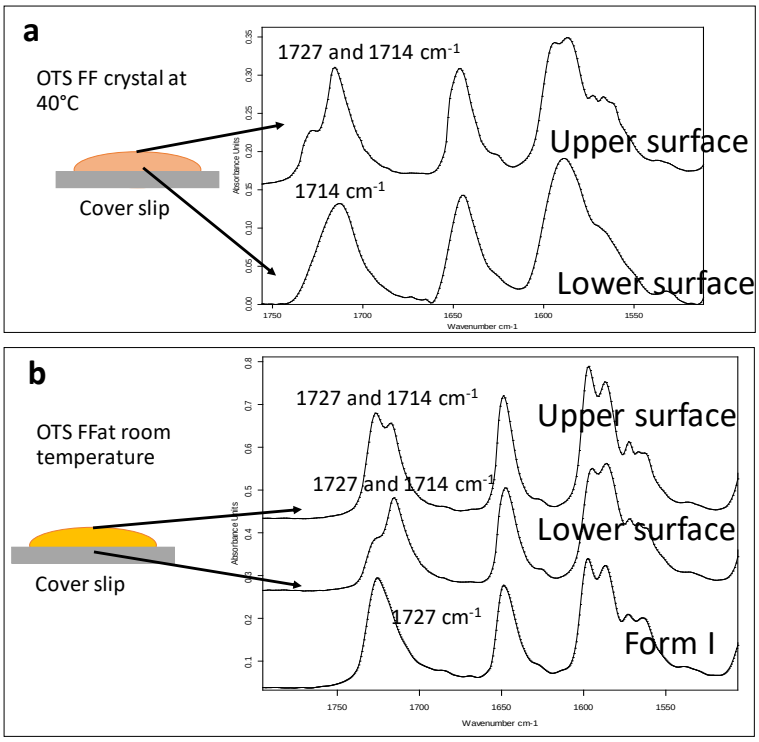

Figure 3.3 Partial ATR-FTIR spectra (1760-1500 cm^{-1}) that were acquired on the upper and lower surfaces of (a) OTS-FF 40°C and (b) OTS-FF RT. The two carbonyl stretching position for the C_{17}-O_3 peaks at 1727 and 1714 cm^{-1} reflect a mixture between FF forms I and IIa, whereas the carbonyl stretching of C_{17}-O_3 peak at 1714 cm^{-1} indicates FF form IIa.

3.3.2 Differentiation of form IIa by single crystal structure analysis

It was important to determine the crystal structure of form IIa to gain a better understanding of the transformation between form IIa and the other FF polymorphs. The crystallographic parameters of form IIa in comparison with the other known forms are shown in **Table 3.3**. The FF molecule can be divided into two main parts: two aromatic rings linked by a keto group and flexible aliphatic tail. An ORTEP drawing of the molecular structure of FF form IIa is shown in **Figure 3.4a**. To compare form IIa to the other reported forms (I and IIb), their molecular structures were overlain as illustrated in **Figure 3.4b**. The conformation of FF in form IIa is largely similar to form I, while the orientation of the alkyl fragment relative to the aromatic rings is markedly different in form IIb. The angles between the planes of the two aromatic rings in forms I and IIa are 48.62(7)°and 48.25(10)° respectively, while it is 53.73° in form IIb.

Table 3.3 Crystallographic parameters of known polymorphic forms of FF

Parameter	Form I[a]	Form IIa	Form IIb[b]
Lattice system	Triclinic	Triclinic	Monoclnic
Space group	*P*-1	*P*-1	$P2_1/n$
a (Å)	8.1325	8.1328(5)	13.619
b (Å)	8.2391	8.7088(6)	7.554
c (Å)	14.399	13.6692(9)	17.88
α (°)	93.978	85.976(6)	90
β (°)	105.748	84.815(5)	92.35
γ (°)	95.854	74.344(6)	90
Cell volume	919.03	927.34(11)	1837.909
Density	1.285	1.292	1.304
Crystal size (mm)	0.55 x 0.50 x 0.44	0.12 x 0.13 x 0.46	0.55 × 0.30 × 0.25
Z	2	2	4
R	0.0418	0.1307	3.55
wR2	0.105	0.1265	0.0897
Temperature (K)	193	140(2)	100
Goodness of fit	1.035	1.023	1.026

[a] Obtained from reference (20) and [b] obtained from reference (18)

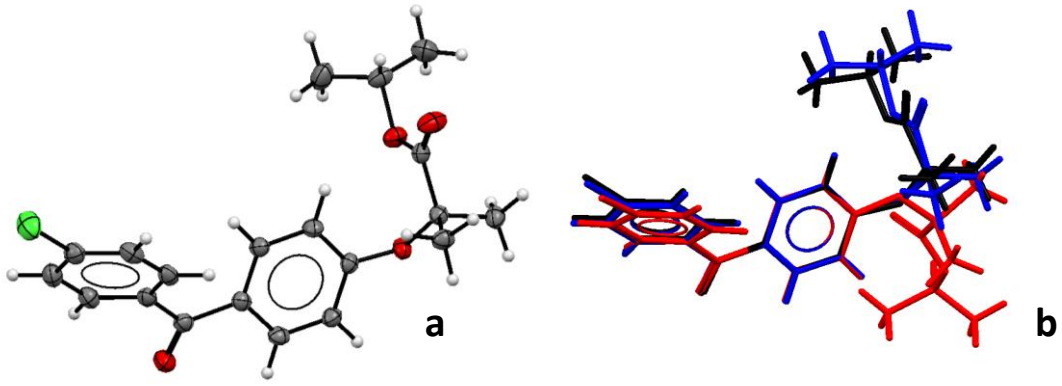

Figure 3.4 (a) ORTEP structure of form IIa; (b) overlay of molecular conformations in FF form I (black), form IIa (blue) and form IIb (red).

Form I, the most stable form, shows two very short intermolecular CH…O interactions between one hydrogen atom from both aromatic rings and the ester carbonyl group. The corresponding CH…O distances, 2.49 Å and 2.61 Å, are more than 0.1 Å shorter than the sum of the atomic van der Waals radii, while the C-H…O angles are 128° and 172°, respectively. These interactions form a layer (**Figure 3.5a**) parallel to (001), which is

supported by another, slightly longer CH…O (ketone) interaction (H…O: 2.62 Å, C-H..O: 156°). The layers are connected to each other through further CH…O interactions, which are formed between isopropyl methyl groups and ketone carbonyl oxygen atoms (2.67 Å, 134°) (**Figure 3.5b**), and offset π-π interactions between parallel chlorobenzene rings at an interplanar distance of 3.5116(6) Å. The interlayer CH…O interactions also facilitate the efficient packing of the isopropyl groups.

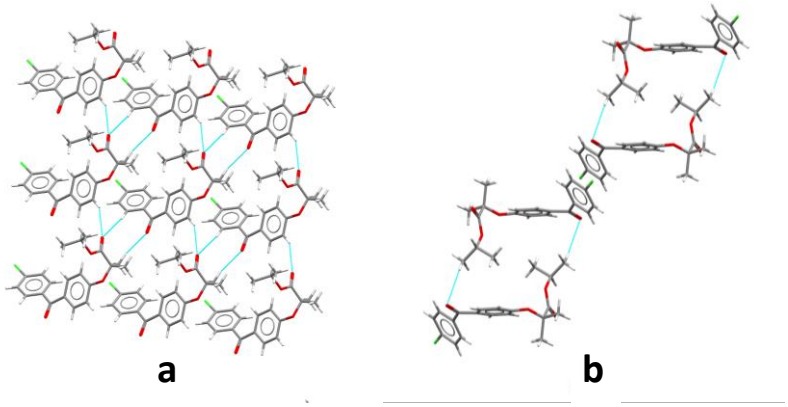

Figure 3.5 Intermolecular interactions in form I: (a) layers formed by CH…O interactions and (b) offset of π-π interactions and CH…O linked dimers that connect the layers.

Pairs of molecules in the unit cell of the polymorph IIa form dimers linked by C-H…O hydrogen bonds between the ester carbonyl group (O_3) and a hydrogen atom of the central benzene ring (H_7) [d(H…O) = 2.662(11) Å, ∠(C-H…O) = 135.2(8)°]. Two of these hydrogen bonds generate a ring motif between the two molecules of the dimer. The large contact surface area between the two molecules suggests that van der Waals interactions play a significant role in stabilising the dimers **(Figure 3.6a**).

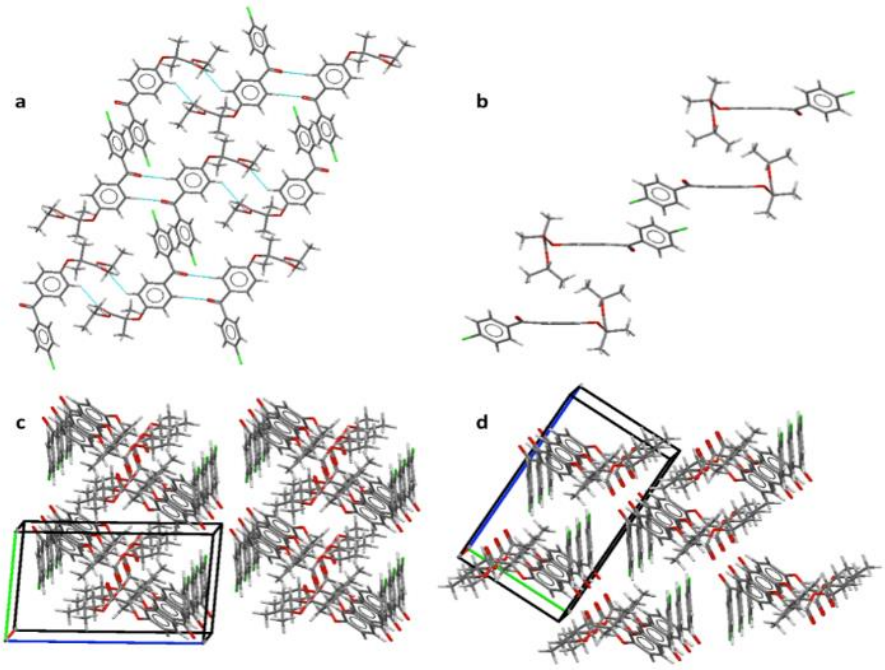

Figure 3.6 (a) Layers formed by CH…O interactions and π-π stacking in form IIa; (b) interactions perpendicular to the layers of form IIa; (c) packing diagram of form IIa; and (d) packing diagram of form I.

Two principal interactions connect adjacent dimers to form layers parallel to the (111) plane: C-H…O hydrogen bonds and π-π interactions. The hydrogen bonds occur between an aromatic hydrogen atom in the central ring (H_5) and the ketone carbonyl group of an adjacent molecule (O1) [d(H…O) = 2.570(17) Å, ∠(C-H..O) = 135.2(8)°] (**Figure 3.7a**). Here again, two of these hydrogen bonds form a ring motif. The offset of the π-π interaction involves the chlorobenzene fragments of two molecules and takes place at an interplanar distance of 3.3029(8) Å between the parallel rings (**Figure 3.7b**). The same stacking interaction was observed in form I with an interplanar distance of 3.5116(6) Å.

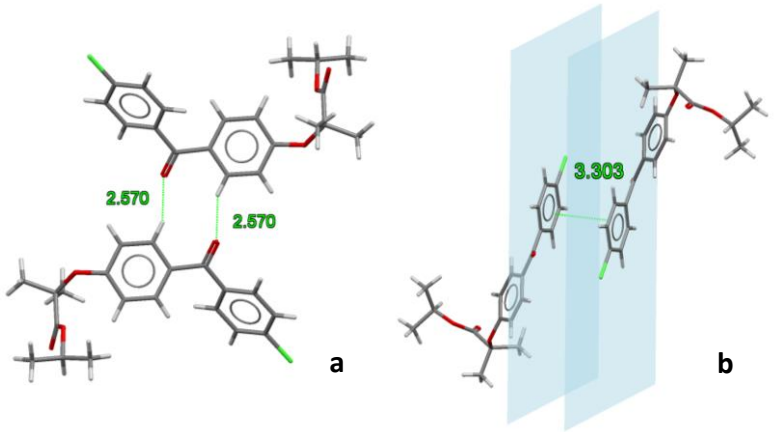

Figure 3.7 (a) Form IIa short interactions and **(b)** form IIa pi-pi interactions.

The most notable interaction between the layers of form IIa involves an ‘embrace’ of the alkyl groups from molecules in neighbouring layers (**Figure 3.6b**). Interestingly, the same

embrace motif is also present in form I, but there it is accompanied by a methyl to ketone C-H…O hydrogen bond. In form IIa the shortest H(methyl)…O(ketone) distance is 3.09 Å, which is much longer than the same contact in form I (2.56 Å). Nevertheless, the relative arrangement of the molecules remains essentially the same in both forms, which suggests that the favourable packing arrangement of the aliphatic groups is more important than the weak CH…O bonds. Combined, the π-π interactions and the alkyl embrace form infinite slabs of molecules (**Figure 3.6b**), which are shared between forms I and IIa, as seen in **Figure 3.5b**. This results in similar overall packing structures for both forms, which can be seen in **Figure 3.6c** and **3.6d**. Therefore, the melting enthalpies of forms I and IIa are expected to be similar. Additionally, the crystalline packing similarity of forms I and IIa may also explain the sensitivity of the FF polymorphic conversion from form I to form IIa by external stimuli, such as mechanical scratching.

The details of the FF IIb packing were discussed by Balendiran et al. (18). Briefly, there are a few short interactions. The carbonyl of the ester group (O_3) forms a bond with the hydrogen from the chlorobenzene ring (H_1) [H…O distance: 2.575 Å; C-H…O angle: 158.25 °]. The carbonyl from the ketone group (O_1) forms a bond CH…O with another hydrogen in the chlorobenzene ring (H_3) [H…O distance: 2.66 Å; C-H…O angle: 167.26°], as can be seen in **Figure 3.8a**. Additionally, form IIb shows the centrosymmetric dimer between the ketone carbonyl (O_1) and the methyl group (H_{20}) [H…O distance: 2.704 Å; C-H…O angle: 175.31°**]**, which is similar to the interaction in forms I and IIa (**Figure 3.8b**). The packing of FF form IIb is illustrated in **Figure 3.8c**. It is remarkably different from the packing for forms I and IIa, as seen in **Figure 3.6c** and **Figure 3.6d**. These results prove the differences between polymorphs IIa and IIb.

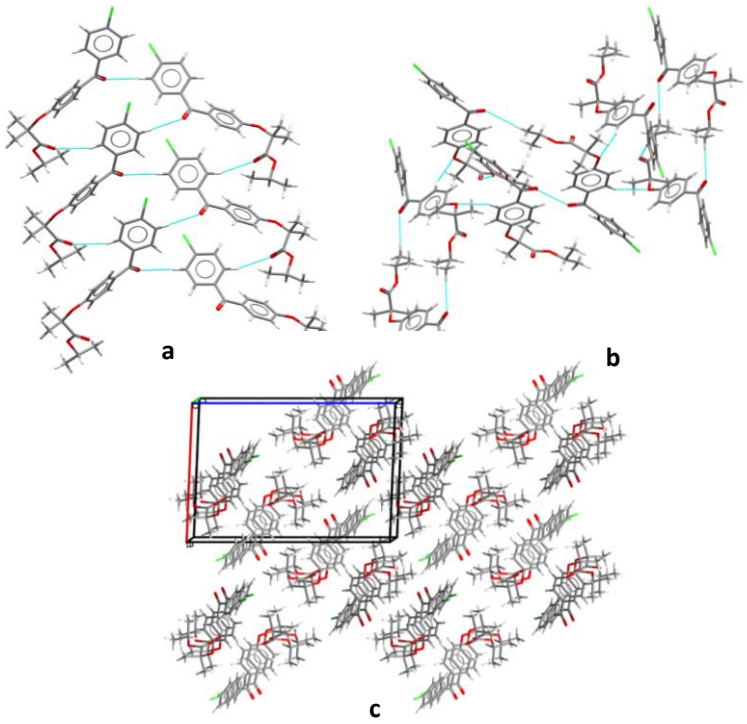

Figure 3.8 Intermolecular CH…O interactions in form IIb (a) forming a tape motif, (b) cross-linking the tapes via dimeric rings similar to those in form I and (c) packing of form IIb.

3.3.3 Effect of crystal growth temperatures on FF crystallisation with OTS

Different growth temperatures were applied during the crystallisation of OTS-FF, and distinctively different visual appearances of the crystal growth were observed. As soon as the crystallisation process was initiated, the OTS-FF samples were immediately stored at room temperature (22°C), 40, 50, 60 and 70°C for 30 minutes, which was a sufficient length of time to allow the complete crystallisation of the FF sample. At room temperature, the continuous growth of fine opaque crystals can be seen underneath the white crystal cluster in the centre where the crystallisation was initiated by mechanical scratching. However, crystal growth at the temperatures of 40, 50 and 60 °C led to the growth of a layer of transparent spherulite crystals beneath the opaque central crystal cluster that was formed first (**Figure 3.9**).

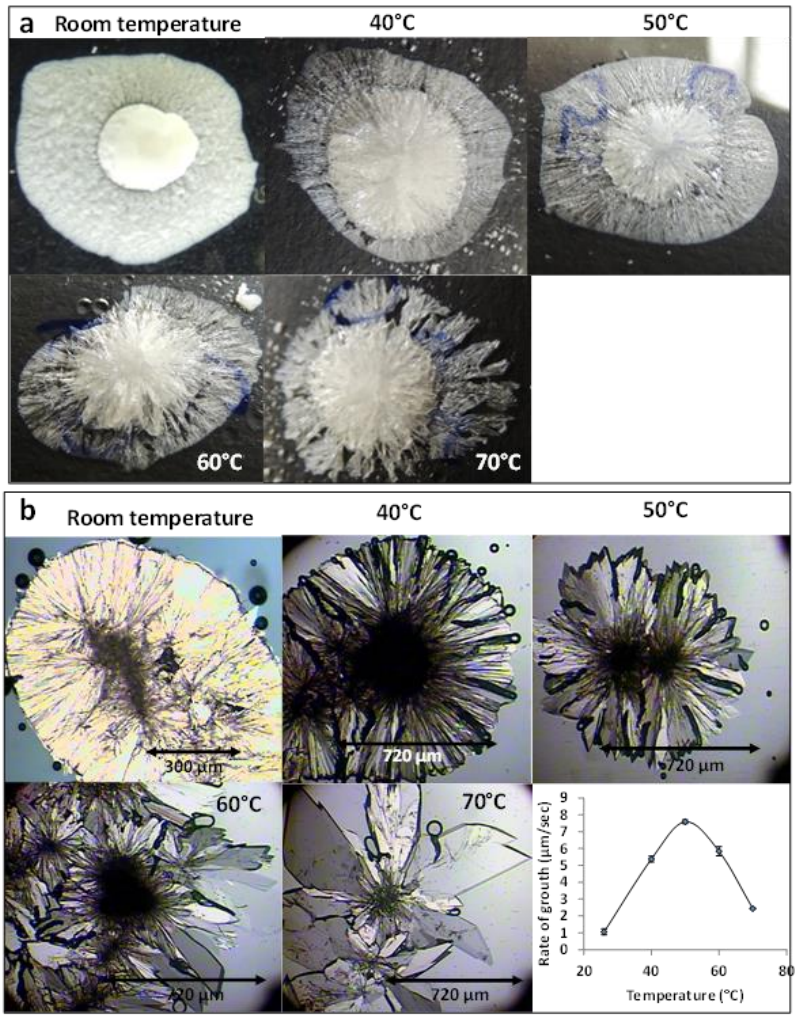

Figure 3.9 (a) Images of OTS-FF growth at different temperatures and (b) PLM images of B-FF growth at different temperatures and the change in crystal growth rate associated with the temperature effect.

The DSC detected two melting transitions at 74 and 80°C in the OTS-FF samples that crystallised at room temperature, 40, 50 and 60°C, which indicates the co-existence of FF forms IIa and I (**Figure 3.10a**). From the melting enthalpy values, one can obtain a semi-quantitative comparison of the amount of form I and form IIa obtained in the samples that were growth at different temperatures (**Figure 3.10b**). At 40 and 50°C a greater amount of form IIa was produced in comparison to form I. For the samples with growth at room temperature and 60 °C, form I was the dominant polymorph with higher melting enthalpies than that of form IIa.

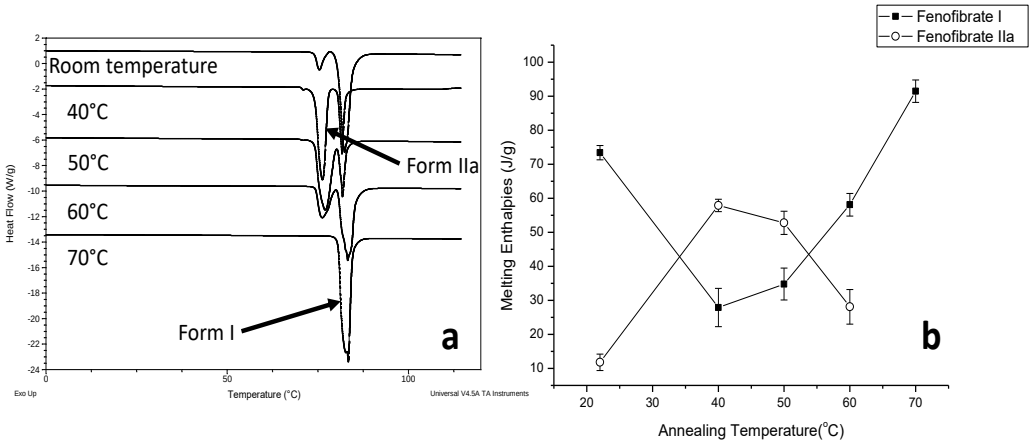

Figure 3.10 (a) DSC thermogram demonstrating melting enthalpies of OTS-FF, which were incubating at different temperatures during their crystallisation, and (b) changes in the melting enthalpies of FF forms I and IIa with incubating temperature.

Two ester carbonyl stretching C_{17}-O_3 peaks at 1714 and 1727 cm^{-1} were observed in the ATR-FTIR spectra of the samples grown at room temperature, 40, 50 and 60°C, which confirmed the co-existence of form I and form IIa (**Figure 3.11a**). The relative peak intensities of these two ester carbonyl peaks reflect the amount of FF form I and form IIa in these samples. The OTS-FF 40 and 50°C demonstrate a higher intensity of the ester carbonyl peak at 1714 cm^{-1} than at 1727 cm^{-1}. This indicates that the OTS-FF 40 and 50°C were dominated by FF form IIa. While the OTS-FF room temperature and 60°C show a greater intensity of ester carbonyl at 1727 cm^{-1} than at 1714 cm^{-1}. This indicates that the OTS-FF RT and 60°C were dominated by FF form I. The ATR-FTIR findings agree with the DSC results. This suggests that 40 and 50°C, with an OTS, are the optimal temperatures for crystal growth of form IIa. The PXRD patterns of the OTS-FF RT and OTS-FF 60°C (**Figure 3.12a**) contain peaks from form I and peaks that match the ones reported by Di Martino and co-workers for their from IIa. This further confirms that the crystals were a mixture of forms I and IIa (16). The PXRD patterns of the OTS-FF crystallised at 40 and 50 °C are clearly not FF form I, but some diffraction peaks are at similar diffraction angles to the B-FF RT, including the diffraction peaks at 12.9, 17.6, 19.5, 26.0 and 27.6° (**Figure 3.12**).

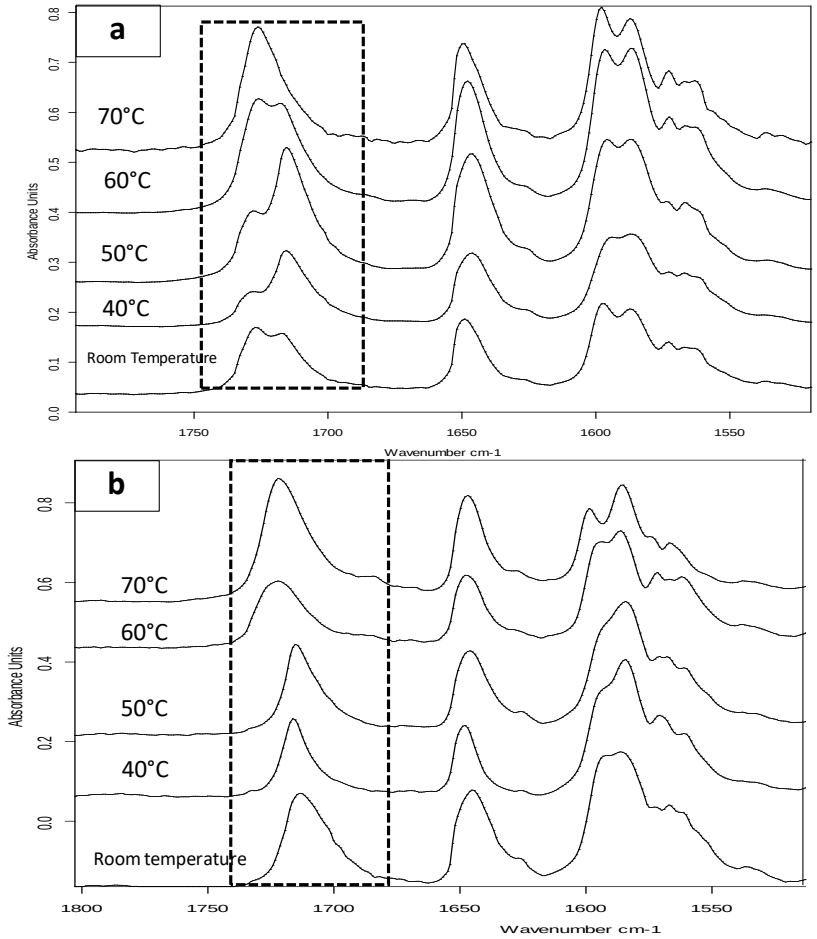

Figure 3.11 Partial ATR-FITR spectra (1800-1500 cm^{-1}) of (a) OTS-FF and (b) B-FF that were crystallised at various growth temperatures (70, 60, 50, 40 °C and room temperature).

As the growth temperature was increased to 70°C, the crystal habits of both the top and bottom layers of the growth gradually changed to blade-like shapes, as seen in **Figure 3.9a**. At 70°C, only form I with a single melting point at 80°C was detected by DSC. The single form I ester carbonyl stretching at 1727 cm^{-1} observed by ATR-FTIR confirms the crystallisation was solely FF form I. The PXRD of the OTS-FF 70°C showed a similar PXRD pattern to the reference FF form I (**Figure 3.12a**).

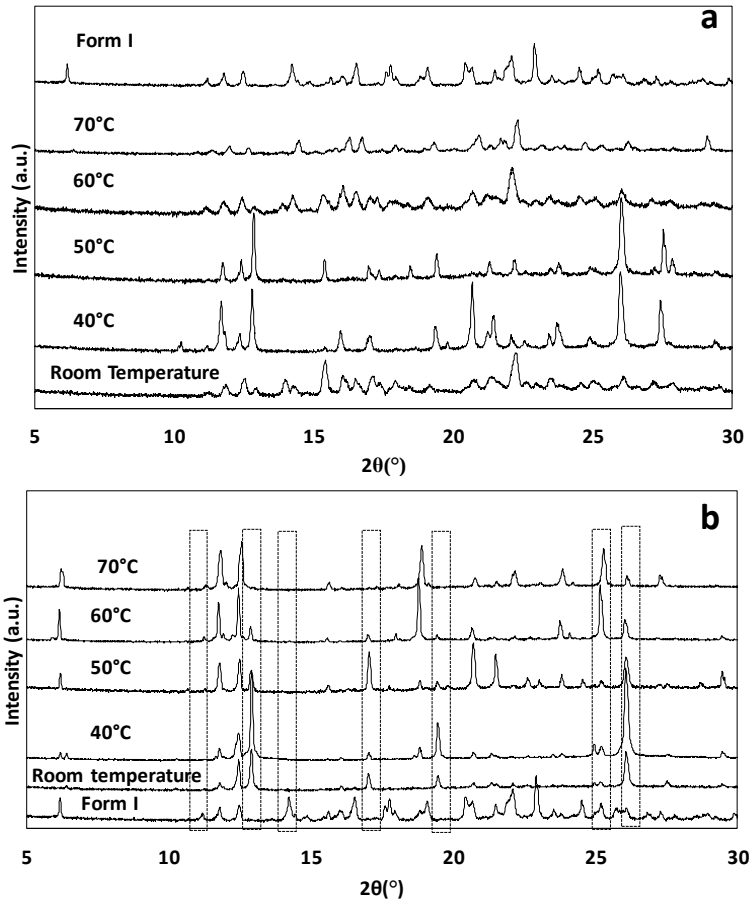

Figure 3.12 PXRD patterns of (a) OTS-FF and (b) B-FF at different crystal growth temperatures.

3.3.4 Effect of crystal growth temperatures on FF crystallisation in the bulk

For the B-FF samples, the crystal morphology changed significantly with changes in the growth temperature. At room temperature, the crystals spread rapidly in a symmetrical spherulite manner. When 50, 60 and 70 °C were used as the crystal growth temperatures, the FF crystals became a blade-like shape and expanded asymmetrically (**Figure 3.9b**). The crystal growth rate also showed high sensitivity to the changes in the incubation temperature. As seen in **Figure 3.9b**, the crystal growth rates were 1.05, 5.37, 7.58, 5.83 and 2.4 μm.sec^{-1} at room temperature (22ºC), 40, 50, 60 and 70 ºC, respectively. The maximum crystal growth rate of the FF was observed at 50 °C.

ATR-FTIR was used to examine the polymorph of the B-FF samples. At least three ATR-FTIR spectra were acquired on the B-FF samples to ensure homogeneity throughout the B-FF samples. The B-FF that crystallised at 40 and 50°C resulted in FF form IIa, as the signature peaks of form IIa, including the methyl stretching region and ester carbonyl stretching, match the pure form IIa spectrum (B-FF RT) (**Figure 3.11b**). The ATR-FTIR spectra of B-FF 60 and 70°C closely resembled the FF form I. The few differences were

the ester carbonyl shifting to 1721 cm^{-1}, which is between the ester carbonyl positions of forms I and IIa, the different intensity of the benzene ring carbonyl stretching and the absence of the benzene ring in-plane deformation vibration peak at 1098 cm^{-1}(**Figure 3.13a**). The spectrum subtraction of the B-FF 60 and 70°C for FF form I was performed in the methyl stretching region (3400-2600 cm^{-1}). The rationale for choosing this region was due to the flat base line in comparison to the range 1800-1300 cm^{-1}, this would make it easy to perform the spectrum subtraction. A straight line was obtained from the spectrum subtraction (**Figure 3.13b**), which indicates that B FF 60 and 70 °C had an identical match to the FF form I at the methyl stretching region. In addition, it should be noted that the FF form I spectrum was observed in one of the three spectra acquired from the B-FF 70°C. It is possible that the B-FF 70 and 60 °C could be a new polymorph of FF that has a similar molecular packing to the FF form I or a polymorphic mixture of the new form with form I. Another possibility is that it could be the preferred orientation of the crystal that influences the optics of the ATR resulting in the peak position shift (21). PXRD was performed to confirm the polymorph of FF in this sample.

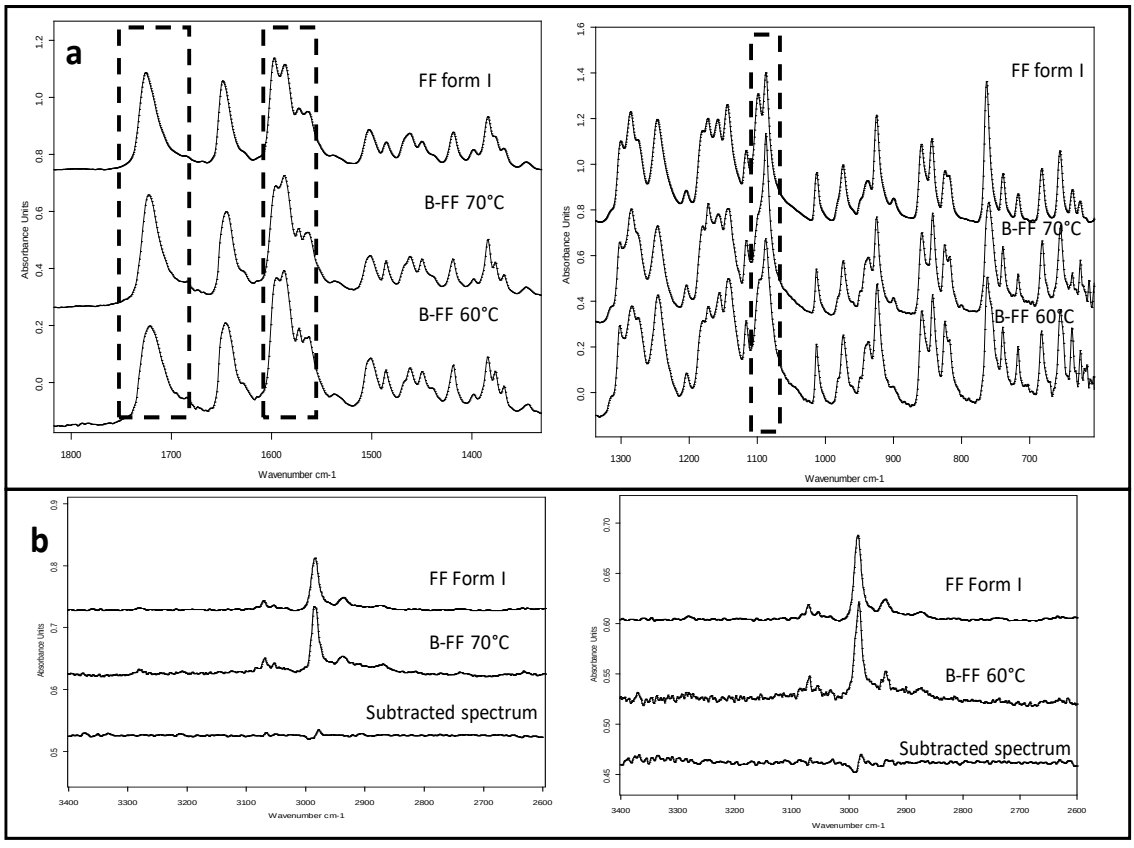

Figure 3.13 ATR-FTIR spectra of (a) B-FF 60 and 70°C in comparison to the reference form I spectrum (1800-600 cm^{-1}) and (b) the subtracted spectra of B-FF 60 and 70°C from the form I spectrum at 3400 to 2600 cm^{-1}.

The PXRD results also show the changes in the diffraction patterns of B-FF with changes in the growth temperatures (**Figure 3.12b**). Example diffraction peaks are highlighted in **Figure 3.12b** and they show the clear differences between the known form I and the growth of the B-FF at different temperatures. As the ATR-FTIR suggested, B-FF 60 and 70°C might have similar PXRD patterns to the FF form I. However, the PXRD of the B-FF 60 and 70°C are significantly different to the reference form I PXRD. This could be the preferred orientation effect in these B-FF samples. Therefore, PXRD may not be a suitable technique to examine the B-FF samples. Thermal analysis by structural characterisation (TASC) is an optical analogue micro-thermal analysis that employs a similar principle to a hot-stage microscope. It takes account of the pixel changes while recording a series of images during the heating or cooling program and changes them to quantitative data (22, 23). TACS has been used to measure the T_g of polymers and the melting points of crystalline materials (22, 23). TASC could be a potential means to clarify the polymorph of the B-FF by observing the melting points. Additionally, a B-FF sample with a glass substrate can be inserted into the TACS to perform thermal analysis without damaging the sample, as occurs with the DSC sample preparation.

3.3.5 Physical stability of FF IIa

- **OTS-FF**

OTS-FF 40°C was chosen as the representative sample to study the physical stability of FF IIa in an OTS sample because it contains the greatest amount of the FF IIa. **Figure 3.14** shows the PXRD patterns of the OTS-FF 40°C. The stability study was conducted for six months at room temperature using PXRD. The figure **Figure 3.14** indicates that while ageing at room temperature, there is no clear evidence of the continuous polymorphic transformation of form IIa to I in the mixtures, since the PXRD of the OTS-FF 40°C at six months was very similar to the fresh sample (only small peaks near 10° and 20° disappear).

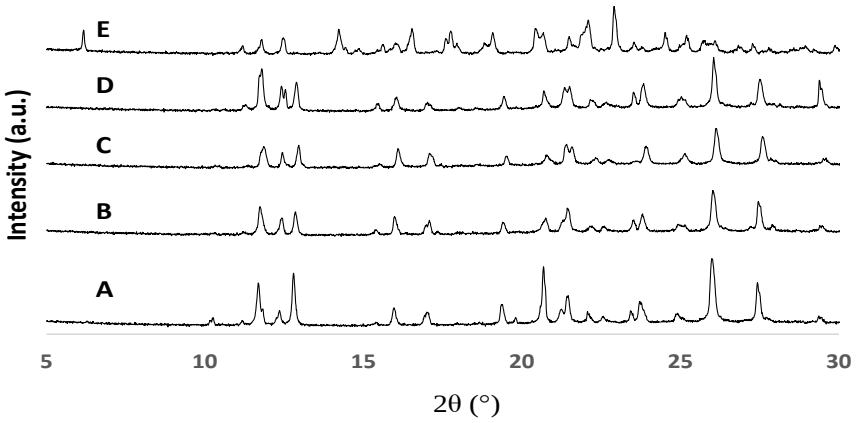

Figure 3.14 PXRD analysis of six months physical stability under ambient conditions of OTS-FF, which was crystallised at 40°C, fresh (A), one month (B), three months (C), six months (D) and intact crystalline form I (E).

As seen in **Figure 3.15**, clear melting of form IIa followed by recrystallisation of form I can be observed by DSC heating at 2°C.min^{-1} . However, with an increase in the heating rate to 20°C.min^{-1}, only the melting transitions of form IIa and form I could be observed. This is due to there being less time available for the conversion and the completion of the recrystallisation of form I. This was confirmed by the decreased melting enthalpy of form I with an increase in the heating rate.

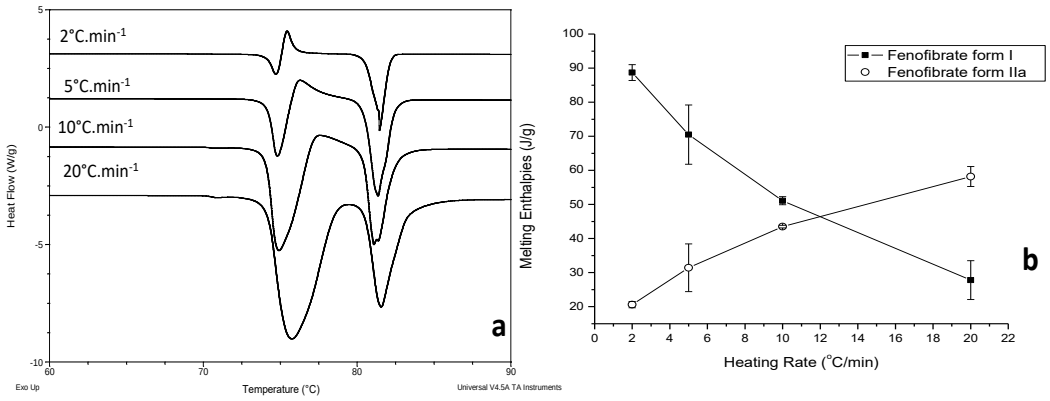

Figure 3.15 (a) DSC thermogram demonstrating different heating rates being applied to OTS-FF at 40°C (which generated FF form IIa rich crystals) and (b) changes in melting enthalpies of forms I and IIa with the heating rates used in the DSC experiments.

The heating effect on the conversion of form IIa to form I was studied at temperatures below and above the melting point of the FF crystalline form IIa. The OTS-FF 40°C was heated to 76°C, which is slightly higher than the melting point of form IIa, and incubated until the crystallisation of form I was complete (which was approximately two minutes).

As seen in **Figure 3.16**, during the incubating period there was the melting of form IIa at 74°C, which was immediately followed by an exothermic recrystallization of form I. The complete crystallisation of form I after annealing was confirmed by the same single melting point and enthalpy value as the pure crystalline form I.

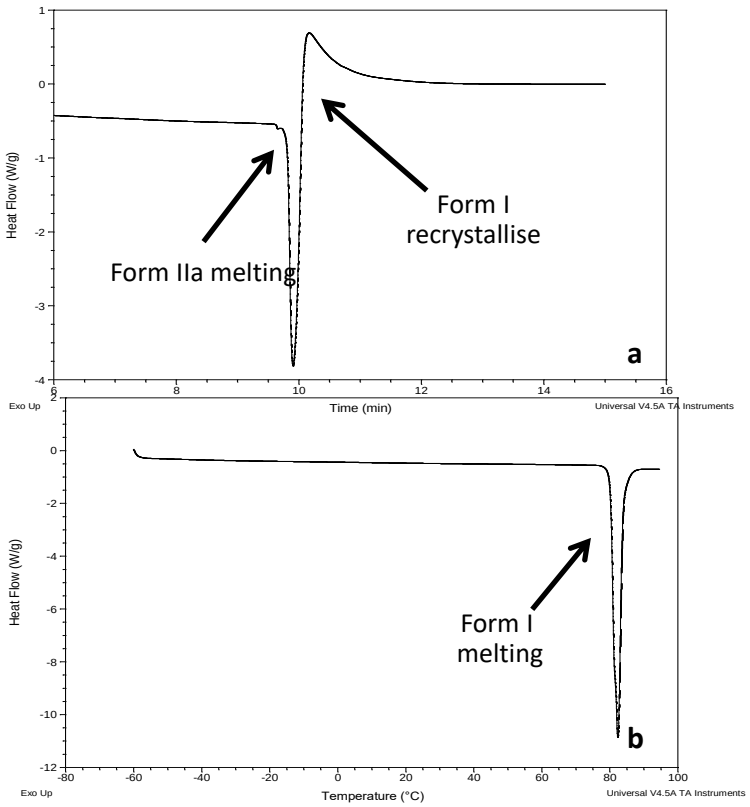

Figure 3.16 (a) Isothermal DSC thermograms of a post polymorphic transformation of FF form IIa rich crystals by melt-recrystallisation when annealing at 76 °C and (b) DSC heating of form IIa after annealing at 76 °C.

Isothermal MTDSC was used to further probe the thermal impact on the form IIa to form I conversion. It has been reported previously that a change in the C_p during an isothermal DSC experiment is related to the polymorphic conversion (24). As seen in **Figure 3.17**, a more significant surge of the reversing C_p signal was observed at the beginning of the annealing period at 70 °C than at 60 °C. The peak observed in the reversing C_p signal is associated with the polymorphic conversion of form IIa to form I, which was completed within 11.3±1.2 minutes for annealing at 70 °C and 4.8±0.2 minutes at 60 °C. A standard DSC was used to confirm the nature of the C_p change after the isothermal MTDSC experiment. Only the melting of form I was detected in the OTS-FF 40°C samples that annealed at 70°C. This indicates that the change in the C_p is associated with the complete polymorphic transformation of form IIa to form I; whereas, the melting of form IIa can still be observed in the sample that annealed at 60°C, but with a reduced enthalpy value and

accompanied by the melting of form I. The reduced enthalpy of FF form IIa is again associated with an incomplete conversion of form IIa to form I during annealing at 60 °C.

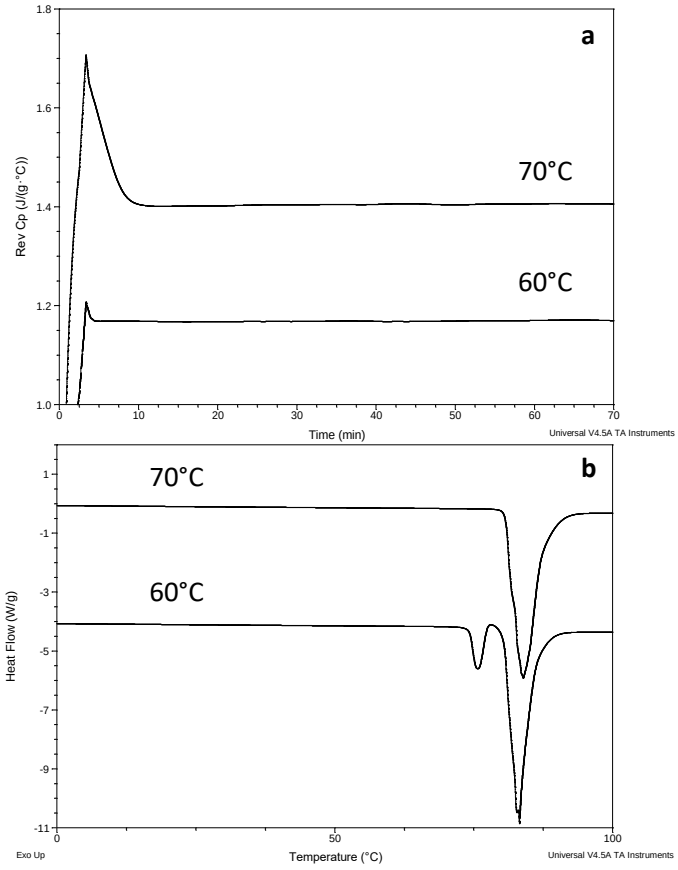

Figure 3.17 (a) Isothermal MTDSC thermogram of OTS-FF IIa rich crystals at 60 and 70°C for 120 min and (b) DSC heating of a OTS-FF 40°C sample after isothermal MTDSC at 60 and 70°C.

Variable temperature ATR-FTIR spectroscopy of the OTS-FF 40°C sample that annealed at 70°C revealed the transformation of the two ester carbonyl stretching peaks at 1714 and 1727 cm^{-1} to a single peak at 1727 cm^{-1} within approximately 15 minutes (similar to the time scale detected by the isothermal MTDSC experiments), which agrees well with the DSC results confirming the conversion of form IIa to form I **Figure 3.18**.

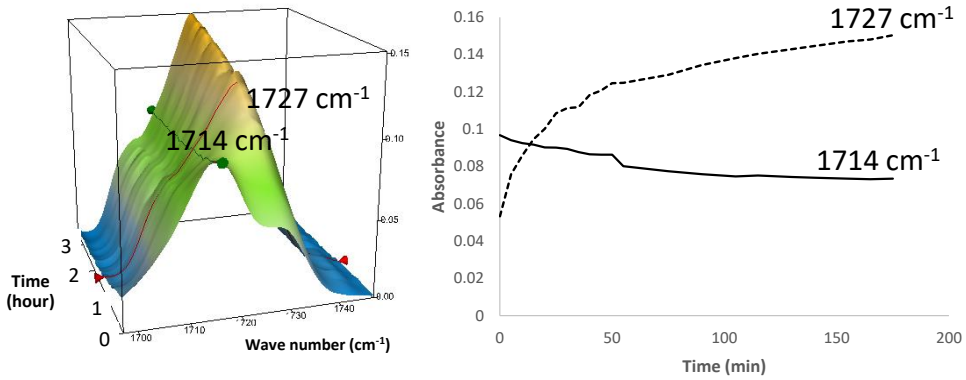

Figure 3.18 Change in ester carbonyl stretching peak intensity during variable temperature ATR-FTIR of OTS-FF40°C: the indicator peak at 1714 cm^{-1}(form IIa) shifted to 1727 cm^{-1} (form I). This is an indication of the transformation of form IIa to form I after annealing at 70°C for 3 hrs.

- **B-FF**

After the complete crystallisation of amorphous FF at room temperature, PXRD was used to monitor the six month physical stability of form IIa stored at room temperature. The PXRD results showed that B-FF samples remained as form IIa during the six month period without conversion into form I (**Figure 3.19**).

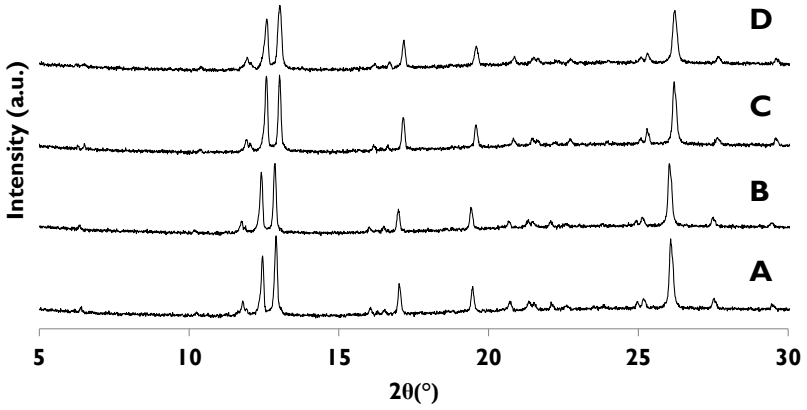

Figure 3.19 PXRD pattern of B-FF physical stability for six months under ambient conditions: fresh (A), one month (B), three months (C) and six months (D).

Form IIa converts into form I due to further mechanical stress, such as scratching with a stainless steel spatula, or thermal treatment. The mechanical stress effect was described previously in section 3.3.1. As demonstrated by the variable temperature ATR-FTIR spectroscopy results (**Figure 3.20**), the completely crystallised form IIa converts to form I during incubation at 70°C. Form IIa is identified by an intense peak at 1714 cm^{-1} that

indicates ester carbonyl stretching. The polymorphic conversion is indicated by a reduction in this peak and an increase in the intensity of the ester carbonyl peak at 1721cm^{-1}. As discussed earlier, this is an indication of FF form I.

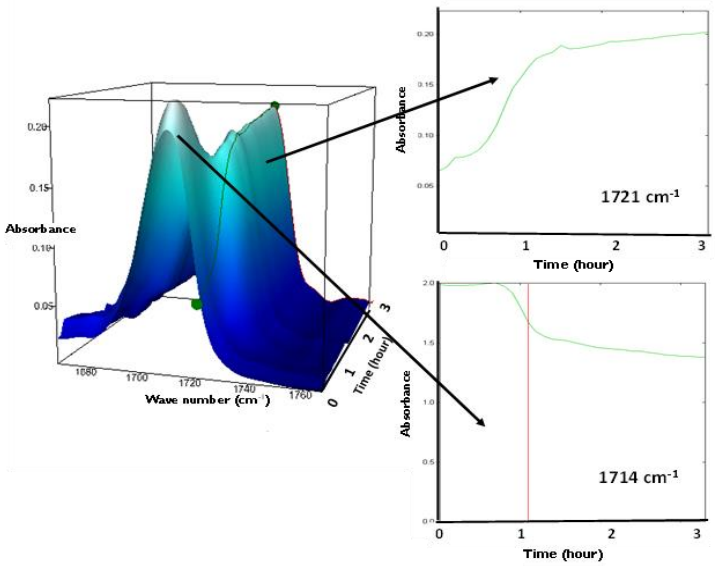

Figure 3.20 Changes in ATR-FTIR spectra of B-FF after removing coverslips and placing on the variable temperature ATR-FTIR for 3 hr at 70°C. It should be noted that the characteristic peak of FF form II at 1714 cm^{-1} gradually shifted to 1721 cm^{-1} that indicated the polymorphic conversion of form II to I.

3.3.6 Effect of OTS on FF crystal growth mode switching

This section presents an investigation of the effect of using an OTS to switch the crystal growth mode in the partially crystallised FF sample. The FF crystallisation was initiated via surface disruption to activate heterogeneous nucleation (**Figure 3.21a**). A top coverslip was immediately placed on the amorphous FF to limit the OTS. The spherulite form IIa crystals, which were identified by the ester carbonyl at 1714 cm^{-1} using ATR-FTIR spectroscopy, expand radially from the nucleation site throughout the amorphous FF, as seen in **Figure 3.21a-c**. The removal of the top coverslip before the completion of the crystallisation of the amorphous FF terminated the expansion of the form IIa. From this point, needle-like clusters of crystals could be seen growing rapidly (**Figure 3.21d-f**). These needle-like clusters were identified as form I by the measured shift of the ester carbonyl stretching peak to 1727 cm^{-1} using ATR-FTIR spectroscopy (**Figure 3.21g**). This phenomenon, in which the crystalline form IIa initiates form I, is likely to be due to cross-nucleation (14, 25-28). Therefore, an OTS shows a significant impact on the crystal growth mode of the amorphous FF.

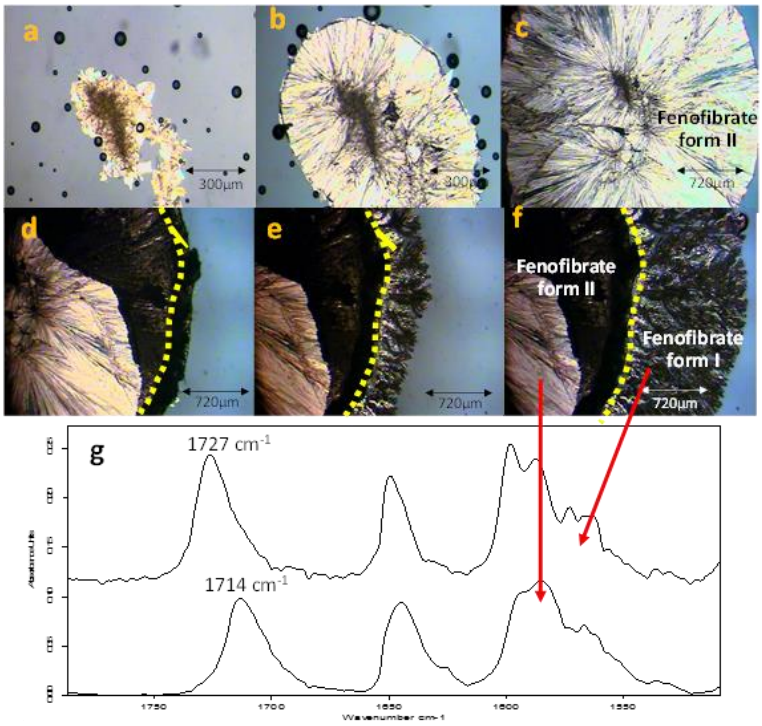

Figure 3.21 Images of FF crystal growth mode being switched from form IIa to form I after top coverslip removal. (a-c) FF form IIa crystals grown between sandwiched coverslips at room temperature over 17 minutes (a = initial, b = 5 min, c = 15 min); (d-f) following top cover slip removal, form IIa crystal growth was terminated and form I crystallisation occurred throughout the remaining amorphous FF (d = initial, e = 5 min, f = 15 min); and (g) spherulite and needle-like crystalline regions were distinguished as two separate domains using ATR-FTIR in which the ester carbonyl stretching peaks at 1714 and 1727 cm^{-1} indicates the presence of forms IIa and I, respectively.

3.4 Discussion

3.4.1 Origin of FF IIa crystallisation and FF cross-nucleation

In the bulk of the melt, molecules are being pulled by their neighbour's molecules at all of the directions. This is resulting in the small molecular mobility in the bulk. In contrast, at the boundary between the melt and the air, the molecules at the interface are not surrounded like in the bulk. They are being pulled inward by their neighbour molecules. This action resulting in the melt to minimise its surface area. Therefore, this leads to the molecules at the interface between the air, and the melt has a higher energy and mobility than the molecules that stay in the bulk of the melt. Consequently, at the interface is a preferential site for the nucleation and crystal growth because the molecules at this site have high energy and mobility. The fast molecular mobility and high surface energy at the OTS possibly lead to a crystallisation of the thermodynamically more stable polymorph (14, 15,

29, 30). The results of this chapter indicate that OTS crystallisation favours the formation of the stable form I. This result is in good agreement with other studies, such as the surface crystallisation of indomethacin that led to the generation of a stable gamma polymorph (29). On the other hand, in the bulk where molecular mobility is slow, the molecules may integrate to the crystal slower and cause the different polymorph in comparison to the OTS crystallisation. In this study, the metastable FF form IIa shows a preference for the site at the interface that was in contact with the glass substrate. This phenomenon is likely due to the substrate induced phase (SIP) effect. The SIP effect has been reported to influence the polymorphic form of APIs (31). Reischl et al. reported the use of SIP to induce a metastable polymorph of phenytoin. The authors explained that the surface of the substrate has a tremendous effect on the phenytoin crystal alignment that leads to a formation of the metastable polymorph of phenytoin (32). Therefore, it is possible to speculate that the origin of FF form IIa is from the SIP effect of the glass substrate that induces the FF molecular alignment into the polymorph IIa.

Once completely crystallised in a closed environment, the crystal structure is stable for at least six months at room temperature after the top substrate is removed. This indicates that at room temperature, energetically, form IIa is relatively stable, which is confirmed by the single crystal structural study. However, if there is still non-crystallised amorphous material available, removing the top substrate led to the termination of the crystallisation to form IIa, and the growth of form I. This is due to the top substrate removal introducing an OTS to the amorphous FF. As a consequence, the amorphous FF switched crystal growth mode from FF IIa to I because FF form I is more favourable than form IIa in the presence of an OTS. This phenomenon corresponds to the cross-nucleation in which the crystals of form IIa nucleated the crystal growth of form I after the top coverslip was removed (14, 25-28).

Cross-nucleation is a phenomenon in which one crystalline polymorph is nucleated to the other polymorph that has higher or lower thermodynamic stability. It has been reported in the literature (14, 25-28). Cross-nucleation has been observed in some APIs and pharmaceutical excipients. Tao et al. observed that the seed crystals of mannitol forms β and δ induced the crystallisation of mannitol form α at a temperature below 150°C. While mannitol form β was the only form that crystallised at a temperature greater than 150°C (14). Gunn et al. reported that the nifedipine form α crystal resulted in the crystal growth of nifedipine form β at 110°C or below. A temperature greater than 120°C lead to the crystallisation of the nifedipine α form (28). Hence, the cross-nucleation of mannitol and nifedipine is temperature dependent (14, 28). To the best of our knowledge, the cross-nucleation that results from the availability of an OTS has not been reported previously.

This chapter carries a significant finding of the OTS effect on the polymorphic form of FF, which can be a potential means to select the polymorph for the other APIs.

3.4.2 Optimal crystal growth condition of form IIa

The second significant finding of this study was the optimal crystal growth of form IIa at 40 to 50°C for OTS-FF while the maximum crystal growth rate of FF IIa in the bulk was at 50°C. This agrees with Amstad's study that the maximum crystal growth rate of FF is at 50°C (9). However, in contrast to other studies, the results of this study highlighted the importance of the combination of both growth temperature and OTS on the optimal growth of metastable form IIa. The OTS-FF RT yielded a mixture of forms IIa and I, in which form I was the dominant polymorph. This suggests that form IIa nucleation and growth occurs beneath the surface of the amorphous FF. The higher form I yield at higher crystallisation temperatures can be attributed to the combination of a lower form IIa crystallisation driving force and the conversion of crystallised form IIa into form I.

3.5 Conclusion

The results presented in this chapter demonstrate that polymorphic form selection of FF could be achieved by the availability of an OTS during its crystallisation. The use of a thermal treatment in addition to an OTS can fine tune the selection of the crystallisation of FF form I and form IIa. The crystal growth mode switching form IIa to form I occurs when an OTS is introduced to the incomplete crystallisation of form IIa. This indicates that the crystallisation of form I is highly dependent on the OTS. This chapter reports for the first time the crystallographic data of metastable FF form IIa, which confirmed the similarity of it to the molecular packing of the stable form I and clarified the confusion between the FF form IIs in the literature. This chapter has produced new insights into how to use an OTS to manipulate and control the crystallisation of FF, which could be useful for industrial applications.

3.6 References

1. Tran TH, Ramasamy T, Truong DH, Choi H-G, Yong CS, Kim JO. Preparation and Characterization of Fenofibrate-Loaded Nanostructured Lipid Carriers for Oral Bioavailability Enhancement. Aaps Pharmscitech. 2014;15(6):1509-15.
2. He H, Yang R, Tang X. In vitro and in vivo evaluation of fenofibrate solid dispersion prepared by hot-melt extrusion. Drug development and industrial pharmacy. 2010;36(6):681-7.
3. Hossen SM, Sarkar R, Towhid MHA, Sultan MT, Aziz NA. Study on the effect of different polymers on in-vitro dissolution profile of Fenofibrate by solid dispersion technique. Journal of Applied Pharmaceutical Science Vol. 2014;4(06):056-60.
4. Patel T, Patel L, Patel T, Makwana S, Patel T. Enhancement of dissolution of Fenofibrate by Solid dispersion Technique. Int J Res Pharm Sci. 2010;1(2):127-32.

5. Srinarong P, Faber JH, Visser MR, Hinrichs WLJ, Frijlink HW. Strongly enhanced dissolution rate of fenofibrate solid dispersion tablets by incorporation of superdisintegrants. European Journal of Pharmaceutics and Biopharmaceutics. 2009;73(1):154-61.
6. Zhou D, Zhang GGZ, Law D, Grant DJW, Schmitt EA. Physical stability of amorphous pharmaceuticals: Importance of configurational thermodynamic quantities and molecular mobility. Journal of pharmaceutical sciences. 2002;91(8):1863-72.
7. Sailaja U, Thayyil MS, Kumar NSK, Govindaraj G. Molecular dynamics of amorphous pharmaceutical fenofibrate studied by broadband dielectric spectroscopy. Journal of Pharmaceutical Analysis. 2015.
8. Tipduangta P, Takieddin K, Fábián L, Belton P, Qi S. A New Low Melting-Point Polymorph of Fenofibrate Prepared via Talc Induced Heterogeneous Nucleation. Crystal Growth & Design. 2015;15(10):5011-20.
9. Amstad E, Spaepen F, Weitz DA. Crystallization of undercooled liquid fenofibrate. Physical Chemistry Chemical Physics. 2015;17(44):30158-61.
10. Kawakami K, Usui T, Hattori M. Understanding the glass-forming ability of active pharmaceutical ingredients for designing supersaturating dosage forms. Journal of pharmaceutical sciences. 2012;101(9):3239-48.
11. Crowley KJ, Zografi G. The use of thermal methods for predicting glass-former fragility. Thermochimica Acta. 2001;380(2):79-93.
12. Angell CA. Why C1 = 16–17 in the WLF equation is physical—and the fragility of polymers. Polymer. 1997;38(26):6261-6.
13. Baird JA, Van Eerdenbrugh B, Taylor LS. A classification system to assess the crystallization tendency of organic molecules from undercooled melts. Journal of Pharmaceutical sciences. 2010;99(9):3787-806.
14. Tao J, Jones KJ, Yu L. Cross-nucleation between D-mannitol polymorphs in seeded crystallization. Crystal Growth and Design. 2007;7(12):2410-4.
15. Zhu L, Wong L, Yu L. Surface-enhanced crystallization of amorphous nifedipine. Molecular Pharmaceutics. 2008;5(6):921-6.
16. Di Martino P, Palmieri G, Martelli S. Evidence of a metastable form of fenofibrate. Die Pharmazie. 2000;55(8):625-6.
17. Heinz A, Gordon KC, McGoverin CM, Rades T, Strachan CJ. Understanding the solid-state forms of fenofibrate–a spectroscopic and computational study. European Journal of Pharmaceutics and Biopharmaceutics. 2009;71(1):100-8.
18. Balendiran GK, Rath N, Kotheimer A, Miller C, Zeller M, Rath NP. Biomolecular Chemistry of Isopropyl Fibrates. J pharm sci. 2012;101(4):1555-69.
19. Socrates G. Infrared and Raman characteristic group frequencies: tables and charts: John Wiley & Sons; 2004.
20. Henry R, Zhang G, Gao Y, Buckner I. Fenofibrate. Acta Crystallographica Section E: Structure Reports Online. 2003;59(5):o699-o700.
21. Stuart BH. Spectral Analysis. Infrared Spectroscopy: Fundamentals and Applications: John Wiley & Sons, Ltd; 2005. p. 45-70.
22. Reading M, Morton M, Antonijevic M, Grandy D, Hourston D, Lacey A. New methods of thermal analysis and chemical mapping on a micro and nano scale by combining microscopy with image analysis. Microscopy: advances in scientific research and education Formatex Research Center. 2014:1083-9.
23. Alhijjaj M, Reading M, Belton P, Qi S. Thermal Analysis by Structural Characterization as a Method for Assessing Heterogeneity in Complex Solid Pharmaceutical Dosage Forms. Analytical chemistry. 2015;87(21):10848-55.
24. Qi S, Craig DQM. The Development of Modulated, Quasi-Isothermal and Ultraslow Thermal Methods as a Means of Characterizing the α to γ Indomethacin Polymorphic Transformation. Molecular Pharmaceutics. 2012;9(5):1087-99.
25. Chen S, Xi H, Yu L. Cross-Nucleation between ROY Polymorphs. Journal of the American Chemical Society. 2005;127(49):17439-44.
26. Yu L. Nucleation of One Polymorph by Another. Journal of the American Chemical Society. 2003;125(21):6380-1.
27. Tao J, Yu L. Kinetics of Cross-Nucleation between Polymorphs. The Journal of Physical Chemistry B. 2006;110(14):7098-101.
28. Gunn E, Guzei IA, Cai T, Yu L. Polymorphism of Nifedipine: Crystal Structure and Reversible Transition of the Metastable β Polymorph. Crystal Growth & Design. 2012;12(4):2037-43.
29. Wu T, Yu L. Surface Crystallization of Indomethacin Below T g. Pharm Res. 2006;23(10):2350-5.
30. Sun Y, Zhu L, Kearns KL, Ediger MD, Yu L. Glasses crystallize rapidly at free surfaces by growing crystals upward. Proceedings of the National Academy of Sciences. 2011;108(15):5990-5.
31. Jones AOF, Chattopadhyay B, Geerts YH, Resel R. Substrate-Induced and Thin-Film Phases: Polymorphism of Organic Materials on Surfaces. Advanced Functional Materials. 2016;26(14):2233-55.
32. Reischl D, Röthel C, Christian P, Roblegg E, Ehmann HMA, Salzmann I, et al. Surface-Induced Polymorphism as a Tool for Enhanced Dissolution: The Example of Phenytoin. Crystal Growth & Design. 2015;15(9):4687-93.

4. Chapter 4: New Low Melting-point Polymorph of FF Prepared via Talc Induced Heterogeneous Nucleation

4.1 Introduction

In the previous chapter, the melt-cooled amorphous FF had its crystallisation behaviour explored with respect to the availability of an OTS (open top surface) and the crystal growth temperature. The FF form IIa crystallisation was found to be sensitive to an OTS and crystal growth temperature (previously reported in Chapter 3). The heterogeneous nucleation approach by scratching the amorphous FF with a stainless steel spatula was used to initiate the FF crystallisation. However, in practice, heterogeneous nucleation and crystallisation induced by mechanical triggers are often extremely difficult to control; whereas, the addition of an impurity is a much more controllable approach for initiating heterogeneous nucleation and crystallisation (1-3). The interaction between the impurity and the drug molecules can often be used to control the crystallisation of a certain polymorph (4, 5). Poornachary et al demonstrated the use of LD-aspartic acid and glutamic acid to specifically inhibit the nucleation of α-glycine. This resulted in the control of the crystallisation of the supersaturated glycine to crystallise into γ-glycine (5). It is believed that the polymorphic control from additives occurs through one of two main mechanisms, which are 1) the lattice match between the impurity surface and the aggregate molecules and 2) the molecular ordering according to the morphological features of the additive's surface (2). Therefore, there has been an increasing number of reports on using heterogeneous nucleation as a novel means to selectively produce desirable polymorphic forms in the pharmaceutical industry (2, 3, 6-8). For example, Chadwick and co-workers reported the use of a 4-aminophenylacetic acid to induce the crystallisation of amorphous PCM into its polymorph II (2). Lang et al. successfully used hydroxypropyl cellulose, poly(4-methylpentene), poly(R-methylstyrene) and poly(p-phenylene ether-sulfone) to crystallise amorphous carbamazepine into its polymorph IV (8).

Talc ($Mg_3Si_4O_{10}(OH)_2$) is a generally recognized as safe (GRAS) excipient widely used in pharmaceutical oral solid dosages as a tableting excipient (9). In this chapter, the use of a low quantity of talc to induce the heterogeneous nucleation of FF from the melt was explored. It was expected that the talc additives would induce crystallisation of amorphous FF by enhancing the nucleation process of amorphous FF via heterogeneous nucleation.

In this part of the study, talc was used to crystallise a new polymorphic form (form III) of FF, which has not been reported previously. The physicochemical properties of FF form III were characterized along with the crystal growth condition optimization. The single crystal structure of FF III was elucidated in comparison to the previously reported FF polymorphs. Additionally, the mechanism of FF form III crystallization with the presence

of talc was investigated. Furthermore, the transformations of this form to other known polymorphs are also described in this Chapter.

4.2 Methodology

4.2.1. Sample preparation

The FF form I and talc powders were precisely weighed at proportions of 80:20, 90:10, 95:5, and 99:1. The powders with a total weight of approximately 300 mg were transferred to glass vials and physically mixed with a metal spatula. The samples were heated to 100 °C until all FF crystals had completely melted. After complete melting, the vials were carefully removed from the heat source and immediately transferred to 0% RH desiccators (using P_2O_5 as the desiccating agent). The amorphous FF obtained by cooling the melt that contained talcum powder completely recrystallized within 24 h. When preparing form III, caution should be taken because if the amorphous FF containing 1% talc experiences any mechanical shock, such as scratching with metal implements or knocking on the outside of the glass vial containing the molten FF, the recrystallization of FF forms I and II could occur instead of form III (this will be explained in page 137-8, **Figure 4.2**).

4.2.2 Characterisation methods

In this chapter, the FF crystals with talc additives (1-20%) were characterised by a range of characterisation technique, as follows: DSC, MTDSC, TGA, ATR-FTIR, SEM, PXRD and SCXRD. The details of the DSC, MTDSC, TGA, ATR-FTIR, SCXRD, PXRD and SEM techniques are included in Chapter 2, sections 2.4.1.2, 2.4.2.2, 2.4.3.2, 2.4.5.2, 2.4.7.2, 2.4.7.4 and 2.4.8.2, respectively. The crystal structure of FF form III was determined according to the procedure stated in section 2.4.7.3.

4.3 Results

4.3.1 Identification and optimization of new form III crystallisation

The nucleation and crystallisation of form III are strongly affected by the talc concentration suspended in the molten FF. **Figure 4.1** shows the crystallisation of form III, which has a distinct low melting point of approximately 50°C. This form only occurred when the talc concentration was 1% (w/w). The absence of a glass transition in the DSC result confirmed that the material was fully crystallised. Following the melting of form III, exothermic crystallisation occurred immediately at 57.6°C. The product of the crystallisation is

confirmed to be form I as form I melting can be observed at 80°C with a melting enthalpy of 89.8±0.6 J/g.

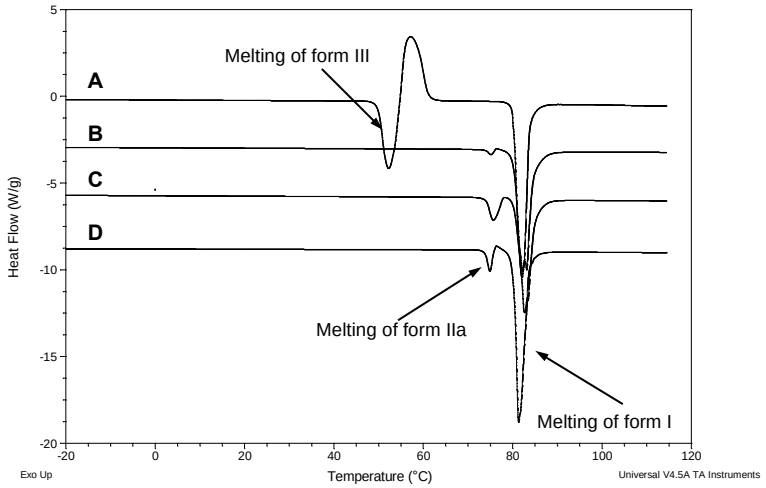

Figure 4.1 DSC thermograms of FF crystallised from melt containing (A) 1% w/w, (B) 5% w/w, (C) 10% w/w and (D) 20% w/w talc.

The use of talc concentrations greater than 1% resulted in the crystallisation of mixtures of the metastable form IIa (melting point of approximately 74°C) and the stable form I (melting point of approximately 80°C). Judging by the enthalpy values of the peaks associated with forms I and IIa, more form I was crystallised than form IIa in the samples containing 5-20% talc (10). It is important to emphasize that careful control of the crystallisation conditions is imperative for obtaining form III with a high purity. In our experiments, the absence of humidity and complete avoidance of any mechanical shocks were necessary to increase the chance of crystallising the new form III with a high purity. As shown in **Figure 4.2**, despite the addition of 1% talc and cooling and storing the sample at 0% RH, a low level of mechanical shock (i.e., the container being bumped against the wall of the desiccator) can potentially cause the failure of the form III crystallisation and result in a mixture of forms I and IIa crystallising.

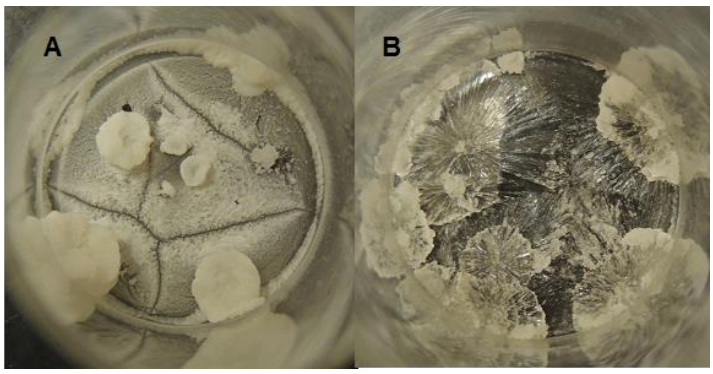

Figure 4.2 Optical images of crystalline FF-containing 1% talc that was obtained from the melt-cooling process: (A) crystallisation initiated by mechanical shock resulting in a mixture of forms I and IIa with form I being the dominatant form and (B) non-disruptive spontaneous crystallisation of form III in the presence of talc.

4.3.2 Physicochemical characterisation of FF form III

The morphology and spectroscopic features of the new FF form III were further characterised using SEM, PXRD and ATR-FTIR. **Figure 4.2** demonstrates the macroscopic differences between the appearance of the form I/form IIa mixture and form III. The form I and IIa mixture shows the presence of fine crystals. Form III, on the contrary, shows a flat and spreading habit of a mass of slender crystals. Macroscopically, form III is semi-translucent. **Figure 4.3** further confirms the significant crystal habit difference between form III and the stable form I. The SEM image of form I reveals large triclinic shaped form I crystals, which agrees well with the literature (11, 12). The radiating habit is further confirmed by the SEM image of form III.

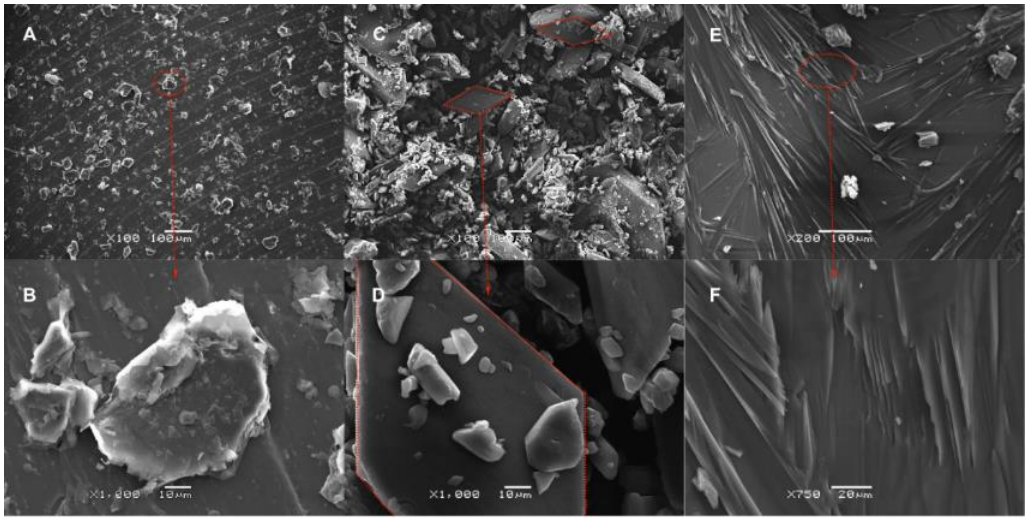

Figure 4.3 SEM images of (A and B) talc powders, (C and D) FF powder polymorph I as received and (E and F) form III crystallized in presence of 1% talc.

The ATR-FTIR results for form III show a clear fingerprint of form III, which is distinctively different from the known forms I and IIa at the methyl group stretching region, benzene ring stretching, benzene ring in plane deformation and benzene ring out of plane deformation, as highlight in **Figure 4.4**. The peak shifts in these regions indicate the differences in the molecular interactions of the FF functional groups, which cause the different crystal packing of form III in comparison to forms I and IIa. The functional groups associated with the vibrational bands shown in the IR spectra are summarised in **Table 4.1**.

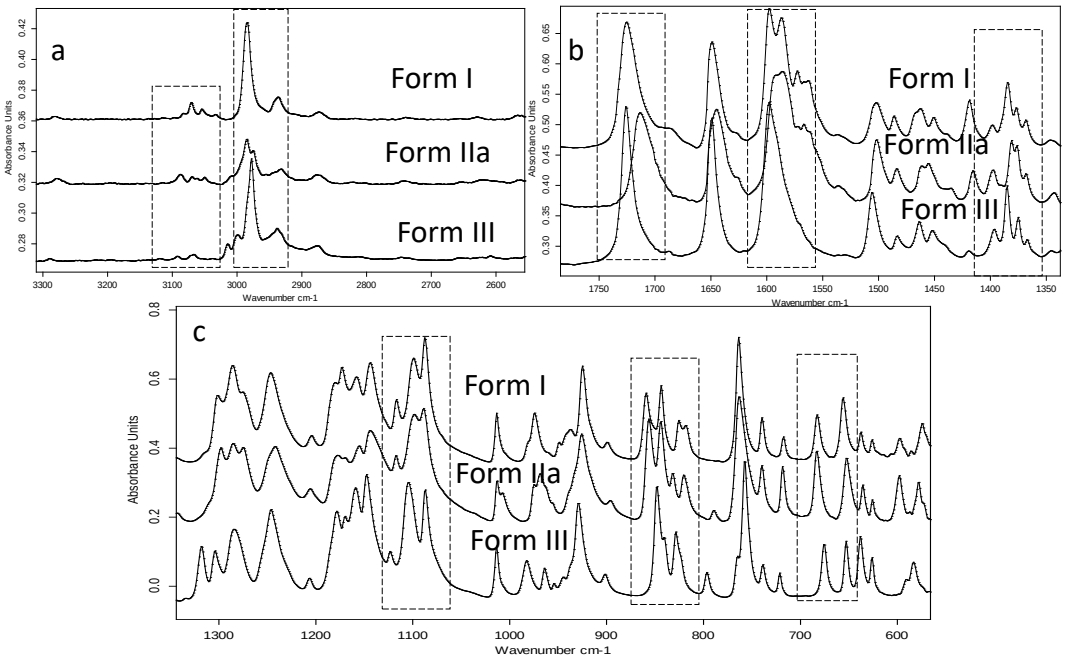

Figure 4.4 Comparison of ATR-FTIR spectra of FF polymorphic froms I, IIa and III: (a) spectra of 3300 to 2700 cm^{-1} region, (b) spectra of 1850 to 1350 cm^{-1} region and (c) spectra of 1350 to 550 cm^{-1} region. The differences between form I and form III spectra are highlighted in the dashed-line boxes.

PXRD is a technique that is highly sensitive to molecular packing arrangements. A clear and sharp PXRD diffraction pattern for form III with the absence of a background halo was obtained, as seen in **Figure 4.5**; this indicates that form III was crystallised by the method described in this Chapter and has a reasonably high purity. Additionally, the FF form III PXRD pattern is distinctively different from the known stable forms I and IIa, which were reported by Di Martino and co-workers (13). This refers to the difference in the crystalline packing of FF form III in comparison to FF forms I and IIa. Therefore, the results of the ATR-FTIR and PXRD both confirm the successful crystallisation of the new FF polymorph form III.

Table 4.1 Assignment of ATR-FTIR peaks of amorphous FF, FF form I, form IIa and form III.

Band assignment	**Peak position (cm^{-1})**			
	Amorphous fenofibrate	**FF polymorph I**	**FF polymorph IIa**	**FF polymorph III**
=CH-H of benzene ring	3070	3071, 3055, 3034	3087, 3069, 3050	3068, 3015
Methyl group stretching	2982, 2938	2985, 2937	2984, 2975, 2931	2978, 2939, 2876
O_3-C_{17} ester carbonyl stretching	1728	1727	1714	1727
O_1-C_7 Aryl ketone carbonyl stretching	1654	1650	1645	1650
-CH=CH- benzene stretching	1505, 1466	1520, 1463	1518, 1483	1506, 1484
C-O-C of ester	1143	1143	1144	1148
Aryl ether	1284	1285	1286	1284
Benzene ring in plane deformation vibration	1248, 1172, 1116, 1014, 972	1247, 1173, 1117, 1014, 975	1241, 1177, 1117, 1013, 968	1247, 1179, 1104, 1014, 983
Benzene ring out of plane deformation vibration	852, 838, 679	860, 844, 680	858, 844, 683	849, 829, 680
C_{l1}-C_3 bending	762	765	763	765, 758

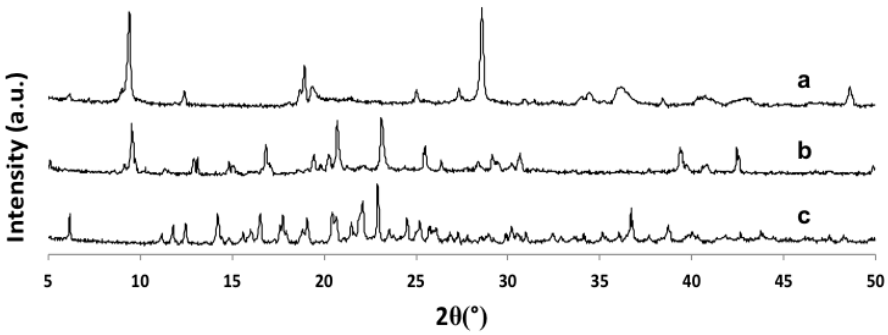

Figure 4.5 PXRD diffraction patterns of (a) pure talc, (b) FF form III and (c) form I.

4.3.3 Crystal structure of FF form III

In this section, the crystal structure of form III will be presented and compared to the crystal structures of forms I, IIa and IIb. The basic crystallographic parameters of these forms are given in **Table 4.2.**

Table 4.2 Crystallographic parameters of available polymorphic forms of FF.

Parameter	Form I[a]	Form IIa	Form IIb[b]	Form III[c]
Lattice system	Triclinic	Triclinic	Monoclnic	Triclinic
Space group	*P*-1	*P*-1	$P2_1/n$	*P*-1
a (Å)	8.1325	8.1328 (5)	13.619	9.4803 (6)
b (Å)	8.2391	8.7088 (6)	7.554	9.7605 (6)
c (Å)	14.399	13.6692 (9)	17.88	10.9327 (8)
α (°)	93.978	85.976 (6)	90	110.840 (6)
β (°)	105.748	84.815 (5)	92.35	90.352 (5)
γ (°)	95.854	74.344 (6)	90	99.701 (5)
Cell volume	919.03	927.34 (11)	1837.909	929.53 (11)
Density	1.285	1.292	1.304	1.289 (2)
Crystal size (mm)	0.55 x 0.50 x 0.44	0.12 x 0.13 x 0.46	0.55 × 0.30 × 0.25	0.12 × 0.15 × 0.34
Z	2	2	4	2
R	0.0418	0.1307	3.55	0.0653
wR2	0.105	0.1265	0.0897	0.149
Temperature (K)	193	140(2)	100	140
Goodness of fit	1.035	1.023	1.026	1.016

[a] obtain from reference (14), [b] is from reference (12) and [c] measured in this study

As the parameters suggest, the conformation of the FF molecules in forms I, IIa and III show a close similarity. The orientation of the tail group relative to the aromatic rings is markedly different in form IIb compared to forms I, IIa and III, and the angle between the plane of the two aromatic rings in form III is 45.73 (9)° (**Figure 4.6**). The crystalline structures of the stable from I and metastable IIa with their interactions on the crystal packing were discussed in Chapter 3.

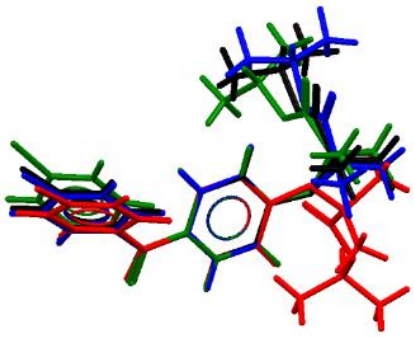

Figure 4.6 Overlay of molecular conformations in FF form I (black), form IIa (blue), form IIb (red) and form III (green).

Similar to form I, the molecules of form III are linked into layers by CH…O bonds parallel to the crystallographic (100) plane (**Figure 4.7a** and **4.7b**). The interaction between a hydrogen of the isopropyl group and the ketone carbonyl group of an adjacent molecule [H…O distance: 2.56 Å; C-H…O angle: 160°] generates a chain that is shared between forms I and III **(**diagonal in **Figures 3.5a** and **4.7a)**. The aromatic hydrogen to ester carbonyl contacts of form I are replaced by another isopropyl to ketone CH…O bond in form III. These interactions lead to remarkably similar layers in forms I and III, however, these are not superimposable. The relative positions of the molecules perpendicular to the plane in **Figures 3.5a** and **4.7a** are different in the two forms. A further shared interaction between forms I and III is the offset π-π interaction of the chlorobenzene rings, which links pairs of layers. In form III, this interaction is formed with an interplanar distance of 3.5719 (8) Å. The layers are further connected through an interaction that involves a short repulsive hydrogen–hydrogen contact (2.25 Å) between the central aromatic rings of the inversion related molecules (**Figure 4.7b**). Presumably, this contact can form because its unfavourable effect is compensated by a pair of long CH…O interactions (2.92 Å, 162°). This set of contacts replaces the dimeric rings formed through the CH…O (ketone) bonds in form I (**Figure 3.5b**), thus a clearly favourable interaction is replaced by a strained one, which explains the low stability of form

III. The crystal packing of form IIb has been discussed in Chapter 3. As expected from the different conformations, it is distinct from forms I, IIa and III (**Figures 3.5**, **3.8** and **4.7**).

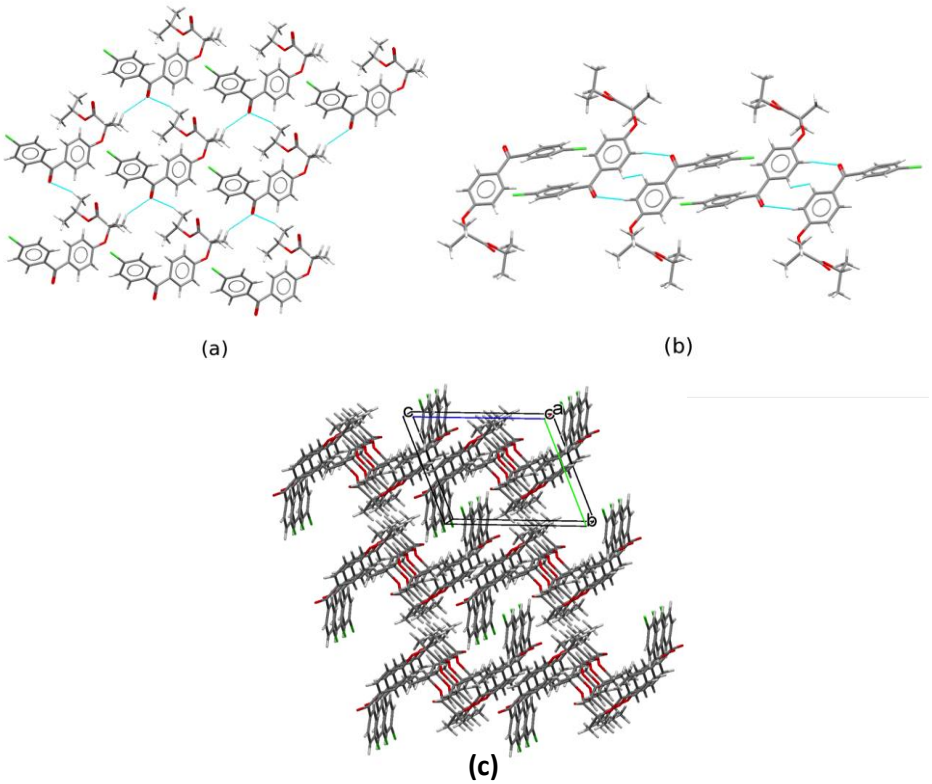

Figure 4.7 Intermolecular interactions in form III: (a) layer formed by CH…O interactions, (b) offset π-π interactions and CH…O linked dimers that connect the layers and (c) packing of form III.

4.3.4 Verifying epitaxial relationship of talc and FF form III

The mechanism by which talc induces the crystallisation of form III is not clear. Thus, it was hypothesized that the FF form III crystallisation may be related to heterogeneous nucleation on the surface of talc particles. Talc is a mineral crystal that exhibits basal cleavage, which exposes the (001) face (15). Increasing the talc concentration in the mixtures may have increased the chance of aggregation of talc particles, thereby reducing the relative amount of accessible (001) talc surfaces.

Two-dimensional epitaxy has been successfully applied to control polymorphism in the past (16). Therefore, the existence of an epitaxial relationship between talc and form III was verified. This could explain the preferential nucleation and growth of form III in the presence of talc. The method of Ward and co-workers was used to identify possible matches

with the dominant (001) face of talc (17, 18). For both forms, the best overlay on talc was possible with their respective (100) faces (**Figure 4.8**). The two-dimensional lattice parameters used for talc were $a_1 = 5.29$ Å, $a_2 = 9.18$ Å and $\alpha = 90.03°$, while for form I they were $b_1 = 8.27$ Å, $b_2 = 14.51$ Å and $\beta = 93.95°$. The optimal azimuthal angle was $\theta = 129.4°$. While there are overlapping lattice points, no common matching for the two-dimensional superlattice can be identified (**Figure 4.8a**). In **Figure 4.8b,** the two-dimensional lattice parameters used for talc were $a_1 = 5.29$ Å, $a_2 = 9.18$ Å and $\alpha = 90.03°$, while for form III they were $b_1 = 9.76$ Å, $b_2 = 10.93$ Å and $\beta = 110.8°$. The optimal azimuthal angle was found to be $\theta = 69.3°$. The points of the 1 x 3 form III superlattice approximately coincide with the talc lattice, which suggests a possible epitaxial relationship between the two. The geometrical match between the two lattices is much better in the case of form III, which suggests that this form could preferentially nucleate on the surface of talc crystallites.

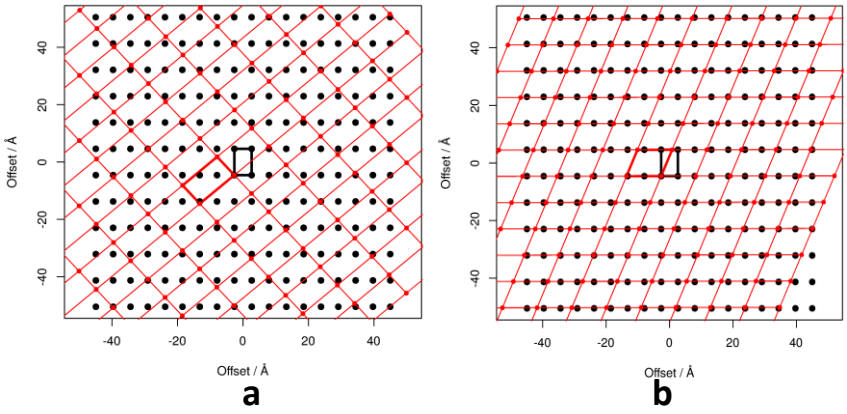

Figure 4.8 Optimal lattice overlay between (001) plane of talc (black) and (100) plane (red) of forms I (a) and III (b). The reference unit cells are drawn with thick lines.

4.3.5 Investigation into physicochemical stability of FF form III

No change was observed in the thermal decomposition behaviour of form III in comparison to form I, as seen in **Figure 4.9**. This indicates the good chemical stability of form III. It was observed that FF form III converts to its more stable polymorphic forms I and IIa. This polymorphic transformation can be triggered by increased temperature, crystal damage and aging. The metastable nature of form III is obvious, as the melting of form III is followed by immediate crystallisation of form I, as seen in **Figure 4.1**. MTDSC experiments on form III revealed a hidden exothermic event on the non-reverse heat flow signal at approximately 48°C (indicated by black arrows) prior to the melting of form III, as seen in **Figure 4.10**. This suggests that there is a high possibility of a polymorphic transformation occurring before the melting point.

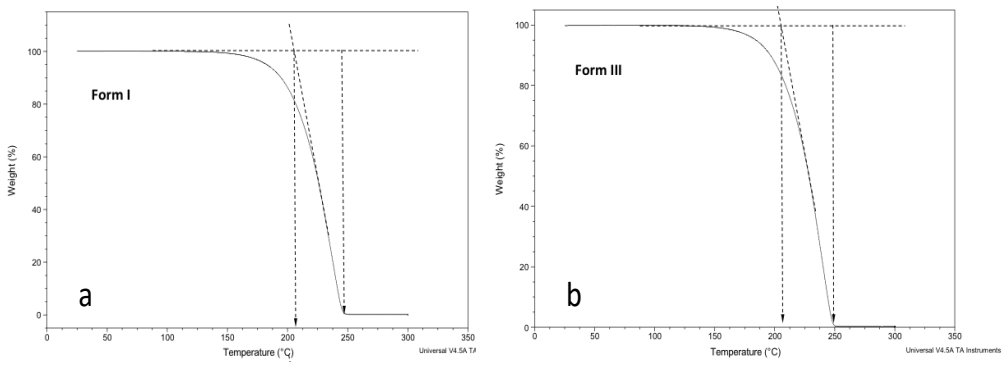

Figure 4.9 TGA results of **(**a**)** FF polymorphic form I and **(**b**)** new form III**.**

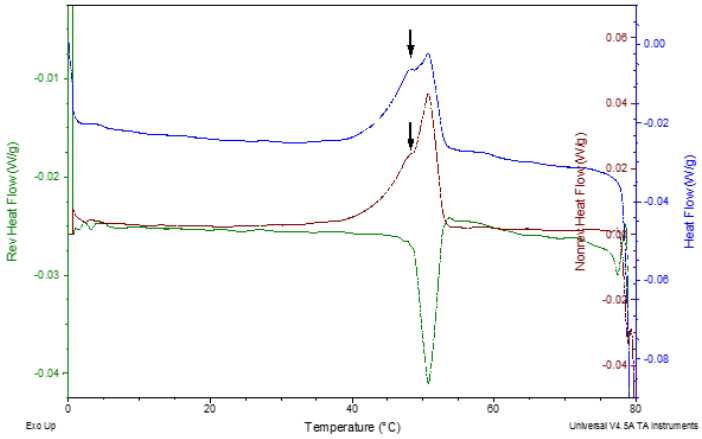

Figure 4.10 MTDSC result of FF from III with underlying heating at 2° C/min with± 0.318°C amplitude every 60 s; (blue) total heat flow, (green) reversing heat flow and (red) non-reversing heat flow.

To investigate the transformation prior to the melting point of FF form III, isothermal MTDSC experiments were conducted at 35, 40 and 45°C. Small surges of reversing C_p signals were observed at the beginning of every experiment, followed by a gradual decrease in the reversing C_p until reaching the equilibrium state (**Figure 4.11a**). The reversing C_p of the isothermal samples at 45 and 40 °C returned to their equilibrium values within 17±9 and 53±16 min, respectively. Meanwhile, the 35°C isothermal sample demonstrated a consistently flat reversing C_p signal. These observations suggest that a polymorphic transformation occurred during the isothermal experiments above 35°C, in which the kinetics of the transformation were temperature dependent. To confirm the polymorphic conversion phenomenon, the samples were examined by standard DSC after the isothermal experiment finished (**Figure 4.11b**). The melting peaks of form I at 80°C and small melting peaks of from IIa at 74°C were observed after annealing the samples at 40 and 45°C. This confirmed that the observation of the reverse C_p changes during the isothermal MTDSC experiments was evidence of a polymorphic transformation. A melting peak with a reduced

enthalpy value in form III was still present for the sample annealed at 35°C, and it was accompanied by an immediate exothermic recrystallisation and melting of from I.

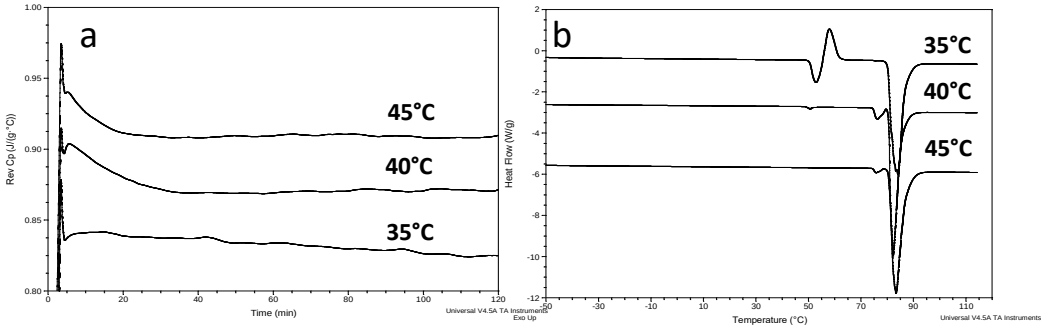

Figure 4.11 (a) Isothermal MTDSC thermograms of FF form III at 45, 40 and 35°C and (b) DSC heating of form III after the isothermal MTDSC experiments at 45, 40 and 35°C for 2 h.

To investigate whether the DSC sample preparation (scratching crystalline samples from the glass vial and loading into the DSC pan) had an effect on the transition, crystalline form III was milled in a mortar and then examined using standard DSC after different time intervals (2 and 5 h) after being milled. The melting enthalpies of form III significantly decreased after the sample was milled and gradually declined until a complete conversion to form I after 5 h (**Figure 4.12**).

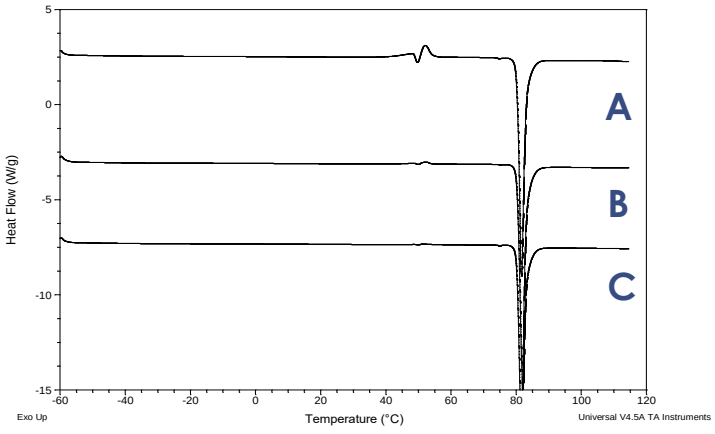

Figure 4.12 DSC thermogram demonstrating stability after milling FF form III: immediately after milling (A), 2 h after milling (B) and 5 h after milling (C).

Finally, the physical stability of the intact crystalline form III on aging was investigated. Some small opaque spots were observed on the crystals on day one, which later completely consumed the translucent crystals (**Figure 4.13**). The DSC thermogram in **Figure 4.13**

shows that the opaque crystal obtained after two days of ageing was dominated by form I with a minor component of form IIa and a tiny amount of form III. This result further confirmed the instability of FF form III, which thermodynamically converts to its more stable form on ageing.

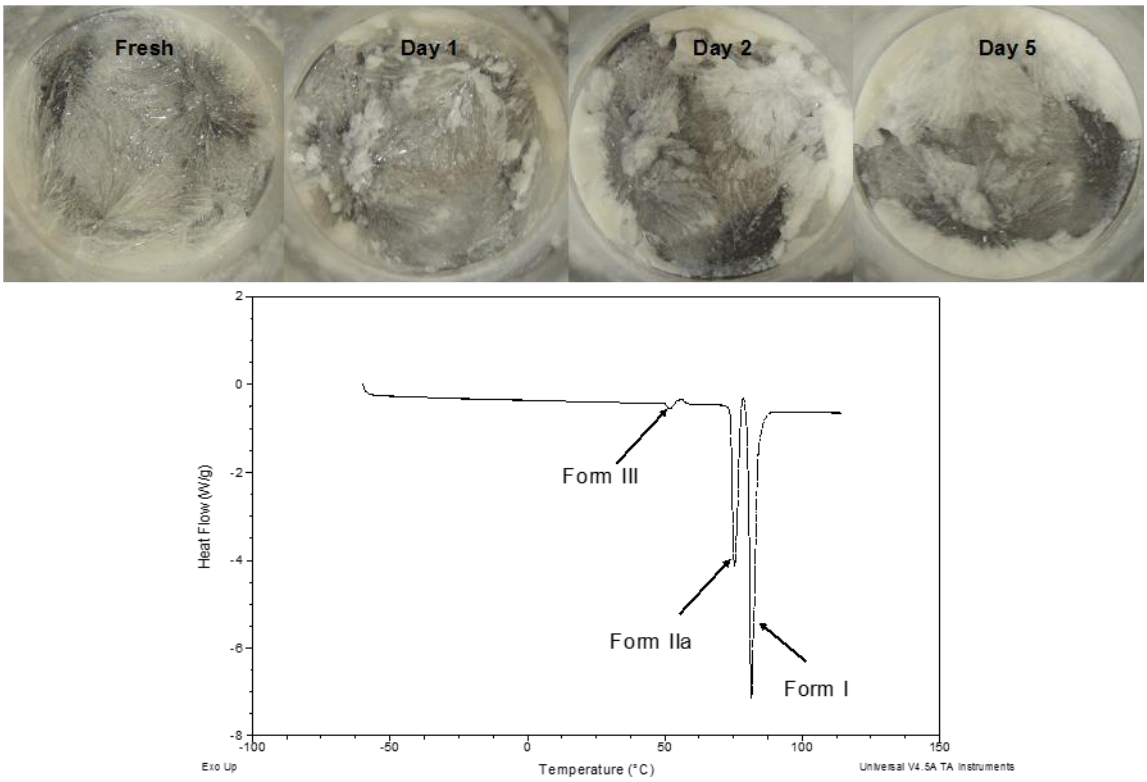

Figure 4.13 Appearance of aged FF form III under 0% RH at room temperature for different periods of time and the corresponding DSC thermogram of the sample aged for two days.

4.4 Discussion

With 1% talc dispersed in the amorphous FF, the new FF form III was successfully crystallised. It has a distinct melting point at 50°C. However, the higher talc ratios resulted in a crystalline mixture of forms I and IIa (I>>IIa). This suggests that the talc concentration is not relevant to the polymorphic selection between forms I and IIa, but it has a unique effect on the nucleation and growth of form III. It is possible to speculate that at talc concentrations above 1%, the talc particles were acting as non-specific foreign solids to induce heterogeneous nucleation of form I with a low level of nucleation of metastable form IIa. While at the 1% concentration talc provides a monolayer surface of talc crystals, which is favourable for nucleating the FF III polymorph. This hypothesis was confirmed by the two-dimensional epitaxy calculations that crystalline FF form III perfectly fitted with the unit cell dimensions on specific planes of the talc crystals. It is possible that other

materials apart from Talc can be used to induce the nucleation of FF. The property that requires is a matching between the epitaxial calculation of the material surface and crystalline surface. If this condition is satisfied, then it potentially leads to the crystallisation of the specific polymorph, such as FF form III. The principle of epitaxial crystalline matching induces nucleation can be potentially applied to other API to induce their nucleation. The FF form III demonstrated characteristic fingerprints from ATR-FTIR and PXRD. The fingerprint data are implied that the intermolecular interactions and crystalline packing of FF III are clearly different from the other known FF polymorphs. The depth details about FF form III molecular interactions and crystalline packing was further investigated by SCXRD. The crystalline structure of FF form III is very similar to the stable form I. However, the interaction of the isopropyl methyl groups and ketone carbonyl oxygen atoms that support the proposed link between these structural motifs in form I was replaced by a short repulsive hydrogen-hydrogen contact in form III. Hence, the strain interaction of form III results in the instability of this polymorph which transforms to I with ease. The polymorphic conversion of FF form III can proceed through melt-recrystallisation can be induced by increased temperature or mechanical triggers and occurs spontaneously on ageing. Melt-recrystallisation results in a complete conversion of form III to form I. Annealing FF form III samples below their melting point and milling both led to a crystalline mixture of FF forms dominated by form I with form IIa as a minor product. The ageing of intact form III crystals leads to a mixture of forms I and IIa, in which the amount of form IIa was greater than in samples that were subjected to annealing or milling. On the basis of the data presented in Chapters 3 and 4, the polymorphic conversion pathways of FF form III can be summarised as shown in **Figure 4.14**.

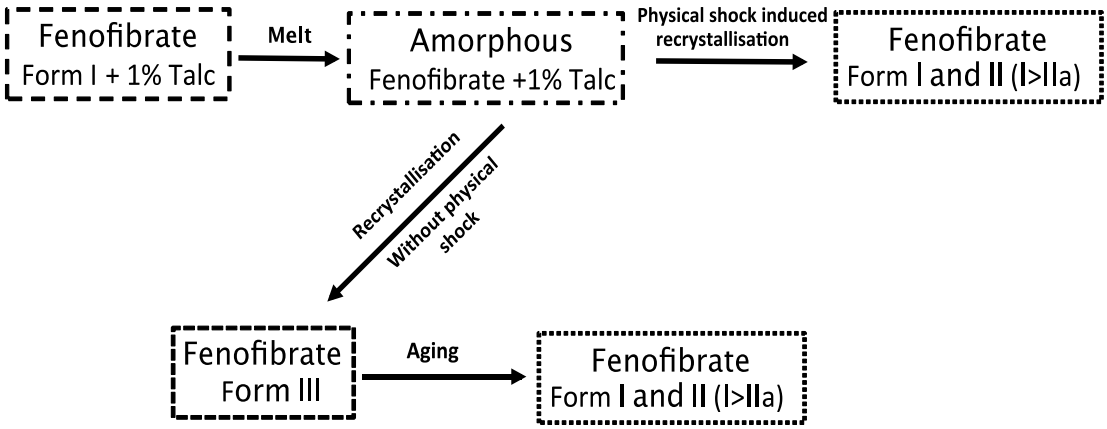

Figure 4.14 Schematic diagram depicting FF form III preparation and polymorphic transformation pathways of metastable polymorphs to forms I and IIa.

4.5 Conclusion

This Chapter described a heterogeneous crystallisation method to obtain a new FF polymorph, form III, with high purity. A low quantity (1%) of pharmaceutical grade talc was used to induce the crystallisation of form III, which can tentatively be explained by an epitaxial relationship between the talc and form III. The new form III was fully characterised by microscopic, thermal, spectroscopic and structural methods. This new form has a very low melting point of 50°C. It exhibits high thermal instability and converts to the stable polymorphs of forms I and IIa via melt-recrystallization on heating, milling and aging. This study also demonstrates the prospect of using safe pharmaceutical excipients to selectively crystallise metastable polymorphs of APIs, and this can be potentially expanded for largely scale industrial production.

4.5 References

1. Lu L, Dahle AK, StJohn DH. Heterogeneous nucleation of Mg–Al alloys. Scripta Materialia. 2006;54(12):2197-201.
2. Chadwick K, Myerson A, Trout B. Polymorphic control by heterogeneous nucleation-A new method for selecting crystalline substrates. CrystEngComm. 2011;13(22):6625-7.
3. Boukerche M, Mangin D, Klein JP, Monnier O, Hoff C. Inducing the stable polymorph using heterogeneous primary nucleation. Chemical Engineering Research and Design. 2010;88(11):1474-8.
4. Takenaka H, Kawashima Y, Lin SY. Polymorphism of spray-dried microencapsulated sulfamethoxazole with cellulose acetate phthalate and colloidal silica, montmorillonite, or talc. Journal of pharmaceutical sciences. 1981;70(11):1256-60.
5. Poornachary SK, Chow PS, Tan RBH. Influence of Solution Speciation of Impurities on Polymorphic Nucleation in Glycine. Crystal Growth & Design. 2007;8(1):179-85.
6. Parambil JV, Poornachary SK, Tan RB, Heng JY. Template-induced polymorphic selectivity: the effects of surface chemistry and solute concentration on carbamazepine crystallisation. CrystEngComm. 2014;16(23):4927-30.
7. Price CP, Grzesiak AL, Matzger AJ. Crystalline Polymorph Selection and Discovery with Polymer Heteronuclei. Journal of the American Chemical Society. 2005;127(15):5512-7.
8. Lang M, Grzesiak AL, Matzger AJ. The Use of Polymer Heteronuclei for Crystalline Polymorph Selection. Journal of the American Chemical Society. 2002;124(50):14834-5.
9. Rowe RC, Sheskey PJ, Quinn ME. Handbook of pharmaceutical excipients: Pharmaceutical press; 2009.
10. Górniak A, Wojakowska A, Karolewicz B, Pluta J. Phase diagram and dissolution studies of the fenofibrate–acetylsalicylic acid system. Journal of thermal analysis and calorimetry. 2011;104(3):1195-200.
11. Heinz A, Gordon KC, McGoverin CM, Rades T, Strachan CJ. Understanding the solid-state forms of fenofibrate–a spectroscopic and computational study. European Journal of Pharmaceutics and Biopharmaceutics. 2009;71(1):100-8.
12. Balendiran GK, Rath N, Kotheimer A, Miller C, Zeller M, Rath NP. Biomolecular Chemistry of Isopropyl Fibrates. Journal of pharmaceutical sciences. 2012;101(4):1555-69.
13. Di Martino P, Palmieri G, Martelli S. Evidence of a metastable form of fenofibrate. Die Pharmazie. 2000;55(8):625-6.
14. Henry R, Zhang G, Gao Y, Buckner I. Fenofibrate. Acta Crystallographica Section E: Structure Reports Online. 2003;59(5):o699-o700.
15. Haubruge HG, Daussin R, Jonas AM, Legras R, Wittmann JC, Lotz B. Epitaxial Nucleation of Poly(ethylene terephthalate) by Talc: Structure at the Lattice and Lamellar Scales. Macromolecules. 2003;36(12):4452-6.
16. Mitchell CA, Yu L, Ward MD. Selective Nucleation and Discovery of Organic Polymorphs through Epitaxy with Single Crystal Substrates. Journal of the American Chemical Society. 2001;123(44):10830-9.
17. Rayner J. The crystal structure of talc. Clays and Clay Minerals. 1973;21:103-14.
18. Last JA, Hooks DE, Hillier AC, Ward MD. The Physicochemical Origins of Coincident Epitaxy in Molecular Overlayers: Lattice Modeling vs Potential Energy Calculations. The Journal of Physical Chemistry B. 1999;103(32):6723-33.

5. Chapter 5: Fenofibrate loaded solid dispersions prepared by electrospinning and their moisture sorption behaviour

5.1 Introduction

Electrospining can be used for producing solid dispersion formulations in which micro to nano sized polymer fibres can be fabricated by employing electrostatic forces (1-4). Thus, these fibres form three-dimensional porous matrices that have the great advantage of their large surface area to volume ratio (3, 4). This high surface area to volume ratio shows an improved dissolution of poorly water soluble drugs (5-7). The high surface area to volume is a remarkable advantage, however, it can promote moisture uptake in electrospun fibre formulations.

The application of polymer blends in solid dispersions demonstrates many promising advantages, including increased physical stability of amorphous solid dispersions and reduced moisture uptake of the formulations (8). Additionally, blending a suitable electrospinning filament-forming agent with a poorly spinnable polymer can improve the total spinnability of the system. Electrospinning was used as the primary means for producing solid dispersion formulations in this chapter. The electrospun fibres were prepared from blends of hydrophilic polymers and hydrophobic polymers. The rationale for using a combination of the hydrophilic and hydrophobic polymers is to minimise the moisture uptake of the electrospun formulations that would impede the amorphous drug crystallisation. PVP-90 is a good filament forming polymer for blending with low molecular weight polymers as it can enhance the spinnability of the blends (9). Thus, it was selected as the hydrophilic electrospun matrix for blending with low hygroscopic polymers, including dimethyl- aminoethyl methacrylate (Eudragit E), polyvinyl caprolactam - polyvinyl acetate - polyethene glycol graft copolymer (Soluplus) and hypromellose acetate succinate (HPMCAS). Two drugs were used in this Chapter: FF and PCM, with FF being a poorly water-soluble drug. In Chapters 3 and 4 the crystallisation behaviour of FF was discussed. It is a challenging drug that demonstrates a high possibility of recrystallisation in a solid dispersion matrix (10). PCM is another drug that has demonstrated hydrogen bonding with PVP (11, 12). Hydrogen bonding between the drug and polymer is an essential parameter that enhances the miscibility of the drug and polymer and also prevents the drug from recrystallisation under a stressed environment (13). PCM-PVP-HPMCAS fibres were used for a comparison to the FF solid dispersions to study the effect of hydrogen bonding on the physical stability of the electrospun fibres under a high humidity environment.

The moisture uptake in a solid dispersion leads to phase separation and amorphous drug crystallisation (14, 15). This irreversible change in solid dispersion formulations

significantly reduces the dissolution of the solid dispersion formulation (16). The influence of moisture uptake on the stability of the solid dispersion formulations prepared from hot-melt extrusion and co-evaporation has been studied (17, 18). However, little is known about the moisture sorption of electrospun fibre solid dispersions. The presence of moisture may lead to fibrous structure deformation, drug-polymer phase separation and provoke amorphous drug crystallisation. These events are expected to occur faster than with other solid dispersion formulations that are prepared by hot melt extrusion and co-evaporation because of the larger surface area to volume ratio of electrospun fibres.

This chapter aims to develop polymer blended electrospun fibrous formulations that potentially stabilise the drugs in their amorphous state and enhance the dissolution of FF. Secondly, we also studied the influence of moisture sorption on the miscibility of the polymer-polymer and drug-polymer in the electrospun fibrous films. The chapter renders a fundamental understanding of the moisture uptake kinetics in electrospun fibres along with an in-depth investigation of the phase separation and drug recrystallization on the electrospun fibres.

5.2 Methodology

5.2.1 Stock solution preparation

There are two types of stock solution used in this chapter: placebo and drug loaded stock solutions. The placebo solutions were prepared by dissolving 10 % w/v of the polymer blends at a ratio of 1:1 of PVP with Eudragit, HPMCAS or Soluplus in 7:3 ethanol:DCM. Then, the solutions were stirred until all of the components were dissolved. The solid-state drug content was fixed at 25%. The drug was added into single (PVP, HPMCAS, Eudragit Eand Soluplus) solutions or polymer blended solutions (ratio of 1:1 of PVP:HPMCAS, PVP:Eudragit E and PVP:Soluplus) in 7:3 ethanol:DCM solvent. These were stirred until clear solutions were obtained.

5.2.2 Sample preparation

In this chapter, two types of polymer films were prepared, which were cast films and electrospun fibrous films. In the cast films, 1 ml of the stock solution was applied to a Teflon plate and a casting knife with a 50 µm gap was used to obtain a smooth flat cast film. Then, the films were left in a fume hood for 24 h to allow the organic solvent to evaporate. On the other hand, a custom-made electrospinning apparatus was used to prepare the electrospun fibres. The stock solution was filled into a plastic syringe that was equipped with a syringe pump (Cole-Parmer, UK). The feed rate was set at 1.5 $ml.hr^{-1}$ by applying a voltage of 15 kV from an ES40P-20W high voltage power supply (Gamma High Voltage

Research Inc., Ormond Beach, FL, USA). The drum collector was used to collect the electrospun fibres at 500 RPM. The distance between the spinnerette and the collector was fixed at 15 cm. The electrospinning was conducted under ambient humidity at room temperature (temperature 24°C and 45-55% RH). All electrospun samples were stored in a 0% RH desiccator filled with phosphorus pentaoxide.

5.2.3 Characterisation methods

In this chapter, a range of characterisation techniques was employed to characterise the ternary blended formulation, including MTDSC, ATR-FTIR, FT-IR microscopy, PXRD and SEM. The experimental methods of MTDSC, ATR-FTIR, PXRD and SEM are referred to in Chapter 2 in sections 2.4.2.2, 2.4.5.2, 2.4.7.4 and 2.4.8.2, respectively.

5.2.4 Moisture sorption and kinetic model study

DVS was used to perform the sorption isotherm and isohume experiments of the electrospun fibres and cast films. For the experimental method of DVS refer to section 2.4.4.2. Then, the kinetic sorption data were fitted to the mathematical models described in Chapter 2 section 2.7.2, including GAB, Peleg and DE models. The data fitting were performed by TableCurve 2D version 5.01 (Systat Software Inc., Chicago, USA)

5.2.5 *In vitro* drug release study

All *in vitro* drug release experiments were performed according to the method described in section 2.6.1.2. A 50 rpm paddle rotation speed and 500 ml of British Pharmacopoeia HCl dissolution medium (pH 1.2) with 0.5% sodium lauryl sulphate were used for each vessel and the temperature of the vessel was controlled at 37±0.5 °C. Pieces of the electrospun fibre mats that contain the equivalent of 10 mg FF (calculated by weight) were used for the release tests to ensure sink conditions. The media (5 ml) from each vessel were sampled at predetermined time intervals, filtered through 0.45 μm filters (Minisart Sartorius, Goettingen, Germany) and then diluted with 5 ml of ethanol. As all dissolution tests were performed under sink conditions, no recrystallization of the model drug as nanocrystals was expected after release from the formulation; therefore, the filtration method for treating the dissolution samples was appropriate. The FF content in each sample was measured by a UV spectrometer (Perkin-Elmer Lamda XLS, USA) at 290 nm. All measurements were performed in triplicate.

5.2.6 Solubility parameter estimation

The Fedor's group contribution method was used to estimate the solubility parameter of the drug and polymers in this study (19). This approach relies on additive atomic and group contributions of vapourisation energy at a given temperature. Further details of the theory

behind this approach and its applications were discussed in section 1.4.2.3. It was applied to calculate the solubility parameter of the model drugs and polymers. In the polymers, the solubility parameter was estimated from a single unit of the monomer. The following shows an example of how to calculate the solubility parameter using the Fedor's group contribution method (**Table 5.1**).

Table 5.1 Parameters used for Fedor's group contribution calculation of FF.

Group	Quantity	E_{coh}(kJ/mol)	V(cm^3/mol)
CH_3	4	4710	33.5
Cl	1	11550	24
C=O	2	17370	10.8
O	2	3350	3.8
Benzene ring (para substitution)	2	31940	52.4

$$\delta = \left(\frac{\sum E_{coh}}{\sum V}\right)^{1/2} \quad \text{.....(5.1)}$$

ΣE_{coh} = [(4,710*4)+(11,550*1)+(17,370*2)+(3350*2)+(31,940*2)]= 135,710

ΣV = [(33.5*4)+(24*1)+(10.8*2)+(3.8*2)+(52.4*2)]= 292

$(\Sigma E_{coh}/ \Sigma V)^{1/2}$ = 21.5 $MPa^{1/2}$

The solubility parameters (δ) used in this study are 28.2, 20.5, 23.5, 21.5 and 27.2 $MPa^{1/2}$ for PVP, Eudragit E, Soluplus, FF and PCM, respectively. The solubility parameter (δ) of HPMCAS is 22.4 $MPa^{1/2}$ (taken from the values reported by Mark et al. (20)).

5.2.7 Theoretical T_g calculation using Gordon-Taylor (GT) equation

The GT equation was originally used to estimate the T_g of two-component mixtures. In this study, the formulations are a ternary complex of polymer blended with a model drug. Therefore, the GT equation was modified according to Lu et al. for calculating the ternary mixture (21). The theoretical T_g of the FF and PCM with polymer blend matrices were calculated using this approach. **Equation 5.2** is the adapted GT equation for the ternary system, and *K* can be calculated based on the Couchman-Karasz model (**equation 1.12**), which was slightly modified to obtain K_1 and K_2, as seen in the **equation 5.3**.

$$T_g = \frac{W_1 T_{g1} + K_1 W_2 T_{g2} + K_2 W_3 T_{g3}}{W_1 + K_1 W_2 + K_2 W_3} \quad \text{..... (5.2)}$$

$$K_1 \approx \frac{\Delta C_{p2}}{\Delta C_{p1}} \; and \; K_2 \approx \frac{\Delta C_{p3}}{\Delta C_{p1}} \quad \text{..... (5.3)}$$

Where W_1, W_2 and W_3 are the weight fractions of FF or PCM, PVP and HPMCAS, Soluplus or Eudragit; T_{g1}, T_{g2} and T_{g3} are the glass transition temperatures of FF or PCM, PVP and HPMCAS, Soluplus or Eudragit; and ΔC_{p1}, ΔC_{p2} and ΔC_{p3} are the heat capacity changes of FF or PCM, PVP and HPMCAS, Soluplus or Eudragit. The theoretical glass transition temperatures of the ternary blends are reported in **Table 5.3**.

5.2.8 Physical stability study

The stabilities of the FF loaded electrospun fibres were monitored for six months. The fibres were stored at 0%RH in a desiccator filled with phosphorus pentaoxide. Their stabilities were monitored using MTDSC to detect the FF recrystallization. The MTDSC experimental parameters are described in detail in section 2.4.2.2.

5.3 Results

5.3.1 Physical characterisation of placebo and FF loaded electrospun fibres and cast films

- **Fresh placebo**

The electrospun fibres of HPMCAS, Eudragit E and Solulpus could not be prepared because the concentration of these polymers used in this study (10% w/v) was not suitable to fabricate electrospun fibres (**Figure 5.1**). Eudragit E and Solulpus form microparticles, which have a size less than approximately 5 µm (**Figure 5.1 a** and **c**). HPMCAS forms beaded fibres that are very fragile and cannot be used as fibrous films (**Figure 5.1b**). PVP is the most suitable polymer for electrospinning as it fabricates a smooth fibrous structure at concentrations of 5% w/v (**Figure 5.1d**). The average diameter of PVP prepared from solution concentrations of 5 and 10% w/v were 0.50±0.17 and 0.75±0.24 µm, respectively. Blending HPMCAS, Eudragit E or Solulpus with PVP at the ratio of 1:1 enhances the spinnability of HPMCAS, Eudragit E and Soluplus**.** The electrospun fibres illustrate a random direction arrangement of smooth cylindrical fibres. The placebo electrospun fibres showed average diameters of 1.29±0.41, 0.82±0.22 and 1.07±0.25 µm for PVP-HPMCAS, PVP-Eudragit E and PVP-Soluplus fibres, respectively **(Figure 5.1f-h)**.

The SEM images shown in **Figure 5.2** reveal the surfaces of the placebo cast films, which are largely flat and smooth. The polymer blended cast films of PVP-HPMCAS and PVP-

Soluplus also demonstrate smooth PVP films. Only PVP-Eudragit E cast films show rough surfaces with hemispherical island features.

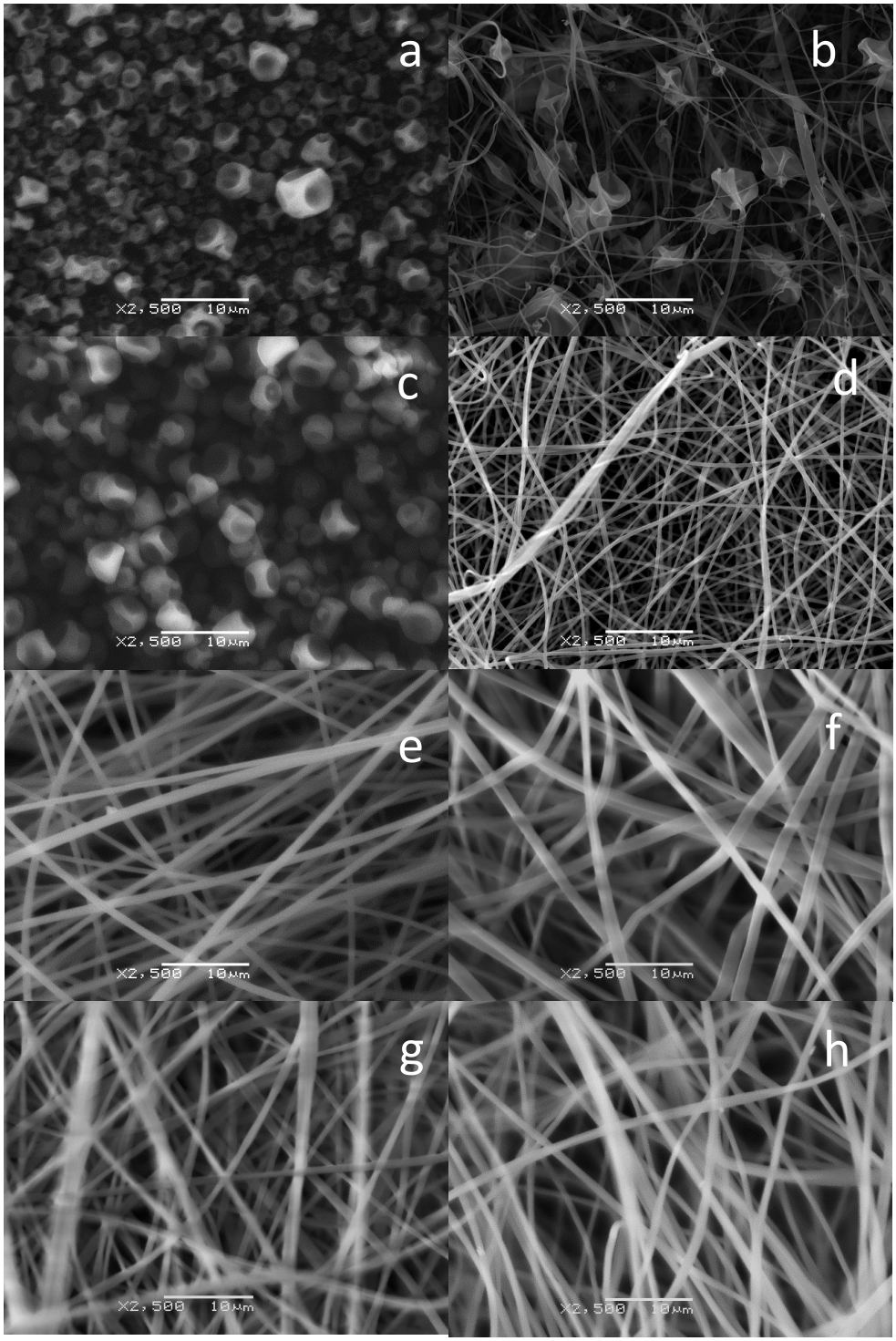

Figure 5.1 SEM images of single polymer and polymer blend (ratio 1:1) electrospun (a)10% w/v Eudragit, (b) 10% w/v HPMCAS, (c)10% w/v Soluplus, (d) 5% w/v PVP, (e)10% w/v PVP, (f) 10% w/v PVP-HPMCAS, (g) 10% w/v PVP-Eudragit E and (h)10% w/v PVP-Soluplus.

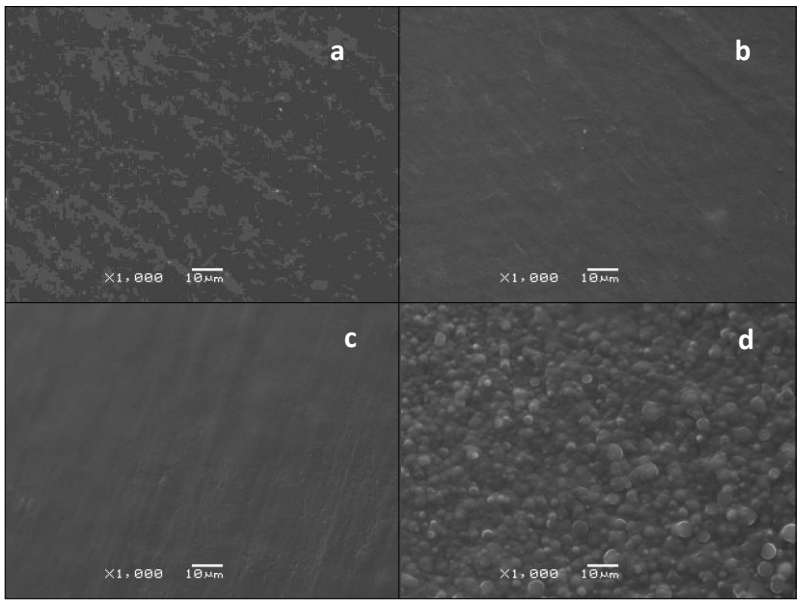

Figure 5.2 SEM images of surface of cast film: (a) PVP, (b) PVP-HPMCAS, (c) PVP-Soluplus and (d) PVP-Eudragit E.

MTDSC was used to investigate the phase separation in the polymer blended electrospun fibres and cast films. Double T_gs were observed for the PVP-Soluplus and PVP-Eudragit E for both cast films and electrospun fibres (**Figure 5.3a**), while PVP-HPMCAS cast and electrospun fibres demonstrated a single T_g at 152.5±1.3 and 152.4±1.0 °C, respectively. The single T_g indicates that these polymers are miscible after film casting.

FTIR transmission mapping has been used to study the phase separation of poly(3-hyroxybutyrate) with poly(l-lactic acid) and poly(Ɛ-caprolactone) (22). This technique is based on an infrared microscope to raster a map with a high spatial resolution. In the FTIR spectroscopy, the intensity of the acquired spectrum is related to the thickness of the sample (23). A thick sample results in high IR beam absorption, while a thin area has a lower IR beam absorption. Therefore, a suitable sample for the FTIR transmission mapping should have a consistent thickness throughout the sample (23), and a flat surface to ensure a consistent focus across the area. In this chapter, the cast films were examined by FTIR transmission imaging because they have a flat surface and relatively consistent thickness, of approximately 10 μm. In contrast, the electrospun fibrous mats are not suitable for FTIR transmission mapping because of their porous structure that is constructed from random arrangement of electrospun fibres. Thus, it results in optical problems, mainly from light scattering. FTIR mapping is created from the integral area or the ratio between two integral peak areas from the acquired FTIR spectra. The different colours in the FTIR map reflect different integral values in the site of interest. In **Figure 5.4,** all plots are autoscaled blue being the lowest and red being the highest. Each plot has different scale as labeled.

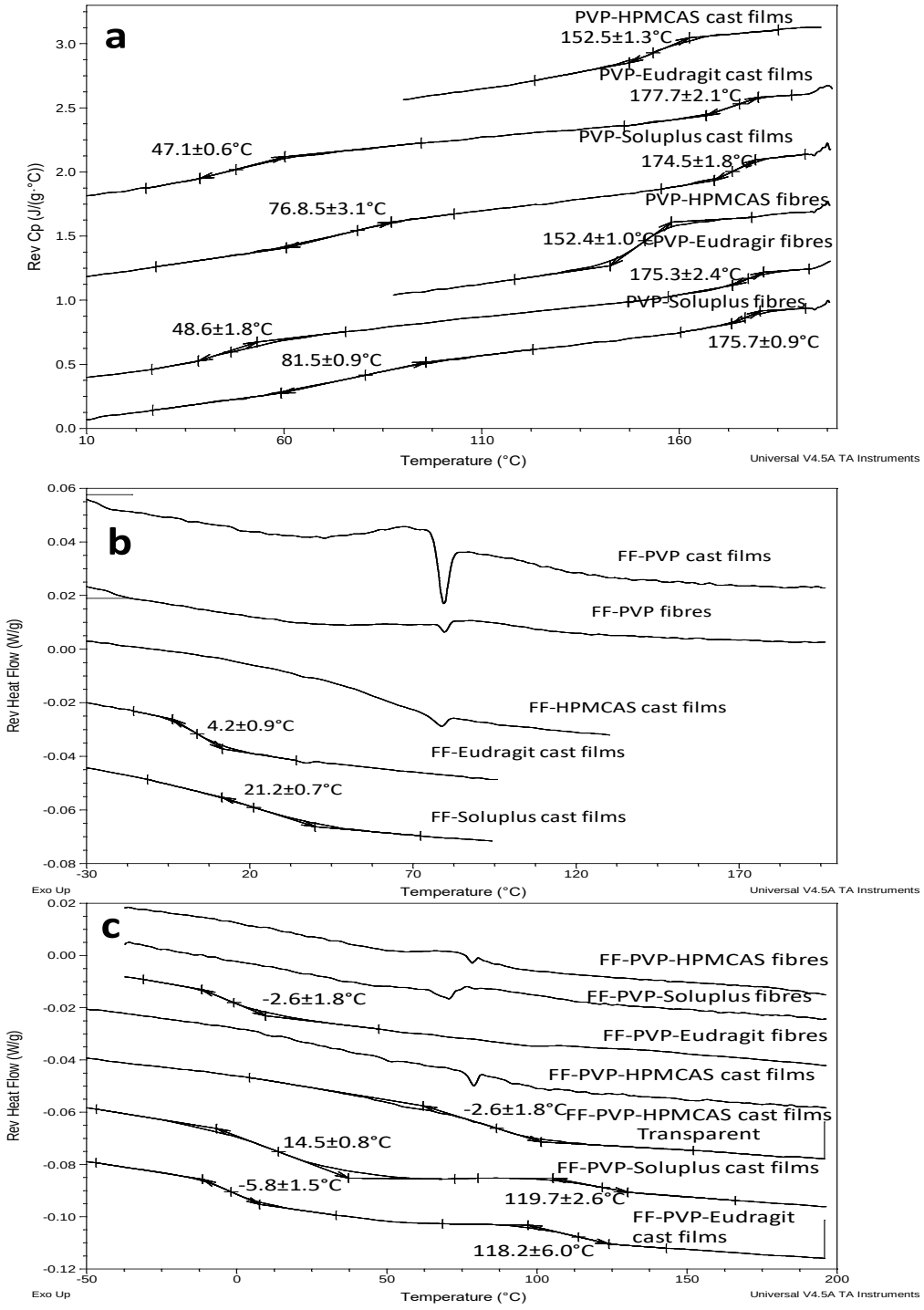

Figure 5.3 MTDSC results of placebo and FF loaded cast films and electrospun fibres: (a) placebo blends, (b) single polymer with FF loading and (c) polymer blends with FF loading.

The phase separations of the PVP-HPMCAS, PVP-Eudragit E and PVP-Soluplus were studied using FTIR transmission mapping. Theoretically, a characteristic peak of each polymer is need to construct the FTIR image. A wavenumber in the range between 2000 to 1500 cm^{-1} cannot used to construct the map because of the inconsistent integral values from the signal overshoot (intensity is much greater than one absorption unit). At an absorbance greater than one, the relationship between the substance concentration and absorbance is not linear. The signal overshoot in strong bands is due to the errors of the instrument data processing when the observed light transmission approaches zero. At 1500 to 600 cm^{-1}, there are too many overlapping peaks for these polymers, which are difficult to assign clearly to one component and not suitable to construct a chemical map. Although this is not ideal, the ratio of the absorption of the methyl stretching of the polymers at 2910 cm^{-1} (integral range 3000 to 2800 cm^{-1}) and OH stretching at 3450 cm^{-1} (integral range 3700 to 3100 cm^{-1}) is used to construct an FTIR image. The area that shows a low ratio of methyl stretching/OH stretching integral peaks represents a PVP rich region. This is due to PVP attracting water molecules more than the HPMCAS, Eudragit E and Soluplus. The PVP-Eudragit E and PVP-HPMCAS FTIR mapping demonstrate similar spectra through the mapping area . The variation across the area is actually very small scale. Thus, the observed colour changes show essentially the experimental error during the mapping. This indicates a homogeneous dispersion of the polymer blends or a phase separation domain that is smaller than the spatial resolution of the FTIR mapping (25µm) (**Figure 5.4 a and b**). In **Figure 5.4 c**, two distinguished domains are clearly observed in the PVP-Soluplus cast films. The blue and green colours reflect the higher PVP content in comparison to the red area, and the phase separation of the PVP-Soluplus cast films can be seen as circular domains with sizes of approximately 50 to 100 µm.

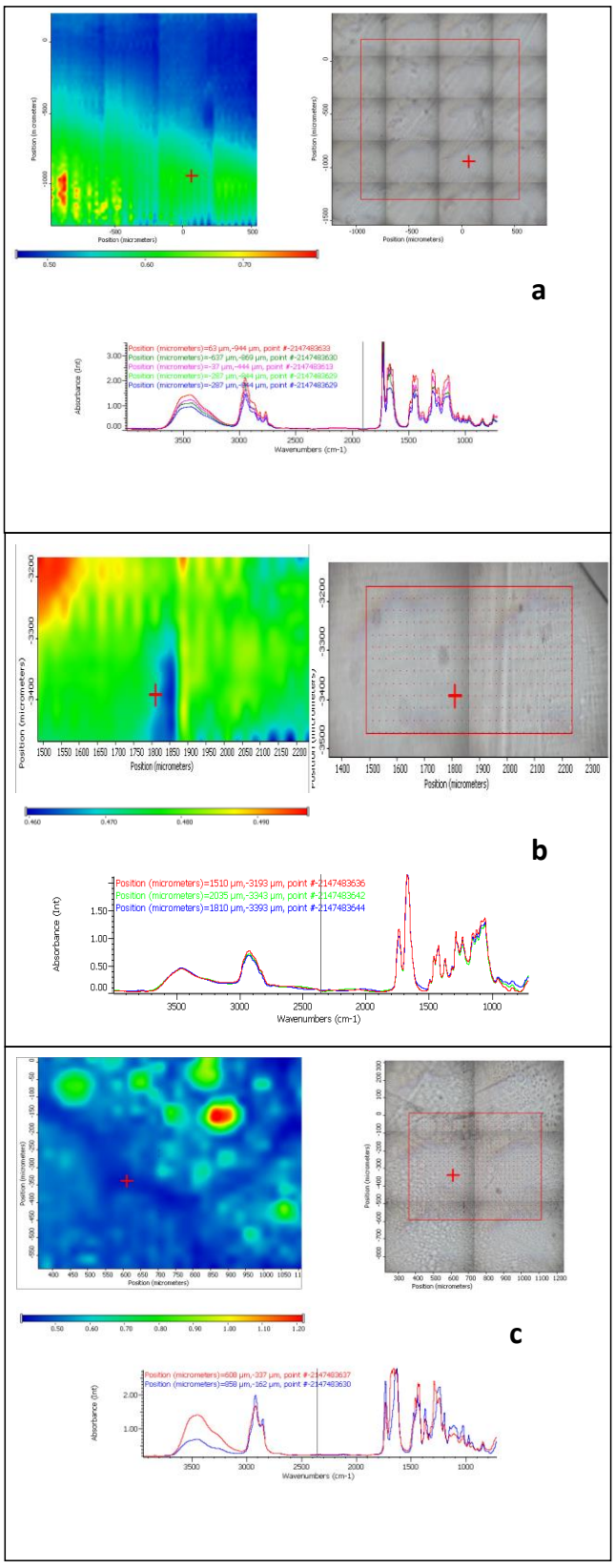

Figure 5.4 Phase separation detected by FTIR transmission microscopy in the placebo blended cast ilms; (a) PVP-Eudragit E cast films, (b) PVP-HPMCAS cast films, (c) PVP-Soluplus cast films. The left panel shows a FTIR transmission map calculated from (a-c) in which the ratio of the integral peak area of the methyl stretching/OH stretching. The righ

panel demonstrates a visible image of the area of the map and the bottom panel is the representative FTIR spectra that was used to construct the FTIR mapping

- **Fresh FF loaded solid dispersions**

The FF-HPMCAS, FF-Eudragit E and FF-Soluplus were prepared only as cast films because these polymers are not spinnable, as discussed earlier. FF-PVP was produced as both cast films and electrospun fibres. Electrospinning and film casting were used to prepare the ternary drug-polymer blends. The paracetamol loaded PVP-HPMCAS (PCM-PVP-HPMCAS) was prepared only by electrospinning for comparing the moisture sorption and physical stability at 75% RH to the FF loaded polymer blended solid dispersions. ATR-FTIR was used to study the interaction between the FF and the polymers. As seen in **Figure 5.5**, neither the polymer peaks nor drug peaks demonstrated any shift from their original positions. This implies that FF does not show any strong interaction with PVP, HPMCAS, Eudragit E and Soluplus. It should be noted that the O_1-C_7 carbonyl stretching (1655 cm^{-1}) of FF was absent in the FF-Soluplus cast films. However, other peaks showed no shift. It is possible that the FF carbonyl peak merged with a broad carbonyl peak in the caprolactam group of Soluplus at 1625 cm^{-1}.

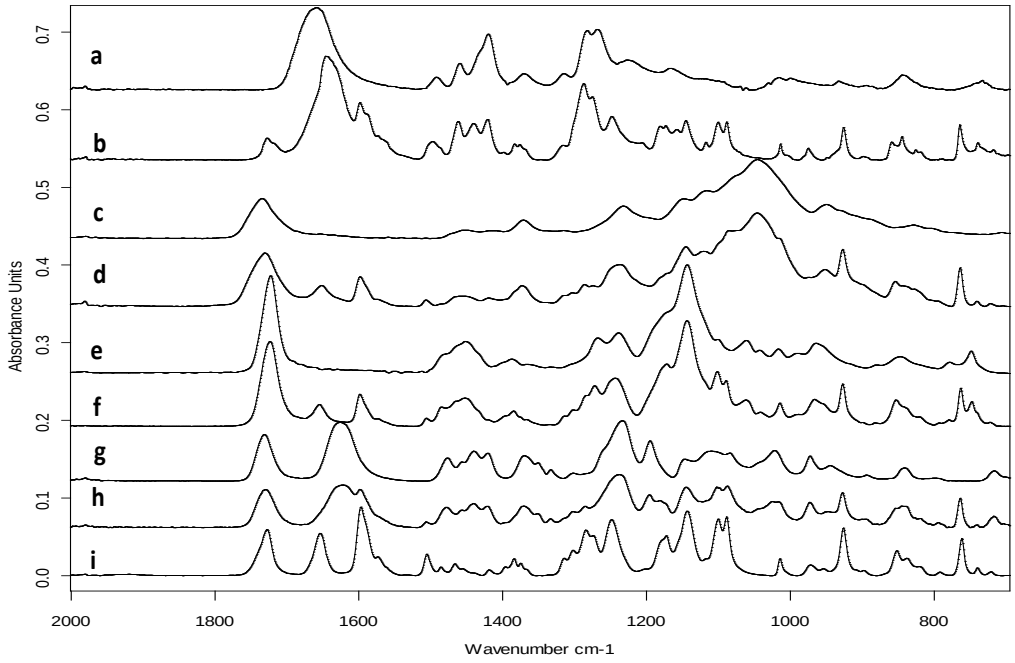

Figure 5.5 ATR-FTIR of raw materials and cast films of FF-polymer: (a) PVP, (b) FF-PVP, (c) HPMCAS, (d) FF-HPMCAS, (e) Eudragit, (f) FF-Eudragit, (g) Soluplus, (h) FF-Soluplus and (i) amorphous FF.

In **Figure 5.3b,** the melting enndotherms of FF at 80°C indicate that form I were seen in the electrospun fibres and cast films of FF-PVP, but no T_g was observed. It should be noted that FF-PVP cast films demonstrate higher melting enthalpies than the electrospun fibres. The melting enthalpy values of these samples are summarised in **Table 5.2**. This result implies that the electrospinning can minimise FF crystallisation in the FF-PVP dispersions in the fresh samples. The FF-HPMCAS also showed a small melting enthalpy of FF at 80°C, and its T_g can be observed at 54.3 ±1.3°C. The melting enthalpies reflect a partial miscibility between the drug and the polymers. The majority of the FF molecules are in the amorphous state while some of the drug recrystallized in the dispersions. The FF-Eudragit E and FF-Soluplus cast films demonstrate a single T_g without melting at 4.2±0.9°C and 21.2±0.7°C, respectively (**Figure 5.3b**). The physical appearance of the FF-Eudragit E and FF-Soluplus cast films were transparent and viscid due to their T_gs being slightly lower than room temperature. As seen in **Figure 5.6**, the experimental T_gs of the FF-HPMCAS, FF-Eudragit E and FF-Soluplus cast films are lower than the T_gs that are calculated from the GT equation (**equation 5.2**). In the literature, such a negative deviation from the GT theoretical calculation has been interpreted as the interaction between the drug-drug and the polymer-polymer being stronger than the drug-polymer interaction in these binary systems (24).

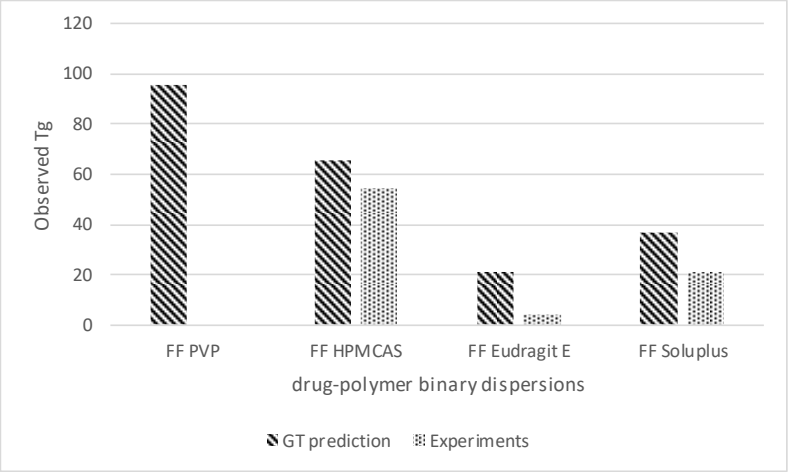

Figure 5.6 Differences between T_gs as predicted by GT equation and experimental observation.

For the drug loaded polymer blend cast films, double T_gs were detected in the FF-PVP-Eudragit E and FF-PVP-Soluplus cast films. The T_gs of the FF-PVP-Eudragit E cast films were at -5.8±1.5 and 119.0±6.0°C, and the T_gs of the FF-PVP-Soluplus cast films were at 13.5±0.8 and 119.7±2.62 °C, respectively. A double T_g is an indication of a phase separation in the polymer blends and also indicates an uneven FF distribution among the two phases. A poor reproducibility was observed in the MTDSC results of the FF-PVP-Soluplus cast film. One of the three replicates of the FF-PVP-Soluplus cast film showed a

small melting endotherm on the reversing heat flow signal, but in the total heat flow moisture evaporation was superimposed on the melting peak. This indicates that the FF crystals located inconsistently in the FF-PVP-Soluplus cast film. The FF-PVP-HPMCAS cast film shows two different areas that are transparent and opaque areas (**Figure 5.7**). The small melting peak at 80°C was observed in the opaque area without a T_g, and this indicates the presence of FF crystals.

Table 5.2 Heat of fusion of FF in the polymer blend cast films and electrospun fibres that are fresh and after DVS experiment. Some of the melting enthalpies of the FF superimpose on the water evaporation. Thus, the overlapping FF melting enthalpies are measured from the reversing heat flow and indicated as [a] and the non-overlapping melting enthalpies are measured from the total heat flow signal indicated as [b].

Materials	***Melting enthalpies of fresh samples (J/g)***	***Melting enthalpies after DVS (J/g)***
FF	89.6±0.6[b]	-
Cast films		
FF-PVP	2.65±0.3[a]	6.67±0.2[a]
FF-HPMCAS	0.78±0.17[b]	1.36±0.14[a]
FF-Soluplus	-	-
FF-Eudragit E	-	-
FF-PVP-HPMCAS	0.32±0.1[a]	0.66±0.2[a]
FF-PVP-Eudragit E	-	1.73±1.3[a]
FF-PVP-Soluplus	0.58[a]*	1.85±0.6[a]
Electrospun fibres		
FF-PVP	0.43±0.2[a]	3.48±0.5[a]
FF-PVP-HPMCAS	0.38±0.2[a]	11.9±3.7[b]
FF-PVP-Eudragit E	-	1.86±0.25[a]
FF-PVP-Soluplus	0.70±0.2[a]	2.82±0.27[a]

Conversely, the transparent area demonstrates a single T_g at 85.5±2.6°C (**Figure 5.3c**). The T_g of the FF-PVP-HPMCAS cast transparent region is similar to the GT prediction at 80.2°C. However, one needs to bear in mind that the FF-PVP-HPMCAS cast film already showed crystalline FF on its surface. Hence, the drug remaining in the transparent phase must be less than the initial loading (25%w/w), and its T_g was expected to be higher than the observed value in the case of the ideal ternary mixing. The partial crystallisation in this sample suggests a low level of inter-molecular interaction among the FF, PVP and HPMCAS.

Figure 5.7 Polymer blended cast films with FF loading: (a) FF-PVP-HPMCAS, (b) FF-PVP-Eudragit E and (c) FF-PVP-Soluplus cast films. The FF PVP-HPMCAS films show different transparent and opaque areas. The opaque area has crystallised FF on the surface of the cast films, whereas the FF-PVP-Eudragit E and FF-PVP-Soluplus cast films demonstrate transparent areas.

No T_g was observed in the FF-PVP-HPMCAS and FF-PVP-Soluplus electrospun fibres, but small melting enthalpies of the FF crystals were detected (**Figure 5.3c**). The difficulty in finding the T_g of the FF-PVP-HPMCAS and FF-PVP-Soluplus electrospun fibres may be due to the combination of weak T_g and the fibrous samples not being flat and not being able to establish good contacts with the bottom of the DSC pan. The FF-PVP-Eudragit E fibres show a single T_g at -2.6±1.8°C. This T_g is similar to the lower T_g of the double T_g of the FF-PVP-Eudragit E cast films.

SEM images revealed that the FF-Eudragit E and FF-Soluplus cast films have smooth surfaces; whereas, some drug crystals can be observed at the surface of the FF-PVP and FF-HPMCAS cast films. These results were confirmed by the drug melting observed in the MTDSC results of these samples (**Figure 5.3b).** In the drug-loaded blended cast films, some densely packed crystals were present on the surfaces of the FF-PVP-HPMCAS films and isolated large crystals were observed on the surface of the FF-PVP-Soluplus films; whereas, no FF crystal was observed on the surface of the FF-PVP-Eudragit E films **(Figure 5.8)**. These findings also agree with the previous MTDSC results indicating that FF is partially miscible with PVP and HPMCAS. The FF-PVP fibres show an average fibre diameter of 0.51±0.02 µm. The diameters of the FF loaded polymer blend electrospun fibres are 0.77±0.17 µm, 1.03±0.39 µm and 0.77±0.16 µm for the FF-PVP-Eudragit, FF-PVP-HPMCAS and FF-PVP-Soluplus, respectively. The PCM-PVP-HPMCAS electrospun fibres show an average fibre diameter of 0.75±0.2 µm **(Figure 5.8)**. There is no significant difference between the average diameter of the placebo and drug loaded fibres.

Table 5. 3 Comparison of experimental and theoretical T_gs of all formulations predicted using GT equation. *T_g of FF-PVP-HPMCAS cast film was measured from its transparent area.

Material	***T_g 1 (°C)***	***T_g 2 (°C)***	***GT predicted T_g (°C)***
FF	-20±0.5	-	-
PVP	176.4±2.0	-	-
HPMCAS	122.0±2.2	-	-
Soluplus	77.0±0.8	-	-
Eudragit E	55.8±0.5	-	-
Cast films			
FF-PVP	-	-	95.7
FF-HPMCAS	54.3±1.5	-	65.4
FF-Soluplus	21.2±0.7	-	36.5
FF-Eudragit E	4.2±0.9	-	21.2
FF-PVP-HPMCAS*	85.5±2.6	-	80.2
FF-PVP-Eudragi Et	-5.8±1.5	119.0±6.0	60.0
FF-PVP-Soluplus	13.50±0.8	119.7±2.62	66.0
Electrospun fibres			
FF-PVP	-	-	95.7
FF-PVP-HPMCAS	-	-	80.2
FF-PVP-Eudragit E	-2.6±1.8	-	60.0
FF-PVP-Soluplus	-	-	66.0

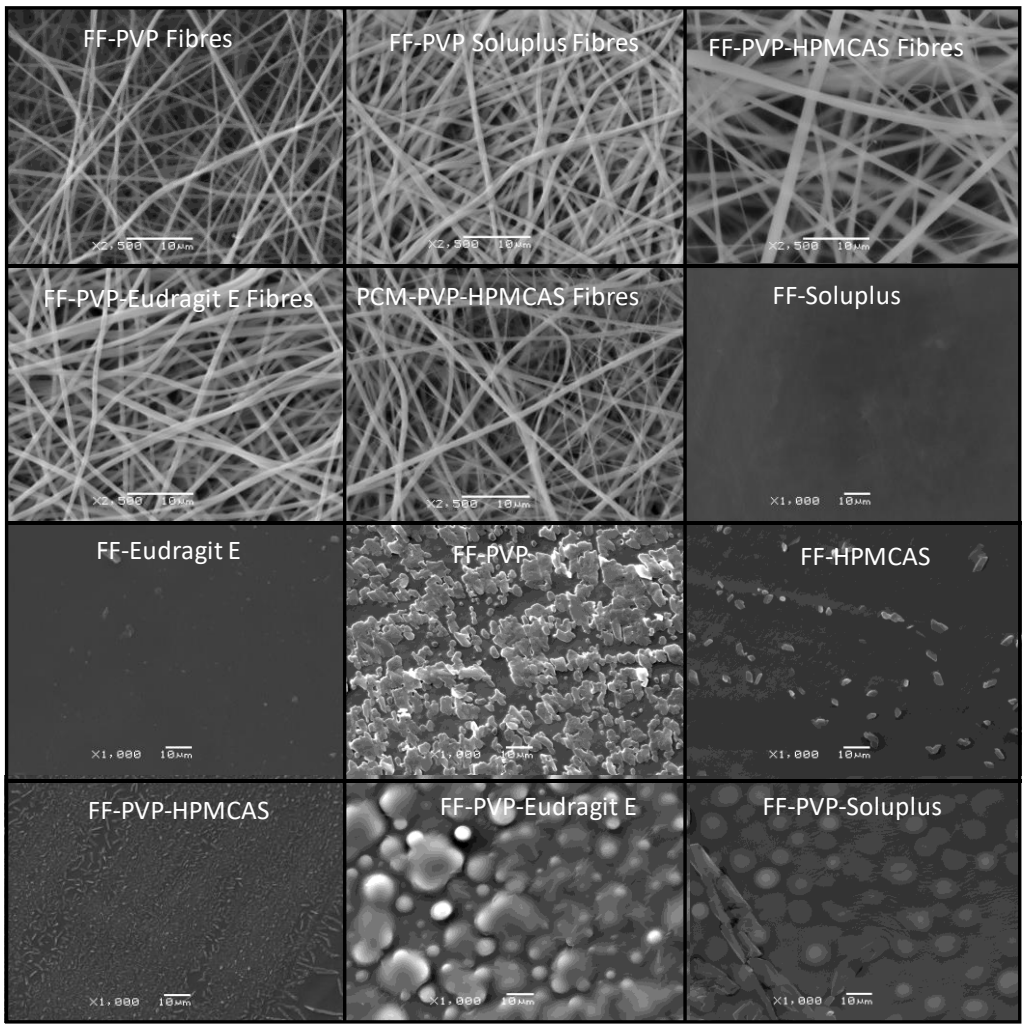

Figure 5.8 SEM images of freshly prepared placebo and drug-loaded electrospun fibres as well as freshly prepared placebo and FF loaded cast films

FTIR transmission mapping was used to study the drug loaded cast films. This was based on the distribution of the integral peak area of the =CH-H stretching at 3070 and 3054 cm^{-1} with a selected baseline from 3100 to 3020 cm^{-1}; these are characteristic peaks of the crystalline FF form I. The rationale of selecting this region was because it is neither overlapping with the polymer peaks nor the overshooting signal. In **Figure 5.9c**, the FTIR transmission mapping shows the FF crystals on the FF-PVP-HPMCAS cast film. This result agrees with its optical microscopic image in which the FF crystals were observed on the surface. However, from the low peak intensity of the FF form I, it is possible to deduce that the FF crystals were only located on the surface of the films. The big circular spots observed in both the FTIR mapping and optical image were FF crystals that recrystallized on the surface of the FF-PVP-HPMCAS cast films. This result indicates the co-existence of amorphous and crystalline FF in the FF-PVP-HPMCAS cast films. Additionally, the FTIR microscopic mapping of the FF-PVP-Soluplus cast film shows a suspect area indicated by the red spot that may be FF crystals and green lines may be surface defects that FF could also accumulate, as seen in **Figure 5.9d.** From the microscopic images, it is

likely to be a single crystal of FF that is located on the surface of the FF-PVP-Soluplus cast films. The FF-PVP-Eudragit E and FF-PVP showed that the drug was in an amorphous phase throughout the bulk of these cast films, because the scale of the variation across the map was consistently small, which showed only experimental variability. The smooth image could also mean that the crystalline FF size was smaller than the resolution of the IR mapping (25µm per pixel), as seen in **Figure 5.9 a** and **b**.

To investigate the drug crystallisation of the surfaces of the cast films, ATR-FTIR was used to examine both sides of the FF loaded cast films. In this study, we used a single reflection and the ATR crystal was made from a diamond with the angle of incidence of 45°. The estimated penetration depth of the evanescent IR waves were approximately 0.5-2 µm (25). **Figure 5.10** shows that the crystalline FF form I characteristic peaks (3070 and 3054 cm^{-1}) are observed on at least one side of the FF-PVP and FF PVP-HPMCAS, whereas they are absent in the FF-PVP-Eudragit E and FF-PVP-Soluplus films. This is an indication of FF crystal growth occurring on the surface of the FF-PVP and FF-PVP-HPMCAS cast films.

In the FF loaded electrospun fibres, no peaks indicative of crystalline FF were present in the ATR-FTIR spectra as seen in **Figure 5.11**. However, small melting endotherms were observed in the FF-PVP and FF-PVP-HPMCAS fibres, as seen in **Figure 5.3c**. The lack of IR indicative peak is likely caused by a combination of the sample containing a low amount of FF crystals and the porous structure of the fibrous mats that may reduce the penetration depth of the beam (25,26), thus it cannot detect the crystal located in the interior of the fibrous mats.

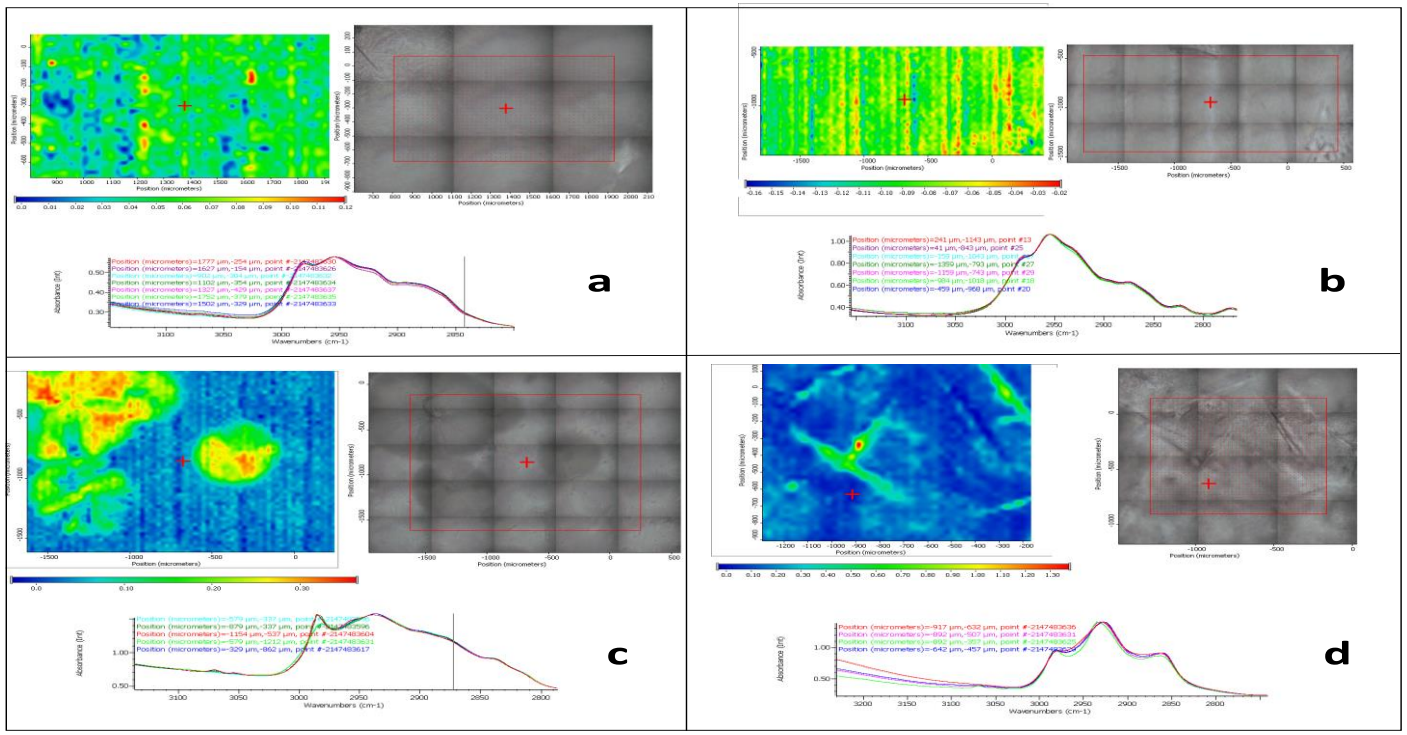

Figure 5.9 Phase separation detected by FTIR transmission microscopy in FF loaded cast films (a) FF-PVP cast films, (b) FF-PVP-Eudragit E cast films, (c) FF-PVP-HPMCAS cast films and (d) FF-PVP-Soluplus cast films. The left panel shows a FTIR transmission map calculated from the integral of the =CH-H stretching at 3070 and 3054 cm^{-1} are the characteristic peaks of FF form I. The righ panel demonstrates a visible image of the area of the map and the bottom panel is the representative FTIR spectra that was used to construct the FTIR mapping.

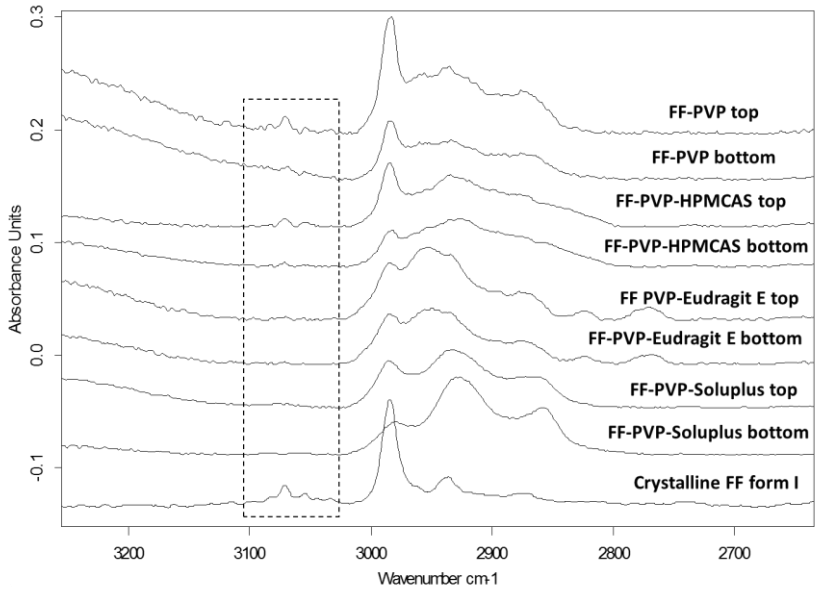

Figure 5.10 ATR-FTIR spectra of FF-PVP, FF-PVP HPMCAS, FF-PVP-Eudragit E and FF-PVP Soluplus cast films for both top and bottom sides of the films.

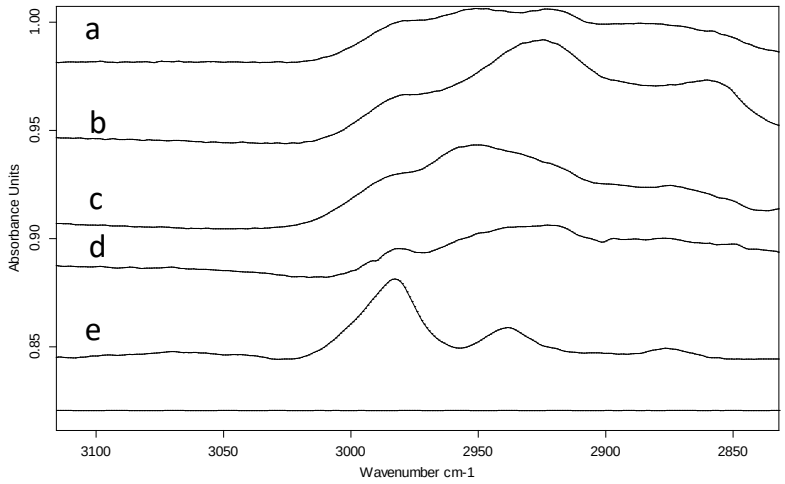

Figure 5.11 ATR-FTIR spectra of FF loaded polymer blend fibrous film: (a) FF-PVP, (b) FF-PVP-Soluplus, (c) FF-PVP-Eudragit E, (d) FF-PVP-HPMCAS and (e) amorphous FF. These spectra demonstrate that the FF in the polymer blended fibrous mats is in the amorphous state because of the absence of the FF crystalline marker peaks at 3070 and 3054 cm^{-1}.

5.3.2 *In vitro* drug release of fresh FF polymer blend electrospun fibres and their physical stability at 0% RH for six months

As illustrated in **Figure 5.12**, all of the electrospun formulations demonstrate greater and faster FF dissolutions than the FF form I powder under sink conditions. The previous characteristic results confirmed that the FF was partially converted into its amorphous state in the fibre dispersions. Its amorphous state offers a higher aqueous solubility and fast dissolution in comparison to its crystalline counterpart. The FF-PVP electrospun fibres showed the fastest drug release, which reached 100% drug release within 10 min. PVP is well-known for being used as an ultrafast electrospun fibrous matrix for improving the solubility of BCS class II drugs (7). The FF-PVP-Eudragit E fibres also showed an immediate drug release because both the PVP and Eudragit E rapidly dissolve in an acidic media. The release from the FF-PVP-Soluplus is slower than from the FF-PVP and FF-PVP-Eudragit E fibres. This may be caused by a slow dissolution of the Soluplus in comparison to the PVP. Nagy et al. also observed that spironolactone loaded Soluplus fibres did not show as quick a release as PVP electrospun formulations (6). As expected, FF-PVP-HPMCAS demonstrated the slowest drug release rate among these formulations as HPMCAS is not soluble in an acidic media. Therefore, this blend can potentially be used for a sustained-release application. Chapter 6 will further explore the potential of this blend to be used as a modified release matrix.

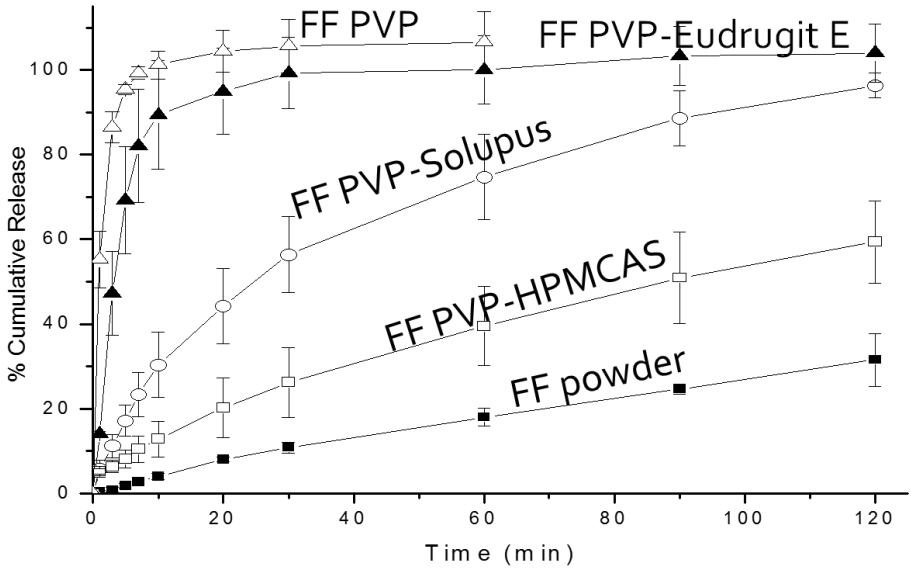

Figure 5.12 *In vitro* drug release profiles of FF loaded PVP single phase, polymer blend fibres with different PVP:Eudragit E, HPMCAS or Soluplus ratios at 1:1 and FF form I powder in pH 1.2 media with 0.5%w/v SLS.

5.3.3 Physical stability of FF polymer fibrous formulation under 0%RH

The physical stability of the FF loaded polymer blended fibres was studied at 0%RH for six months. MTDSC was used to examine the crystallinity of the FF polymer blended fibres at different time intervals to monitor their physical stability. As seen in **Figure 5.13**, all FF loaded electrospun fibrous formulations developed a low level of crystallisation through the six month period of the stability study at 0% RH. The FF-PVP electrospun fibres demonstrated higher FF melting enthalpies than the polymer blend fibres. Therefore, these results indicate that the polymer blend matrices have better stabilisation effects for the amorphous FF than pure PVP. Among the polymer blend electrospun matrices, the FF-PVP-HPMCAS showed the lowest level of FF crystallisation in comparison to the FF-PVP-Eudragit E and FF-PVP-Soluplus fibres under 0%RH.

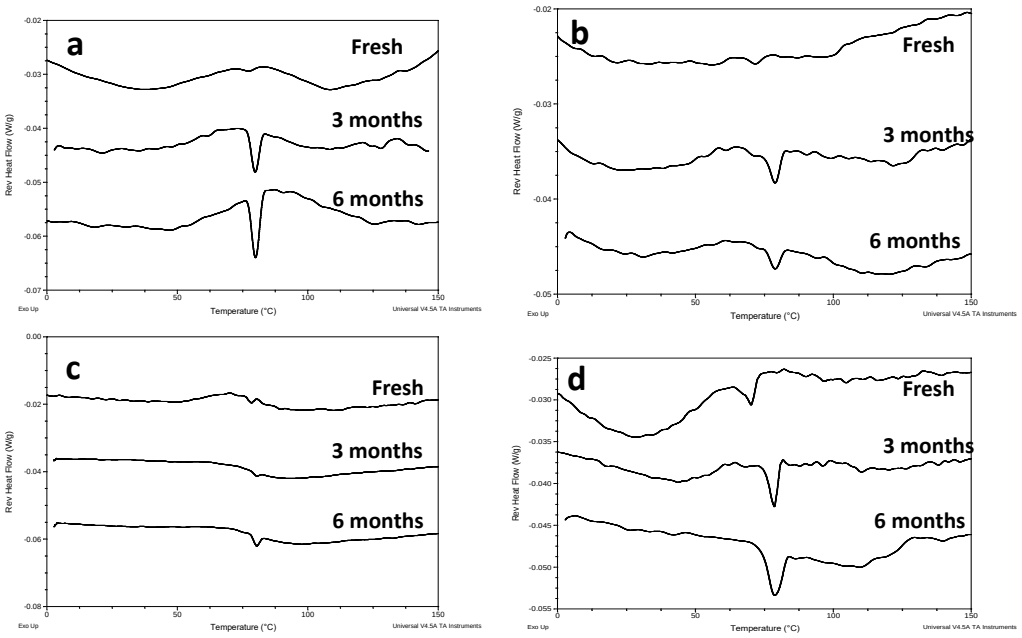

Figure 5.13 Physical stability monitoring by MTDSC of FF loaded electrospun fibres stored at 0%RH for six months: (a) FF-PVP, (b) FF-PVP-Eudragit E, (c) FF-PVP-HPMCAS and (d) FF-PVP-Soluplus.

5.3.4 Kinetics of moisture sorption of placebo and drug loaded dispersions

- **Sorption isotherm and GAB model fitting**

The sorption isotherm experiments were performed at 25°C for the placebo and drug loaded electrospun fibres. The moisture uptakes of these formulations are reported in the ratios of water sorption in grams to polymers in grams ($G_{water}/G_{polymer}$), as seen in **Figure 5.14**. The moisture sorption of the electrospun fibres is RH dependent. The amount of water absorbed

in all the electrospun fibre formulations increased in a linear fashion until 70% RH, and then above this RH, the moisture sorption showed an exponential increase (**Figure 5.14**). The $G_{water}/G_{polymer}$ of the FF-PVP-HPMCAS, FF-PVP-Soluplus and FF-PVP fibres slightly decreased in comparison to the PVP-HPMCAS and PVP placebo fibres. The small difference in moisture absorption may imply that the FF increases the hydrophobicity of these systems. The PVP-Eudragit E blends demonstrated a resemblance of the $G_{water}/G_{polymer}$ of the placebo and FF loaded electrospun fibres. Therefore, FF does not significantly alter the water sorption property of the polymer blend electrospun fibres. Interestingly, the PCM-PVP-HPMCAS fibres demonstrated a lower moisture uptake than their placebo and FF loaded PVP-HPMCAS blends. Forster et al. previously reported that the API that forms a hydrogen bond with PVP could reduce the moisture uptake as PVP has less free carbonyl groups to attract water molecules (26).

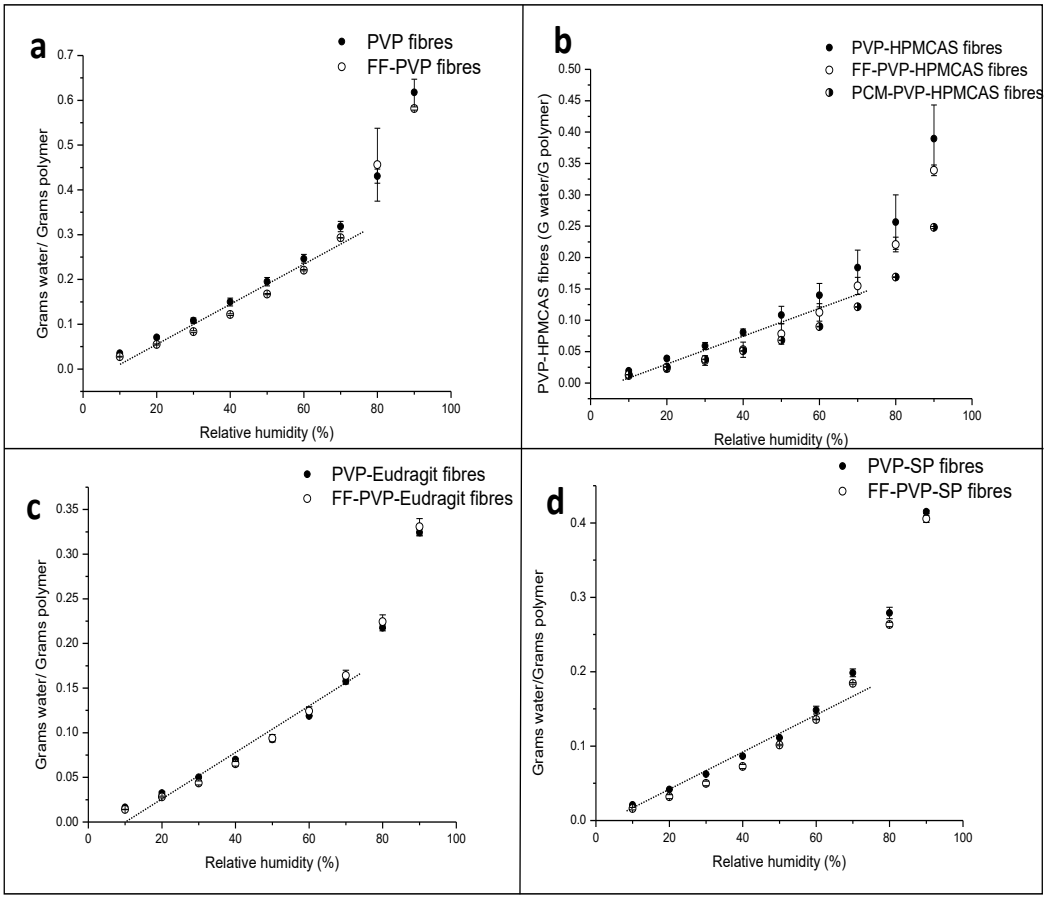

Figure 5.14 Sorption isotherms of FF and PCM loaded and placebo electrospun fibres of blends and single polymers: (a) PVP, (b) PVP-HPMCAS, (c) PVP-Eudragit E and (d) PVP-Soluplus.

The Guggenheim-Anderson-de Boer (GAB) model is a versatile mathematical model to describe non-linear moisture sorption behaviour in foods and pharmaceutical materials that is isothermal type II (sigmoidal shape) (27-29). In this Chapter, it was used to fit the sorption data from 0% to 90% RH to describe and understand the water sorption behaviour

of the electrospun fibres. The details of the GAB model are described in Chapter 2 (**equation 2.12**). There are three GAB parameters: M_0, C_G and K; M_0 is the monolayer moisture content, C_G is the Guggenheim constant and K is the compensating constant for multilayer moisture adsorption that can be obtained from fitting the sorption isotherm data to the GAB equation. The fitting of the electrospun fibres sorption isotherm data to the GAB model is shown in **Figure 5.15**. A good fit is obtained from fitting the sorption isotherm data to the GAB model, which is shown from the R^2 values (>0.99). The values of M_0, C_G and K are reported in **Table 5.4**. There is an unclear relationship between the M_0 of FF loaded formulations in comparison to the placebo blends. In contrast, the decrease in the M_0 of PCM-PVP-HPMCAS reflects a lower surface moisture adsorption. The FF loaded electrospun fibres show a C_G less than two, which indicates that the moisture sorption is not the sigmoidal shape. Thus, the GAB parameters do not have any physical meaning in the FF loaded electrospun fibres (30); they can be used to parametise and predict the moisture sorption as an empirical model. The placebo fibres and PCM-PVP-HPMCAS show a C_G greater than two. Therefore, **equation 5.4** can be used to estimate the water activity (a_w) that the fibres have when saturated with a monolayer of water, which indicates from the inflextion point of the sigmoid curve.

$$a_w = \frac{(C_G-1)^{2/3}-1}{K[(C_G-1)+(C_G-1)^{\frac{2}{3}}]} \quad \text{.....(5.4)}$$

Lewicki reported that the GAB parameters should be in the range $5.67 \leq C_G \leq \infty$ and $0.25 \leq K \leq 1$ to minimise the error of the true water monolayer prediction (≤ 15% deviation) (30). From **Table 5.4**, the C_G values of the placebo electrospun fibres and the PCM-PVP-HPMCAS fibres are between 2 and 3. Thus, the GAB model is a good way to parametrise and predict the water sorption behaviour of the placebo electrospun fibres and the PCM-PVP-HPMCAS fibres, but it is not possible to calculate the moisture sorption monolayer of these fibres.

Table 5.4 GAB model parameter values of placebo and drug loaded electrospun fibres.

Fibres	M_0	C_G	K	R^2
PVP-Eudragit E	0.075	2.72	0.87	0.999
PVP-HPMCAS	0.084	2.89	0.88	0.999
PVP-Soluplus	0.095	2.54	0.87	0.999
PVP	0.158	3.01	0.85	0.999
FF-PVP	0.167	1.84	0.83	0.999
FF-PVP-Eudragit E	0.096	1.66	0.84	0.999
FF-PVP-HPMCAS	0.100	1.08	0.85	0.999
FF-PVP-Soluplus	0.094	1.81	0.88	0.999
PCM-PVP-HPMCAS	0.059	2.40	0.87	0.999

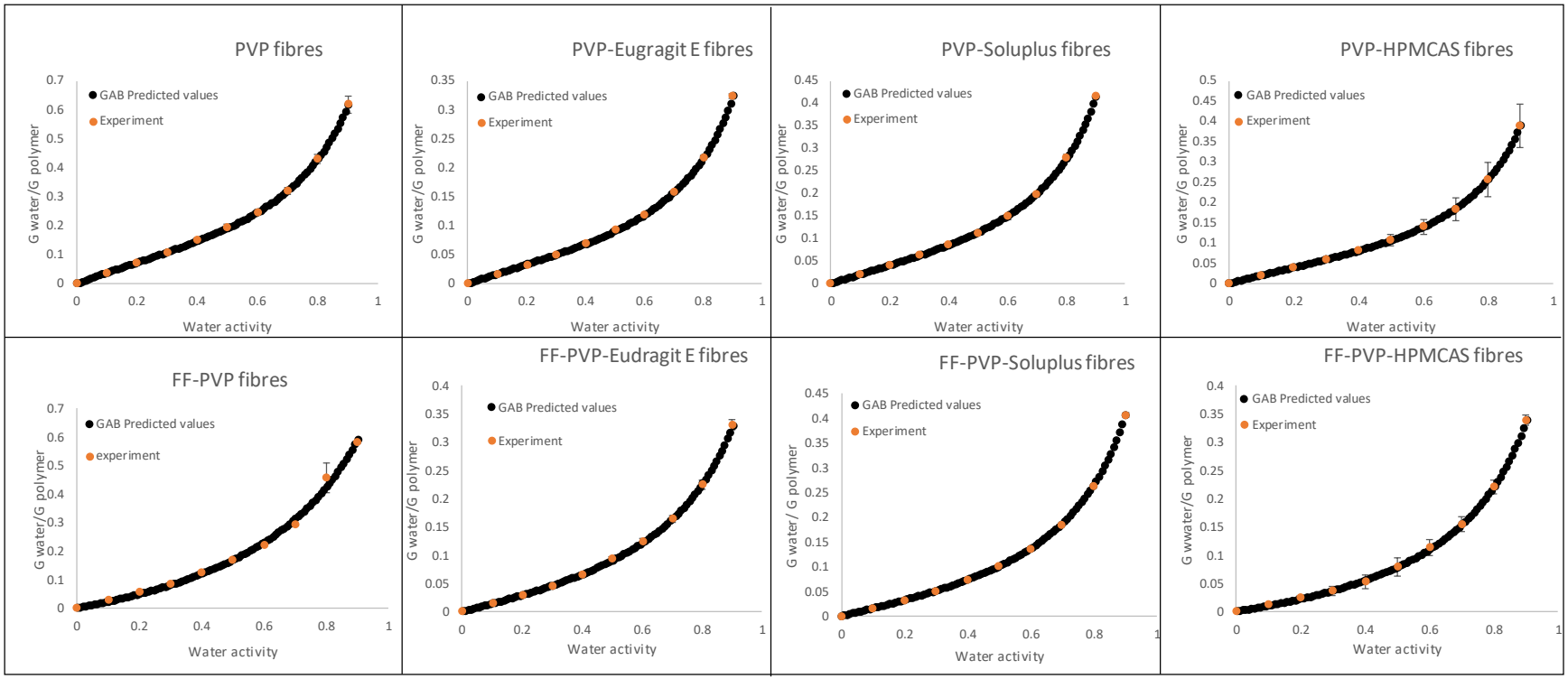

Figure 5.15 Sorption isotherm data fitting with GAB model of placebo and drug loaded electrospun fibres.

- **Moisture sorption of solid dispersions at 75% RH**

The isohumic sorption at a fixed 75% RH is the standard condition for determining the accelerated stability for pharmaceutical products (31). Therefore, this test was applied to the raw materials, placebo and drug loaded electrospun fibre and cast film formulations. The $G_{water}/G_{polymer}$ of the raw materials are 0.34±0.0001, 0.108±0.0003, 0.0640±0.0001 and 0.018±0.001 for PVP, Soluplus, HPMCAS and Eudragit E, respectively. These data clearly demonstrate the order of the hygroscopicity of these polymers as PVP>Soluplus>HPMCAS>Eudragit E (**Figure 5.16a)**. The electrospinning and film casting were used to prepare the blends of PVP and hydrophobic polymer (HPMCAS, Eudragit E and Soluplus). The rationale of these experiments was to compare the moisture sorption between simple solid films produced by the film casting method and the networked fibrous structure prepared by the electrospinning technique. The moisture uptakes of the formulations are reported in $G_{water}/G_{polymer}$. **Figure 5.16** presents the moisture uptakes of the placebo and drug-loaded electrospun fibres and cast films.

The placebo PVP cast films and electrospun fibres demonstrate similar moisture uptakes. After blended with HPMCAS, Eudragit E and Soluplus, the systems illustrate a significant reduction in the overall moisture absorption in both the placebo cast films and fibres in comparison to PVP alone (**Figure 5.16b**). The PVP-HPMCAS and PVP-Eudragit E electrospun fibres absorbed moisture significantly more than their cast film counterparts by about 5.7 and 2.5 times, respectively. On the other hand, PVP-Soluplus showed only a slight difference between the cast film and electrospun fibres. PVP and PVP-Soluplus demonstrated a higher hygroscopicity than HPMCAS and Eudragit.

In the PVP-HPMCAS and PVP-Eudragit, it can be speculated that the fibres absorb a greater amount of moisture than the cast films because of the capillary condensation of the moisture in the fibrous structure. In the case of PVP and PVP-Soluplus, both cast films and electrospun fibres show similar moisture uptakes because the fibrous structure collapsed upon the moisture sorption. The fibre collapse is possibly due to the relaxation of PVP and Soluplus when they absorb water during the sorption experiment. Hence, this phenomenon minimises the surface area of the fibres. The details of the fibrous structure deformation after the moisture sorption will be discussed in the next section.

The FF-PVP cast films and electrospun fibres demonstrate similar moisture uptake capacities as their placebo counterparts. The moisture absorption of FF-HPMCAS and FF-Soluplus cast films decreased to half in comparison to their raw materials, while the FF-Eudragit E cast films showed a similar moisture sorption to the raw materials. Incorporating FF into the polymers, including HPMCAS, Eudragit E and Soluplus cast films, resulted in enhancing the hydrophobicity of the blends. This leads to a decrease in the moisture uptake

in comparison to their raw materials. In contrast, no significant moisture sorption was observed in both the fibres and cast films of FF-PVP in comparison to their placebo fibres and cast films. This is because the FF molecules did not affect the free carbonyl group of PVP, thus, they could attract water in a similar manner to their placebo.

Drug incorporation of polymer blended formulations showed an impact on their moisture uptake capacities in comparison to their placebos for both cast films and electrospun fibres. The moisture uptakes of the FF-PVP-HPMCAS and FF-PVP-Soluplus electrospun fibres slightly decreased in comparison to their placebo fibres. Although the moisture uptake of FF-PVP-Eudragit E fibres slightly increased in comparison to their placebo fibres, the difference in these trends was not significant. Thus, FF did not significantly affect moisture sorption in the electrospun mats. In contrast, PCM-PVP-HPMCAS electrospun fibres demonstrated a notable decrease (1.4 times) in their moisture uptake in comparison to their placebo fibres. In the cast films, the $G_{water}/G_{polymer}$ of the FF-PVP-Soluplus slightly decreased in comparison to its placebo. Although, FF-PVP-Eudragit E and FF-PVP-HPMCAS cast films demonstrated higher moisture uptakes than their placebos (approximately 2.3 and 3.3 times, respectively), the mechanism behind the increases in the moisture uptakes of FF-PVP-HPMCAS and FF-PVP-Eudragit E cast films is unclear. It is speculated that the PVP rich phase contributed to the moisture absorption in the FF-polymer blended cast films.

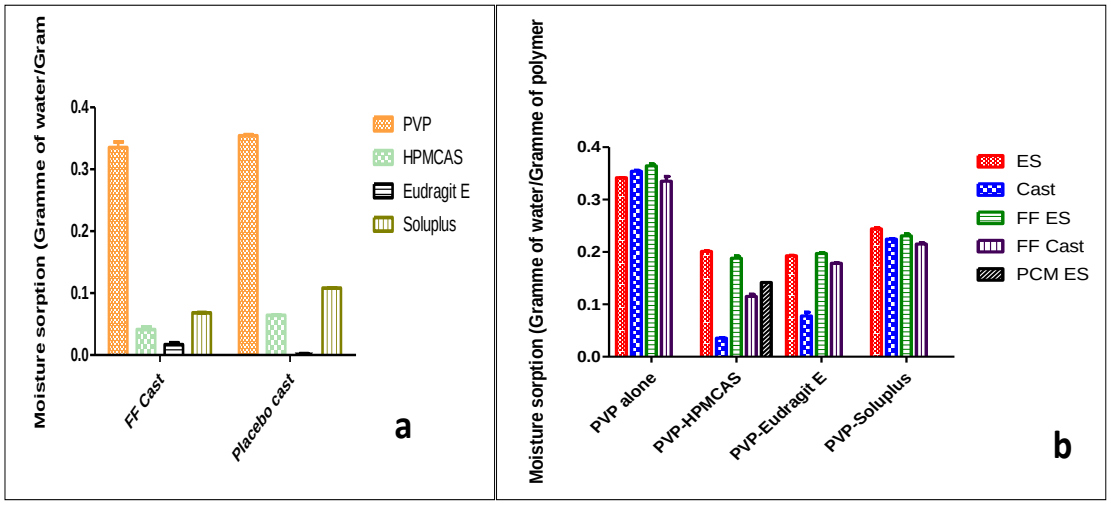

Figure 5.16 Moisture uptake in $G_{water}/G_{polymer}$ of the polymer of raw materials, cast films and fibrous films at 75%RH and 25°C.

- **Moisture sorption kinetics under 75%RH**

The isohumic water absorption data of electrospun fibres and cast films were fitted to Peleg and double exponential (DE) models to obtain kinetics information of the water absorption in these formulations. The water sorption data from the initial state until the equilibrium state of the electrospun fibres and cast films were fitted to the Peleg model. Overall, fibrous water sorption data showed better fits to the Peleg model than the water sorption data from the cast films. In the initial state (0-25 min), the experimental values agree well with Peleg's prediction in both cast films and electrospun fibres (**Figure 5.17a** and **b)**. However, the Peleg predictive values significantly deviated from the experimental values in the intermediate state (25-75 mins) and before reaching an equilibrium state (75-200 min), as seen from **Figure 5.17c** and **d** for both cast and fibrous films. Therefore, the Peleg model was used to fit only the initial state (0-25 min) of the moisture sorption where it showed a good predictive capacity.

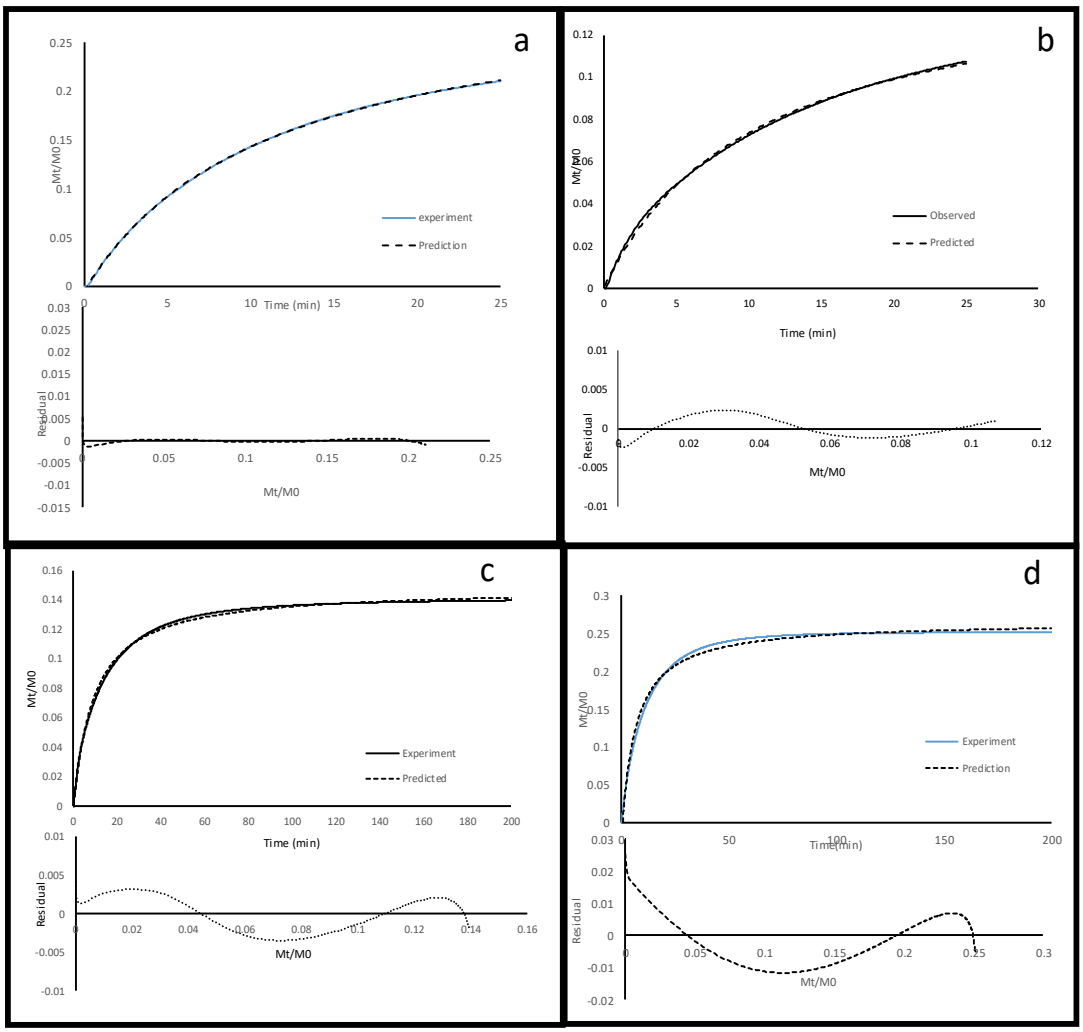

Figure 5.17 Examples of Peleg model fitting and fitting residual to the moisture sorption behavior of FF loaded cast films and electrospun fibres: (a) 25 min FF-PVP cast films, (b)

25 min FF-PVP-HPMCAS electrospun fibres, (c) 200 min FF-PVP cast films and (d) 200 min FF-PVP-HPMCAS fibrous films.

The details of the Peleg equation are described in Chapter 2 (**equation 2.13**). The parameters involved in the Peleg equation are Peleg rate (A_1), Peleg capacity (A_2) and initial mass (M_0) that can be obtained from fitting the isohumic data to the Peleg model. The fitting parameters of the placebo and FF loaded electrospun fibres and cast films are reported in ***Table 5.5*** with their R^2 values. The smaller values of A_1 and A_2 indicate a fast moisture absorption rate and higher moisture absorption capacity, respectively. The comparison of the Peleg rate and the Peleg capacity of electrospun fibres and cast films are shown in **Figure 5.18**. Overall, the electrospun fibres show a faster moisture sorption rate than the cast films, except for the FF-PVP blend fibres, in which the FF-PVP cast films absorbed moisture quicker than the fibre. The Peleg capacity parameter corresponds to the moisture uptake, which agrees with the previous moisture uptake study at 75%RH, as discussed in the moisture sorption results. The Peleg capacity of the electrospun fibres and cast films are similar in the PVP, PVP-Soluplus, FF-PVP, FF-PVP-Eudragit E and FF-PVP-Soluplus. While the PVP-HPMCAS, PVP-Eudragit E and FF-PVP-HPMCAS demonstrated that electrospun fibres have greater moisture uptake than their cast films.

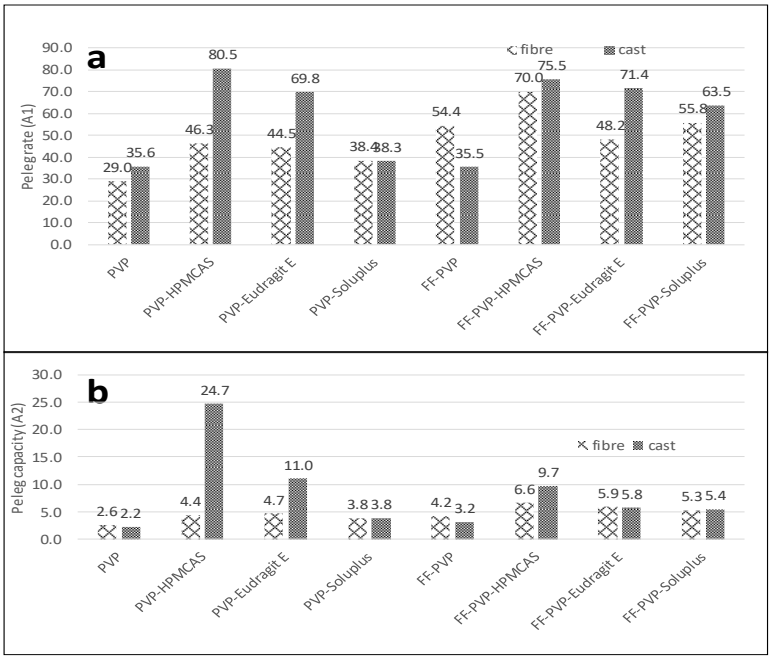

Figure 5.18 Comparison of (a) Peleg rate and (b) Peleg capacity parameters of electrospun fibres and cast films. The smaller values of Peleg rate and Peleg capacity indicate a faster moisture absorption rate and higher moisture absorption capacity, respectively.

Table 5.5 Peleg model fitting parameters of electrospun fibres and cast films at isohumic 75% RH.

Fibres (200 min)	**M_0**	**A_1**	**A_2**	**R^2**	**Cast films (200 min)**	**M_0**	**A_1**	**A_2**	**R^2**
PVP	-0.025	21.59	2.61	0.997	PVP	-0.034	22.63	2.41	0.991
PVP-HPMCAS	-0.008	36.81	4.42	0.994	PVP-HPMCAS	-0.004	55.10	24.38	0.989
PVP-Eudragit E	-0.008	35.36	4.68	0.995	PVP-Eudragit E	-0.009	45.96	11.11	0.989
PVP-Soluplus	-0.012	34.35	3.74	0.997	PVP-Soluplus	-0.018	25.60	3.91	0.990
FF-PVP	-0.008	42.36	3.29	0.997	FF-PVP	-0.03	20.78	3.38	0.987
FF-PVP-HPMCAS	-0.004	59.14	6.57	0.995	FF-PVP-HPMCAS	-0.008	50.00	10.22	0.986
FF-PVP-Eudragit E	-0.004	40.00	6.39	0.997	FF-PVP-Eudragit E	-0.021	37.91	6.14	0.984
FF-PVP-Soluplus	-0.005	47.98	5.46	0.999	FF-PVP-Soluplus	-0.013	44.92	5.61	0.994

Fibres (25min)	**M_0**	**A_1**	**A_2**	**R^2**	**Cast films (25 min)**	**M_0**	**A_1**	**A_2**	**R^2**
PVP	-0.005	28.97	2.55	0.999	PVP	-0.006	35.57	2.24	0.999
PVP-HPMCAS	-0.003	46.31	4.44	0.999	PVP-HPMCAS	-0.002	80.47	24.69	0.999
PVP-Eudragit E	-0.001	44.54	4.70	0.999	PVP-Eudragit E	-0.002	69.78	11.03	0.999
PVP-Soluplus	-0.002	38.40	3.81	0.999	PVP-Soluplus	-0.001	38.26	3.83	0.999
FF-PVP	0.0001	54.35	4.21	0.999	FF-PVP	-0.005	35.51	3.19	0.999
FF-PVP-HPMCAS	0.0002	69.99	6.62	0.998	FF-PVP-HPMCAS	-0.002	75.48	9.65	0.999
FF-PVP-Eudragit E	-0.003	48.17	5.93	0.999	FF-PVP-Eudragit E	-0.003	71.41	5.80	0.999
FF-PVP-Soluplus	-0.001	55.80	5.33	0.999	FF-PVP-Soluplus	-0.003	63.45	5.44	0.999

The fibre network collapse upon moisture sorption is key to explaining the moisture sorption behaviour of the electrospun fibres. The FF-PVP cast films show a faster moisture sorption rate than the electrospun fibres because the FF-PVP fibres demonstrate a dramatic fibrous structure deformation. Hence, this structure deformation could potentially impede moisture uptake in the FF-PVP fibres. On the other hand, PVP-HPMCAS, PVP-Eudragit E and FF-PVP-HPMCAS show minor or no structural collapses**.** Therefore, the capillary condensation that occurs in the fibrous structure resulted in the greater amounts of moisture sorption than the cast films. The similar Peleg capacity between the electrospun fibres and cast films of PVP, PVP-Soluplus, FF-PVP-Eudragit E and FF-PVP-Soluplus is speculated to be due to the major fibre structure deformation that occurs in these samples. Hence, it results in a smaller effect of capillary condensation. Consequently, the electrospun fibres show similar moisture absorption to their cast films. The details of the fibre structure deformation will be discussed in the next section.

The Peleg parameters are only capable of explaining the initial stage of the moisture sorption, during which the systems had not reached the equilibrium yet. These result suggest that a single kinetic term is insufficient to explain the process of water absorption on both the cast films and electrospun fibres. The water absorption process of these samples may involve more than one kinetic process. Therefore, the DE model that has two terms for the kinetic process was used to fit the isohumic water sorption of both cast films and electrospun fibres. The details of the DE model are described in Chapter 2 using **equation 2.14**. k_1 and k_2 are the sorption rate constants and A_1 is the fraction contribution to the different sorption constants.

The DE model demonstrated a better predictive capacity than the Peleg model. It precisely predicted the water sorption data at all states of the absorption in both cast films and fibrous films (**Figure 5.19a**) The DE model fitting parameters are reported in **Table 5.6**. However, slight deviations in the data fitness that indicate the lower quality fits were observed in the FF-PVP-HPMCAS fibres and FF-PVP-Soluplus cast films. These deviations from the DE model potentially referred to another complicated water absorption process that occurs in these samples. This confirmed that at least two kinetic processes happen during the water sorption process. The two processes could potentially be moisture absorption in combination with structural change. The water absorption in the cast films and electrospun fibres is a complicated process in which both the Peleg and DE models could partially explain the absorption process and parametrised the absorption data.

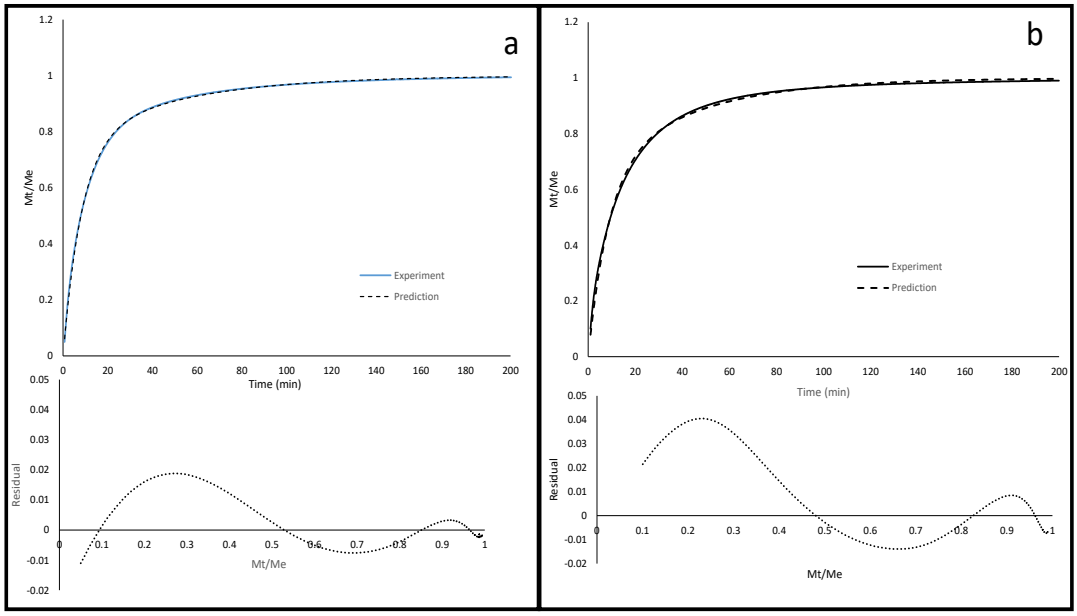

Figure 5.19 Example of DE model fitting and fitting residual to the moisture sorption behaviour of FF loaded electrospun fibres: (a) good fitting of FF-PVP-Eudragit E fibres and (b) slight deviation for FF-PVP-HPMCAS fibres.

Table 5.6 DE model fitting parameters of fibrous and cast films at isohumic 75% RH.

Fibres	**A_1**	**K_1**	**K_2**	**R^2**	**Cast films**	**A_1**	**K_1**	**K_2**	**R^2**
FF-PVP	0.328	0.017	0.077	0.999	FF PVP	0.369	0.041	0.123	0.999
FF-PVP-Eudragit E	0.247	0.02	0.120	0.999	FF PVP-Eudragit E	0.271	0.036	0.102	0.999
FF-PVP-HPMCAS	0.352	0.024	0.116	0.997	FF PVP-HPMCAS	0.335	0.041	0.157	0.999
FF-PVP-Soluplus	0.263	0.014	0.106	0.998	FF PVP-Soluplus	0.163	0.011	0.085	0.997
PVP-Eudragit E	0.467	0.035	0.157	0.999	PVP-Eudragit E	0.360	0.049	0.192	0.999
PVP-HPMCAS	0.552	0.038	0.162	0.999	PVP-HPMCAS	0.268	0.061	0.299	0.998
PVP-Soluplus	0.508	0.032	0.156	0.999	PVP-Soluplus	0.509	0.044	0.165	0.999
PVP	0.291	0.021	0.106	0.999	PVP	0.616	0.091	0.029	0.999

5.3.5 Structure deformation caused by moisture sorption

The increase in moisture sorption leads to the plasticisation of the polymer fibres by water that enhances the molecular mobilities in the system. Therefore, phase separation of the drug and polymer occurs, followed by recrystallization of the amorphous drug. The scenario is of moisture provoking drug crystallisation to occur during the moisture uptake process (14, 15). The visual appearance of the formulations before and after being incubated in a humid environment is the simplest way to indicate the physical and structural changes. Therefore, 4x4 cm pieces of the placebo and drug loaded fibrous films were incubated in a 75% RH desiccator at room temperature for 24 h to demonstrate fibre structure deformations due to moisture absorption. The placebo fibres were dense and flexible before incubation in the desiccator, as seen in **Figure 5.20a** and **b**. However, the texture of the PVP placebo electrospun fibres significantly deformed; they became shrunken, fragile and rigid after being in the humid environment. While the PVP-Eudragit E and PVP-Soluplus became more rigid and shrunk slightly. This shrinkage is an indication of the fibre structures undergoing structural changes. PVP-HPMCAS fibres did not change their texture after being incubated in the humidity desiccator. In the FF loaded polymer blended electrospun fibres, the FF-PVP, FF-PVP-Soluplus and FF-PVP-Eudragit E fibrous textures dramatically distort, including significant shrinkage and increased rigidity. The FF-PVP-HPMCAS electrospun fibres texture did not change after being incubated in the 75% RH desiccator, as seen in **Figure 5.20c** and **d**.

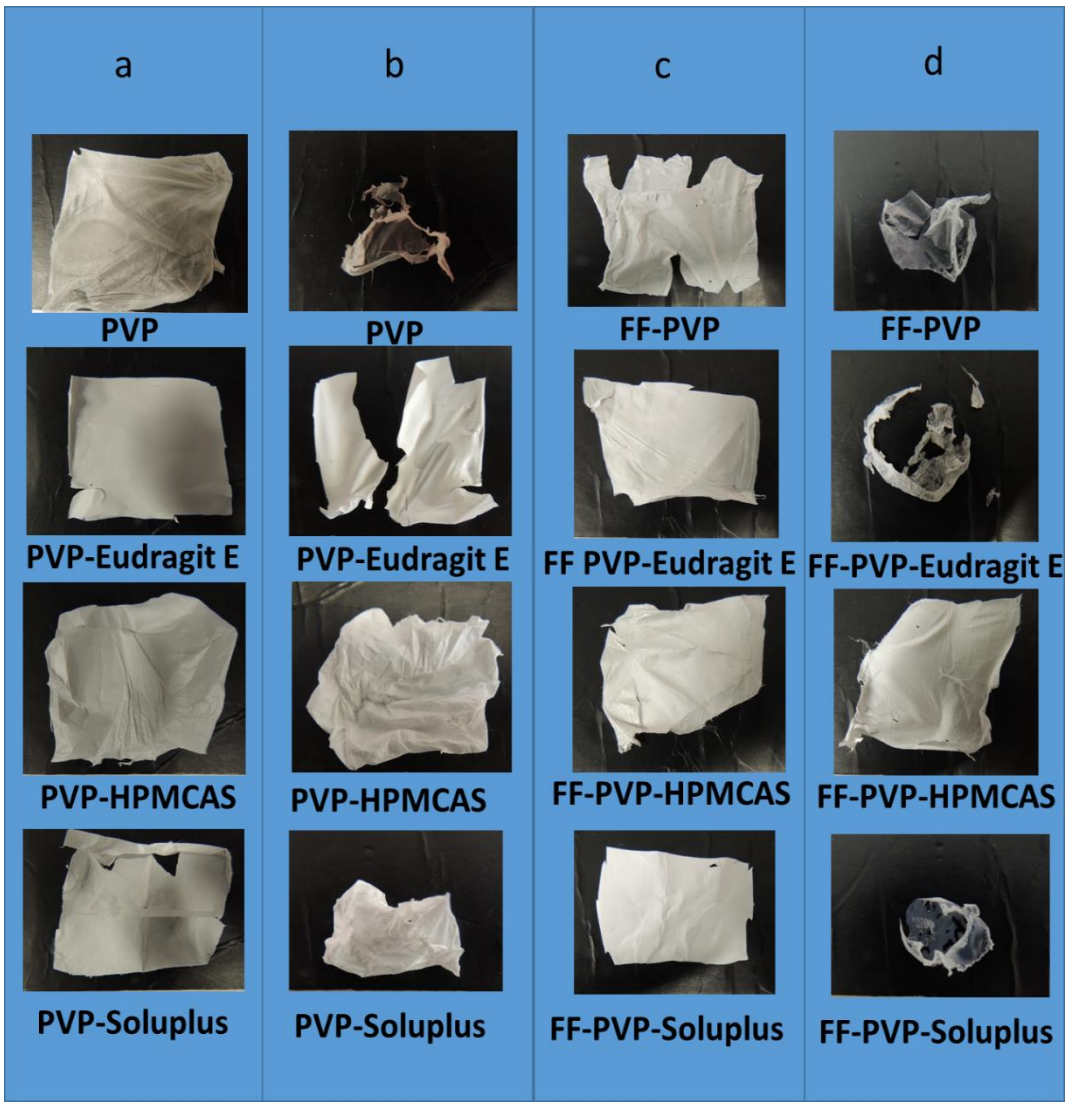

Figure 5.20 Optical images of placebo and FF loaded electrospun fibres before and after incubation in 75% RH desiccator for 24 h. (a) Placebo electrospun fibres before and (b) placebo electrospun fibres after incubation. (c) FF loaded electrospun fibres before and (d) FF loaded electrospun fibres after incubation.

SEM and MTDSC were performed on the placebo and drug loaded cast and electrospun fibres after the isohumic test at 75%RH by DVS at 25°C for 4 h. SEM results revealed evidence of fibre structure deformation after the DVS experiments. The PVP fibres were tremendously swollen and their fibrous structures completely collapsed. It is clearly observed that the gap spaces between the fibres disappeared as the fibres merged. Other fibre structure deformations, including swelling and distorting, are observed in PVP-Eudragit E and PVP-Soluplus fibres, as seen in **Figure 5.22**. These microscopic fibrous structure deformations are highly likely to result in macroscopic fibre shrinkages. On the contrary, the fibrous network of the PVP-HPMCAS placebo fibres remained unchanged. Consequently, the PVP-HPMCAS fibres can maintain the original texture after exposure to 75% RH. The diameters of the placebo PVP, PVP-Eudragit, PVP-Soluplus and PVP-

HPMCAS are 3.2±0.8, 1.3±0.3, 1.7±0.2 and 0.94±0.2 µm, respectively. It can be seen that the diameters of the electrospun fibres increase after moisture sorption in comparison to the dry fibres, indicating swelling (**Figure 5.21**).

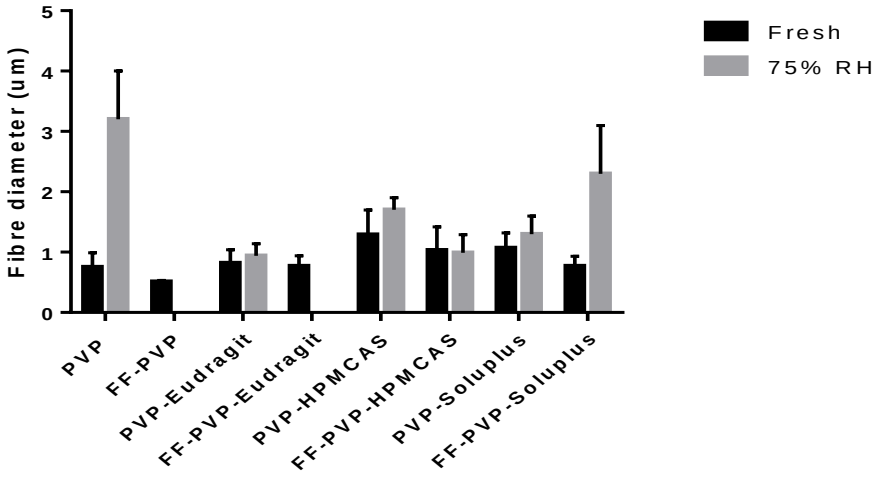

Figure 5.21 Comparison of fibre diameter in fresh fibres and after moisture sorption at 75% RH. It is noted that the diameter of FF-PVP and FF-PVP-Eudragit E fibres cannot be measured due to dramatic fibrous structure collapse and fibres merging.

Significant structural deformations of the FF loaded polymer blend electrospun fibres were observed by SEM (**Figure 5.22**). Fibrous structural collapses occurred in FF-PVP, FF-PVP-Eudragit E and FF-PVP-Soluplus fibres. The fibrous diameter of the FF-PVP-and FF-PVP-Eudragit E could not be measured because of the dramatic structure collapse and fibres merging. This results in an unclear boundary of the fibres, which hinders the diameter measurement. The dramatic fibre collapse in the FF-PVP fibres, in which fibres are fused together as a sheet, can potentially hinder moisture sorption resulting in a slower moisture sorption rate than its cast film. FF-PVP-HPMCAS and FF-PVP-Soluplus showed diameters of 0.99±0.3 and 2.3±0.8 µm, respectively. The fibre diameters of FF-PVP-HPMCAS after the moisture sorption resembled their dry fibre diameter, while the FF-PVP-Soluplus fibre diameters increased approximately two fold in comparison to their dry fibres (**Figure 5.21**). The dramatic deformation of the FF loaded fibres is due to a synergistic effect of FF and water plasticising the samples. Unlike the other electrospun fibres, the fibrous structure of the FF-PVP-HPMCAS fibres remained after exposure to 75% RH. However, some microcrystals were observed on the surface of the FF-PVP-HPMCAS fibres instead (as seen with higher magnification image in **Figure 5.22**). These microcrystals were suspected to be FF crystals. The PCM-PVP-HPMCAS electrospun fibres showed fibre swelling without a structural collapse after the DVS moisture sorption test. Its average diameter was 1.6±0.4 µm, which was approximately twice its dry state.

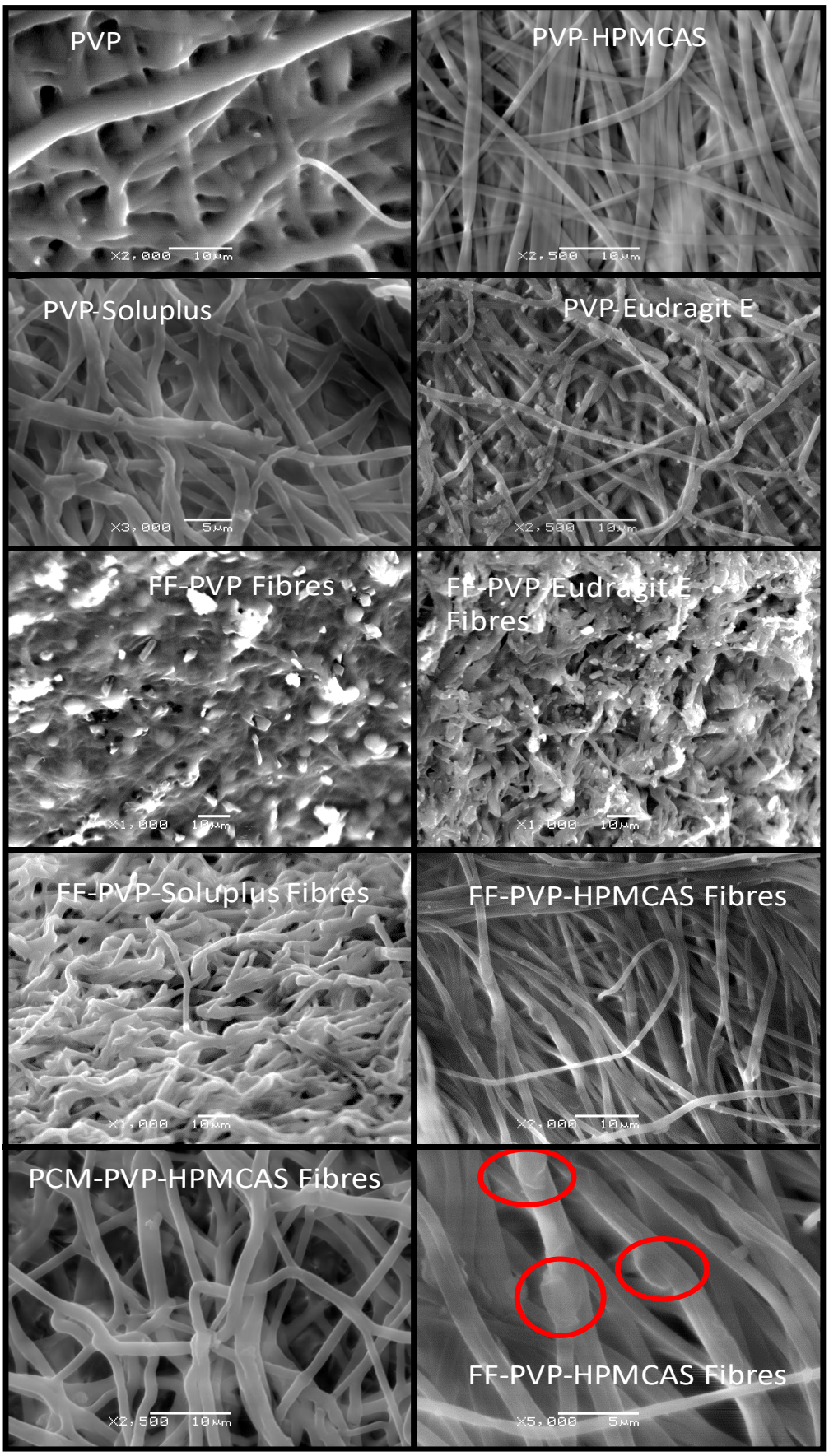

Figure 5.22 SEM images of placebo and drug-loaded electrospun fibres after isohume 75% RH in DVS. Red cycles highlight micro crystals of FF on the fibres.

The SEM images of the FF loaded cast films are shown in **Figure 5.23**. FF crystals were observed on the surface of the FF-PVP, FF-HPMCAS, FF-PVP-HPMCAS, FF-PVP-Soluplus and FF-PVP-Eudragit E after the DVS experiments. This may be an indication of the moisture induced drug crystallisation on the surface of these cast films. On the contrary, FF-Soluplus and FF-Eudragit E cast films presented smooth surfaces. This suggests that Soluplus and Eudragit E prevented FF crystallisation at 75% RH for 400 min.

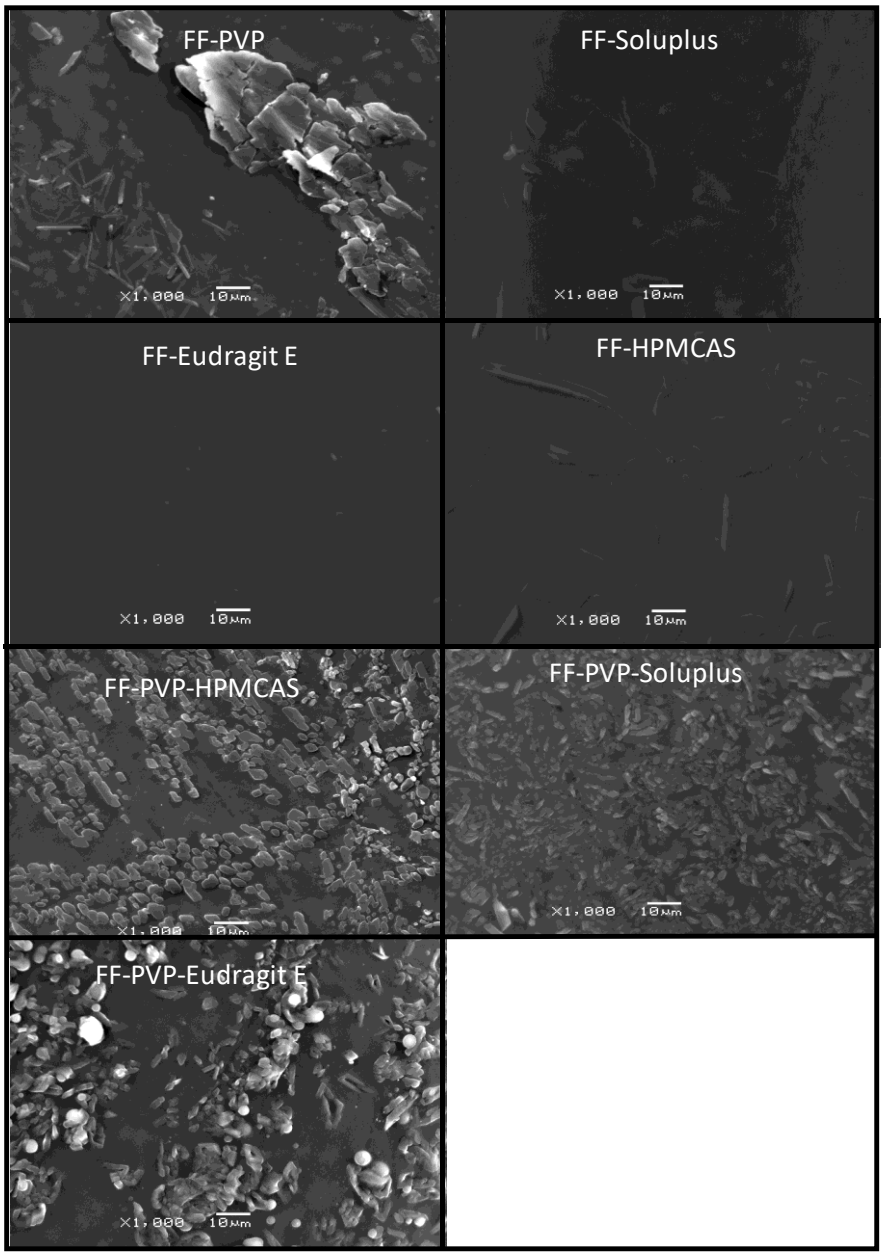

Figure 5.23 SEM images of FF loaded cast films after isohume 75%RH in DVS.

The presence of FF crystals in both electrospun fibres and cast films seen in the SEM results was confirmed by MTDSC. As seen in **Figure 5.24a** and **b**, melting endotherms were observed for FF-PVP and FF-HPMCAS cast films; whereas, no FF melting can be detected in the FF-Soluplus and FF-Eudragit E cast films. These findings agree well with the previous SEM results. In the FF loaded polymer blend dispersions, small melting peaks were observed in the total heat flow signal in the FF-PVP-Eudragit E and FF-PVP-Soluplus fibres and cast films that had absorbed moisture in the DVS, as shown in **Figure 5.24b**. However, the melting enthalpies cannot be measured from the total heat flow signal. This is because of the non-flat baseline that is caused by the water evaporation being superimposed on the melting signals. As the melting was shown in both the total heat flow and reversing heat flow, the melting enthalpies were measured from the reversing heat flow signal, which showed a flat baseline (**Figure 5.24c**), and the values are reported in **Table 5.1**. The measurement of FF melting enthalpies from the reversing heat flow is only for comparative purposes between the formulations. The reversing heat flow cannot be used to quantify the amount of FF crystals, because it is part of the total heat flow, which is responsible for the reversible event (T_g), and the integral area of the pure crystals melting peak in the reversing heat flow is not equal to the melting enthalpy measured from the total heat flow. The majority of the FF loaded polymer blended dispersions show a melting peak for the FF at 80°C, which refers to FF form I recrystallization. However, the FF-PVP-Soluplus cast films and the FF-PVP-Eudragit E and FF-PVP-Soluplus fibres had a drug melting point at 73°C. This could be attributed to either a melting point depression due to the presence of polymers or that the FF crystallised as its metastable polymorph IIa (32). The highest melting enthalpy value (11.9±0.11 g/J) was observed in the FF-PVP-HPMCAS fibres with the equivalent of 53.3% FF form I recrystallization. This melting peak confirmed that the microcrystals in the FF-PVP-HPMCAS fibres were FF crystals. On the reversing heat flow signal, FF-PVP-Eudragit E cast films demonstrated double T_g values similar to those obtained for the fresh sample. However, no T_g was observed in the other cast films and electrospun fibres (**Figure 5.24c**).

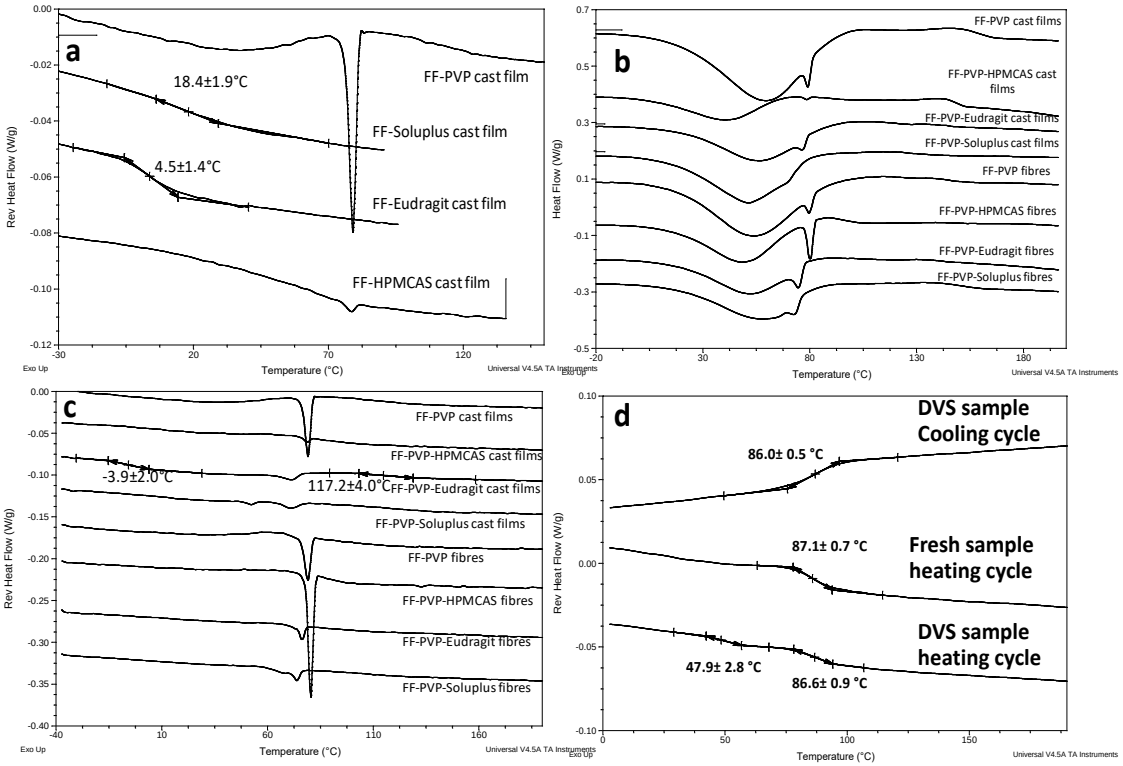

Figure 5.24 MTDSC of FF loaded cast films and electrospun fibres after being incubated in DVS at 75%RH: (a) single polymer cast film, (b) total heat flow of polymer blended dispersion, (c) reversing heat flow of polymer blended dispersion and (d) PCM-PVP-HPMCAS fresh and sample after DVS experiment.

Again, for comparative purposes, the PCM loaded system was also studied. The PCM-PVP-HPMCAS fibres showed a double T_g at 47.9 ± 2.8 and 86.6± 0.9 °C, but no melting of PCM was observed (**Figure 5.24d).** From the ΔC_p, approximately one-third of the PCM-PVP-HPMCAS phase demonstrated a separation at the lower T_g phase. A single T_g was obtained from the cooling cycle (86.0± 0.5°C). The fresh PCM-PVP-HPMCAS fibres demonstrated a T_g at 87.1±0.7°C, which is similar to the second T_g of the DVS sample and the T_g from the cooling cycle. Therefore, the first T_g of the PCM-PVP-HPMCAS fibre could be the moisture that was bound to the PVP during the moisture sorption experiment. It is speculated that the hydrogen bond in the PVP-PCM enhances the physical stability of the PCM-PVP-HPMCAS fibres under 75% RH. However, the FF did not establish the hydrogen bond with neither the PVP nor the HPMCAS. Thus, this results in the amorphous FF recrystallization in the FF-PVP-HPMCAS fibres under 75% RH.

PXRD was used to further confirm the crystallinity and the polymorphic form of the FF present in the electrospun fibres. The amount of sample obtained from the DVS experiments was inadequate for the PXRD experiments. Hence, the fibrous samples were incubated in the 75% RH desiccator instead. As seen in **Figure 5.25**, initially no FF crystals were detected by PXRD in the electrospun fibres. Later, after exposure to 75% RH, there were some FF crystallised in the FF loaded polymer blended fibres. In comparison to the physical mixture of FF form I and polymers, the peak intensity of the FF polymer blends is relatively low and the peaks are broad. This indicates that there was a small amount of FF crystals or poor crystallinity in these samples. Considering the diffracted peak positions observed in **Figure 5.25a**, it is unclear which FF polymorph crystallised in these samples, but it is likely to be FF form I because it is the polymorph which usually observe in the recrystallization of amorphous FF under 75% RH (10).

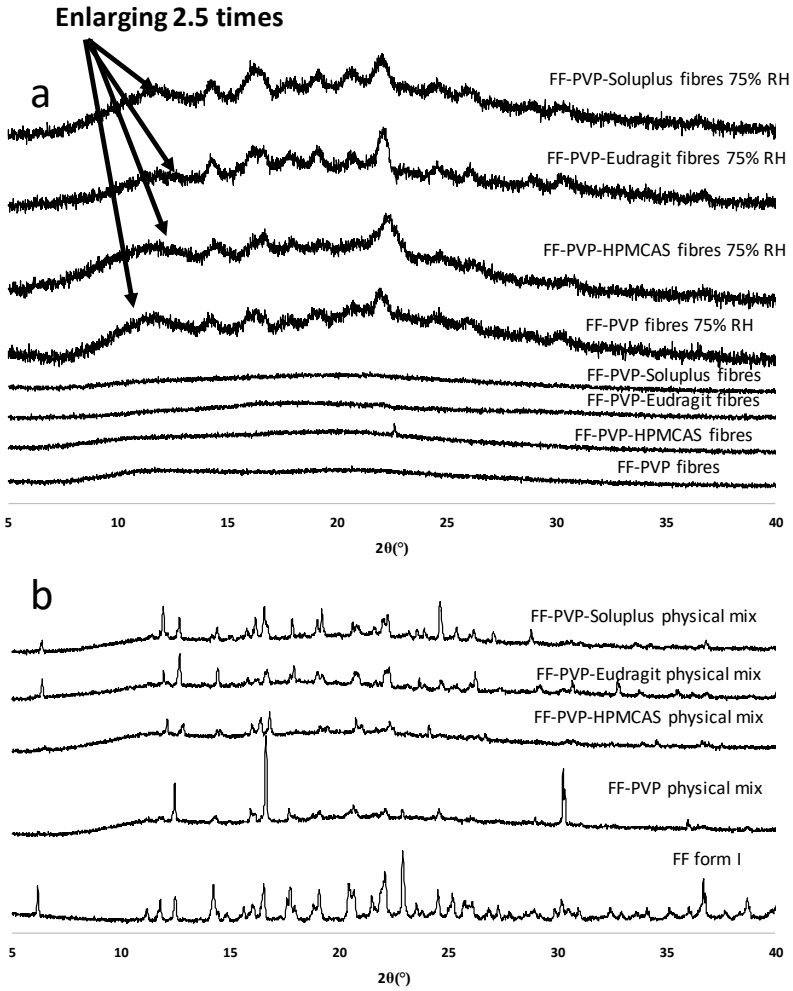

Figure 5.25 PXRD of FF loaded electrospun fibres: (a) before and after expose to 75%RH and (b) physical mixtures of FF and polymer in comparison to FF form I powder.

5.4 Discussion

5.4.1 Effect of moisture sorption on drug-polymer binary dispersions

The clarification of the drug-polymer and the polymer-polymer miscibility is an important piece of information before dealing with a complex system composed of a drug in a polymer blend matrix. The PVP-HPMCAS pair is miscible because it showed a single T_g. However, PVP-Eudragit E and PVP-Soluplus blends are immiscible and phase separation was observed in these systems (double T_g). The results of polymer miscibility are consistent in both cast films and electrospun fibres. FF showed different miscibilities among the polymers that had been used in this study. In the literature, theoretical miscibility could be divided into three different classes according to the differences in the solubility parameter (δ) between the two components: they are likely miscible ($\Delta\delta < 2$ MPa$^{1/2}$), partially miscible ($\Delta\delta$ between 2 and 10 MPa$^{1/2}$) and immiscible ($\Delta\delta > 10$ MPa$^{1/2}$) (33). Considering the δ values of FF with PVP, HPMCAS, Eudragit E and Soluplus in **Table 5.7**, it suggests that FF is miscible with HPMCAS, Eudragit E and Soluplus but only partially miscible with PVP. On the contrary, PCM is theoretically highly miscible with PVP but partially miscible with HPMCAS.

The experimental results indicated that FF is highly miscible with Eudragit E and Soluplus, in which no FF crystal was observed. However, it is partially miscible with PVP and HPMCAS, as seen from the recrystallization of the FF on the surface of the FF-PVP and FF-HPMCAS cast films. PVP and FF have only carbonyl groups that are a hydrogen acceptor in their structure. Thus, a weak hydrogen bond between the carbonyl group and acidic C-H or dipole-dipole interaction can be established (34). This results in partial miscibility between PVP and FF. From the HPMCAS structure in **Figure 2.7**, it has a carboxylic group that can potentially form a hydrogen bond with a carbonyl group of FF. However, the amount of carboxylic groups in HPMCAS is considered low (1 mmol.g^{-1}), and the steric hindrance of the HPMCAS structure impedes the hydrogen donor group from bonding with FF (34). Therefore, FF and HPMCAS have weak molecular interactions that contribute to a partial miscibility. From this information, it is possible to speculate that the FF crystals observed in the FF-PVP-HPMCAS, FF-PVP-Eudragit E and FF-PVP-Soluplus ternary solid dispersions are likely due to a partial miscibility of FF-PVP or FF-HPMCAS.

The PCM and PVP demonstrate a hydrogen donor (hydroxyl) and a hydrogen acceptor (carbonyl) in their structure. Thus, they form a hydrogen bond in which they promote their miscibility (11). On the contrary, the PCM and HPMCAS show a partial miscibility because a hydrogen bond between PCM and HPMCAS is difficult to form. The structural hindrance of a polymer chain and low number of carboxylic groups impedes the interaction

between PCM and HPMCAS (34). The details of the PCM interaction with PVP and HPMCAS is discussed in Chapter 6.

Table 5.7 Calculated solubility parameter from Fedor's method and Δδ between the model drugs and polymers.

Materials	***δ(MPa$^{1/2}$)***	***Δδ of polymer and FF***	***Δδ of polymer and PCM***
FF	21.5	-	-
PCM	27.1	-	-
PVP	28.2	7.7	1.1
HPMCAS[a]	22.4	0.9	4.7
Eudragit E	20.5	1.0	-
Soluplus	23.5	2.3	-

[a] Taken from reference (20).

Humidity demonstrates a significant impact on the miscibility of the drugs and polymers. The molecular mobility of the polymers and drug increases due to the plasticization effect of the moisture. This results in an enhanced phase separation between the polymer-polymer and drug-polymer (14, 15). The FF-PVP pair is partially miscible and the system is not in equilibrium. Hence, the addition of moisture accelrelates the FF-PVP system toward to the equilibrium which FF and PVP are phase separated. Futhermore, moisture also increases the hydrophilicity of PVP. Consequently, the environment is less favourable for FF. Thus, the miscibility of FF-PVP is reduced. In the PVP electrospun fibres, it is likely that the structure collapse is due to the PVP domain absorbing moisture and weakening the entanglement of the polymer chains in the fibres.

FF-HPMCAS is another example that shows a partial miscibility between the drug and polymer. However, the amount of the crystalline FF observed remained the same after the DVS isohumic 75%RH experiment. It is likely that FF increased the hydrophobicity of the blends, which is supported by the reduction in the moisture absorption in comparison to the HPMCAS raw material. In this particular case, the moisture does not affect the drug recrystallization in the FF-HPMCAS system. The polymer-drug miscibility plays a greater role than the moisture in the drug recrystallization.

No FF crystals were observed in the FF-Eudragit E cast films. The hydrophobicity of the blend resulted in reduced moisture absorption in the FF-Eudragit E blends because the

moisture absorption decreased in comparison to the Eudragit E raw material. It should be noted that the T_g of the FF-Eudragit E is lower than room temperature, hence the system is in the rubbery state. The FF-Eudragit E system has high mobility but does not interact with water. This is because of the hydrophobic propensity of FF and Eudragit. Despite the fact that the FF-Soluplus cast film absorbed moisture more than the FF-HPMCAS and FF-Eudragit E cast films and that it has a T_g close to room temperature, no FF crystals were observed after the 75%RH isohumic experiment. From these results, the recrystallization of FF in the FF-HPMCAS, FF-Eudragit E and FF-Soluplus pairs were not affected by moisture. Thus, these polymers can prevent drug recrystallization in a high humidity environment.

5.4.2 Effects of moisture sorption on ternary drug-polymer blend system

Incorporating FF into the system at 25% solid content did not significantly affect the physical appearance of the electrospun fibres, since the overall appearance and average diameter of the placebo and API loaded fibres were almost the same. Overall, both the FF loaded and placebo electrospun fibres demonstrated a greater moisture sorption rate than the cast films. This could be attributed to the higher surface area to volume ratio of the fibres. The large surface area to volume ratio is one of the advantages of the electrospun fibre formulations to increase the aqueous solubility of poorly water-soluble drugs (5, 35). However, it is a double-edged sword, which potentially increases the moisture absorption rate and results in fibrous structure deformation and recrystallization of the amorphous drug.

- **FF-PVP-Eudragit E and FF-PVP-Soluplus**

The deformation of the electrospun fibres was macroscopically observed as fibre shrinkage, which was a consequence of the fibre network collapsing. The minor fibrous structure collapse was observed in the placebo PVP-Eudragitand PVP-Soluplus blends. In contrast, the FF loaded polymer blended fibres demonstrated a more dramatic morphological deformation (fibres bent and twisted) than the placebo fibres. The mechanism of the fibre structure deformation has not yet been reported in the literature. However, Rasekh et al. and Yu et al previously described the mechanism of PVP electrospun dissolution (11, 36). The authors explained that the dissolution process of a PVP electrospun fibre roots from the polymer-solvent interaction being stronger than the polymer-polymer attractive force, for example, PVP interacts with water better than with PVP. Therefore, PVP absorbed water molecules rapidly leading to an increase in the volume of the polymer matrices. Consequently, the polymer chains loosen from their coiled shape as fibres. The drug entrapped in the PVP is released to the media (11). It is possible to speculate that at a high

RH (75%), PVP polymer chains of electrospun fibres loosen because water molecules were absorbed and plasticised the fibres. However, this process is incomplete, unlike in the dissolution process. The loose polymer chains cause an increase in their volume as seen from the swelling of the fibres. Therefore, this leads to the shrinkage of the electrospun fibre structure due to the uncoiled polymer chains, and the fibre structure collapses as observed in the placebo and FF loaded PVP-Eudragit E and PVP-Soluplus electrospun fibres.

Only a small amount of FF crystals were observed in the FF-PVP-Eudragit E and FF-PVP-Soluplus fibres and cast films after the moisture sorption. It is speculated that the drug probably distributes unevenly in the phase-separated polymers, in which FF likely partitions to the Eudragit E or Soluplus domains rather than the PVP domain. This is because of the dipole-dipole interaction of the drug and polymers (37) or because of their similar hydrophobicity. Therefore, the majority of the amorphous drug is stabilised in the Eudragit E or Soluplus phase, while the minority of the amorphous drug is crystallised in the PVP phase. To strengthen the hypothesis of the uneven FF distribution among the phase separation, the GT equation was used to estimate the amount of FF distributed throughout each phase. However, we have to bear in mind that the experimental T_g of the FF loaded in the Eudragit E and Soluplus demonstrated a negative deviation from the GT prediction (approximately 15-17°C). This is a consequence of the stronger interaction among the like-molecules (drug-drug and polymer-polymer) than the unlike molecules (drug-polymer) (38). In addition, the T_g of the FF-PVP is not detectable in either the cast films or the electrospun formulations.

Assuming that the FF is completly distributed to the Eudragit E or Soluplus phases in the FF-PVP-Eudragit E and FF-PVP-Soluplus solid dispersions, the FF content in the Eudragit E or Soluplus would be 40% because the polymer blend matrices contain PVP: Eudragit E or Soluplus 1:1. The T_gs that were calculated from the GT equation at 40% FF in the Eudragit E and Soluplus phases are 8.5 and 20 °C, respectively. We need to take into account the negative deviation from the predicted values of approximately 15°C that was observed in FF-Eudragit E and FF-Soluplus cast films. The expected T_g of the completely distribution of FF into Eudragit E and Soluplus phases are -6.5 and 5°C, respectively. The first T_gs that were detected by MTDSC in the FF-PVP-Eudragit E cast film, FF-PVP-Soluplus cast film and FF-PVP-Eudragit E electrospun fibres are -5.8±1.5, 13.5±0.8 and -2.6±1.8°C, respectively. This result indicates the uneven FF distribution in the FF-PVP-Eudagit and FF-PVP-Soluplus that the majority of FF partitions to the Eudragit E and Soluplus rich phases. The second T_g at 120°C is likely to be the PVP phase. However, the T_g of the FF-PVP could not be measured from the cast films nor electrospun fibres. Hence,

it is difficult to estimate the amount of FF in the PVP phase because of the unknown deviation of the experimental and predicted values.

Being on the safe side, it is certain that FF is less miscible in PVP than Eudragit E and Soluplus. This was shown previously from the melting enthalpies observed in the FF-PVP formulations and the $\Delta\delta$ of the FF and PVP. It is possible to conclude that the majority of FF would distribute to the Eudragit E or Soluplus domains rather than the PVP. This approach may not be a straightforward method that directly and precisely quantifies the absolute amount of FF in each polymer phase, but it can be a rough guideline that indicates the drug distribution to each phase due to their miscibility.

The small amount FF crystals observed in the FF-PVP-Eudragit E and FF-PVP-Soluplus electrospun fibres after the moisture sorption at 75% RH was due to the majority of FF molecules being in either the Eudragit E or Soluplus phases so that the FF was protected from moisture. Therefore, the uneven distribution of the drug in the immiscible polymer blends enhances the physical stability of the formulations. **Figure 5.26a** illustrates the FF uneven distribution between the PVP and Eudragit E or Soluplus domains.

- **FF-PVP-HPMCAS**

The PVP-HPMCAS polymer blend fibres exhibit an inverse property to the previous systems (PVP-Eudragit E and PVP-Soluplus). The fibres withstand 75% RH without a fibre structure rupture, even though they took up some moisture. The fibrous structure of the FF-PVP-HPMCAS electrospun fibres also did not collapse, but numerous FF crystals were observed on the fibre surface, with evidence from both MTDSC and SEM. Approximately 53% drug loaded recrystallized as FF form I after the fibres were incubated at 75% RH. The mechanism behind this phenomenon is unclear but it is possible to speculate that it may correlate to both moisture and the miscibility in this ternary solid dispersion, since the FF-PVP-HPMCAS fibre structure could withstand 75% RH without the fibre structure collapsing. Moisture could infiltrate into the whole fibrous architecture and induce crystallisation of the amorphous FF in the interior fibrous structure. Additionally, the recrystallization of the FF-PVP-HPMCAS fibres could contribute to the polymer-polymer pair that has a better miscibility than the drug-polymer pair, in which the FF previously showed a partial miscibility in both PVP and HPMCAS. Hence, it is speculated that the amorphous drug domains initially blended homogeneously with the polymer matrices in the dry state, as illustrated in (**Figure 5.26b**). After exposing the FF-PVP-HPMCAS fibres to moisture, the PVP domains attract the moisture and lead to the increased mobility of the FF molecules. This results in amorphous FF that does not interact with neither PVP nor HPMCAS and was forced to mobilise to the surface of the fibres and crystallise. In contrast, the FF-PVP-HPMCAS cast film showed a tiny amount of FF crystallinity after exposure to

75% RH because the moisture only triggers the FF crystallisation on the surface of the cast films. This made the surface even more hydrophobic resulting in the prevention of moisture from penetrating into the bulk of the cast film.

- **PCM-PVP-HPMCAS**

Unlike the FF-PVP-HPMCAS dispersion, the PVP forms a hydrogen bond with PCM in the PCM-PVP-HPMCAS electrospun fibres. These hydrogen bonds result in the moisture protective effects of this formulation. They reduced the water uptake of the formulation and prevented the drug from recrystallizing during exposing to 75% RH. The scenario for the PCM-PVP-HPMCAS fibre moisture sorption is illustrated in **Figure 5.26c**. Most of PCM molecules are allocated in the PVP phase rather than the HPMCAS due to the hydrogen bond formation with PVP. After exposing the PCM-PVP-HPMCAS fibres to moisture, a phase separation occurred as shown by the double T_g. The lower T_g phase, which belonged to the free carbonyl PVP bond with water molecules, and the other phase was at 85°C, which was similar to the T_g of the fresh PCM-PVP-HPMCAS fibres. The single T_g at 85 °C was again obtained after complete water removal on the cooling cycle. In this case, a double T_g did not contributed to a phase separation of PCM-PVP and PCM-HPMCAS. If this scenario occurs, the T_g of each phase will show a larger difference due to the T_g of the PCM-PVP shifting to a higher temperature than 85°C (the T_g of the PCM-PVP estimated by the GT equation is at 119°C).

Furthermore, no crystallisation of PCM has been observed in the PCM-PVP-HPMCAS fibres after the moisture sorption. Forster et al. reported that the solid dispersion of indomethacin and PVP prepared by hot melt extrusion remained amorphous after storage at 75% RH/25°C for eight weeks. While the extrudates of nifedipine and lacidipine with PVP had their hydrogen bonds degraded due to 75% RH immediately crystallised (26). The authors explained that the presence of hydrogen bonding in the solid dispersion resulted in less free PVP carbonyl groups. Hence, they attracted less moisture. On the contrary, an absence or degradation of the hydrogen bonding of the drug and PVP caused a greater amount of free carbonyl groups, which potentially attracts moisture from the environment. The high moisture absorbed by the PVP plasticised the solid dispersion, which leads to a phase separation of the drug rich amorphous phase and eventually crystallisation (13). This explanation agrees with the findings of FF-PVP-HPMCAS and PCM-PVP-HPMCAS as ternary solid disprsions. The FF-PVP-HPMCAS fibres and cast films showed a greater level of moisture sorption than the PCM-PVP-HPMCAS fibres. This potentially caused a greater number of free carbonyl groups in FF-PVP-HPMCAS than PCM-PVP-HPMCAS. Approximately half of FF loaded in the FF-PVP-HPMCAS fibre films crystallised into FF form I, whereas no crystallisation of the PCM was observed in the PCM-PVP-HPMCAS

fibres after moisture sorption. This is a consequence of the hydrogen bonding of PVP and PCM stabilising the drug in its amorphous state.

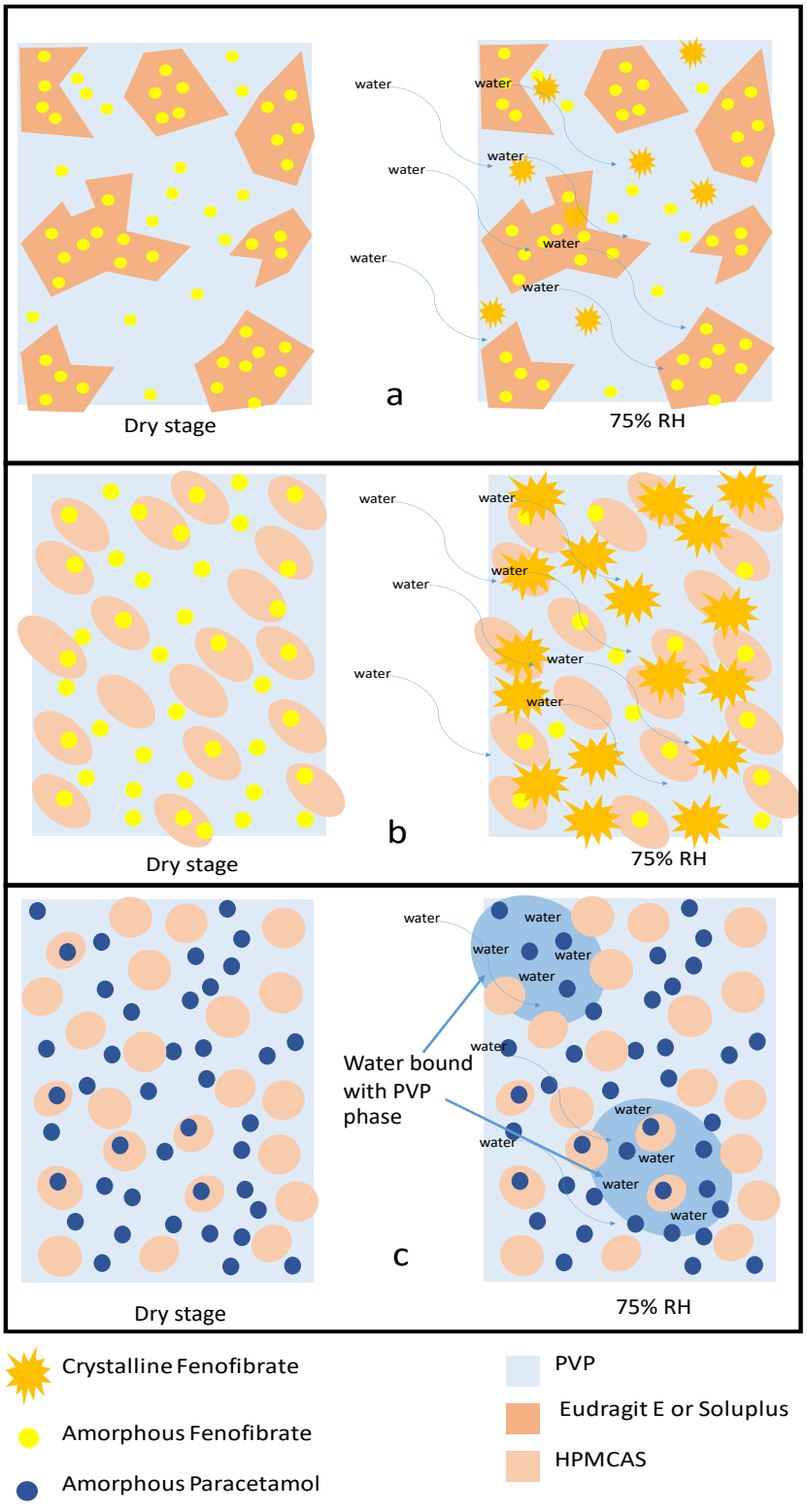

Figure 5.26 Schematic diagrams illustrating three different scenarios for the ternary blend phase transformation under the influence of humidity: (a) drug miscible in one polymer more than the other, (b) polymer-polymer more miscible than drug and (c) drug binds to one polymer by hydrogen bonding (highly miscible).

5.4.4 Effect of preparation method and polymer-drug miscibility on physical stability of dispersions

The preparation methods demonstrated a greater impact on the stability of the FF-PVP formulations. The cast films of FF-PVP showed a higher degree of crystallisation than their electrospun fibres from melting enthalpy. This result suggests that the preparation method significantly influences the physical stability of the formulations. Nagy et al. and Brettmann et al. reported that the solid dispersions prepared by electrospinning are better than the solid dispersions prepared by hot melt extrusion in terms of minimising drug-polymer phase separation and a lower degree of drug recrystallization (6, 39, 40). Nagy and co-workers reported finding some spironolactone crystals on the hot melt extrudates, but observed no drug crystals in the electrospun fibres of 20%w/w spironolactone in Soluplus (6). Brettmann and colleagues also demonstrated that the electrospun fibres of aliskiren PVP had a smaller domain of phase separation than the same formulation prepared from the hot melt extrusion method (40). The phase separation domain was 2-10 nm and greater than 100 nm in the electrospun fibres and extrudates, respectively. The authors explained that the high stability of electrospinning contributes to an immediately vitrified (approximately a few millisecond) drug and polymer, which was caused by the ultra-fast solvent evaporation during electrospinning (41). Consequently, the mobility of drug molecules was suddenly kinetically frozen in the glassy polymer, and the viscosity was estimated to be greater than 10^{12} Pa.s (42). Molecular mobility is present in the processes that have a longer vitrification time, such as hot melt extrusion and film casting. This mobility potentially causes drug-polymer phase separation and eventually recrystallisation on ageing.

The miscibility of the drug and polymer is an important factor, which plays a greater role than the preparation method in the PVP blended with Eudragit or HPMCAS or Soluplus solid dispersions. This is shown by the insignificant differences in the FF crystals in the polymer blended cast films and electrospun fibres. The ternary system of drug and polymers is a complicated system. It involves uneven drug distribution between the two phases. In this study, we demonstrated that the FF partitioned to the Soluplus or Eudragit E rather than PVP. This directly contributes to the stability of the amorphous drug. The FF molecules distribute to the hydrophobic polymer phase due to the better drug-polymer miscibility. This could be a potential means to prevent drug recrystallization. The crystalline drugs are coming from a minority proportion that distributes to the PVP phase. This results in a similar amount of FF crystals in both cast films and electrospun fibres.

The high surface area to volume ratio of electrospun fibre formulations is a double-edged sword, which enhanced the aqueous solubility of the FF formulations and increased the moisture uptake in the formulations. Hence, the storage condition of the electrospun fibres strongly influences the stability of the formulations. The FF electrospun fibre formulations

demonstrated a small degree of crystallisation under a 0% RH condition. All FF loaded electrospun fibres developed fibre structure deformations in the presence of moisture. Therefore, if the electrospun fibre formulations in this study were developed as an oral dosage form, their containers would be an important factor that dictates the physical stability of the dosage form. Thus, the recommended package of electrospun fibres should be a single use unit that is made from polyvinylchloride laminated on aluminium foil because moisture cannot penetrate this material (43). Therefore, it completely protects the dosage forms from environmental humidity.

5.5 Conclusion

This study demonstrated the prospect of developing electrospun ternary solid dispersions for oral drug delivery. The polymer blended electrospun fibres showed a remarkable improvement for the FF dissolution in comparison to the crystalline FF. Additionally, the use of PVP-HPMCAS blends demonstrated a potential for sustained release applications as FF demonstrated the slowest release rate among the polymer blend formulations. We speculated that the drug in PVP phase released first then follow by the sustained drug from HPMCAS phase which was insoluble in the acidic media. In the moisture sorption study, electrospun fibres showed a notably greater rate of moisture absorption than the cast film formulations. This was attributed to the high surface area to volume ratio of the electrospun fibres. Upon moisture sorption, the fibres underwent fibre structure deformation and recrystallization of the amorphous FF. The drug-polymer miscibility played a major role in stabilising the amorphous drug under the high humidity environment. Amorphous FF was protected from moisture as the drug distributed to the Eudragit E or Soluplus rather than the PVP because the drug has a higher miscibility to Eudragit E and Soluplus. In the FF-PVP-HPMCAS blends, the PVP-HPMCAS pair has a better miscibility than the drug-polymer pair, which resulted in the FF crystallising on the fibres. On the other hand, the PCM molecules demonstrated a strong interaction with the PVP via hydrogen bonding. This can stabilise the PCM in an amorphous form under the high humidity stress and reduced the moisture uptake of the formulations. Therefore, polymer-polymer and drug-polymer miscibility are important parameters that influence the physical stability of the ternary blends of solid dispersions.

5.6 References

1. Huang Z-M, Zhang YZ, Kotaki M, Ramakrishna S. A review on polymer nanofibers by electrospinning and their applications in nanocomposites. Composites Science and Technology. 2003;63(15):2223-53.
2. Munj HR, Nelson MT, Karandikar PS, Lannutti JJ, Tomasko DL. Biocompatible electrospun polymer blends for biomedical applications. Journal of Biomedical Materials Research Part B: Applied Biomaterials. 2014;102(7):1517-27.
3. Richard-Lacroix M, Pellerin C. Molecular Orientation in Electrospun Fibers: From Mats to Single Fibers. Macromolecules. 2013;46(24):9473-93.
4. Rutledge GC, Fridrikh SV. Formation of fibers by electrospinning. Advanced Drug Delivery Reviews. 2007;59(14):1384-91.
5. Lopez FL, Shearman GC, Gaisford S, Williams GR. Amorphous formulations of indomethacin and griseofulvin prepared by electrospinning. Molecular Pharmaceutics. 2014;11(12):4327-38.
6. Nagy ZK, Balogh A, Vajna B, Farkas A, Patyi G, Kramarics Á, et al. Comparison of electrospun and extruded soluplus®-based solid dosage forms of improved dissolution. Journal of Pharmaceutical sciences. 2012;101(1):322-32.
7. Yu D-G, Shen X-X, Branford-White C, White K, Zhu L-M, Bligh SA. Oral fast-dissolving drug delivery membranes prepared from electrospun polyvinylpyrrolidone ultrafine fibers. Nanotechnology. 2009;20(5):055104.
8. Yang Z, Nollenberger K, Albers J, Craig D, Qi S. Microstructure of an Immiscible Polymer Blend and Its Stabilization Effect on Amorphous Solid Dispersions. Molecular Pharmaceutics. 2013;10(7):2767-80.
9. Tipduangta P, Belton P, Fábián L, Wang LY, Tang H, Eddleston M, et al. Electrospun Polymer Blend Nanofibers for Tunable Drug Delivery: The Role of Transformative Phase Separation on Controlling the Release Rate. Molecular Pharmaceutics. 2016;13(1):25-39.
10. Alsulays BB, Park J-B, Alshehri SM, Morott JT, Alshahrani SM, Tiwari RV, et al. Influence of molecular weight of carriers and processing parameters on the extrudability, drug release, and stability of fenofibrate formulations processed by hot-melt extrusion. Journal of Drug Delivery Science and Technology. 2015;29:189-98.
11. Yu D-G, Branford-White C, White K, Li X-L, Zhu L-M. Dissolution improvement of electrospun nanofiber-based solid dispersions for acetaminophen. AAPS PharmSciTech. 2010;11(2):809-17.
12. Nair R, Nyamweya N, Gönen S, Martínez-Miranda LJ, Hoag SW. Influence of various drugs on the glass transition temperature of poly(vinylpyrrolidone): a thermodynamic and spectroscopic investigation. International Journal of Pharmaceutics. 2001;225(1–2):83-96.
13. Vasanthavada M, Tong W-QT, Joshi Y, Kislalioglu MS. Phase behavior of amorphous molecular dispersions II: Role of hydrogen bonding in solid solubility and phase separation kinetics. Pharmaceutical research. 2005;22(3):440-8.
14. Marsac PJ, Rumondor AC, Nivens DE, Kestur US, Stanciu L, Taylor LS. Effect of temperature and moisture on the miscibility of amorphous dispersions of felodipine and poly (vinyl pyrrolidone). Journal of Pharmaceutical Sciences. 2010;99(1):169-85.
15. Rumondor AC, Marsac PJ, Stanford LA, Taylor LS. Phase behavior of poly (vinylpyrrolidone) containing amorphous solid dispersions in the presence of moisture. Molecular Pharmaceutics. 2009;6(5):1492-505.
16. Djuris J, Nikolakakis I, Ibric S, Djuric Z, Kachrimanis K. Preparation of carbamazepine–Soluplus® solid dispersions by hot-melt extrusion, and prediction of drug–polymer miscibility by thermodynamic model fitting. European Journal of Pharmaceutics and Biopharmaceutics. 2013;84(1):228-37.
17. Rumondor ACF, Stanford LA, Taylor LS. Effects of Polymer Type and Storage Relative Humidity on the Kinetics of Felodipine Crystallization from Amorphous Solid Dispersions. Pharmaceutical Research. 2009;26(12):2599-606.
18. Alshahrani SM, Lu W, Park J-B, Morott JT, Alsulays BB, Majumdar S, et al. Stability-enhanced Hot-melt Extruded Amorphous Solid Dispersions via Combinations of Soluplus® and HPMCAS-HF. AAPS PharmSciTech. 2015;16(4):824-34.
19. Fedors RF. A method for estimating both the solubility parameters and molar volumes of liquids. Polymer Engineering & Science. 1974;14(2):147-54.
20. Marks JA, Wegiel LA, Taylor LS, Edgar KJ. Pairwise Polymer Blends for Oral Drug Delivery. Journal of Pharmaceutical Sciences. 2014;103(9):2871-83.
21. Lu Q, Zografi G. Phase Behavior of Binary and Ternary Amorphous Mixtures Containing Indomethacin, Citric Acid, and PVP. Pharmaceutical research. 1998;15(8):1202-6.
22. Vogel C, Wessel E, Siesler HW. FT-IR Imaging Spectroscopy of Phase Separation in Blends of Poly(3-hydroxybutyrate) with Poly(l-lactic acid) and Poly(ϵ-caprolactone). Biomacromolecules. 2008;9(2):523-7.
23. Kazarian SG, Chan KLA. Sampling Approaches in Fourier Transform Infrared Imaging Applied to Polymers. In: Grundke K, Stamm M, Adler H-J, editors. Characterization of Polymer Surfaces and Thin Films. Berlin, Heidelberg: Springer Berlin Heidelberg; 2006. p. 1-6.
24. Konno H, Taylor LS. Influence of different polymers on the crystallization tendency of molecularly dispersed amorphous felodipine. Journal of Pharmaceutical Sciences. 2006;95(12):2692-705.
25. Application note: ATR – Theory and Applications2011.

26. Forster A, Hempenstall J, Rades T. Characterization of glass solutions of poorly water-soluble drugs produced by melt extrusion with hydrophilic amorphous polymers. Journal of Pharmacy and Pharmacology. 2001;53(3):303-15.
27. Qi S, Belton P, McAuley W, Codoni D, Darji N. Moisture uptake of polyoxyethylene glycol glycerides used as matrices for drug delivery: kinetic modelling and practical implications. Pharmaceutical research. 2013;30(4):1123-36.
28. Al-Muhtaseb AH, McMinn WAM, Magee TRA. Moisture Sorption Isotherm Characteristics of Food Products: A Review. Food and Bioproducts Processing. 2002;80(2):118-28.
29. Andrade P RD, Lemus M R, Perez C CE. Model of Sorption Isoterms for Food: Uses and Limitations. Vitae. 2011;18:325-34.
30. Lewicki PP. The applicability of the GAB model to food water sorption isotherms. International Journal of Food Science & Technology. 1997;32(6):553-7.
31. Waterman KC, Adami RC. Accelerated aging: Prediction of chemical stability of pharmaceuticals. International Journal of Pharmaceutics. 2005;293(1–2):101-25.
32. Di Martino P, Palmieri G, Martelli S. Evidence of a metastable form of fenofibrate. Die Pharmazie. 2000;55(8):625-6.
33. Forster A, Hempenstall J, Tucker I, Rades T. The potential of small-scale fusion experiments and the Gordon-Taylor equation to predict the suitability of drug/polymer blends for melt extrusion. Drug Development and Industrial Pharmacy. 2001;27(6):549-60.
34. Kestur US, Van Eerdenbrugh B, Taylor LS. Influence of polymer chemistry on crystal growth inhibition of two chemically diverse organic molecules. CrystEngComm. 2011;13(22):6712-8.
35. Ignatious F, Sun L, Lee C-P, Baldoni J. Electrospun nanofibers in oral drug delivery. Pharmaceutical research. 2010;27(4):576-88.
36. Rasekh M, Karavasili C, Soong YL, Bouropoulos N, Morris M, Armitage D, et al. Electrospun PVP–indomethacin constituents for transdermal dressings and drug delivery devices. International Journal of Pharmaceutics. 2014;473(1–2):95-104.
37. Marsac PJ, Li T, Taylor LS. Estimation of Drug–Polymer Miscibility and Solubility in Amorphous Solid Dispersions Using Experimentally Determined Interaction Parameters. Pharmaceutical research. 2008;26(1):139-51.
38. Taylor LS, Zografi G. Sugar–polymer hydrogen bond interactions in lyophilized amorphous mixtures. Journal of Pharmaceutical sciences. 1998;87(12):1615-21.
39. Nagy ZK, Balogh A, Drávavölgyi G, Ferguson J, Pataki H, Vajna B, et al. Solvent-free melt electrospinning for preparation of fast dissolving drug delivery system and comparison with solvent-based electrospun and melt extruded systems. Journal of pharmaceutical sciences. 2013;102(2):508-17.
40. Brettmann B, Bell E, Myerson A, Trout B. Solid-state NMR characterization of high-loading solid solutions of API and excipients formed by electrospinning. Journal of Pharmaceutical Sciences. 2012;101(4):1538-45.
41. Reneker DH, Yarin AL. Electrospinning jets and polymer nanofibers. Polymer. 2008;49(10):2387-425.
42. Hancock BC, Zografi G. Characteristics and significance of the amorphous state in pharmaceutical systems. Journal of Pharmaceutical Sciences. 1997;86(1):1-12.
43. Guilbert S, Cuq B, Gontard N. Recent innovations in edible and/or biodegradable packaging materials. Food Additives & Contaminants. 1997;14(6-7):741-51.

6. Chapter 6: Electrospun Polymer Blend Nanofibers for Tunable Drug Delivery: The Role of Transformative Phase Separation on Controlling the Release Rate

6.1 Introduction

In the previous chapter we explored the use of electrospun fibrous formulations of polymer blends of hydrophilic, PVP and hydrophobic polymers, including Eudragit E, Soluplus and HPMCAS, to enhance the aqueous solubility and the physical stability of the FF. However, the results showed the apparent miscibility of the polymer-polymer and the drug-polymer as being the key parameter that determined the physical stability of the formulations. The apparent miscibility of the polymer-polymer and drug-polymer can be alternated using different solvents (1). Al-obidi et al. showed that using acetone/water and acetone/methanol as the vehicle for a griseofulvin-PVP-poly[N-(2-hydroxypropyl) methacrylate] (PHPMA) ternary solid dispersion resulted in different T_g values and physical stabilities of the drug (1). The preparation methods can influence the phase separation scale of the drug-polymer binary system. Brettman and Nagy reported that the use of electrospinning can minimise the phase separation of the drug and polymer to the nanoscale in comparison to HME (2, 3). Preparation methods can be a potential means to intentionally manipulate different scales of phase separation. In addition, the PVP-HPMCAS blend showed the potential of providing a modified release formulation. Modified release is often a desirable feature for certain types of controlled drug release. Yu et al. prepared a polymer blend of PVP and ethyl cellulose using coaxial electrospinning, which manipulated the core-shell structure phase separation in the electrospun fibre structures (4). This resulted in modified drug loading, in which the outer layer of PVP released the API as a burst release and then there was a sustained release from the ethyl cellulose phase. Therefore, this chapter will focus on exploring the tuneability of the modified release feature of PVP-HPMCAS blends.

One of the aims of this chapter was to provide an improved understanding to fill this knowledge gap. The use of dichloromethane (DCM) and ethanol (3:7) as a solvent for PVP-HPMCAS resulted in the blend being miscible (Chapter 5). In this chapter, 9:1 ethanol: water was used for the blending of PVP-HPMCAS. It was expected to alter the apparent miscibility of the PVP-HPMCAS blend. The use of different solvent systems can affect the polymer conformation after the solvent removal process (1). Consequently, the apparent miscibility of the polymer can be modified using different solvents. Another aspect of this is to evaluate different preparation methods, including film casting, spin-coating and electrospinning, which have different rates of solvent evaporation. This is expected to influence the scale of the phase separation in the PVP-HPMCAS blends.

To produce controlled drug delivery systems using electrospun fibres, it has been empirically accepted in the literature that the blending of hydrophilic and hydrophobic polymers can improve the drug loading efficiency and reduce the burst release of drugs (5-9). However, there is little known on how the phase behaviour of the polymer blends contributes to the *in vitro* drug release behaviour of the electrospun fibres. Therefore, the transformation of the phase separation of the electrospun blend fibres upon wetting was investigated. For the PVP-HPMCAS blends, PVP is a hydrophilic polymer that can provide a fast drug release (10, 11), while HPMCAS is a pH dependent dissolved polymer that can only dissolve at a pH greater than five (12). Therefore, this blend can potentially provide a modified drug release. The mechanism of the modified release was evaluated. The PVP-HPMCAS fibres were loaded with a model drug, PCM. In contrast to other electrospinning techniques, such as co-axial electrospinning in which different polymer phases are artificially separated to create a core and outer coating shell (5, 7, 8), the behaviour of the nanofibers containing two polymers and a model drug produced via solvent evaporation during single spinneret electrospinning is expected to be more complex. In this chapter, co-axial electrospinning (CS-ES) fibres that should have a designed core-shell structure were used in comparison with the behaviour of the single spinneret electrospinning (SS-ES) polymer blend fibres.

6.2 Methodology

6.2.1 Preparation of cast film, spin-coated films and electrospun fibers of PVP-HPMCAS blends

A 10% w/v PVP-HPMCAS solution was prepared for film casting, spin-coating and SS-ES. PVP and HPMCAS at a weight proportion of 1:1 were precisely weighted and dissolved in ethanol:water (9:1 v/ v). The solution was stirred and sonicated until all solid material was completely dissolved. For film casting, 500 μL of the solution was applied to a Teflon coated plate (20 × 20 cm) and dried under ambient conditions in a fume cupboard for 24 h. For spin-coated samples, a few drops of the PVP-HPMCAS solution were applied on a glass substrate, which was spun at 2000 rpm for 3 min using a SCS G3P-8 lab scale spin coater (Indianapolis, USA). A custom-made single spinneret electrospinning device was used to prepare the polymer blend fibres at a constant flow rate of 1.5 $mL.h^{-1}$ and a voltage of 15 kV. The distance from the spinneret to the grounded rotating drum collector (coated with aluminium foil) with a spinning rate of 500 rpm was fixed at 15 cm. For CS-ES, ethanol:DCM (7:3 v/v) was used as the solvent to ensure rapid solvent evaporation and to minimize the mixing at the core-shell interface. The solutions of the core (HPMCAS) and sheath (PVP) layers were prepared separately. The solutions of the core and sheath

layers were fed from separate syringe pumps at rate 0.5 $mL.h^{-1}$ to the coaxial needle. All electrospinning experiments were performed under the conditions of 20 ± 2 °C and 40 ± 5% RH. After the electrospinning process, the fibre mats were peeled from the collector and stored in a 0% RH desiccator filled with phosphorus pentaoxide prior to analysis.

6.2.2 Preparation of drug loaded electrospun fibres

The solid state drug contents for all formulations studied were fixed at 25% (w/w). SS-ES solutions with a 10% w/v solid content were prepared by dissolving precisely weighed PVP and HPMCAS at weight ratios of 3:1, 1:1 and 1:2 into an ethanol-water mixture. PCM was then dissolved into the polymer solutions. The solutions were stirred and sonicated until all solid content was dissolved. The solid-state drug loading for the core and shell layers of the CS-electrospun fibres was 12.5% (w/w). The same SS- ES and CS-ES operation parameters as described above were used for the preparation of the drug loaded fibre mats.

6.2.3 T_g estimation using GT equation

The GT equation, as modified by Lu et al. (13), was used to estimate the T_g of the placebo PVP-HPMCAS blend and the ternary PCM-PVP-HPMCAS blends at PVP:HPMCAS ratios of 3:1, 1:1 and 1:2. The GT equation was described in section 5.2.7. The ΔC_p values of PVP, HPMCAS and PCM were experimentally measured using MTDSC as 0.290, 0.270 and 0.508 $J.g^{-1}\cdot C^{-1}$. The estimated T_gs of the polymer blends and ternary blends are reported in **Table 6.2**.

6.2.4 Characterisation methods

In this chapter, a range of characterisation techniques were employed to characterise the ternary blended formulations of PCM-PVP-HPMCAS, which were MTDSC, ATR-FTIR, PXRD, LTA and ss-NMR. For the experimental details of these characterisation techniques refer to sections 2.4.2.2, 2.4.5.2, 2.4.7.4, 2.4.11.3 and 2.4.12.2, respectively.

6.2.5 Fibrous morphology study

SEM and TEM were used to investigate the external and internal morphologies of the placebo PVP-HPMCAS fibres and ternary PCM-PVP-HPMCAS fibres. SEM and TEM analyses were performed according to the procedures described in sections 2.4.8.2 and 2.4.9.2, respectively.

6.2.6 Disintegration and wettability studies of electrospun fibre mats

Pieces of drug-loaded SS-ES and CS-ES fibre mats were cut into areas of approximately 4x4 cm and transferred to plastic Petri dishes filled with 10 ml of British Pharmacopoeial HCl dissolution medium (pH 1.2). The disintegration processes of different electrospun fibre mats were recorded using a COOLPIX P510 digital camera (Nikon, Japan).

6.2.7 *In vitro* drug release studies of drug loaded electrospun fibre mats

All *in vitro* drug release experiments were performed according to the procedure described in section 2.6.2. British Pharmacopoeia HCl dissolution medium (900 mL) (pH 1.2) was used for each dissolution vessel. Electrospun fibre mats containing the equivalent of 5 mg PCM were used for the release tests to ensure sink conditions. The PCM released from the electrospun fibres was evaluated by UV-VIS spectroscopy, which was described in section 2.6.3. All UV-VIS measurements were performed in triplicate.

6.2.8 Release data analysis and statistical evaluation

The PCM release kinetics of the polymer blended electrospun fibres were assessed by fitting to the power law (**equation 2.7**) and biphasic released model (**equation 2.9**) to investigate the drug release mechanism. The principles of these mathematic models were described in sections 2.7.1.1 and 2.7.1.2, respectively. Then, the AICc statistical analysis was performed to assess the quality of these models. The procedure for the AICc analysis is referred to in section 2.7.1.3.

6.3 Results

6.3.1 Processing effect on phase separation of PVP-HPMCAS blends

The theoretical miscibility of PVP and HPMCAS was estimated to provide an indication of the intrinsic mixing behaviour of the two polymers in the absence of any effects induced by processing. The most widely used method for miscibility estimation is comparing the solubility parameters (δ) of the two polymers. Similar solubility parameter values indicate good miscibility between the two components (14). In the literature, miscibility predictions are categorised based on the Δδ values being likely miscible (Δδ <2 $MPa^{1/2}$), partially miscible (Δδ between 2 and 10 $MPa^{1/2}$) and immiscible (Δδ >10 $MPa^{1/2}$) (14). From the solubility parameter calculated by Fedor's group contribution method, the δ are 28.2, 27.2 and 22.4 $MPa^{1/2}$ for PVP, PCM and HPMCAS, respectively (15, 16). The Δδ between HPMCAS and PVP is 5.8, suggesting partial miscibility between the two polymers. For

such partially miscible blends, the non-equilibrium apparent miscibility is expected to be affected by additional processing. To gain a comparative understanding of the effect of processing on the phase separation behaviour of polymer blends, four different solvent evaporation based methods were used to prepare PVP-HPMCAS 1:1 (w/w) blends. These include conventional film casting, spin-coating and SS- and CS-electrospinning. The thicknesses of the cast and spin-coated PVP-HPMCAS blend films were 90±5μm and 5±1.5μm, respectively. These films were opaque and brittle after complete solvent removal, whereas the electrospun fibre mats were flexible and easily peeled off from the collector surface.

The SEM images reveal a rougher surface morphology of the cast films, containing cracks and holes in comparison to the spin-coated films (**Figure 6.1A** and **B**). The spin-coated film surface is densely packed with sub-micron semi-spherical morphologies. These surface features were further characterised using AFM and LTA. As seen in **Figure 6.1C** and **D**, the diameters of the semi-spherical islands are circa 6±1.8μm and below 1μm for the cast and spin-coated films, respectively.

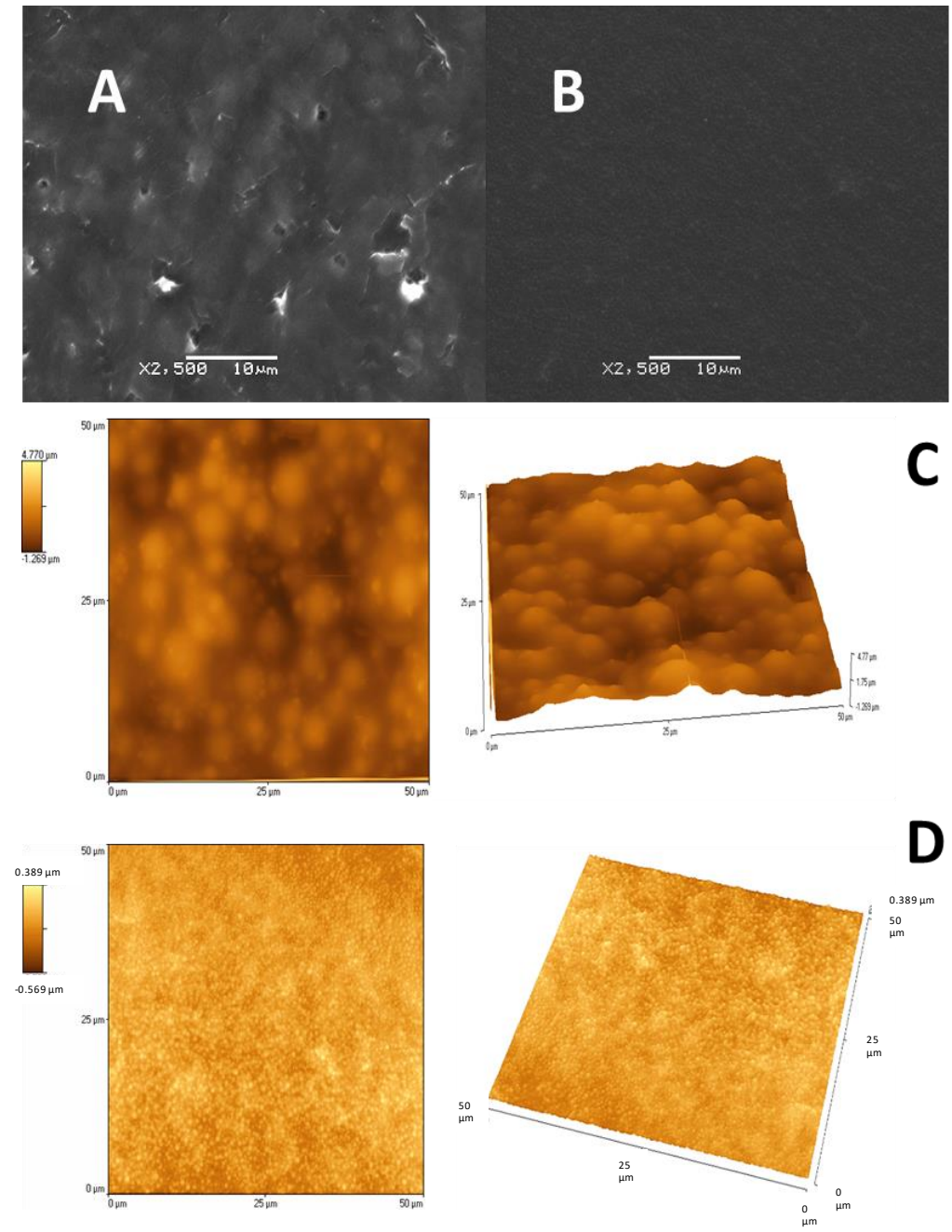

Figure 6.1 Morphologies of PVP-HPMCAS 1**:**1 blend films using SEM**: (**A**)** cast film and **(**B**)** spin-coated film, and AFM**: (**C**)** cast film and **(**D**)** spin-coated film, with 2D **(**left**)** and 3D **(**right**)** topography images**.**

The LTA results of the cast and spin-coated films are shown in **Figure 6.2**. The temperature at the onset of the deflection of the nano-TA signal indicates the softening temperature of the tested material surface. The spin-coated pure HPMCAS films show a transition temperature at approximately 158±2.5 °C, which is about 20°C higher than the T_g of the polymer when tested using MTDSC. This phenomenon has been observed and reported in the literature previously when comparing LTA measurements with DSC responses (34). It is believed that the measurable transition using LTA is a softening response relative to the pressure exerted by the probe, which is different from the T_g of the bulk material measured

using DSC. The rapid heating rates used for LTA experiments could also contribute to the overshoot of the transition measured by LTA. The LTA results of the spin coated PVP K90 films show continuous softening from the ambient temperature (**Figure 6.2B**), which indicates the high fluidity of the surfaces of the PVP films. Similar results have been reported previously for PVPVA films (35). This may be associated with the highly hygroscopic nature of the polymer, which leads to significantly plasticized surfaces of the films with a high moisture content. The LTA results for the PVP-HPMCAS cast films (**Figure 6.2C**) are similar to the results of the pure PVP films, with continuous softening from the ambient temperature. This may indicate the likelihood of PVP covering the outer surfaces of the blend films prepared by the conventional casting method. The relatively slow solvent evaporation may allow the phase separation of the two polymers into layers. The LTA results of the spin coated films (**Figure 6.2D**) show a higher softening temperature at approximately 55°C, which is still much lower than the T_g of the individual polymers and the predicted T_g of the PVP:HPMCAS 1:1 blend. The fact that the softening temperature has shifted to a higher temperature in comparison to cast films indicates less phase separation of the PVP from the blend and the presence of a certain proportion of HPMCAS at the top surface of the spin-coated films.

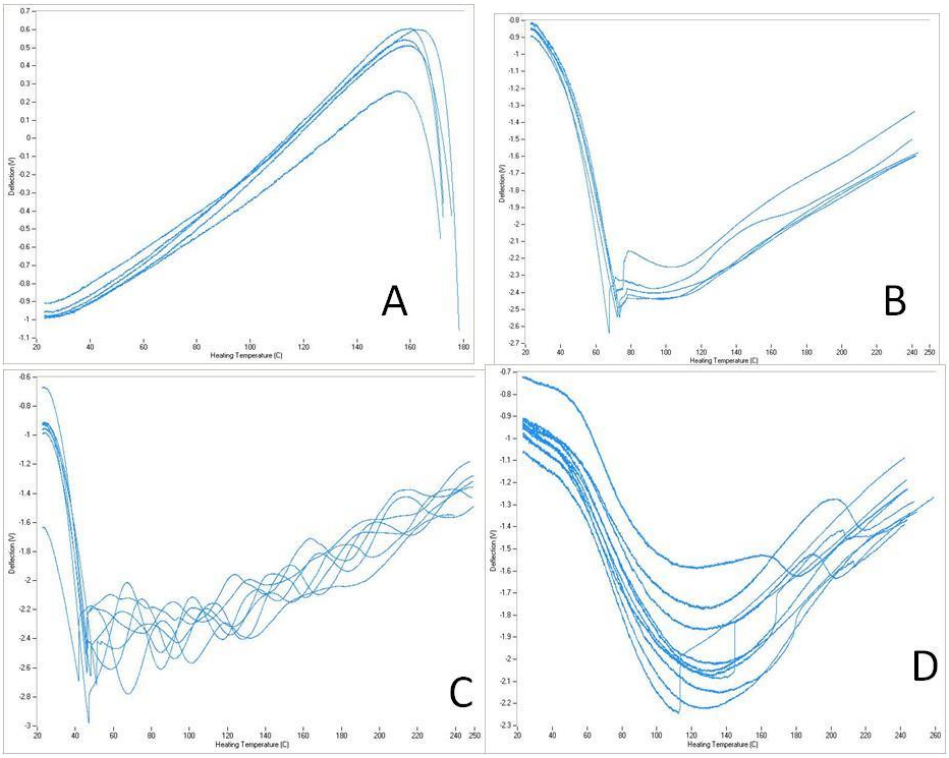

Figure 6.2 LTA results of (A) spin-coated HPMCAS film, (B) spin-coated PVP film, (C) PVP-HPMCAS 1:1 cast film and (D) PVP-HPMCAS spin-coated film.

Pure PVP and HPMCAS had distinct T_g, which were 176.4±2.0°C and 122.0±2.2°C, respectively. The phase separations in the cast and spin-coated films are clearly evident in

the MTDSC results for the films. As seen in **Figure 6.3**, there is a double T_g in the MTDSC result for the physical mixture of PVP-HPMCAS with a 1:1 ratio. These two T_gs are highly similar to the T_g of each polymer alone, which indicates the low miscibility between the two polymers (3). As illustrated in **Figure 6.3**, double T_gs at similar temperatures to those observed in the physical mixtures are also seen in the cast and spin-coating blend films, which indicates a significant phase separation of the PVP and HPMCAS phases in these films.

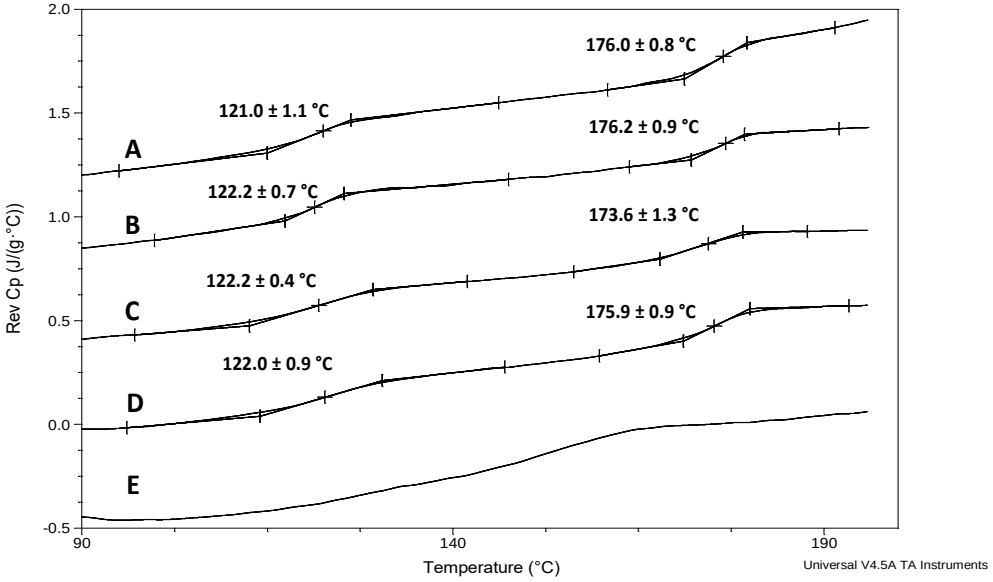

Figure 6.3 Reversing signals of MTDSC results of (A) physical mixture of PVP and HPMCAS (1:1 w/w), (B) conventional cast polymer blend films, (C) spin-coated polymer blend films, (D) co-axial CS-electrospun fibres with PVP as the shell and HPMCAS as the core and (E) SS-electrospun polymer blend fibres.

The electrospun fibre mats are flexible films on a macroscopic scale. The SEM images of the electrospun fibres show smooth surfaces with no beading (**Figure 6.4**). The average diameters of the SS- and CS-electrospun fibres are 0.41± 0.22 μm and 1.37±0.47 μm, respectively. A bimodal diameter distribution is observed for both types of fibres, which contributes to the high standard deviation values seen in both cases. This relatively large variation in diameter, in particular for the SS-electrospun fibres, may be caused by clogging at the tip of the spinnerets, which leads to multi-Taylor cone formation during the electrospinning (12).

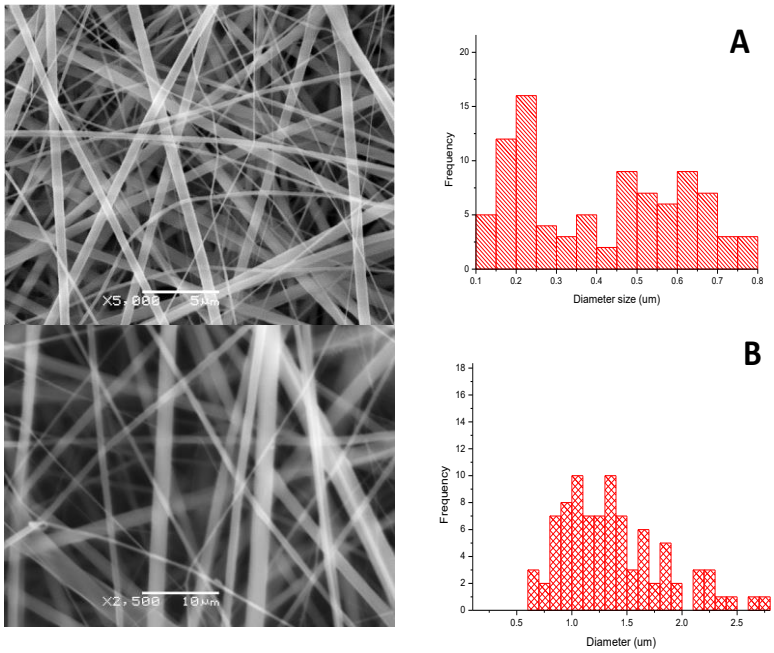

Figure 6.4 SEM images and histograms of fibre diameter distributions of (A) SS-electrospun PVP-HPMCAS 1:1 blend fibres and (B) CS-electrospun PVP-HPMCAS 1:1 blend fibres.

The phase separation in the PVP: HPMCAS (1:1) electrospun fibres was first examined using thermal methods. Due to the submicron dimensions of each single fibre, a localised single-point characterisation by the LTA on the fibres was extremely challenging, thus making it difficult to obtain reliable results. Therefore, LTA was not used to study the fibres, but MTDSC was used to determine the phase separation of the fibres as a bulk mat. Clearly separated double T_gs are shown in the MTDSC results for the CS-ES core-shell fibre mats. This was expected as the polymers were not blended, but separately formed as the core and shell of the fibres. The formation of well-separated core and shell layers was confirmed by the TEM results for the CS-electrospun fibres (**Figure 6.5**). However, for the SS-ES fibres, no clear double T_g could be detected using the reversing C_p signal.

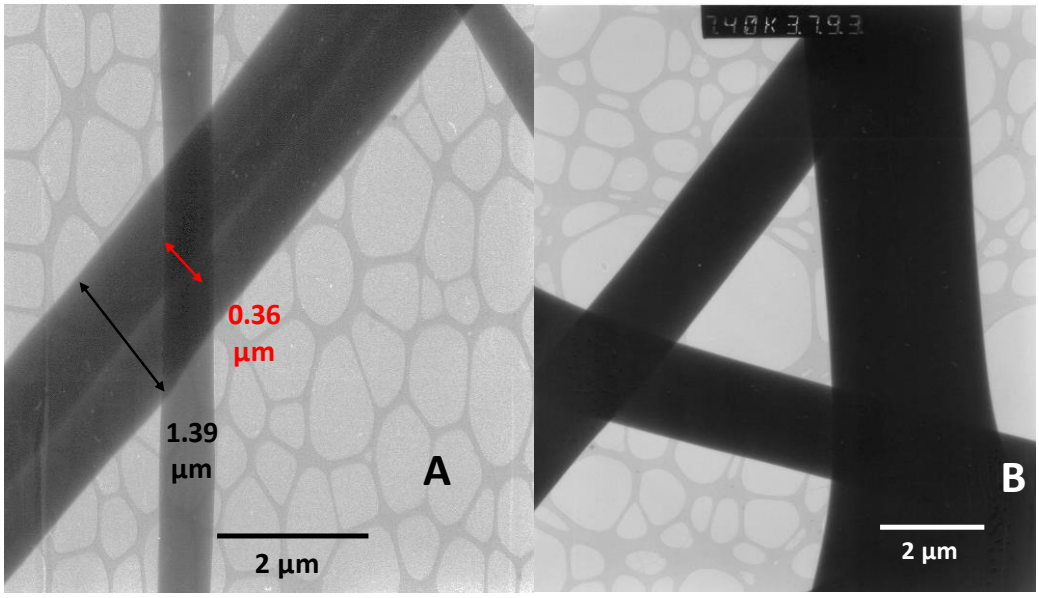

Figure 6.5 TEM images of (A) the placebo CS-electrospun fibres with PVP as the shell layer and HPMCAS as the core and (B) the CS-electrospun PVP and HPMCAS fibres after PCM incorporation into both core and shell with equal loading.

To further characterise the phase separation behaviour of the blends (PVP: HPMCAS 3:1, 1:1 and 1:2 w/w) proton-NMR relaxometry was used (2, 17-19). The ^{1}H spin lattice relaxation time in the laboratory frame (T_1) and the spin lattice relaxation time in a rotating frame ($T_{1\rho}$) of the placebo SS-electrospun fibres are summarised in **Table 6.1**. It can be seen that for all fibre samples a single T_1 relaxation time was obtained, whereas a double exponential $T_{1\rho}$ relaxation was detected for all blended fibres. The presence of a two-component $T_{1\rho}$ behaviour indicates that on this time scale two separately relaxing domains exist; whereas, for the T_1 time scale, the polarisation exchange rates are such that complete mixing of the polarisation occurs. Assuming that mixing is by the process of spin diffusion, it is possible to use these results to estimate the order of magnitude of the domains involved (17). For laminar geometry the criterion for diffusive exchange between two regions that is slow enough to allow the observation of two or more relaxation processes is given by:

$$2\sqrt{2}(A^2/\pi^2 D)|\Delta\gamma| > 1 \quad \text{.....(6.1)}$$

where A is the laminar dimension, D is the relevant diffusion coefficient and $\Delta\gamma$ is given by:

$$\Delta\gamma = \left(\frac{1}{T_a} - \frac{1}{T_b}\right) \text{.....(6.2)}$$

where T_a and T_b are the relaxation time of the phase a and b, respectively. Note that it is important to use the differences in relaxation rate rather than a single relaxation rate. In the case of the T_1 data, it is apparent (**Table 6.1**) that blending the polymers using electrospinning resulted in a single T_1 that is shorter than the T_1 of either of the polymers

on their own. If the values of relaxation times converge on mixing, then $|\Delta\gamma|$ is around zero and no discrimination between sites is possible. If, however, the differences between components remain the same order as in the separate components, then $|\Delta\gamma|$ has a value of about 1. The value of *D* may be as high as $8x10^{-16}$ m^2s^{-1} in immobile polymers (18) but as low as $0.5x\ 10^{-16}$ m^2s^{-1} in mobile polymers (19), thus the possible range of *A* is between 8 and 30 nm. However, the observation of a single relaxation time of the polymer blends could imply a complete mixing of the polymers. Alternatively, if some immiscibility exists, since $|\Delta\gamma|$ is unknown and may be greater or less than 1 a definitive estimate of the domain size is not possible. The observation of a single exponential relaxation, therefore, cannot be used as a reliable guide for domain size. However, the change in T_1 is such that it cannot be the weighted average of the individual T_1's of the polymers and is indicative of some physical or chemical change in the system on electrospinning.

Table 6.1 ss-NMR results (T_1 (^{1}H) and $T_{1\rho}$ (^{1}H)) of the raw materials and blend formulations with (25% w/w) and without PCM.

Material	T_1(^{1}H)(ms)	$T_{1\rho}$(^{1}H)(ms)	
PVP	269	6.9	
HPMCAS (LF)	214.0	3.0	
Crystalline PCM	93000	N/A	
PVP:HPMCAS 3:1	165.0	1.4 ± 0.3	10 ± 2.0
PVP:HPMCAS 1:1	150.0	1.0 ± 0.3	5.9 ± 0.6
PVP:HPMCAS 1:2	175.0	1.0 ± 0.2	5.5 ± 0.4
PCM PVP:HPMCAS 3:1	277.0	0.32 ± 0.09	3.1 ± 0.3
PCM PVP:HPMCAS 1:1	293.0	0.2 ± 0.04	2.5 ± 0.1
PCM PVP:HPMCAS 1:2	299.0	1.51	
PCM:PVP	199.0	1.7	
PCM:HPMCAS	222.0	0.7	

Better estimates of domain size are afforded by the observation of multiple exponential $T_{1\rho}$ relaxations. The observation of a double exponential decay implies that there must be at least two populations of protons in the system. However, it cannot be concluded that the two systems are not in exchange since the ratios of the populations of the two relaxation components do not scale with the relative proton populations of the polymers in the materials. This may be due to mixed but separate phases being formed or because of the mixing of the spin populations by spin diffusion. Assuming that the differences in relaxation rates of the two populations are the same as that for the pure components and recognising that under spin locking conditions the value of *D* is halved (i.e., $D=4x10^{-16}$) (20), the upper limit for *A* is 3 nm. If *D* is at the lower limit the value of *A* is of the order of 0.5 nm. If the difference in relaxation rates is taken as that between the two components measured in the mixtures, the values are in the order of 1.5 and 4 nm. Given the approximations involved, the conclusion is that the dimensions of the separated phases must be greater than a few nanometers.

6.3.2 Effect of drug incorporation on phase separation of electrospun blend fibres

Drug incorporation led to a slight morphological change in the SS-ES blend fibres. As seen in **Figure 6.6**, smooth cylindrical fibres can be seen without beading or obvious drug crystals for all PVP: HPMCAS blend ratios. The average diameters of the drug loaded SS-ES blend fibres are 1.15±0.48 μm, 0.52±0.24 μm and 1.69±0.30 μm for PVP-HPMCAS with ratios of 3:1, 1:1 and 1:2, respectively. Bimodal distributions of the diameters of the fibres are still observed in the PVP-HPMCAS blends with ratios of 3:1 and 1:1, but with a 1:2 ratio a more uniform fibre diameter is achieved. Interestingly, for the CS-ES fibres after drug incorporation, despite no obvious morphological changes, the separation of the core and shell layers is no longer evident by TEM (**Figure 6.5**). The average diameters of the drug loaded core-shell fibres were 1.1± 0.2 μm. This is likely to be a result of the change in the miscibility between the phase-separated domains after the drug partitioning into the phases. Therefore, the miscibility of the PCM in the two polymers was first estimated using the solubility parameter method (14, 21). The $\Delta\delta$ of the PCM-PVP and PCM-HPMCAS were 1 and 4.8, respectively, which indicates that the PCM has a better miscibility with PVP than HPMCAS and the PCM-PVP and PCM-HPMCAS phases are partially miscible. This suggests that there is likely to be a higher partition of PCM into the PVP-rich phase than the HPMCAS-rich phase. This prediction was further tested using ATR-FTIR spectroscopy, MTDSC and ss-NMR.

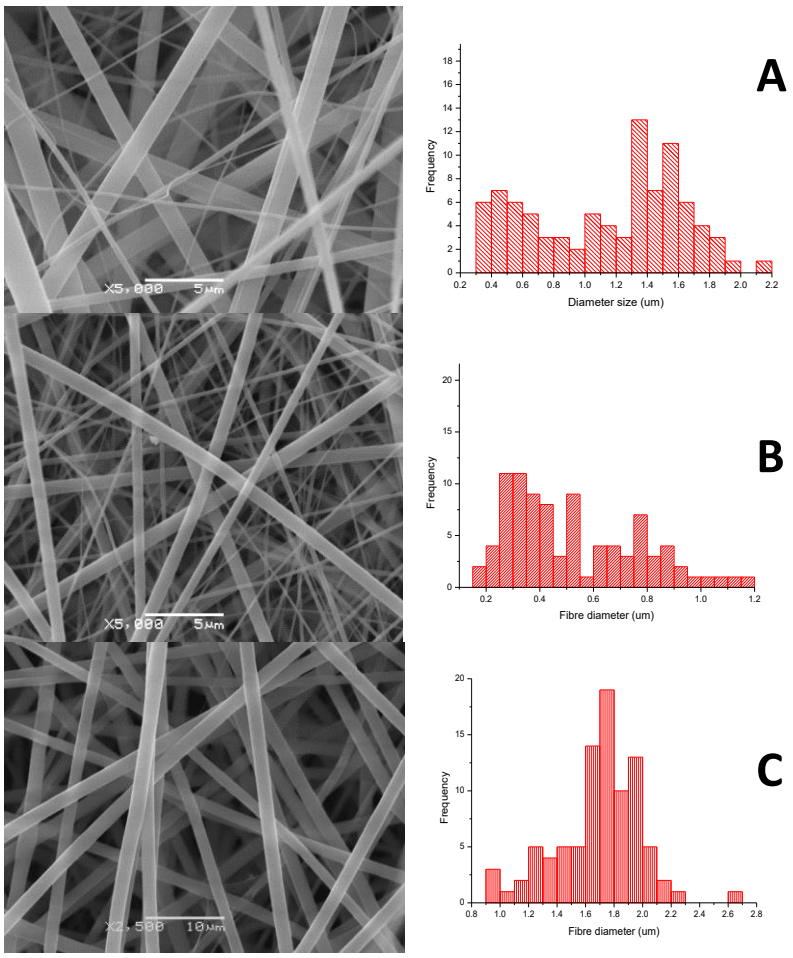

Figure 6.6 SEM images and histograms of the diameter distributions of SS-electrospun 25% PCM loaded PVP-HPMCAS blends fibres with PVP: HPMCAS ratios of (A) 3:1, (B) 1:1 and (C) 1:2.

In the first instance, the contribution of the drug-polymer molecular interaction to the miscibility was assessed using ATR-FTIR spectroscopy. After incorporation into the polymer fibres, the PCM related peaks in the ATR-FTIR spectra of the drug-loaded fibres all show clear amorphous features (**Figure 6.7**). The carbonyl stretching of HPMCAS (at 1732 cm^{-1}) in the spectra of HPMCAS-PCM fibres shows no significant shift in position in comparison to that of pure HPMCAS (at 1735 cm^{-1}). The single PVP carbonyl peak (which is at 1663 cm^{-1} for pure PVP) developed into a doublet peak at 1657 and 1650 cm^{-1} in the spectra of the PVP-PCM fibres. This indicates a hydrogen bonding interaction between the PVP and the PCM (22). This PVP-PCM interaction is likely to contribute to the higher miscibility between the two in comparison to the PCM-HPMCAS system.

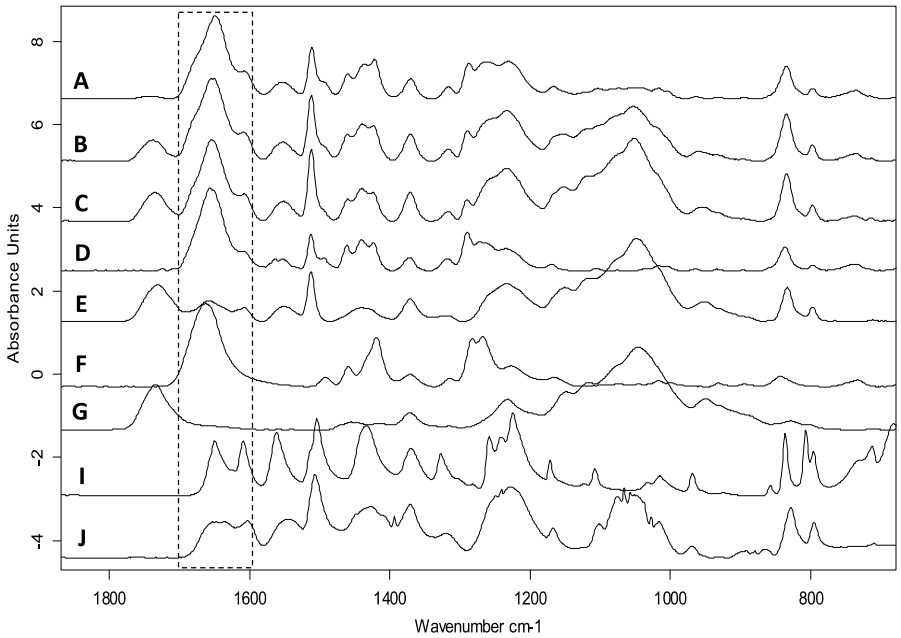

Figure 6.7 Partial ATR-FTIR spectra of raw materials and 25% PCM loaded SS-electrospun fibres (A) PCM PVP-HPMCAS 3:1, (B) PCM PVP-HPMCAS 1:1, (C) PCM PVP-HPMCAS 1:2, (D) PCM-PVP, (E) PCM-HPMCAS, (F) PVP as received, (G) HPMCAS as received, (I) PCM form I and (J) amorphous PCM prepared by melt-cool method. (The dashed line box highlights the PVP carbonyl peak that shifted to a lower wavenumber after the incorporation of PCM.)

The spectra of the PVP-HPMCAS-PCM fibres show similar trends to the carbonyl peak of PVP shifting to lower wavenumbers and no significant shift for HPMCAS. For these blend samples, the doublet carbonyl peaks at 1656 and 1651 cm^{-1} can be clearly seen. These peaks are associated with hydrogen bonded PVP and PCM. The shift of the PVP carbonyl peak to lower wavenumbers is more significant than that of the HPMCAS carbonyl peak in the spectra of the blend formulations. This suggests that in the blend formulations PCM has a more favourable and stronger interaction with PVP via hydrogen bonding than with HPMCAS. This leads to the prediction of more PCM partitions into the PVP-rich phases than the HPMCAS-rich phases in the drug-loaded fibres. This could potentially have significant implications in modulating the drug release of such fibres.

The phase separation was further studied using MTDSC. As seen in **Figure 6.8**, the DSC results of the single polymer-PCM fibres show single T_gs at 115.1±1.1 and 57.6±1.4°C for PVP-PCM and HPMCAS-PCM, respectively. According to the GT prediction (under ideal mixing), the experimental PCM-PVP T_g was relatively close to the predicted value, whereas a significant negative deviation was observed between the prediction and experimental T_g values of the PCM-HPMCAS blend (**Table 6.2**). In the literature, a

negative deviation from the GT prediction is usually attributed to stronger drug-drug and polymer-polymer intermolecular interactions than drug-polymer interactions (23). This again indicates the low level of PCM-HPMCAS interaction in comparison to that of the PVP-PCM. A small melting enthalpy was detected in the PCM-HPMCAS fibres at 153.3±0.2°C, which is likely to be the depressed melting of the crystalline PCM. The presence of the crystalline PCM in the HPMCAS fibres further indicates the lower miscibility between the HPMCAS with PCM in comparison to the PVP.

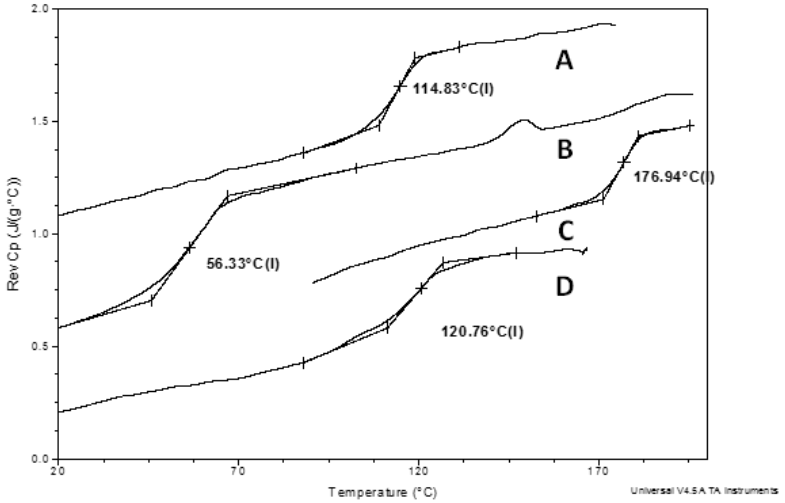

Figure 6.8 MTDSC results of SS-ES fibres of (A) PCM-PVP and (B) PCM-HPMCAS as well as (C) raw material PVP and (D) HPMCAS.

In comparison to the inconclusive MTDSC results of the placebo SS-electrospun fibres, the MTDSC results of all drug loaded SS-electrospun blend fibre samples exhibit a single T_g with no melting of PCM (**Figure 6.9**), which suggests the fibres are molecular dispersions of PCM in polymers. This is a significant observation and a clear indication of the improved miscibility between the components of the ternary system (PCM-PVP-HPMCAS), which is a result of the drug incorporation. This was further confirmed by the PXRD results (**Figure 6.10**). As seen in **Table 6.2**, the experimental T_g of the PCM loaded polymer blend fibres demonstrated greater negative deviations from the GT predictions with increasing HPMCAS content in the formulation (24). This can be attributed to the weaker PCM-HPMCAS interaction suggested previously by the ATR-FTIR spectroscopy data. The PCM loaded CS-ES core-shell fibres (PVP:HPMCAS 1:1) also show a single T_g at 86.2±1.5°C, which indicates mixing of the core and shell layers of the fibres with drug incorporation.

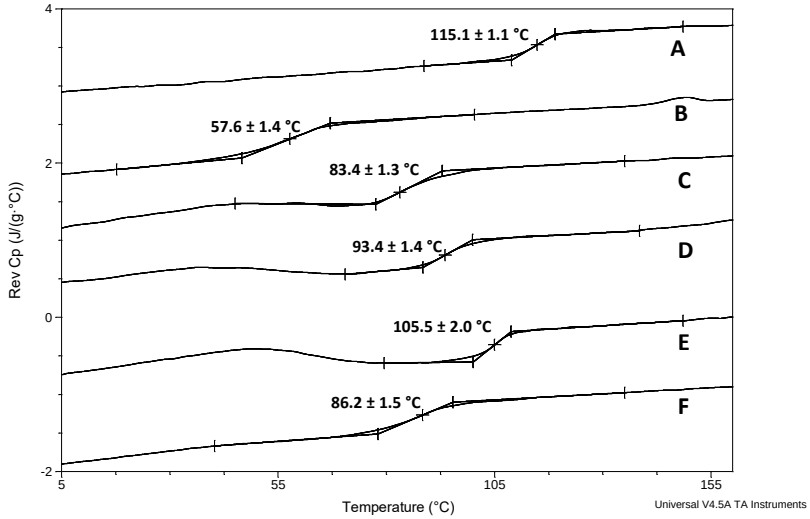

Figure 6.9 MTDSC results of 25% PCM loaded single polymer fibre mats and PVP-HPMCAS blend fibre mats. (A) PCM-PVP, (B) PCM-HPMCAS, (C) PCM-PVP-HPMCAS 1:2, (D) PCM-PVP-HPMCAS 1:1, (E) PCM-PVP-HPMCAS 3:1 and (F) PCM-PVP-HPMCAS 1:1 core-shell electrospun fibres.

Table 6.2 Comparison of experimental and theoretical glass transition temperatures (T_g) of all formulations predicted using GT equation.

Materials	T_g (°C)	GT predicted T_g(°C)
PCM	25.3±1.3[a]	-
PVP	176.4±2.0[a]	-
HPMCAS	122.0±2.2[a]	-
PCM-PVP	115.1±1.1[b]	119
PCM-HPMCAS	57.6±1.4[b]	86
PVP-HPMCAS		
3:1	163.4±1.2[b]	160
1:1	149.2±1.3[b]	151
1:2	139.3±2.1[b]	140
PCM-PVP-HPMCAS		
3:1	105.5±2.0[b]	110
1:1	93.4±1.4[b]	101
1:2	83.4±1.3[b]	96

[a] Measured by MTDSC from raw materials**.**

[b] Measured by MTDSC using electrospun materials**.**

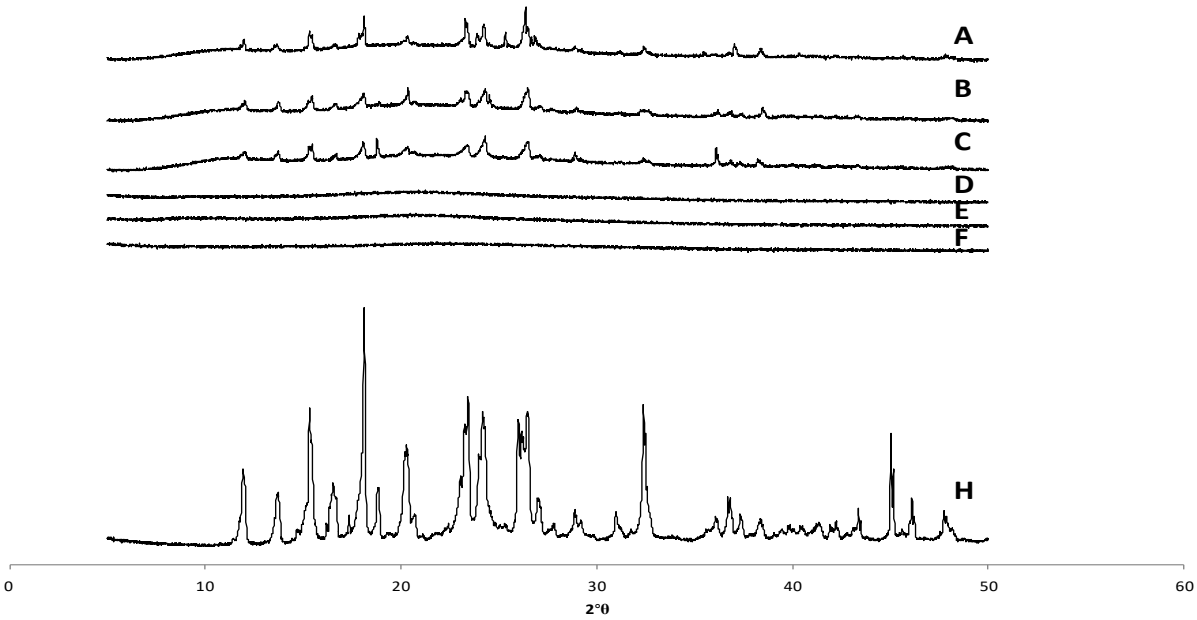

Figure 6.10 Comparison of PXRD patterns of physical mixtures (PVP, HPMCAS and PCM powder) and PVP-HPMCAS blend electrospun fibres loaded with PCM. PVP-HPMCAS physical mixture ratios (w/w) of 3:1 (A), 1:1 (B) and 1:2 (C). The PVP-HPMCAS blend electrospun fibres with polymer ratios of 3:1 (D), 1:1 (E), 1:2 (F) and PCM crystalline form I (H).

The phase separation of the PCM loaded polymer blend fibres was further investigated using NMR relaxometry. Relaxation times were measured in all PCM-loaded fibres (**Table 6.1**). Single exponential T_1's were observed for all samples, but were lengthened in comparison to the unloaded samples. In contrast, the $T_{1\rho}$ values, whether single or double exponential, were shortened. This is consistent with the lengthening of the correlation times on incorporation of the drug. Due to the long correlation time side of the T_1 minimum, an increase in the correlation time will result in a lengthening of T_1. If, however, the correlation time is on the short side of the $T_{1\rho}$ minimum, which occurs at a longer correlation time than the T_1 minimum, the $T_{1\rho}$ will shorten.

The single exponential $T_{1\rho}$s observed in the mixtures with single polymer components indicate that the length scale of any phase separation must be sub-nanometre and is consistent with a completely homogeneous material with the drug molecularly dispersed. Similarly, although two component behaviour is seen in the 3:1 and 1:1 samples with the drug incorporated, the likeliest explanation is that this is due to polymer phase separation as drug phase separation would result in the observation of a long $T_{1\rho}$ component corresponding to the drug phase. The conclusions from these data are therefore consistent with the formation of a molecularly dispersed drug in both polymer phases.

6.3.3 Transformation of phase separation of electrospun blend fibres upon wetting

Prior to the drug release study, the disintegration and wetting behaviour of the fibre mats were assessed. The ultra-fast disintegration and dissolution of the placebo and drug loaded PVP electrospun fibres were complete within a few seconds following immersion in the medium (**Figure 6.11**). With the blending of HPMCAS, which is insoluble at pH 1.2, the PVP-HPMCAS blend fibres showed a change in appearance of the mat when it was wetted. Clearly separated translucent and opaque domains were observed for the wetted mat. It was also noted that the overall dimensions of the SS-ES polymer blend fibre mats shrunk significantly to one-third of their original size after they were immersed in the media (**Figure 6.12**). Interestingly, this was not observed in the CS-ES core-shell PVP-HPMCAS fibres. This indicates that this macroscopic contraction behaviour is unique to the SS-ES polymer blends and may be associated with the changes in the phase separation behaviour of the fibres after being wetted.

The changes in the phase separation behaviour during *in vitro* drug release were further investigated by recovering the fibre mats during the course of the drug release followed by an analysis of the dried material using ATR-FTIR spectroscopy. Due to the high PVP content, it was impossible to recover the material after dissolution for the PCM-loaded 3:1 PVP: HPMCAS blend. Macroscopically, the PCM loaded SS-ES fibres transformed into a gel-like mass with a translucent surface layer and opaque centre after 5 min of being immersed in the dissolution media. After drying, the surface layer and the opaque centre could be separated easily, and the ATR-FTIR spectra of the surface coating and the centre were acquired. The ATR-FTIR spectra of both 1:2 and 1:1 PVP: HPMCAS formulations are shown in **Figure 6.13**. High relative peak intensities of PVP and PCM related peaks indicate that the translucent areas predominately have high concentrations of PVP and PCM, whereas the opaque areas mainly contain HPMCAS, in comparison to the PVP-rich areas. It is reasonable to suggest that this rapid macro-scale layered phase separation is a result of a sequence of events including wetting, migration of PVP to the surface due to the hydrophobicity difference between the HPMCAS and PVP and the formation of the PVP-rich surface coating layer. The results indicated that this re-configuration of the PVP-rich and the HPMCAS-rich phases from nanoscale separation in a dry state to macroscopically layered separation after wetting is a transformation with fast kinetics.

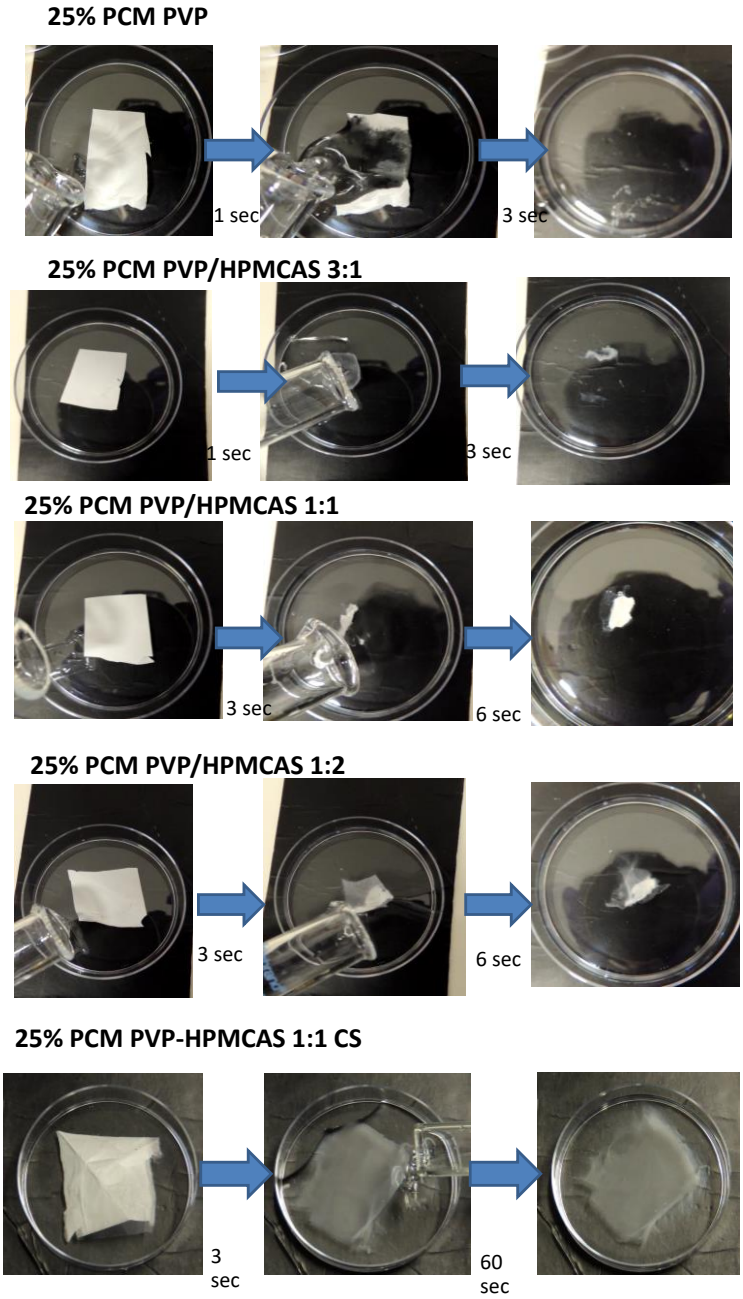

Figure 6.11 Visual observation of the effect of PVP to HPMCAS ratio on the disintegration and dissolution rate of the electrospun fibres.

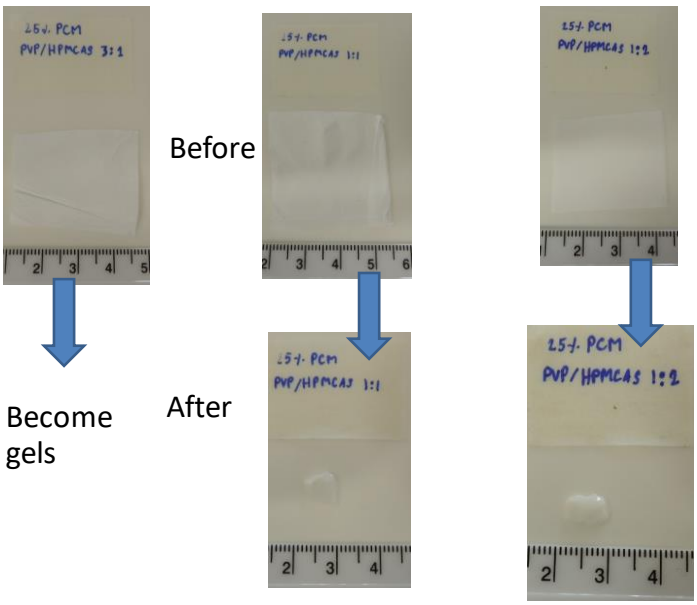

Figure 6.12 Visual observation of shrinkage of SS-electrospun PVP-HPMCAS fibre mats after immersion into pH 1.2 dissolution media for 3 min.

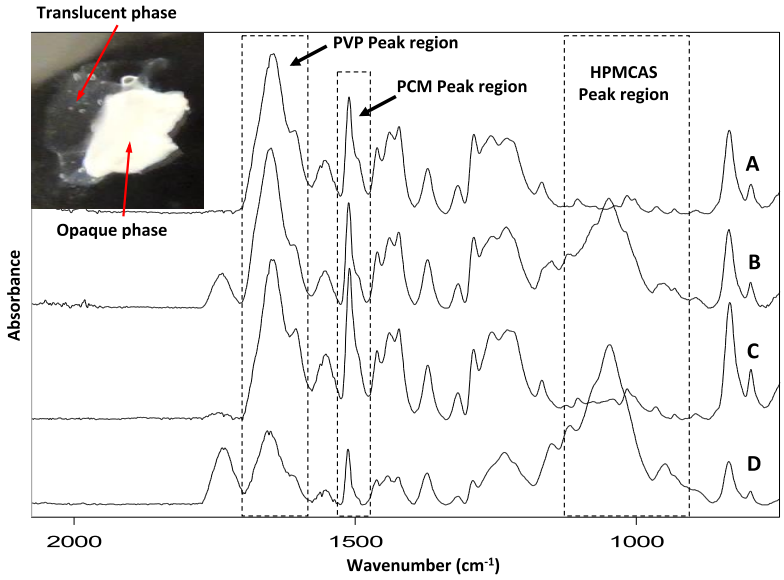

Figure 6.13 Partial ATR-FTIR spectra of wetted PCM loaded PVP-HPMCAS fibre mats with translucent coating and opaque centre as illustrated in the image insert: A and C are spectra taken from translucent areas of the formulations with PVP-HPMCAS 1:1 and 1:2, respectively, and B and D are their corresponding opaque central areas. Dashed boxes highlight signature peaks of PVP and HPMCAS at 1660 and 1072 cm^{-1}, respectively.

Further testing was conducted to follow the course of the phase separation changes during the dissolution. In these tests, spectra were acquired from samples that had been removed from the dissolution media at different stages of the *in vitro* dissolution testing and dried. As seen in **Figure 6.14**, after 5 min of dissolution testing, signature peaks of PVP, PCM and HPMCAS at 1655, 1554 and 1072 cm^{-1}, respectively, could be clearly identified, which indicated the presence of all components in the wetted mat. With increases in the dissolution time, the relative peak intensity of the 1072 cm^{-1} HPMCAS peak increased, while the relative intensities of the PVP and PCM related peaks decreased in both formulations. Using the relative intensity as a coarse measure, the relative concentration changes of the components could be estimated. The ratios of PCM, PVP and HPMCAS were 34:51:15, 23:37:40, 0:19:81 and 0:21:79 for 5, 15, 30 and 60 min of dissolution, respectively. This reflects the dissolution and release of PVP and PCM to the media, whereas insoluble HPMCAS remained largely intact. The low quantity of the remaining PVP in the HPMCAS phase can be attributed to the partial miscibility of PVP and HPMCAS. This may impact the drug release behaviour of the formulations as the PVP-rich phase tends to have a faster drug release rate, while the HPMCAS-rich phase reserves the drug as HPMCAS is insoluble at the acidic pH 1.2.

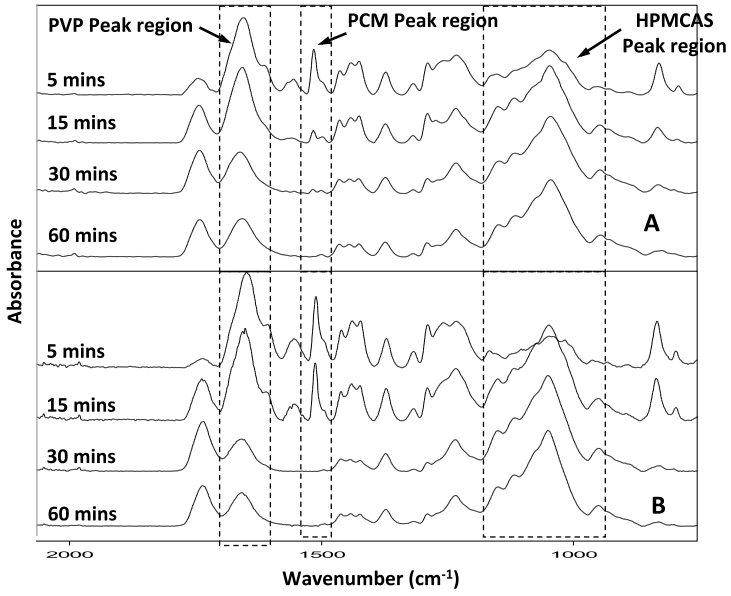

Figure 6.14 Partial ATR-FTIR spectra of PCM loaded PVP-HPMCAS blended fibre mats with polymer ratios of (A) 1:1 and (B) 1:2 when sampled at different time intervals during dissolution experiments. Dashed boxes represent signature peaks of PVP, PCM and HPMCAS at 1660, 1512 and 1072cm^{-1}, respectively.

6.3.4 *In vitro* drug release kinetics of electrospun blend fibres

The PCM release profiles were obtained from all blend formulations, as seen in **Figure 6.15**. The PVP-PCM fibres exhibited an immediate release with complete drug release being obtained within 5 min. The PCM-HPMCAS drug release study was not conducted because the HPMCAS alone is an extremely poor fibre forming material and no proper fibre mat could be generated. The PCM-PVP-HPMCAS blend fibres demonstrated an initial burst release with up to 50% of the PCM released within 10 min and 100% released in 1 h for PVP:HPMCAS mats with weight ratios of 3:1 and 1:1, but only approximately an 80% release for the PVP:HPMCAS 1:2 blend. Despite the polymer ratio difference, the core-shell HPMCAS(core)-PVP(shell) 1:1 fibres showed a similar trend of drug release to the PVP: HPMCAS 1:2 blends with 50% PCM release in the first 10 min and 85% release in 1 h.

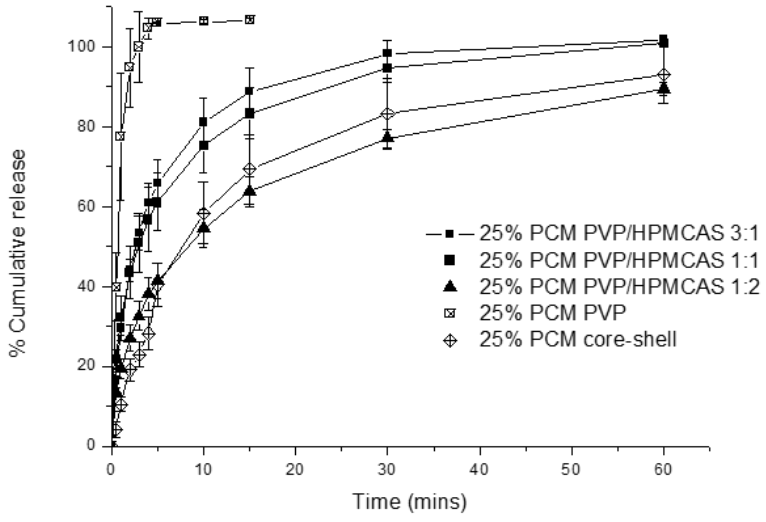

Figure 6.15 *In vitro* drug release profiles of PCM loaded PVP single phase, polymer blend fibres with different PVP: HPMCAS ratios and coaxial electrospun fibre.

Data fitting to the power law and biphasic models was performed to obtain insights into the mechanism of the drug release from the formulations. As seen in **Table 6.3**, the coefficients of determination (R^2) of the power law fitting for only 60% drug release data (25) were greater than 0.98 for all blend formulations. The exponents (n) of the SS PVP-HPMCAS 3:1 blend and CS-ES core-shell fibre formulations were in the range of 0.45-0.89, which indicates the drug release was dominated by anomalous transportation, which refers to a combination of Fickian diffusion and case II transport (25). For SS-ES PVP-HPMCAS blends with ratios of 1:1 and 1:2, the n values of 0.42 and 0.43 were obtained, respectively. This indicates that Fickian diffusion was the dominant release mechanism for these formulations (25, 26). However, it should be highlighted that ignoring the remaining 40%

release, which is much slower than first 60% for all blend formulations, may give misleading results with regard to the release mechanisms of these phase-separated nanofiber blend mats.

When the power law and biphasic release models were fitted to the entire 60-minute release data, the R^2 values of the power law fit decreased significantly, whereas the biphasic model fit gave R^2 values greater than 0.99 (**Table 6.3**). The biphasic model allowed the estimation of the amount of drug release (M_a and M_b) and kinetic exponential (k_a and k_b) of both phases (assumed to be completely phase-separated PVP-PCM and HPMCAS-PCM phases). The fact that M_a and M_b did not together come to 100% can be explained by some miscibility between the PVP and HPMCAS, as discussed earlier. The k_a and k_b values of all polymer blends and core-shell formulations were found to differ significantly, with k_a being approximately six times greater than k_b. This refers to PCM being released faster from one phase (likely the PVP-rich phase) than the other phase (likely the HPMCAS-rich phase).

It should be kept in mind that the biphasic model contains more variables for fitting in comparison to the power law model. This may lead to better data fitting and higher R^2 values for the biphasic model, without necessarily being a truly more accurate description of the dissolution process. To test the relative likelihood of these two possibilities, AICc was employed. The AICc scores of the biphasic model fitting of all SS-ES PVP-HPMCAS blend fibres are significantly lower (which means distinctively better suitability) than the ones of the power law model. Therefore, the biphasic model is universally superior to a descriptive drug release model for SS PVP-HPMCAS blend fibres. The AICc scores of the biphasic fitting for the CS PVP-HPMCAS 1:1 fibres are also lower than those of the power law fittings, which indicates the biphasic model as being a better descriptive model of the drug release behaviour.

Table 6.3 Kinetic parameters obtained from fitting 60 min dissolution experimental data of PCM loaded nanofibers to power law and first order biphasic model.

PVP-HPMCAS ratio	Power law			Alkaike test (AICc)	First order bi-phasic						Alkaike test (AICc)
	R^2	k	n		R^2	M_a	M_b	k_a	k_b	M_a+M_b	
SS 3:1	0.81	43.99	0.189	71	0.997	45.01	48.28	0.399	0.098	93.29	45
SS 1:1	0.87	42.56	0.192	65	0.998	49.00	35.99	0.287	0.048	84.99	39
SS 1:2	0.94	26.80	0.271	57	0.999	30.48	57.19	0.112	0.015	87.67	33
CS 1:1	0.70	29.70	0.267	67	0.994	54.98	43.97	0.15	0.043	98.95	65

PVP-HPMCAS ratio	Power law (data fitting for 60% of drug release)		
	R^2	k	n
SS 3:1	0.984	28.45	0.56
SS 1:1	0.991	31.27	0.42
SS 1:2	0.996	24.2	0.43
CS 1:1	0.98	12.25	0.69
PVP alone	0.81	67.12	0.41

6.4 Discussion

6.4.1 Improved apparent miscibility of polymer blends by processing and drug incorporation

- **Effect of solvent**

The seemingly contradictory results of this study and other recent literature on the apparent miscibility of PVP and HPMCAS should first be clarified. In the literature, PVP and HPMC blends were established as miscible by Karavas and co-workers by a cast film method, but with weak interactions between the carbonyl group of the PVP and the hydroxyl group of the HPMC (27). More recently, Marks and co-workers prepared HPMCAS and PVP K29/32 blends by spray drying using 1:1 ethanol:DCM as a solvent and observed that they were miscible based on MTDSC data (15). In the previous chapter, when PVP K 90 was used with HPMCAS, which was dissolved in 3:7 DCM:ethanol, and prepared by film casting and SS-ES, they showed a single T_g that indicated a miscibility between the PVP and the HPMCAS. However, in this chapter, a double T_g was observed from the cast film formulation of PVP-HPMCAS, which was dissolved in 9:1 ethanol:water. This is an indication of the phase separation of PVP and HPMCAS. While SS-ES PVP-HPMCAS fibres show the nanophase separation that was observed by ss-NMR relaxometry.

A solvent system can be a potential factor that affects the conformational properties of the polymer in solution (1). There are two types of solvent, related to the capability of the solvent to solvate the polymer: a good solvent and a bad solvent. In the good solvent, the polymer is fully solvated, which results in it displaying swelling and extending conformation. In contract, the bad solvent partially solvates the polymer. Consequently, this leads to a compact conformation because the repeated units of the polymer interact amongst themselves more than the solvent molecules. Therefore, the compact form potentially leads to phase separation (1). Al-obaidi et al. reported the use of different solvent mixtures (acetone-methanol and acetone-water) in spray drying affected the stability and dissolution of the ternary solid dispersion of griseofulvin, PVP and poly[N-(2-hydroxypropyl)methacrylate] (PHPMA) (1). The ternary solid dispersions dissolved in acetone-water demonstrated a better physical stability and dissolution rate than the one dissolved in acetone-methanol. Even though the ternary prepared from an acetone-water solvent had a lower T_g than the ternary prepared from acetone-methanol, their T_gs were 84 and 104°C, respectively. The authors explained that these two solvent systems caused a different polymer conformation in the ternary systems after a complete solvent evaporation resulting in the different physical stabilities and dissolutions. Acetone-methanol enhances the miscibility between the PVP and the PHPMA, which resulted in a phase separation of griseofulvin that later lead to the drug's recrystallization. While acetone-water encouraged

PHPMA to form an interaction with griseofulvin (1). As a consequence, it resulted in a better physical stability in comparison to the other solvent system. In our case, PVP is freely soluble in ethanol, DCM and water (28). While, HPMCAS is soluble in DCM, ethanol and alcoholic aqueous, but insoluble in water (29). DCM and ethanol are good solvents for PVP and HPMCAS in which the polymers demonstrate a conformational extent. In contrast, the polymer chain of HPMCAS may form a compacted conformation because water is a bad solvent for HPMCAS. The use of 9:1 ethanol:water as the solvent could potentially cause a different polymeric conformation of PVP-HPMCAS in comparison to the PVP-HPMCAS that was prepared from 7:3 ethanol:DCM. As a consequence, it led to the immiscibility and phase separation of the PVP-HPMCAS.

- **Effect of preparation methods**

The results of this study suggest that the different rates of solvent evaporation used in the preparation methodology may have a significant impact on the size of the phase separated domains in the blend material. Techniques with slow solvent evaporation rates lead to micron, or even larger, scale phase separations, which were determined by MTDSC and AFM. The rapid solvent evaporation technique, electrospinning, in combination with rapid 2D deformation by elongating the blend into nanosized fibres with highly confined dimensions improved the apparent miscibility. The outcome of the drying process used in the different preparation methods may be determined by the thermodynamics of the system or the kinetics of drying.

The relative rates of ethanol and water evaporation may be important in the determination of the phase behaviour: at 90% ethanol, water shows a positive deviation from Raoult's law and ethanol follows Raoult's law line; therefore, at 90% ethanol and above there is more water in the vapour phase than would be predicted by its pure vapour pressure and concentration. Therefore, the evaporation rates of ethanol may be slower than expected. However, it is not clear if the system is at equilibrium and, as it also contains a polymer and drug, the vapour pressures of the five-component system may not reflect the simple binary system. In addition, as the solvent evaporates, the high polymer concentrations will impede the diffusion of the solvent molecules, and it is possible that water as the smaller molecule may escape faster.

The process of electrospinning is very rapid and the observation of the phase separation will depend on the relative rates of evaporation and polymer phase separation. If the latter process is slow compared to the solvent loss, then a molecularly dispersed polymer mixture will be "frozen in place" despite the differences in the intrinsic solubilities. If the polymer phase separation is fast compared to the evaporation rate, then phase separation may take

place. PCM incorporation significantly affected the phase behaviour of the system and improved the miscibility of the PVP and HPMCAS. It is possible that this is a result of a combination of PCM acting as a molecular solvent and the reduced viscosity of the solution (as PCM replaced the same amount of polymer in the solution), which aids the mixing during the drying stage of the electrospinning process for both SS- and CS-ES.

6.4.2 Effect of wetting and dissolution on phase separation and their impact on drug release

PCM demonstrated a higher degree of partition into the PVP-rich rather than the HPMCAS-rich phase. The length scale of the phase separation was rapidly amplified into the macro-scale layers after the electrospun fibres were wetted by the dissolution media. This rapid dynamic transformation from nanoscale phase separation to layered separation was speculated to be a result of the rapid local phase separation and the migration of the PVP to the surfaces of the wetted mats. As a consequence of such phase separation transformations, in which the majority of the initial drug is released from the PVP-rich phase, and being followed by the slower release from HPMCAS-rich phase, a clear biphasic drug release behaviour was observed in all the blend fibre formulations. This biphasic drug release mechanism was confirmed by the fact that when alternating the ratio of PVP and HPMCAS in the blend, the drug release profile of the fibres could be tuned to the desired rate. It is worth mentioning that HPMCAS is a pH sensitive polymeric excipient, which is known to dissolve at a pH above 5.0 and is often used for enteric coating (30). Therefore, the slower drug release from the HPMCAS than PVP phases, as was observed in the dissolution tests of this study, would be expected. It is likely that the drug contained in the HPMCAS phases of the formulations with high HPMCAS content will be released rapidly once the formulation reaches the small intestine due to the increased solubility of HPMCAS at the intestinal pH. Although a single model drug was used for the proof-of-concept in this project, the use of the dynamic phase behaviour of the polymer blend to control drug release for improved delivery of one or multiple drugs in one formulation should be explored in future.

6.5 Conclusion

Nanofabrication methods, such as electrospinning, have been increasingly used in the preparation of drug delivery systems. This chapter investigated the phase behaviour of blends of a pair of partially miscible polymers, PVP K-90 and HPMCAS, after processing by electrospinning. The results confirmed nanoscale phase separation of the electrospun fibres in contrast to the micron-scale phase separation in the blends prepared by

conventional blending methods, such as film casting and spin-coating. This difference is likely to be a result of the differences in the solvent evaporation rates of the methods. The incorporation of the low molecular weight model drug, PCM, led to enhanced miscibility between the polymers. This improved miscibility of the ternary system was significantly compromised once the fibre mats were placed in the dissolution media. Macroscale layered phase separation of the two polymer-drug phases was detected. This phase behaviour led to a biphasic drug release, which could potentially be used to tune the release rate of the fibre mats through altering the ratio of the polymers in the blend. The results of this chapter have demonstrated the potential of the concept of using *in situ* phase separation of the polymers to tune the drug release rate, which can potentially be adopted for delivering two drugs in a single formulation that has different desired target release areas in the gut.

6.6 References

1. Al-Obaidi H, Brocchini S, Buckton G. Anomalous properties of spray dried solid dispersions. Journal of Pharmaceutical Sciences. 2009;98(12):4724-37.
2. Brettmann B, Bell E, Myerson A, Trout B. Solid-state NMR characterization of high-loading solid solutions of API and excipients formed by electrospinning. Journal of Pharmaceutical Sciences. 2012;101(4):1538-45.
3. Nagy ZK, Balogh A, Vajna B, Farkas A, Patyi G, Kramarics Á, et al. Comparison of electrospun and extruded soluplus®-based solid dosage forms of improved dissolution. Journal of Pharmaceutical sciences. 2012;101(1):322-32.
4. Yu D-G, Wang X, Li X-Y, Chian W, Li Y, Liao Y-Z. Electrospun biphasic drug release polyvinylpyrrolidone/ethyl cellulose core/sheath nanofibers. Acta biomaterialia. 2012.
5. Jiang Y-N, Mo H-Y, Yu D-G. Electrospun drug-loaded core-sheath PVP/zein nanofibers for biphasic drug release. International Journal of Pharmaceutics. 2012.
6. Kim K, Luu YK, Chang C, Fang D, Hsiao BS, Chu B, et al. Incorporation and controlled release of a hydrophilic antibiotic using poly (lactide-co-glycolide)-based electrospun nanofibrous scaffolds. Journal of Controlled Release. 2004;98(1):47-56.
7. Yan S, Xiaoqiang L, Shuiping L, Xiumei M, Ramakrishna S. Controlled release of dual drugs from emulsion electrospun nanofibrous mats. Colloids and Surfaces B: Biointerfaces. 2009;73(2):376-81.
8. Yu D-G, Chian W, Wang X, Li X-Y, Li Y, Liao Y-Z. Linear drug release membrane prepared by a modified coaxial electrospinning process. Journal of Membrane Science. 2012.
9. Yang Z, Nollenberger K, Albers J, Craig D, Qi S. Microstructure of an Immiscible Polymer Blend and Its Stabilization Effect on Amorphous Solid Dispersions. Molecular Pharmaceutics. 2013;10(7):2767-80.
10. Yu D-G, Branford-White C, White K, Li X-L, Zhu L-M. Dissolution improvement of electrospun nanofiber-based solid dispersions for acetaminophen. AAPS PharmSciTech. 2010;11(2):809-17.
11. Yu D-G, Shen X-X, Branford-White C, White K, Zhu L-M, Bligh SA. Oral fast-dissolving drug delivery membranes prepared from electrospun polyvinylpyrrolidone ultrafine fibers. Nanotechnology. 2009;20(5):055104.
12. Tanno F, Nishiyama Y, Kokubo H, Obara S. Evaluation of Hypromellose Acetate Succinate (HPMCAS) as a Carrier in Solid Dispersions. Drug Development and Industrial Pharmacy. 2004;30(1):9-17.
13. Lu Q, Zografi G. Phase Behavior of Binary and Ternary Amorphous Mixtures Containing Indomethacin, Citric Acid, and PVP. Pharmaceutical research. 1998;15(8):1202-6.
14. Forster A, Hempenstall J, Tucker I, Rades T. The potential of small-scale fusion experiments and the Gordon-Taylor equation to predict the suitability of drug/polymer blends for melt extrusion. Drug Development and Industrial Pharmacy. 2001;27(6):549-60.
15. Marks JA, Wegiel LA, Taylor LS, Edgar KJ. Pairwise Polymer Blends for Oral Drug Delivery. Journal of Pharmaceutical Sciences. 2014;103(9):2871-83.
16. Fedors RF. A method for estimating both the solubility parameters and molar volumes of liquids. Polymer Engineering & Science. 1974;14(2):147-54.
17. Belton PS, Hills BP. The effects of diffusive exchange in heterogeneous systems on N.M.R. line shapes and relaxation processes. Molecular Physics. 1987;61(4):999-1018.
18. Clauss J, Schmidt-Rohr K, Spiess HW. Determination of domain sizes in heterogeneous polymers by solid-state NMR. Acta Polymerica. 1993;44(1):1-17.
19. Spiegel S, Schmidt-Rohr K, Boeffel C, Spiess HW. 1H spin diffusion coefficients of highly mobile polymers. Polymer. 1993;34(21):4566-9.

20. McBrierty VJ, Packer KJ. Nuclear magnetic resonance in solid polymers: Cambridge University Press; 2006.
21. Thakral S, Thakral NK. Prediction of drug–polymer miscibility through the use of solubility parameter based flory–huggins interaction parameter and the experimental validation: PEG as model polymer. Journal of Pharmaceutical Sciences. 2013;102(7):2254-63.
22. Anastasiadis SH, Gancarz I, Koberstein JT. Interfacial tension of immiscible polymer blends: temperature and molecular weight dependence. Macromolecules. 1988;21(10):2980-7.
23. Konno H, Taylor LS. Influence of different polymers on the crystallization tendency of molecularly dispersed amorphous felodipine. Journal of Pharmaceutical Sciences. 2006;95(12):2692-705.
24. Taylor LS, Zografi G. Sugar–polymer hydrogen bond interactions in lyophilized amorphous mixtures. Journal of Pharmaceutical sciences. 1998;87(12):1615-21.
25. Ritger PL, Peppas NA. A simple equation for description of solute release I. Fickian and non-Fickian release from non-swellable devices in the form of slabs, spheres, cylinders or discs. Journal of controlled release. 1987;5(1):23-36.
26. Siepmann J, Peppas N. Modeling of drug release from delivery systems based on hydroxypropyl methylcellulose (HPMC). Advanced drug delivery reviews. 2012.
27. Karavas E, Georgarakis E, Bikiaris D. Application of PVP/HPMC miscible blends with enhanced mucoadhesive properties for adjusting drug release in predictable pulsatile chronotherapeutics. European Journal of Pharmaceutics and Biopharmaceutics. 2006;64(1):115-26.
28. Kolter K, Karl M, Gryczke A, Ludwigshafen am Rhein B. Hot-melt extrusion with BASF pharma polymers: extrusion compendium: BASF; 2012.
29. NF Hypromellose acetate succinate Shin-Etsu AQQAT entric coating agent 2005.
30. Friesen DT, Shanker R, Crew M, Smithey DT, Curatolo WJ, Nightingale JAS. Hydroxypropyl Methylcellulose Acetate Succinate-Based Spray-Dried Dispersions: An Overview. Molecular Pharmaceutics. 2008;5(6):1003-19.

7. Chapter 7: Concluding remarks and future outlook

7.1 Crystallisation of amorphous FF

The spontaneous crystallisation of amorphous FF is unpredictable and difficult to control. Hence, heterogeneous nucleation, which is a common means to initiate the crystallisation of APIs (1-3), was used to crystallise the amorphous FF. This method includes the surface disruption technique and use of impurity additives (talc). Additionally, controlling the crystal growth temperature and the presence of an OTS have indicated the prospect of controlling the crystallisation into specific polymorphs (4-8). These approaches were applied to study the crystallisation of amorphous FF in this project. The results of this project lead to a better understanding of the crystallisation of amorphous FF. One of the significant findings in Chapter 3 was a clarification of the confusion in the literature about FF form IIs. Di Martino et al. and Balendiran et al. reported the discovery of FF form IIs (9, 10). The DSC, ATR-FTIR, PXRD and SCXRD results presented in Chapter 3 confirmed that the FF form IIs that were obtained by Di Martino et al. and Balendiran et al. were not the same.

The FF form II that Di Martino reported (referred to as form IIa) was further investigated to determine the factors that influence its crystallisation. We observed that the use of an OTS and crystal growth temperature can control the crystallisation of specific polymorph of FF. The FF form I prefers to grow at the OTS site; in contrast, the form IIa was found to crystallise beneath the surface. The crystallisation of amorphous FF between the sandwiched coverslips (B-FF) resulted in pure FF form IIa. The switching of the crystal growth mode of polymorph IIa to I was observed when the cover was removed during the partial crystallisation of form IIa. Consequently, the rest of the amorphous FF crystallised as form I. This finding corresponds to the cross-nucleation phenomenon in which one polymorph nucleate on the surface of another polymorph (8, 11). Additionally, the environmental temperature during the crystal growth influenced the polymorphs of the FF. The optimal crystal growth temperature of form IIa was determined at 40°C with an OTS while both OTS-FF and B-FF crystallise at 70°C in the pure form I.

In Chapter 4, the addition of talc was used to induce the heterogeneous nucleation of amorphous FF. The crystallisation of the new FF form III was a consequence of using talc as the heterogeneous nuclei. The characteristic data of FF form III were collected, including melting point, ATR-FTIR spectrum, PXRD pattern and single crystal structure. The mechanism of the FF form III crystallisation is due to the talc crystals inducing the form III nuclei. The physical stability data of FF form III showed that it is highly thermodynamically instable, and likely to convert to its more stable polymorphs (forms I

and IIa) upon ageing, on incubated or elevated temperatures or undergoing mechanical stress such as milling.

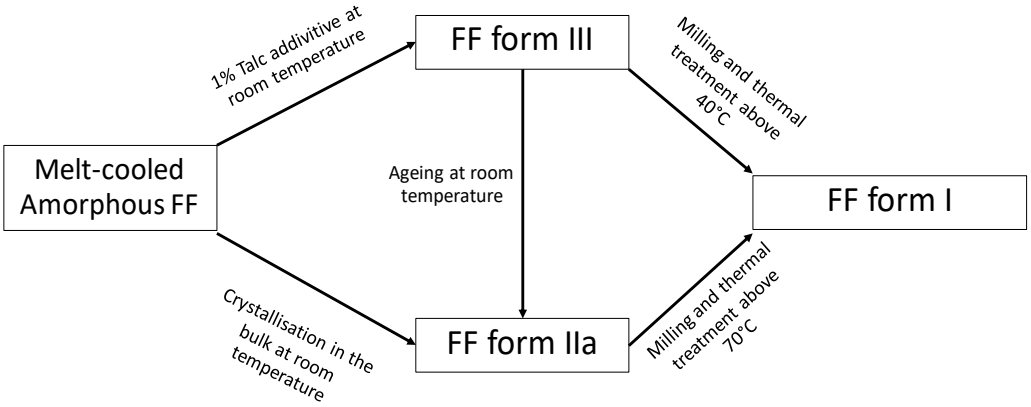

Figure 7. 1 Summary of polymorphic conversions between different polymorphs of FF.

7.2 Solid dispersions for stabilising amorphous FF

Electrospinning was found to be an efficient means to prepare the FF solid dispersions (12, 13). In the literature, it has been used to prepare ultrafast release and sustained-release electrospun fibres for the oral route (14-17). The fresh 25% w/w FF loaded PVP electrospun fibres showed a lower amount of recrystallised FF crystals than the PVP cast films. Blending PVP with poorly spinnable polymers, including HPMCAS, Soluplus and Eudragit, enhanced the spinnability of the blends, which was shown by the reduction in the beading on the fibres and the fibres becoming a more cylindrical shape. The FF-PVP, FF-PVP-Eudragit E, FF-PVP-Soluplus and FF-PVP-HPMCAS fibres significantly improved the dissolution of the FF in comparison with its crystalline form I. FF-PVP and FF-PVP-Eudragit E can be used as an immediate release formulation; whereas FF-PVP-HPMCAS demonstrated its potential in the sustained-release application. The electrospun fibres showed a faster rate of moisture sorption than their cast films. The fibrous structure deformation, including increasing its rigidness and fibre shrinkage, was a consequence of the moisture sorption. In terms of the physical stability, we observed that the polymer blended matrices showed better stabilisation of the amorphous FF than pure PVP.

The polymer-polymer and drug-polymer apparent miscibility are essential pieces of information that need to be taken into account for formulating the ternary solid dispersions as they play an important role in affecting the physical stability of the solid dispersions. FF showed a good apparent miscibility with Eudragit E and Soluplus, which could be potentially attributed to the dipole-dipole interactions between drug and polymer. It was observed that these polymers could stabilise 25% w/w FF under 75% RH and also caused uneven FF distribution in the phase separated FF-PVP-Eudragit E and FF-PVP-Soluplus

solid dispersions. In contrast, FF and PVP blends lack the hydrogen bonding that the drug and polymer have, and so have a low level of molecular interaction. Thus, the polymer matrices could only partially stabilise the amorphous drug. The FF-PVP-HPMCAS blends showed a stronger polymer-polymer dipole-dipole interaction than the drug-polymer interaction. Consequently, half of the 25% w/w FF loaded in the formulation rapidly crystallised when it was exposed to 75% RH. On the contrary, the PCM-PVP-HPMCAS blends showed a high physical stability because PCM forms a hydrogen bond with PVP. Therefore, it can minimise the moisture uptake and inhibit the amorphous PCM recrystallization in the presence of a high moisture environment (75% RH).

The results of this project suggest that the polymer pair needs to be carefully selected by considering their polymer-polymer and drug-polymer miscibility in the ternary solid dispersion. The apparent polymer-drug miscibility is an important factor that maintains the drugs in their amorphous state even in a high humidity environment. The drug that is used in the ternary solid dispersion electrospun fibres should form hydrogen bonds with at least one of the polymers, which is most likely to be the hydrophilic polymers due to the carbonyl group in their structure. Consequently, this will enhance the physical stability of API in the ternary solid dispersions.

7.3 Phase separation behaviour: A key to stabilise amorphous drugs in complex blends and achieving modified drug release performance

Phase separation has been observed in FF-PVP-Eudragit E and FF-PVP-Soluplus solid dispersions in which FF was unevenly distributed among the polymers. The uneven FF resulted in the physical stability enhancement of these formulations, since it can protect the majority of the amorphous drug from recrystallization under 75% RH **Figure 7. 2A**. Apart from stabilising the amorphous drug, the *in situ* phase separation of PCM-PVP-HPMCAS electrospun polymer fibres was observed. The nanophase separation of PCM-PVP-HPMCAS was magnified to the macro scale upon dissolution. The electrospun fibre shrinkage corresponded to the microstructure deformation when the fibres were wetted, and this consequently resulted in the phase separation of the PVP rich phase and HPMCAS rich phase. This phase separation resulted in the modified release of the drug in which the PVP rich phase demonstrated burst drug release while the HPMCAS rich phase provided sustained drug release **Figure 7. 2B**. The rate of the drug release can be tuned by altering the proportions of PVP and HPMCAS.

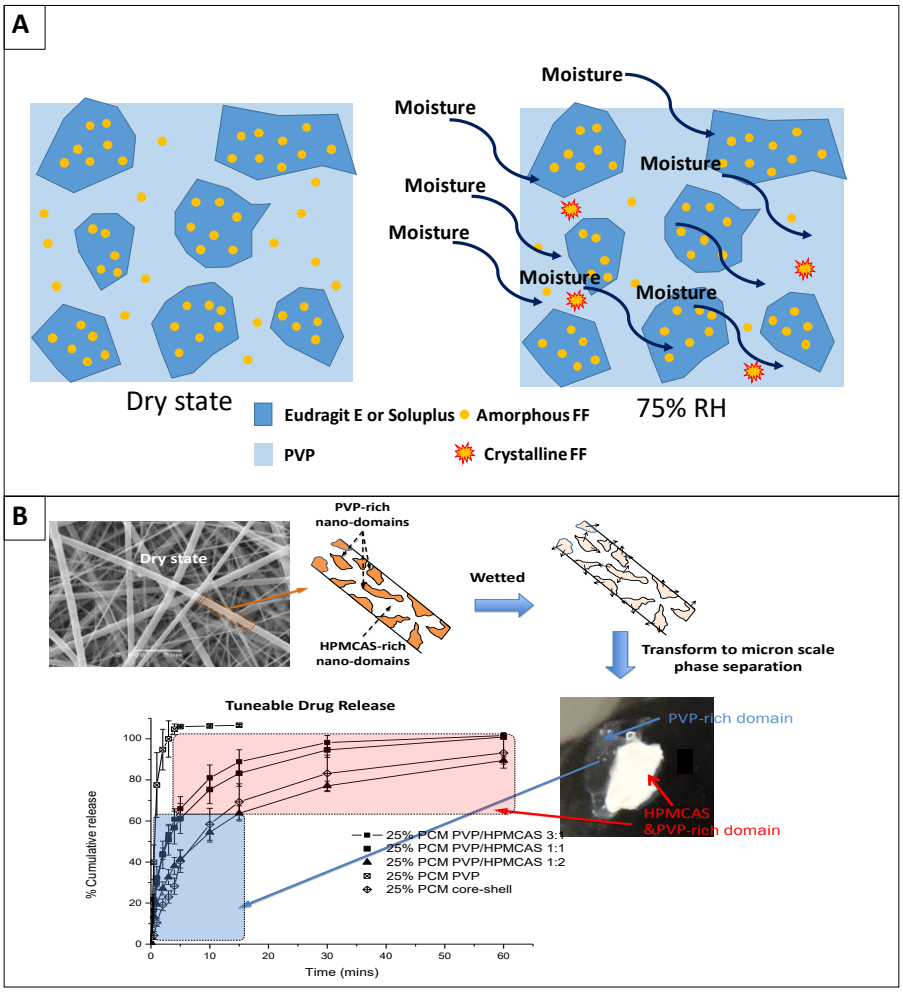

Figure 7. 2 (A) Uneven drug distribution in phase separated FF-PVP-Soluplus and FF-PVP-Eudragit E solid dispersions that results in a stabilisation of the amorphous drug at 75% RH. (B) Nanophase separation in PCM-PVP-HPMCAS fibres that transforms into a macroscopic phase separation when they are wetted. This phase separation resulted in a modified release of the drug so that the immediate release is from the PVP-rich phase while the HPMCAS-rich phase provides a sustained release.

7.4 Future outlook

- **Polymorphic control of the crystallisation of amorphous API**

The approach of using an OTS and controlling the crystal growth temperature can potentially be extended to other APIs to control their polymorphism during their amorphous crystallisation into the desired polymorph. Therefore, it could be produced to create seeds, which are then used for solution crystallisation. In addition, the use of talc as a heterogeneous nucleation is a potential approach that can be applied to the other APIs to induce their crystallisation, particularly with the Baird et al. Class III APIs, which are difficult to spontaneously crystallise, i.e., felodipine, indomethacin, ibuprofen, ketoprofen and ritonavir (18). The talc additive is expected to be a potential means to control the

crystallisation of these APIs (19). Additionally, it is feasible to scale this up to industrial crystallisation.

- **Electrospun fibrous solid dispersions**

The results from this project raise some concerns related to the development of electrospun fibrous formulations. The selection of drug and polymer matrices need to take into account the polymer-polymer and drug-polymer miscibility. Moisture uptake causes serious damage to the fibrous structure and triggers the drug recrystallization. These pieces of information are expected to benefit the development of commercial electrospun fibrous formulations.

In addition, the proof-of-concept blending of hydrophilic and hydrophobic polymers created a biphasic release in the electrospun material from the phase separation of these polymers. Examples of blended polymer pairs that could potentially prepare a biphasic release include PVP-Ethyl cellulose, PVP-Zein, PVP-Eudragit L or S and PVP-Eudragit RL or RS. These polymer pairs are expected to demonstrate similar results to those found in this work. Furthermore, the concept of using hydrophilic and hydrophobic matrices can potentially be applied to dual drug release systems. One drug that has high miscibility to the hydrophilic polymer is expected to provide an immediate drug release while the other drug may bind to the hydrophobic phase with a slow release of the API.

7.5 References

1. Prasad KVR, Ristic RI, Sheen DB, Sherwood JN. Crystallization of paracetamol from solution in the presence and absence of impurity. International Journal of Pharmaceutics. 2001;215(1–2):29-44.
2. Rauls M, Bartosch K, Kind M, Kuch S, Lacmann R, Mersmann A. The influence of impurities on crystallization kinetics – a case study on ammonium sulfate. Journal of Crystal Growth. 2000;213(1–2):116-128.
3. Myerson A. Handbook of industrial crystallization: Butterworth-Heinemann; 2002.
4. Cai T, Zhu L, Yu L. Crystallization of Organic Glasses: Effects of Polymer Additives on Bulk and Surface Crystal Growth in Amorphous Nifedipine. Pharmaceutical research. 2011;28(10):2458-2466.
5. Chen S, Xi H, Yu L. Cross-Nucleation between ROY Polymorphs. Journal of the American Chemical Society. 2005;127(49):17439-17444.
6. Tao J, Jones KJ, Yu L. Cross-nucleation between D-mannitol polymorphs in seeded crystallization. Crystal Growth and Design. 2007;7(12):2410-2414.
7. Tao J, Yu L. Kinetics of Cross-Nucleation between Polymorphs. The Journal of Physical Chemistry B. 2006;110(14):7098-7101.
8. Yu L. Nucleation of One Polymorph by Another. Journal of the American Chemical Society. 2003;125(21):6380-6381.
9. Balendiran GK, Rath N, Kotheimer A, Miller C, Zeller M, Rath NP. Biomolecular Chemistry of Isopropyl Fibrates. J pharm sci. 2012;101(4):1555-1569.
10. Di Martino P, Palmieri G, Martelli S. Evidence of a metastable form of fenofibrate. Die Pharmazie. 2000;55(8):625-626.
11. Sun Y, Zhu L, Wu T, Cai T, Gunn EM, Yu L. Stability of Amorphous Pharmaceutical Solids: Crystal Growth Mechanisms and Effect of Polymer Additives. The AAPS Journal. 2012;14(3):380-388.
12. Ignatious F, Sun L, Lee C-P, Baldoni J. Electrospun nanofibers in oral drug delivery. Pharmaceutical research. 2010;27(4):576-588.

13. Lopez FL, Shearman GC, Gaisford S, Williams GR. Amorphous formulations of indomethacin and griseofulvin prepared by electrospinning. Molecular Pharmaceutics. 2014;11(12):4327-4338.
14. Jiang Y-N, Mo H-Y, Yu D-G. Electrospun drug-loaded core–sheath PVP/zein nanofibers for biphasic drug release. International Journal of Pharmaceutics. 2012;438(1–2):232-239.
15. Kenawy E-R, Abdel-Hay FI, El-Newehy MH, Wnek GE. Controlled release of ketoprofen from electrospun poly(vinyl alcohol) nanofibers. Materials Science and Engineering: A. 2007;459(1–2):390-396.
16. Pattama T, Uracha R, Pitt S. Drug-loaded electrospun mats of poly(vinyl alcohol) fibres and their release characteristics of four model drugs. Nanotechnology. 2006;17(9):2317.
17. Taepaiboon P, Rungsardthong U, Supaphol P. Vitamin-loaded electrospun cellulose acetate nanofiber mats as transdermal and dermal therapeutic agents of vitamin A acid and vitamin E. European Journal of Pharmaceutics and Biopharmaceutics. 2007;67(2):387-397.
18. Baird JA, Van Eerdenbrugh B, Taylor LS. A classification system to assess the crystallization tendency of organic molecules from undercooled melts. Journal of Pharmaceutical sciences. 2010;99(9):3787-3806.
19. Bruce CD, Fegely KA, Rajabi-Siahboomi AR, McGinity JW. The influence of heterogeneous nucleation on the surface crystallization of guaifenesin from melt extrudates containing Eudragit® L10055 or Acryl-EZE®. European Journal of Pharmaceutics and Biopharmaceutics. 2010;75(1):71-78.